HZDR-068

JOINT PROJECT: RETENTION OF RADIONUCLIDES RELEVANT FOR FINAL DISPOSAL IN NATURAL CLAY ROCK AND SALINE SYSTEMS

Subproject 2: Geochemical behavior and transport of radionuclides in saline systems in the presence of repository-relevant organics

Katja Schmeide, Katharina Fritsch, Holger Lippold, Maria Poetsch, Johannes Kulenkampff, Johanna Lippmann-Pipke, Norbert Jordan, Claudia Joseph, Henry Moll, Andrea Cherkouk, Miriam Bader

Wissenschaftlich Technische Berichte
HZDR-068 · ISSN 2191-8708

WISSENSCHAFTLICH-TECHNISCHE BERICHTE

HZDR
HELMHOLTZ ZENTRUM DRESDEN ROSSENDORF

Wissenschaftlich-Technische Berichte
HZDR-068

Katja Schmeide, Katharina Fritsch, Holger Lippold,
Maria Poetsch, Johannes Kulenkampff,
Johanna Lippmann-Pipke, Norbert Jordan, Claudia Joseph,
Henry Moll, Andrea Cherkouk, Miriam Bader

JOINT PROJECT: RETENTION OF RADIONUCLIDES RELEVANT FOR FINAL DISPOSAL IN NATURAL CLAY ROCK AND SALINE SYSTEMS

Subproject 2: Geochemical behavior and transport of radionuclides in saline systems in the presence of repository-relevant organics

HZDR

HELMHOLTZ
ZENTRUM DRESDEN
ROSSENDORF

Druckausgabe: ISSN 2191-8708

Elektronische Ausgabe: ISSN 2191-8716

https://www.hzdr.de/publications/Publ-23251

urn:nbn:de:bsz:d120-qucosa-197327

2016

Herausgegeben vom

Helmholtz-Zentrum Dresden - Rossendorf

Bautzner Landstraße 400

01328 Dresden

Germany

Final Report

BMWi Project No.: 02 E 10971

Joint project: Retention of radionuclides relevant for final disposal in natural clay rock and saline systems

Subproject 2: Geochemical behavior and transport of radionuclides in saline systems in the presence of repository-relevant organics

Katja Schmeide, Katharina Fritsch, Holger Lippold, Maria Poetsch, Johannes Kulenkampff, Johanna Lippmann-Pipke, Norbert Jordan, Claudia Joseph[1], Henry Moll, Andrea Cherkouk, Miriam Bader

Helmholtz-Zentrum Dresden-Rossendorf, Institute of Resource Ecology,
Bautzner Landstr. 400, 01328 Dresden, Germany

[1] Present address: Glenn T. Seaborg Institute, Physical & Life Sciences Directorate, Lawrence Livermore National Laboratory, L-231, P.O. Box 808, Livermore, CA 94550, USA

Das diesem Bericht zugrunde liegende Vorhaben wurde mit Mitteln des Bundesministeriums für Wirtschaft und Energie unter dem Förderkennzeichen 02 E 10971 gefördert. Die Verantwortung für den Inhalt dieser Veröffentlichung liegt bei den Autoren.

Vorhaben:

VERBUNDPROJEKT: Rückhaltung endlagerrelevanter Radionuklide im natürlichen Tongestein und in salinaren Systemen

Teilprojekt 2: Geochemisches Verhalten und Transport von Radionukliden in salinaren Systemen in Gegenwart endlagerrelevanter Organika

Laufzeit des Vorhabens: 01.07.2011 bis 30.06.2015

Projektleiter: Dr. Katja Schmeide

Institut für Ressourcenökologie, Helmholtz-Zentrum Dresden-Rossendorf

Contents

Summary **9**

Zusammenfassung **12**

1 Introduction and objectives **16**

2 Complexation of U(VI) by propionate at different ionic strengths in $NaClO_4$ **21**

2.1 Literature review 21

2.2 Sample preparation 21

2.3 pH measurements at high salinity 22

2.4 DFT calculations and ATR FT-IR spectroscopy 23

2.5 TRLFS spectroscopy and PARAFAC deconvolution 26

2.6 Determination of the complexation constants 28

2.7 Extrapolation to zero ionic strength 29

3 Interaction of radionuclides with microorganisms **32**

3.1 Interaction of Pu with bacterial isolates from Mont Terri Opalinus Clay 32

3.2 Eu(III), Cm(III), and U(VI) interaction with the halophilic archaeon *Halobacterium noricense* (DSM-15987) 46

3.2.1 General remarks 46

3.2.2 Eu(III)/Cm(III) 47

3.2.3 U(VI) 55

4 Dynamics of metal-humate complexation equilibria **59**

4.1 Experimental 59

4.2 Results and discussion 60

5 Influence of higher salinities on the mobilization potential of high-molecular-weight organics towards Tb(III) and Eu(III) **65**

5.1 Dispersion stability of fulvic acid in highly saline solutions (Na^+, Mg^{2+}, Ca^{2+}) 65

5.2 Effects of ionic strength and presence of fulvic acid on the adsorption of Tb^{3+} and Eu^{3+} onto Opalinus Clay 66

5.2.1 Experimental 66
5.2.1.1 Materials 66
5.2.1.2 Adsorption experiments 66
5.2.1.3 Complexation experiments 67
5.2.2 Modeling adsorption in ternary systems 67
5.2.3 Results 68
5.3 TRLFS studies of Eu-fulvate complexes at high ionic strength 71
5.3.1 Experimental 71
5.3.2 Results 72
5.4 Modeling metal binding to fulvic acid 74
5.4.1 NICA-Donnan model 74
5.4.2 Results of modeling 75
6 Tc(VII)/Tc(IV) retention by iron(II)-containing minerals 77
6.1 Experimental 77
6.2 Results and discussion 80
6.2.1 Characterization of magnetite 80
6.2.2 Batch sorption experiments 81
6.2.3 Redox potentials 83
6.2.4 ATR FT-IR spectroscopy 84
6.2.5 X-ray absorption spectroscopy 85
7 U(VI) sorption on montmorillonite at high ionic strengths 87
7.1 Experimental 87
7.1.1 Batch sorption experiments 88
7.1.2 IR and TRLFS spectroscopy 91
7.1.3 Surface complexation modeling 92
7.2 NaCl and $CaCl_2$ systems 93
7.2.1 U(VI) speciation in NaCl and $CaCl_2$ 93
7.2.2 Sorption kinetics 96
7.2.3 Cation exchange 96
7.2.4 Sorption in dependence on pH value and ionic strength 97
7.2.5 ATR FT-IR measurements 99
7.2.6 Surface complexation modeling 101

7.2.7 Extrapolation to zero ionic strength 103
7.3 Mixed electrolyte 104
7.3.1 U(VI) speciation in mixed electrolyte 105
7.3.2 Sorption in dependence on U(VI) concentration and pH value 106
7.3.3 Surface complexation modeling 108
7.4 Conclusions 110

8 Diffusion of U(VI) in Opalinus Clay in the absence and presence of citric acid 111

8.1 Materials and methods 112
8.1.1 Materials 112
8.1.2 Experimental set-up 113
8.1.3 Theoretical background 115
8.1.4 Filter diffusion parameters 116
8.2 Results and discussion 117
8.2.1 HTO diffusion in Opalinus Clay 117
8.2.2 Aqueous U(VI) and citric acid speciation 117
8.2.3 Influence of citric acid on the diffusion of U(VI) in Opalinus Clay 121
8.2.4 Diffusion of citric acid in Opalinus Clay 124
8.2.5 Conclusions 126

9 Diffusion of U(VI) in montmorillonite at high ionic strengths 127

10 Spatiotemporal observation of diffusion processes with PET for determination of heterogeneous effects on the core scale 129

10.1 Aim 129
10.2 Improvement of the PET-imaging procedure 129
10.2.1 Image reconstruction procedure and normalization 129
10.2.2 Scatter correction 130
10.2.3 Error estimation, resolution, and detection threshold 131
10.3 Measurements 132
10.4 Parameter derivation 138
10.5 Conclusions 139

11 Observation of reactive transport in fractured barrier rock 141

11.1 Aim 141

11.2 Method 141

11.3 Conclusions 142

12 References 144

13 Publications of the Helmholtz-Zentrum Dresden-Rossendorf (HZDR) 154

List of figures 159

List of tables 167

Acknowledgements 169

Summary

The objective of this project was to study the influence of increased salinities on interaction processes in the system radionuclide – organics – clay – aquifer. For this purpose, complexation, redox, sorption, and diffusion studies were performed under variation of the ionic strength (up to 4 mol kg^{-1}) and the background electrolyte (NaCl, $CaCl_2$, $MgCl_2$).

The complexation of U(VI) by propionate was studied in dependence on ionic strength (up to 4 mol kg^{-1} $NaClO_4$) by combining time-resolved laser-induced fluorescence spectroscopy (TRLFS), attenuated total reflection Fourier-transform infrared (ATR FT-IR) spectroscopy, and density functional theory (DFT) calculations. U(VI)/propionate complexes with a 1:1, 1:2, and 1:3 stoichiometry were identified. The stability constants were found to vary with ionic strength, whereby the ionic strength influence depended on the charge of the respective complexes. The conditional stability constants, determined for $UO_2(Prop)^+$, $UO_2(Prop)_2^0$ and $UO_2(Prop)_3^-$ complexes at specific ionic strengths, were extrapolated to zero ionic strength.

Microbes, as another source of organics in clay, can change the speciation of released radionuclides. The interaction of bacteria, isolated from Mont Terri Opalinus Clay core samples (Moll et al., 2013), namely *Sporomusa* sp. MT-2.99 and *Paenibacillus* sp. MT-2.2 cells, with Pu was studied in aqueous solution under anaerobic conditions. In a previous project (Moll et al., 2013), only the Pu interaction with *Sporomusa* sp. MT-2.99 cells at pH 6.1 in 0.1 M $NaClO_4$ without adding an electron donor was investigated. Now, these experiments were extended in order to get a more comprehensive overview of the interaction potential of both bacterial isolates towards Pu. The experiments can be divided into experiments without an electron donor where biosorption is favored and experiments with added Na-pyruvate as an electron donor stimulating also bioreduction processes. Additionally, the knowledge to explore actinide/lanthanide interaction processes with bacteria isolated from clay on a molecular level could be extended to microbes occurring in salt rock, another potential host rock for nuclear waste disposal. Within this project, first experiments were performed to study the interactions of the halophilic archaeon *Halobacterium noricense* DSM-15987 with U(VI), Eu(III), and Cm(III) in 3 M NaCl solutions.

Another objective of the project was to further improve process understanding concerning the mobility of radionuclides in systems containing humic matter. Attention was focused on reversibility of elementary processes and their interaction. For humate complexation of multivalent metals, the existence of a dynamic equilibrium was proven in isotope exchange studies for the first time. This is a prerequisite for the applicability of thermodynamic constants in speciation and transport modeling. However, reaction rates decrease considerably as metal concentrations are lowered to levels relevant to contaminant metals, and stabilization processes come into action. The time frames of equilibration and stabilization were investigated. Humic complexes with trace amounts of metals will not be in equilibrium with dissolved reactants or mineral surfaces if conditions change on a time scale shorter than a year. Thus, humic-bound metals are to be regarded as fixed in case of relatively fast transport processes, but not in nearly stagnant systems as present in migration scenarios related to a final repository.

The influence of high salinity (NaCl, $CaCl_2$ and $MgCl_2$ up to 4 M) on the mobilizing potential of humic-like clay organics towards actinides was investigated in radiotracer studies for binary and ternary systems of the (analogue) components [^{152}Eu]Eu(III), [^{160}Tb]Tb(III), [^{14}C]fulvic acid and Opalinus Clay at adequate concentration levels for different pH values. High ionic strengths do not lead to immobilization of fulvic acid by flocculation. Generally, however, possible mobilizing effects cannot be enhanced under highly saline conditions because metal-fulvate complexation is strongly suppressed especially by multivalent electrolytes, whereas the adsorption behavior of the organic component is largely unaffected. Its resultant effect on solid-liquid distribution of the actinide analogues can be derived and predicted from interaction data determined for the binary subsystems, in part quantitatively. This applies to the influence of ionic strength as well as the transition from demobilizing to mobilizing properties with increasing pH already in the neutral range. The effect of electrolytes on fulvate complexation was characterized in detail by luminescence spectroscopy and mechanistic modeling (NICA-Donnan approach).

The sorption of Tc(VII)/Tc(IV) onto the iron(II)-containing minerals magnetite ($Fe^{II}Fe^{III}_2O_4$) and siderite ($Fe^{II}CO_3$), occurring ubiquitously in nature and as corrosion products of carbon steel canisters used for storing radioactive waste, was studied by means of batch sorption experiments as well as ATR FT-IR and X-ray absorption spectroscopy (XAS). The strong Tc retention onto these minerals could be attributed to surface-mediated reduction of Tc(VII) to Tc(IV). It can be concluded that both minerals contribute effectively to the retention of Tc under repository conditions. An influence of ionic strength (0.1 or 1 M) was not observed.

The influence of ionic strength, background electrolyte, pH value and CO_2 absence or presence on U(VI) sorption onto montmorillonite, as model clay, was studied. As background electrolyte, pure NaCl, $CaCl_2$ or $MgCl_2$ electrolytes were used with ionic strengths up to 3 mol kg^{-1} (NaCl) or up to 9 mol kg^{-1} ($CaCl_2$, $MgCl_2$). The U(VI) sorption onto montmorillonite in NaCl and $CaCl_2$ was found to depend strongly on pH value and CO_2 presence. In $CaCl_2$, the U(VI) sorption onto montmorillonite is 0.5 to 1 log K_d units lower than in NaCl. In $MgCl_2$, the U(VI) uptake is governed by (co-)precipitation with magnesium and silicon compounds of low solubility. The influence of ionic strength on U(VI) sorption was found to be small in the investigated ionic strength range. Surface complexation modeling for the interaction of U(VI) with montmorillonite was performed applying the two-site protolysis non-electrostatic surface complexation and cation exchange (2SPNE SC/CE) model (Bradbury and Baeyens, 1997, 1999, 2002). Surface complexation constants could successfully be determined for the NaCl and $CaCl_2$ system for all ionic strengths studied. That means the 2SPNE SC/CE model can be applied to high ionic strengths. The surface complexation constants, generated at different ionic strengths, were extrapolated to zero ionic strength. The U(VI) sorption onto montmorillonite was also studied in a mixed electrolyte which consists of 2.52 mol kg^{-1} NaCl, 0.12 mol kg^{-1} $CaCl_2$ and 0.048 mol kg^{-1} $MgCl_2$ (similar to the groundwater composition in the Konrad mine, Lower Saxony (Brewitz, 1982)). It was found that surface complexation constants derived in pure electrolytes can be used to model surface complexation in mixed electrolytes.

The influence of citrate on U(VI) diffusion in Opalinus Clay was studied using Opalinus Clay pore water as background electrolyte. The diffusion parameter values obtained for the HTO through-diffusion and the U(VI) in-diffusion in the absence of citric acid were in agreement with literature data. In the presence of citric acid the U(VI) diffusion was significantly retarded, which was attributed to a change in speciation. Probably, U(VI) was reduced to U(IV) within the three months the diffusion experiment was conducted. Citric acid diffused slightly faster through OPA than small humic acid colloids, studied previously. The study shows that the chemical system has to be investigated in more detail to clarify the occurring reactions. In particular, the U(VI)-citric acid species formed under these environmentally relevant conditions needs to be described spectroscopically, thermodynamically, and structurally.

PET could be established as a reliable measurement method for quantitative determination of heterogeneous diffusion coefficients in clays and for general tracer transport studies in barrier rocks. The main focus was the improvement of quantification, both by improving image quality and the parameter determination method. Two issues of the image reconstruction procedure were identified and successfully addressed: normalization and scattering. Monte-Carlo simulations of the physical processes, from radioactive decay of the tracer nuclide to detection in the detectors, were conducted in order to estimate and quantify these effects. These studies resulted in an improved image reconstruction procedure that yields tracer concentrations quantitatively, as well as an error estimate.

PET-experiments were conducted on Opalinus Clay samples as test cases for the method and in order to better understand experimental artefacts by sample alteration and damage. Spatiotemporal data sets of the tracer concentration were computed. From these datasets diffusion coefficients were computed by inverse FEM-modeling. These diffusion coefficients are in accordance with literature results derived with through-diffusion experiments in diffusion cells. Indications for deviations from transversal-isotropic behavior on a minor level were found, which could be due to preferential diffusion pathways along silty layers or fractured zones.

Furthermore, PET-imaging was applied to better understand processes in the excavation damage zone. Here, the effect of waterglass impregnations on flow properties and pathways was investigated. The success of injection into void structures depends on a number of factors: the reaction kinetics of the injected waterglass with salt and brines, the nature of the fractures, and the injection velocity. Previously, this rather complex process could not be observed directly, and only the final results could be tested with destructive methods. Now, an improved description of this process was achieved, by which full spatial resolution over the whole time-frame becomes accessible. In these experiments the sealing success was not significant, because the waterglass congealed predominantly at the surface, and only a small portion significantly penetrated into the material.

Zusammenfassung

Ziel dieses Projektes war es den Einfluss erhöhter Salinitäten auf die Wechselwirkungsprozesse im System Radionuklid – Organika – Ton – Aquifer zu untersuchen. Deshalb wurden Komplexierungs-, Redox-, Sorptions- und Diffusionsstudien unter Variation der Ionenstärke (bis 4 mol kg^{-1}) und des Hintergrundelektrolyten (NaCl, $CaCl_2$, $MgCl_2$) durchgeführt.

Die Komplexierung von U(VI) durch Propionat wurde in Abhängigkeit von der Ionenstärke (bis 4 mol kg^{-1} $NaClO_4$) mittels TRLFS, ATR FT-IR Spektroskopie, und DFT-Rechnungen untersucht. Es wurden U(VI)/Propionat-Komplexe mit einer 1:1-, 1:2-, und 1:3-Stöchiometrie identifiziert. Ein Einfluss der Ionenstärke auf die Stabilitätskonstanten wurde nachgewiesen, wobei der Ionenstärkeeinfluss von der Ladung der entsprechenden Komplexe abhängig ist. Die konditionellen Stabilitätskonstanten, welche für $UO_2(Prop)^+$, $UO_2(Prop)_2^0$ und $UO_2(Prop)_3^-$ bei spezifischen Ionenstärken bestimmt wurden, wurden auf Ionenstärke 0 extrapoliert.

Bakterien, eine weitere Quelle für Organika im Ton, können die Speziation freigesetzter Radionuklide beeinflussen. Die Wechselwirkung von Bakterien, welche aus Mont Terri Opalinuston-Bohrkernen isoliert wurden (Moll et al., 2013), namentlich *Sporomusa* sp. MT-2.99 und *Paenibacillus* sp. MT-2.2, gegenüber Pu wurde in wässriger Lösung unter anaeroben Bedingungen untersucht. In einem früheren Projekt (Moll et al., 2013) wurde die Pu-Wechselwirkung mit *Sporomusa* sp. MT-2.99 Zellen bei einem pH-Wert von 6.1 ohne Zugabe eines Elektronendonors untersucht. Auf Basis dieser ersten Experimente wurde in diesem Projekt die Studie fortgeführt, um einen umfassenderen Überblick zu erhalten wie die beiden bakteriellen Isolate die Speziation des Pu beeinflussen können. Die durchgeführten Experimente können in solche ohne Elektronendonor, wo Biosorption dominiert, und solche mit Elektronendonor, wo auch Bioreduktionsprozesse stimuliert werden, aufgeteilt werden. Außerdem, konnten die gewonnenen Erkenntnisse hinsichtlich der komplexen Wechselwirkungsmechanismen der Actiniden/Lanthaniden mit isolierten Ton-Bakterien innerhalb dieses Projektes auf Salz-Mikroben ausgeweitet werden, da Salzgestein eine weitere potentielle Wirtsformation für die sichere Lagerung von nuklearem Abfall darstellt. Innerhalb dieses Projektes wurden erste Experimente zu den Wechselwirkungen des halophilen Archaeon *Halobacterium noricense* DSM-15987 mit U(VI), Eu(III) und Cm(III) in 3 M NaCl durchgeführt.

Ein weiteres Anliegen des Projektes war auch die Verbesserung des Prozessverständnisses hinsichtlich der Mobilität von Radionukliden in huminstoffhaltigen Systemen. Das betrifft insbesondere die Reversibilität und das Zusammenwirken der maßgeblichen Elementarprozesse. Für die Humatkomplexbildung mehrwertiger Metalle konnte die Existenz eines dynamischen Gleichgewichts in Isotopenaustauschstudien erstmals nachgewiesen werden. Dies ist Voraussetzung für die Verwendbarkeit thermodynamischer Konstanten in Speziations- und Transportmodellen. Liegt die Metallkonzentration im Spurenbereich, ist die Dissoziationsgeschwindigkeit allerdings sehr gering und unterliegt kinetischen Stabilisierungsprozessen. Die zugehörigen Zeiträume wurden für verschiedene Huminstoffe erfasst. Metall-Huminstoffkomplexe befinden sich demnach nicht im Gleichgewicht mit gelösten Reaktanden oder Mineraloberflächen, wenn sich Bedingungen in Zeitmaßstäben von weniger als einem Jahr verändern. In relativ schnellen Transportprozessen sind huminstoffgebundene Metalle

daher als fixiert zu betrachten, nicht aber in nahezu stagnierenden Fließsystemen, wie sie in endlagerbezogenen Ausbreitungsszenarien vorliegen.

Die Auswirkung hoher Salinitäten (NaCl, $CaCl_2$ und $MgCl_2$ bis 4 M) auf das Mobilisierungsvermögen von huminstoffartigen Tonorganika gegenüber Actiniden wurde in Radiotracerstudien an binären und ternären Systemen aus den (Analog-)Bestandteilen [^{152}Eu]Eu(III), [^{160}Tb]Tb(III), [^{14}C]Fulvinsäure und Opalinuston unter adäquaten Konzentrationsverhältissen bei verschiedenen pH-Werten untersucht. Hohe Ionenstärken bewirken keine Immobilisierung von Fulvinsäuren durch Ausflockung, können aber deren potentiell mobilisierende Wirkung prinzipiell nicht verstärken, denn während die Metall-Fulvatkomplexbildung vor allem durch mehrwertige Elektrolyte stark unterdrückt wird, bleibt das Adsorptionsverhalten der organischen Komponente weitgehend unverändert. Ihr resultierender Einfluss auf die Fest-Flüssig-Verteilung der Actinid-Analoga lässt sich nach einem kombinierten K_d-Modell z.T. quantitativ aus der Ionenstärkeabhängigkeit der Wechselwirkungen in den binären Randsystemen ableiten und entsprechend prognostizieren, ebenso der Übergang von demobilisierenden zu mobilisierenden Eigenschaften bei pH-Wert-Erhöhung bereits im neutralen Bereich. Der Elektrolyteffekt auf die Fulvatkomplexbildung wurde mittels Lumineszenzspektroskopie und mechanistischer Modellierung (NICA-Donnan-Ansatz) näher charakterisiert.

Die Sorption von Tc(VII)/Tc(IV) an den Fe(II)-haltigen Mineralen Magnetit ($Fe^{II}Fe^{III}_2O_4$) und Siderit ($Fe^{II}CO_3$), welche sowohl in der Natur als auch als Korrosionsprodukte der zur Lagerung des radioaktiven Abfalls genutzten Stahlbehälter vorkommen, wurde mittels Batch-Sorptionsexperimenten sowie unter Anwendung von ATR FT-IR und Röntgenabsorptionsspektroskopie (XAS) untersucht. Die starke Tc-Sorption an diesen Mineralen kann auf die oberflächeninduzierte Reduktion von Tc(VII) zu Tc(IV) zurückgeführt werden. Die Ergebnisse zeigen, dass beide Minerale effektiv zur Tc-Immobilisierung unter Endlagerbedingungen beitragen können. Ein Einfluss der Ionenstärke (0.1 oder 1 M) wurde nicht beobachtet.

Der Einfluss von Ionenstärke, Hintergrundelektrolyt, pH-Wert und CO_2-Abwesenheit bzw. Gegenwart auf die U(VI)-Sorption an Montmorillonit wurde untersucht. Als Hintergrundelektrolyt wurden NaCl-, $CaCl_2$- bzw. $MgCl_2$-Lösungen mit Ionenstärken bis zu 3 mol kg^{-1} (NaCl) bzw. bis zu 9 mol kg^{-1} ($CaCl_2$, $MgCl_2$) verwendet. Die U(VI)-Sorption an Montmorillonit in NaCl und $CaCl_2$ wird stark vom pH-Wert und der Gegenwart von CO_2 beeinflusst. In $CaCl_2$ ist die U(VI)-Sorption an Montmorillonit 0.5 bis 1 Größenordnung niedriger als in NaCl. In $MgCl_2$ wird die U(VI)-Konzentration in der überstehenden Lösung hauptsächlich durch gemeinsame Ausfällung mit Magnesium- und Siliziumverbindungen niedriger Löslichkeit gesteuert. Der Ionenstärkeeinfluss auf die U(VI)-Sorption ist im untersuchten Ionenstärke-Bereich klein. Die Modellierung der Oberflächensorption für die U(VI)/Montmorillonit-Wechselwirkung erfolgte unter Anwendung des “two-site protolysis non-electrostatic surface complexation and cation exchange (2SPNE SC/CE)“-Modells (Bradbury und Baeyens, 1997, 1999, 2002). Oberflächenkomplexierungskonstanten wurden für das NaCl- und das $CaCl_2$-System für alle untersuchten Ionenstärken ermittelt. Das zeigt, dass das 2SPNE SC/CE-Modell für die bei hohen Ionenstärken erhaltenen Sorptionsergebnisse angewendet werden kann. Die für unterschiedliche Ionenstärken erhaltenen Oberflächenkomplexierungskonstanten wurden auf Ionenstärke 0 extrapoliert. Die U(VI)-Sorption an Montmorillonit wurde auch in einem gemischten

Elektrolyten, bestehend aus 2.52 mol kg^{-1} NaCl, 0.12 mol kg^{-1} $CaCl_2$ und 0.048 mol kg^{-1} $MgCl_2$ (vergleichbar zur Grundwasserzusammensetzung im Schacht Konrad, Niedersachsen (Brewitz, 1982)) untersucht. Es zeigte sich, dass die Oberflächenkomplexierung in gemischten Elektrolyten mit den im NaCl- bzw. $CaCl_2$-System bestimmten Oberflächenkomplexierungskonstanten modelliert werden kann.

Der Einfluss von Citrat auf die U(VI)-Diffusion in Opalinuston wurde in Gegenwart von Opalinuston-Porenwasser untersucht. Die Diffusionsparameter, welche für die HTO- und die U(VI)-Diffusion in Abwesenheit von Citronensäure erhalten wurden, stimmten mit Literaturdaten überein. In Gegenwart von Citronensäure, wurde die U(VI)-Diffusion signifikant verzögert, was auf eine Änderung der Speziation hinweist. Wahrscheinlich wird U(VI) während des 3-monatigen Diffusionsexperimentes zu U(IV) reduziert. Citronensäure diffundierte etwas schneller durch Opalinuston als kleine Huminsäure-Kolloide, die in einem früheren Experiment untersucht wurden. Das Diffusionsexperiment zeigt, dass das vorliegende chemische System detaillierter untersucht werden muss, um die ablaufenden Reaktionen besser zu verstehen. Insbesondere muss die sich unter diesen Bedingungen bildende U(VI)-Citratspezies spektroskopisch, thermodynamisch und strukturell beschrieben werden.

Der Nutzen von PET als verlässliche Messmethode für die quantitative Bestimmung von Diffusionskoeffizienten in Ton und generell für Untersuchungen von Tracertransport in Barrieregestein wurde nachgewiesen. Die Verbesserung der quantitativen Auswertung bildete einen Schwerpunkt des Projektes, sowohl bezüglich der Verbesserung der Abbildungsqualität als auch der Ableitung von Parametern. Normalisierung und Streukorrektur wurden als bedeutende Ursachen für unzulängliche Abbildungsqualität gefunden und Abhilfen geschaffen. Hierzu wurden Monte-Carlo Simulationen der PET durchgeführt, die alle für die Bildgebung relevanten physikalischen Prozesse berücksichtigen, vom radioaktiven Zerfall des Traceratoms bis zur Detektion. Das Ergebnis der Untersuchungen ist eine verbesserte Rekonstruktionsprozedur, mit der sich die Tracerkonzentration quantitativ auswerten lässt und mit der auch Fehlerabschätzungen möglich sind.

PET-Experimente wurden als Testmessungen für die Auswertemethode durchgeführt und um das Verständnis experimenteller Artefakte durch Alteration und Beschädigung der Proben zu beurteilen. Räumlich-zeitliche Verteilungen der Tracerkonzentration wurden gemessen. Daraus wurden mit Hilfe inverser FEM-Modellierung Diffusionskoeffizienten berechnet. Die Ergebnisse sind im Einklang mit Literaturergebnissen, die mit Hilfe von „through-diffusion“-Experimenten in Diffusionszellen gewonnen wurden. Darüber hinaus wurden Hinweise auf Abweichungen vom einfachen transversal-isotropen Verhalten gefunden. Diese Abweichungen sind gering; sie könnten sich durch materialbedingte präferentielle Pfade für die Diffusion ergeben, die durch feine Silt-Schichten oder durch Mikrorisse verursacht werden.

Weitere PET-Untersuchungen dienten dem besseren Verständnis von Prozessen in der Auflockerungszone. Hierbei wurde der Einfluss von Wasserglas-Injektionen auf Transportparameter und -wege untersucht. Der Vergütungserfolg hängt von mehreren Faktoren ab: Der Reaktionskinetik des Wasserglases in Kontakt mit Salzgestein und Porenlösungen, den Ei-

genschaften des Risssystems und der Injektionsrate. Bisher konnte dieser komplexe Prozess nur mittels destruktiver Methoden am Endergebnis untersucht werden. Nun gelang es, ihn im zeitlichen Verlauf räumlich aufgelöst darzustellen. Der Vergütungseffekt in diesen Experimenten war allerdings nicht sehr deutlich, sondern das Wasserglas erstarrte überwiegend als Film auf der Probenoberfläche und nur ein geringer Anteil drang in die Probe ein.

1 Introduction and objectives

The long-term disposal of high-level nuclear waste in deep geological formations is discussed worldwide as main strategy for nuclear waste management. In addition to salt and crystalline rock, clay rock has been proposed as potential host rock for nuclear waste repositories (Nagra, 2002). Moreover, clay in form of bentonite is considered as backfill material in a variety of nuclear repository types. Advantages of clay rock as barrier against radionuclide migration are related to its swelling properties, low hydraulic permeability and crack-healing features as well as to the large surface areas of clay minerals leading to a high retention efficiency toward radionuclides (Nagra, 2002; Hoth et al., 2007). However, clay rock and clay minerals are sensitive to high temperatures, show anisotropic behavior and, compared to salt, greater efforts in geotechnical engineering are necessary to stabilize the tunneling in the rock (Hoth et al., 2007).

Clay rock is closely associated with natural organic matter that can be released from the clay under certain conditions. In the pore waters of Callovo-Oxfordian argillite (France) and Opalinus Clay formations, which represent potential host rocks for the disposal of radioactive waste, low molecular weight organic acids such as acetate, propionate, lactate, and formate (up to 1865×10^{-6} M, 127×10^{-6} M, 9×10^{-6} M, and 2×10^{-6} M, respectively) were detected that account for 88 % and 36 % of the total dissolved organic carbon (DOC) in the pore waters of the two host rock formations (Courdouan, 2007a,b). Moreover, fulvic and humic acid-like substances, organic polyelectrolyte molecules, were identified in alkaline extracts of previously acidified rock materials (Claret et al., 2003; Schäfer et al., 2003). In addition, further organic material is often contained in the radioactive waste itself such as citrate and EDTA, used as decontaminants (Hummel, 2008; Suzuki et al., 2010), as well as resins, cellulose, halogenated/non-halogenated polymers (PVC, PE, PP). Their degradation by radiolysis and hydrolysis under repository conditions results in the formation of further organic degradation products. Generally, organic substances, occurring as dissolved species or as colloids in pore waters as well as attached to solids, can affect the mobility of radionuclides in the environment.

Thus, for the assessment and reduction of risks related to the disposal of nuclear waste a detailed knowledge of all interaction processes in the system radionuclide – organics – clay – aquifer is necessary.

While ground and pore waters of South German clay deposits have ionic strengths below 0.5 M, the North German clay deposits are characterized by highly saline ground and pore waters with ionic strengths up to 4 M (Brewitz, 1982). So far, most of the studies with regard to radionuclide complexation by organics or radionuclide retention by clays were performed at low ionic strengths. Consequently, it has to be investigated whether literature data to complexation, sorption, diffusion, and redox chemistry of radionuclides obtained for low ionic strength systems can be used for the prediction of the geochemical behavior of radionuclides in systems with higher salinity. Therefore, the effect of high salt concentrations on interaction processes in the system radionuclide – organics – clay – aquifer is studied in the present work.

With regard to long-term safety assessment of nuclear waste repositories, actinides (mainly uranium, neptunium, plutonium, americium, and curium) are of particular interest, because of their high radio- and chemotoxicity and their very long half-lives. Furthermore, fission products, such as technetium-99 and selenium-79, are elements of concern for the safe storage of high-level nuclear waste, because of their long half-lives and their high mobility under aerobic conditions. Lanthanides, e.g. europium and terbium, are often used as analogues for trivalent actinides.

Exemplary for low molecular weight organic acids, the complexation of U(VI) by propionate is studied as a function of ionic strength (up to 4 mol kg^{-1} $NaClO_4$) by combining time-resolved laser-induced fluorescence spectroscopy (TRLFS), attenuated total reflection Fourier-transform infrared (ATR FT-IR) spectroscopy, and density functional theory (DFT) calculations. The complex stability constants will improve the thermodynamic database.

The sorption and diffusion studies within this project are focusing on model clay minerals (mainly montmorillonite, in some cases illite) as well as on the natural clay rock Opalinus Clay from the Mont Terri rock laboratory (Switzerland). Opalinus Clay is currently internationally investigated as one potential host rock for high-level nuclear waste disposal in Switzerland (Thury and Bossart, 1999; Nagra, 2002).

In order to quantify the influence of ionic strength and background electrolyte on U(VI) sorption onto montmorillonite, U(VI) sorption is studied applying both pure NaCl, $CaCl_2$ or $MgCl_2$ electrolytes with ionic strengths up to 3 mol kg^{-1} (NaCl) or up to 9 mol kg^{-1} ($CaCl_2$, $MgCl_2$) as well as a mixed electrolyte which consists of 2.52 mol kg^{-1} NaCl, 0.12 mol kg^{-1} $CaCl_2$ and 0.048 mol kg^{-1} $MgCl_2$ (similar to the groundwater composition in the Konrad mine, Lower Saxony (Brewitz, 1982)). Surface complexation modeling for the interaction of U(VI) with montmorillonite is performed to determine surface complexation constants. In this context, it will be checked whether the two-site protolysis non-electrostatic surface complexation and cation exchange (2SPNE SC/CE) model, developed by Bradbury and Baeyens (1997, 1999, 2002), can be applied for sorption results obtained at high ionic strengths. The surface complexes are verified by means of TRLFS and ATR FT-IR spectroscopy.

The migration of radionuclides in clay rock is governed by molecular diffusion. This process can be studied by diffusion experiments, whereby diffusion and distribution coefficients (D_e and K_d) are determined. In continuation of diffusion studies performed in the previous project, where U(VI) diffusion in compacted Opalinus Clay was studied in the absence and presence of humic acid at 25 and 60°C (Joseph et al., 2013b), the objective of the present study is to evaluate the influence of citrate, a further representative of low molecular weight organic acids, on U(VI) diffusion in Opalinus Clay. Furthermore, the influence of increased ionic strengths on U(VI) diffusion in compacted montmorillonite is studied applying NaCl solution as well as a mixed electrolyte (similar to Konrad groundwater, see above), both having an ionic strength of about 3 mol kg^{-1}.

Microorganisms that are indigenous in potential host rocks, foreseen for nuclear waste disposal, are able to influence the speciation and therefore the mobility of actinides and their re-

tardation both by direct and indirect pathways (e.g., Lloyd and Gadd, 2011; Swanson et al., 2012; Lütke et al., 2013; Wouters et al., 2013; Moll et al., 2014). Recently, from Mont Terri Opalinus Clay indigenous bacteria were isolated and their interactions with U, Eu and Cm were investigated (Lütke et al., 2013; Moll et al., 2014). Some investigations (Panak and Nitsche, 2001; Neu et al., 2005; Moll et al., 2006; Renshaw et al., 2009; Ohnuki et al., 2009) documented the manifold impact of bacteria on the speciation of Pu. Plutonium can coexist in different oxidation states under environmental conditions which makes interaction studies in biological systems challenging. Therefore, the interactions of the bacterial isolates from Opalinus Clay are investigated in more detail.

In salt rock in addition to bacteria and fungi, archaea are dominating the indigenous microbial community (McGenity et al., 2000; Stan-Lotter and Fendrihan, 2015) as shown in the Waste Isolation Pilot Plant in Carlsbad, New Mexico, USA (Swanson et al., 2012). To date, only a few studies have evaluated the interactions of halophilic microorganisms with U (Francis et al., 2000, 2004) and other actinides (Gillow et al., 2000; Ozaki et al., 2004; Ams et al., 2013) at high ionic strength. Recently, an extremely halophilic archaeon namely *Halobacterium* (*Hbt*.) sp., putatively *noricense* (WIPP strain) was isolated from the WIPP site (Swanson et al., 2012). Its closest phylogenetic relative *Halobacterium noricense* DSM-15987 was originally isolated from a salt mine in Austria (Gruber et al., 2004). Within this project, first experiments are performed to study the interactions of the halophilic archaeon *Halobacterium noricense* DSM-15987 with U(VI), Eu(III), and Cm(III).

Another objective is to obtain an improved understanding of the equilibrium characteristics of metal-humate complexation, particularly with regard to possible stabilization processes and their consequences in respect of reversibility. Complexation with dissolved humic matter can be crucial in controlling the mobility of toxic or radioactive metals. For speciation and transport modeling, a dynamic equilibrium process is commonly assumed, where association and dissociation run permanently. This is, however, questionable in view of reported observations of a growing resistance to dissociation over time (Cacheris and Choppin, 1987; Choppin and Clark, 1991; Rao et al., 1994; Artinger et al., 1998; King et al., 2001; Geckeis et al., 2002). If, in the end, humic-bound metals are to be regarded as "fixed", this will entail completely different predictions of their migration behavior than in the case of a dynamic partitioning process. So far, the existence of a dynamic equilibrium has never been proven. In this project, the isotope exchange principle is employed to gain direct insight into the dynamics of the complexation equilibrium, including kinetic stabilization phenomena.

Different from small ligands, the mobilizing potential of humic or humic-like substances is not only determined by complex stability (and inertness), but also by colloidal stability. Fulvic acids, which are to some extent comparable to high-molecular-weight clay organics, are stable towards flocculation at low ionic strength, but this is possibly not the case at very high electrolyte contents close to saturation. Colloid-borne mobilization of radionuclides could be excluded a priori if flocculation prevents any migration in the fluid phase. For this reason, colloidal stability of fulvic acids in highly saline systems with NaCl, $CaCl_2$ and $MgCl_2$ is systematically investigated at different pH values.

In the absence of flocculation, humic-like clay organics must be regarded as possible carriers. High salinity as well as natural organic matter are known to facilitate migration of multivalent metals, but little is known on their combined influence. Both synergistic and antagonistic effects are conceivable. In general, interaction of metal ions with negatively charged binding sites on mineral surfaces or humic colloids is counteracted at high electrolyte contents. Depending on the type of cation, this may be caused both by charge screening effects and direct competition. Regarding adsorption of humic substances, the influence of high ionic strength is not known. Thus, the behavior of metals in highly saline systems with humic matter is hardly predictable.

Basically, both mobilizing and retarding effects are possible, which is mainly dependent on the pH value (cf. (Lippold et al., 2005) and references therein). The influence of pH and ionic strength on the solid-liquid distribution of a metal in such “ternary” systems (consisting of metal, solid surface and humic colloids) should be explainable by combining the interactions in the constituent binary subsystems (metal adsorption, metal-humic complexation, adsorption of the humic substance). This is a prerequisite for modeling humic-bound transport. However, the applicability of this “linear additive model” is uncertain for several reasons (Lippold et al., 2009).

In this project, complexation of Tb(III) and Eu(III) (as analogues of trivalent actinides) with fulvic acid and their adsorption onto Opalinus Clay are investigated for binary and ternary systems at different pH values in the presence of NaCl, $CaCl_2$, and $MgCl_2$ as a function of ionic strength up to saturation. ^{160}Tb, ^{152}Eu, and ^{14}C-labeled fulvic acid are used as radioactive tracers, allowing studies at very low concentrations to be in accordance with probable conditions in the far-field of a nuclear waste repository. In order to specify the influence of the electrolyte constituents on fulvate complexation, a mechanistic model (NICA-Donnan) is applied. The complexes are characterized by means of TRLFS. The linear additive model is tested for suitability in reconstructing the ternary systems from the corresponding binary systems.

Most geological materials are heterogeneous and highly structured on all scales, starting from the surface structure of each grain, up to the geometry of layers on the field scale. The scaling to the macroscopic scale of processes which are identified and well understood on the molecular scale, like sorption and transport, is a challenging question. An effective volume which depends on the process has to be considered, which specifies the portion of the volume and the particular pathways where the process takes effect. Particularly, effects of preferential pathways and preferential transport direction (anisotropy) were found to be present in Opalinus Clay (e.g. Van Loon et al. 2004; Keller et al., 2011).

Diffusion properties are commonly determined in diffusion cells and on small-sized samples that are considered homogeneous. Directional measurements on a large number of samples could yield information on anisotropy and inhomogeneity on the particular size scale of the sample and are missing deviations on a larger scale, which could be caused by a system of micro-fractures, fine layering, or other structures. Such deviations could become effective as preferential transport zones and therefore delimit the barrier function of the material.

In previous projects, positron emission tomography (PET) was established as an experimental method for process observation that is capable to bridge the scale from processes on the molecular scale to the macroscopic scale. It had been shown that the method was applicable for qualitative imaging. For example, it was possible to visualize the anisotropy of diffusion processes in Opalinus Clay, but the quantitative results were questionable. This was due to the lack of correction methods for samples with high density, because common correction methods are designed for biological tissue. Recently, new data correction methods have become available, which are applicable for geological materials and greatly improve quantitative usability of the PET images.

An intrinsic property of the excavation damage zone is preferential transport behavior due to fracturing caused by pressure release. One option to improve these degradations of the geological barrier is impregnation of waterglass. The success of effective injection into void structures depends on a number of factors: the reaction kinetics of the injected waterglass with salt and brines, the nature of the fractures, and the injection velocity. This rather complex process could not be observed directly, only the final results could be tested with destructive methods. The low contrast between waterglass and water, as well as the experimental conditions, complicate the application of the common µCT-method. In contrast, PET is proposed as appropriate method for observation of such geochemical processes.

A further objective of the project was the evaluation of the retention capacity of iron(II)-containing mineral phases occurring ubiquitously in nature as well as corrosion products of carbon steel canisters used for storing radioactive waste. For instance, magnetite, green rust, mackinawite, or siderite can form during corrosion of large quantities of steel that are planned to be installed throughout a deep geological disposal facility. Siderite forms in anoxic environments rich in carbonates. Such iron(II)-containing mineral phases are expected to be one of the key surfaces of interest for controlling radionuclide behavior under disposal conditions. In this project, the Tc(VII)/Tc(IV) sorption by the iron(II)-containing minerals magnetite ($Fe^{II}Fe^{III}{}_2O_4$) and siderite ($Fe^{II}CO_3$) is studied under anoxic conditions by means of batch sorption experiments as well as ATR FT-IR and X-ray absorption spectroscopy. For comparison, Tc retention on iron(III) minerals hematite (α-Fe_2O_3) and maghemite (γ-Fe_2O_3) is studied.

This research project, funded by the Bundesministerium für Wirtschaft und Energie (BMWi), was performed in collaboration with the R&D projects of the Karlsruher Institut für Technologie (Institut für Nukleare Entsorgung), Johannes Gutenberg-Universität Mainz (Institut für Kernchemie), Technische Universität Dresden (Sachgebiet Strahlenschutz), Technische Universität München (Fachgebiet Theoretische Chemie), Universität Heidelberg (Physikalisch-Chemisches Institut), Universität Potsdam (Institut für Chemie/Physikalische Chemie) and Universität des Saarlandes (Anorganische Festkörperchemie).

2 Complexation of U(VI) by propionate at different ionic strengths in $NaClO_4$

2.1 Literature review

So far, the interaction between U(VI) and propionate at high ionic strength has been scarcely studied in the literature.

Miyake and Nürnberg (1967) and Kirishima et al. (2007) studied this interaction both in 1 M $NaClO_4$, at 20°C and 25°C, respectively. By means of UV-vis spectroscopy, Miyake and Nürnberg (1967) determined the formation of 4 species, namely $UO_2(Prop)^+$, $UO_2(Prop)_2^0$, $UO_2(Prop)_3^-$ and $UO_2(Prop)_4^{2-}$. They postulated a monodentate coordination of the propionate ligand to the uranyl moiety. Kirishima et al. (2007) investigated the complexation of U(VI) by propionic acid by potentiometric and microcalorimetric titration. The formation of $UO_2(Prop)^+$ and $UO_2(Prop)_2^0$ was deduced.

Table 1: Summary of the complexation constants for the U(VI)/propionate system reported in the literature.

	log β (I = 1 M $NaClO_4$)	
Species	Miyake and Nürnberg (1967)	Kirishima et al. (2007)
$UO_2^{2+} + Prop^- \rightleftharpoons UO_2(Prop)^+$	2.53 ± 1.11	2.50 ± 0.01
$UO_2^{2+} + 2\ Prop^- \rightleftharpoons UO_2(Prop)_2^0$	4.68	4.79
$UO_2^{2+} + 3\ Prop^- \rightleftharpoons UO_2(Prop)_3^-$	6.49	
$UO_2^{2+} + 4\ Prop^- \rightleftharpoons UO_2(Prop)_4^{2-}$	8.25	

By combining density functional theory (DFT) calculations, ultraviolet−visible (UV−vis), extended X-ray absorption fine-structure (EXAFS), and attenuated total reflection Fourier-transform infrared (ATR FT-IR) spectroscopy, Lucks et al. (2012) revisited the aqueous speciation of the U(VI)-acetate system. Complexes with the 1:1, 1:2 and 1:3 U:acetate stoichiometry were identified. The U(VI)-acetate complexes exhibited exclusively a bidentate coordination. Since acetic acid and propionic acid only differ by a $–CH_2$ group, a strong analogy on the behavior of both ligands towards U(VI) is to be expected.

2.2 Sample preparation

Sodium propionate from Acros (99.0-100.5 %) and sodium perchlorate monohydrate (p.a.) (Merck Millipore) were used. The concentration of U(VI) was set to 5×10^{-4} mol kg^{-1}. Three molalities (0.75, 2.0 and 4.0 mol kg^{-1}) were studied, imposed by $NaClO_4$. The concentration of propionate was increased from 0.005 mol kg^{-1} to 0.25 mol kg^{-1}. All experiments were performed at 20°C. Samples were analyzed by time-resolved laser-induced fluorescence spec-

troscopy (TRLFS) and the data deconvolution performed using Parallel Factor Analysis PARAFAC (Bro, 1997; Drobot et al., 2015). To get insights on the number of species, additional IR absorption spectroscopy measurements were performed on a Bruker Vertex 80/v instrument using an ATR diamond cell ([U(VI)] = 5×10^{-3} mol kg^{-1}, 0.1 mol kg^{-1} propionate, pH from 0.98 to 5.03). Since perchlorate exhibits a broad peak in the IR spectrum from 1120 to 928 cm^{-1}, these experiments were performed without background electrolyte. Speciation should not be impacted since no coordination between U(VI) and perchloric acid up to 11.5 mol L^{-1} was evidenced by Semon et al. (2001).

2.3 pH measurements at high salinity

At ionic strength higher than 0.1 mol kg^{-1}, the pH measured in solutions (pH_{exp}) is an operational apparent value (Altmaier et al., 2003; Altmaier et al., 2008; Fanghänel et al., 1996; Felmy et al., 1991). It can be related to the molal H^+ concentration as follows:

$$-\log m_{H+} = pH_{exp} + A \quad (2.1)$$

Indeed, the liquid junction potential, which depends on the electrolyte concentration, differs for saline solutions and dilute buffer solutions (used for the calibration of the pH electrode). This variation as well as the individual activity coefficient γ_{H+} are included in the term A, which depends exclusively on the concentration and composition of the solutions (Altmaier et al., 2003; Altmaier et al., 2008; Fanghänel et al., 1996; Felmy et al., 1991).

The following relation was used (Petrov et al., 2011):

$$A(NaClO_4) = -0.0152 + 0.27\ x + 0.0046\ x^2 \quad (2.2)$$

where A is in mol L^{-1}, and x is the concentration of $NaClO_4$, also in mol L^{-1} units.

After conversion to molal units, the pH_{exp}, given in Table 2, were used:

Table 2: Experimental pH_{exp} used.

I (mol kg^{-1})	pH_{exp}	$-\log m_{H+}$
0.75	3.70	3.89
2	3.39	3.89
4	2.94	3.89

Combination pH electrodes (SenTix® MIC from VWR) were used for pH measurements. In order to avoid precipitation of $KClO_4$ in the diaphragm of the electrode, the original junction electrolyte 3 M KCl was replaced by a 3 M NaCl solution. The electrodes were calibrated using standard buffer solutions (WTW).

2.4 DFT calculations and ATR FT-IR spectroscopy

Density Functional Theory (DFT) calculations were performed in an aqueous phase using the Gaussian 09 program employing the density functional theory by using a conductor like polarizable continuum model. Structure optimizations were performed for 1:1, 1:2, and 1:3 complex of uranyl propionate at B3LYP level followed by vibrational frequency analysis at the same level to confirm the absence of imaginary frequencies. The energy-consistent small-core effective core potential and the corresponding basis set suggested by Küchle et al. (1994) were used for uranium. The most diffuse basis functions on uranium with the exponent 0.005 (all s, p, d, and f type functions) were omitted. For carbon, oxygen and hydrogen, the valence triple-z plus polarization basis was used. The spin-orbit effects and basis set superposition error corrections were neglected.

The DFT calculations were performed considering a bidentate coordination of the propionate to the uranium(VI) moiety. The three complexes are represented in Fig. 1.

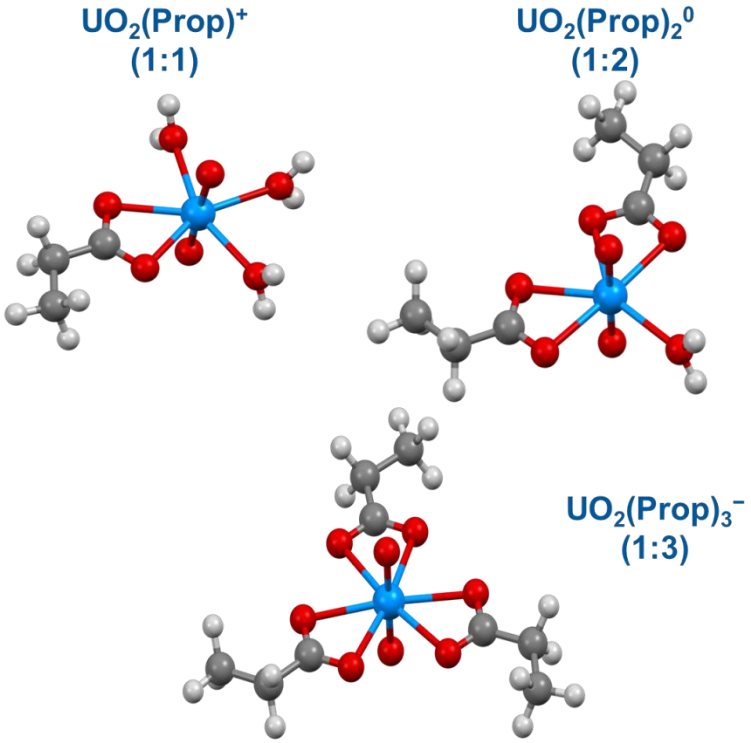

Fig. 1: Proposed structures of the 1:1, 1:2, and 1:3 U(VI) propionate complexes (blue: uranium; red: oxygen; gray: carbon; light gray: hydrogen).

The DFT calculated IR spectra for the $UO_2(Prop)^+$, $UO_2(Prop)_2^0$ and $UO_2(Prop)_3^-$ complexes are shown in Fig. 2a. As it can be seen in Fig. 2a, a large red shift from 986 to 912 cm^{-1} of the asymmetric stretching mode $\nu_3(UO_2)$ of the uranyl moiety upon complexation with propionate is predicted. As already shown by Lucks et al. (2012), this red shift upon complexation is due to the weakening of the axial(ax) $U-O_{ax}$ bond because of the σ and/or π contribution from the propionate ligands. The spectral feature predicted by DFT at around 893 cm^{-1} arises from the *ν*(CC) mode of the propionate ligand.

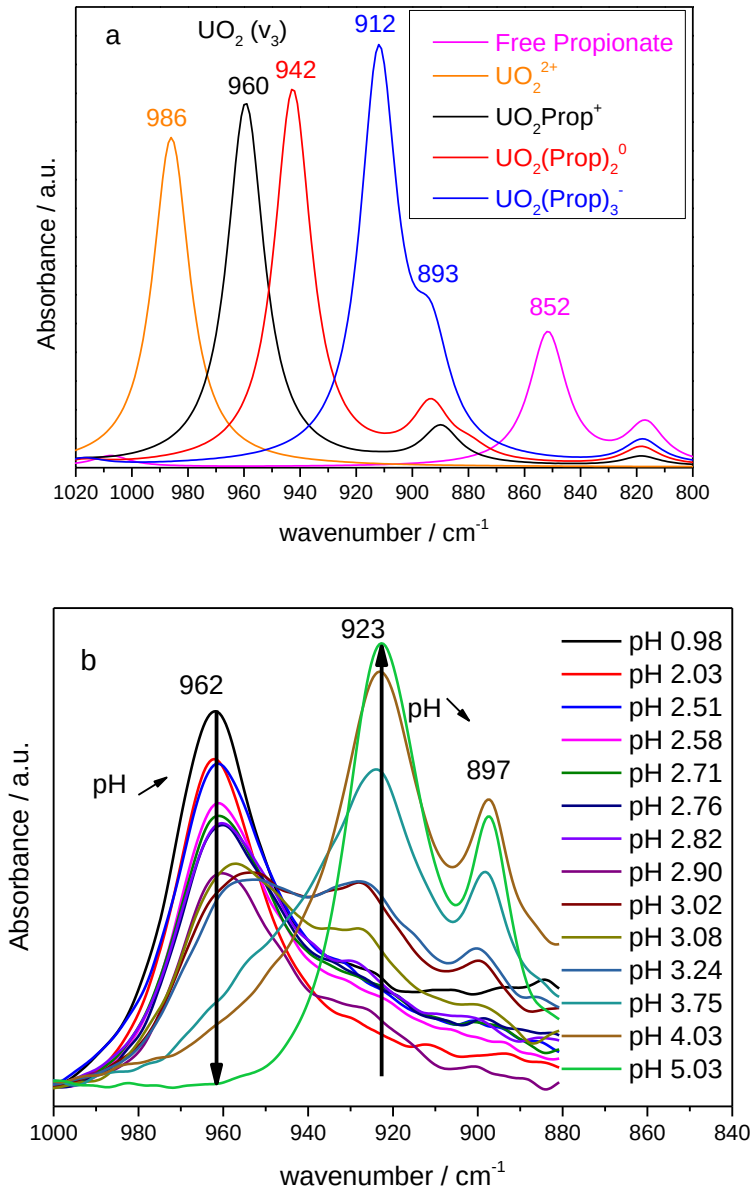

Fig. 2: Comparison of (a) DFT calculated band positions of the asymmetric stretching mode of the uranyl moiety and (b) experimentally observed values in the U(VI) propionate system ([U(VI)] = 5×10^{-3} mol kg^{-1}, 0.1 mol kg^{-1} propionate, pH from 0.98 to 5.03).

Fig. 2b represents the experimental IR spectra of the aqueous U(VI) propionate solutions recorded at pH values ranging from pH 0.98 to pH 5.03 in the spectral range of the $\nu_3(UO_2)$ mode. In agreement with DFT, a large frequency shift from 962 to 923 cm^{-1} is observed upon increasing pH, due to the increasing proportion of U(VI)/propionate complexes. A similar shift as similar frequencies was already observed by Lucks et al. (2012) for the U(VI) acetate system. The contribution of hydrolyzed U(VI) complexes can be neglected due to the excess of ligand. While the peak maxima observed at 962 and 923 cm^{-1} appear to correspond to two pure species, the presence of two additional species showing band maxima at 948 and 933 cm^{-1} are observed (Fig. 2b). The spectral feature at 897 cm^{-1}, also predicted by DFT, exhibits an increasing intensity with increasing number of propionate ligands coordinated to the U(VI).

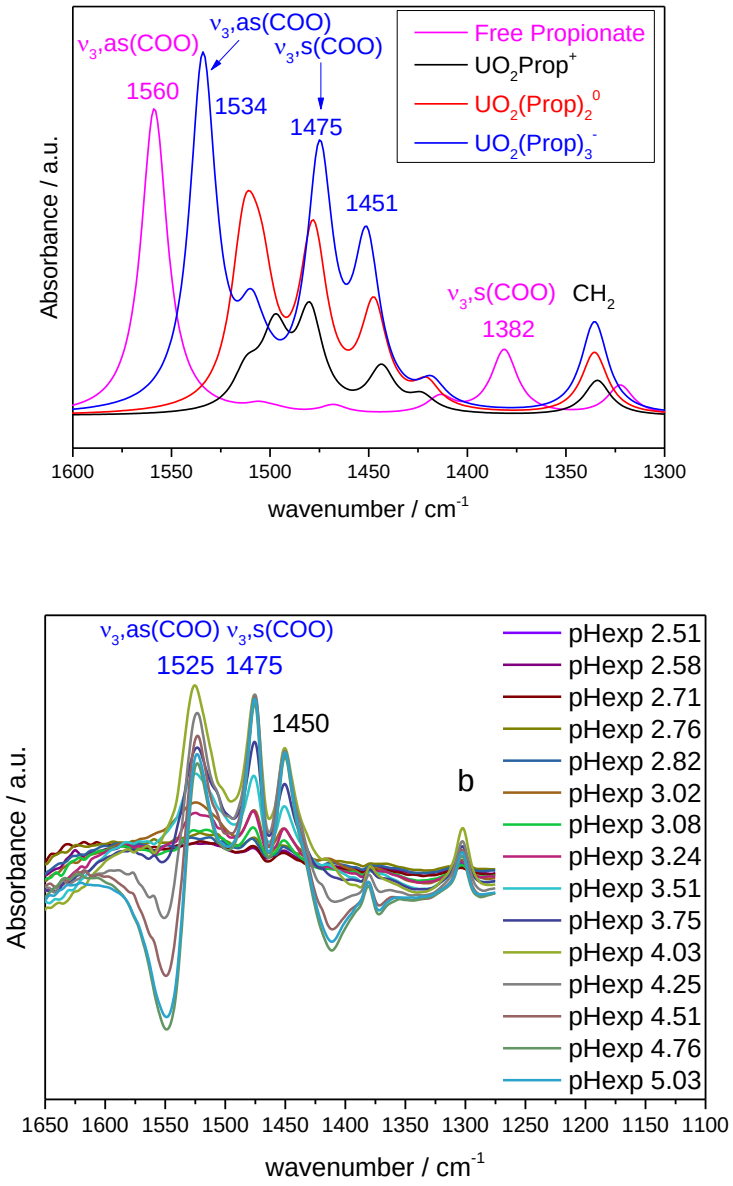

Fig. 3: Comparison of (a) DFT calculated band positions of the carboxylate region and (b) experimentally observed values in the U(VI) propionate system ([U(VI)] = 5×10^{-3} mol kg^{-1}, 0.1 mol kg^{-1} propionate, pH from 2.51 to 5.03).

In the DFT calculated spectra, the bidentately coordinated U(VI) propionate complexes exhibit the antisymmetric and symmetric stretching modes of the carboxyl groups, $\nu_{3,as}$(COO) and $\nu_{3,s}$(COO), at 1534-1520 cm^{-1} and 1475 cm^{-1}, respectively (Fig. 3a). The spectral splitting of these bands ($\Delta\nu$), lying from 37 to 59 cm^{-1}, allows a discrimination of bidentate and monodentate coordination of the carboxyl group (Kahikana et al., 1987; Deacon and Philipps, 1980). According to Kahikana et al. (1987), a splitting lower than 100 cm^{-1} is characteristic to a bidentate coordination, while a monodentate coordination exhibits a spectral splitting larger than 150 cm^{-1}. The band predicted at 1451 cm^{-1} has contributions of both the symmetric stretching modes of the carboxyl groups as well as the $-CH_2$ group. The experimental vibrational modes of the carboxyl group of the propionate ligand after complexation with U(VI) are shown in Fig. 3b. The $\nu_{3,as}$(COO) mode at 1525 cm^{-1} and the $\nu_{3,s}$(COO) mode at 1475 cm^{-1}

are present throughout the whole pH range exhibited. The band splitting $\Delta\nu$ is 50 cm^{-1}, in perfect agreement with DFT predictions. This confirms the bidentate coordination of the carboxylic groups and rules out a monodentate one. Note that the frequency of the band at 1450 cm^{-1} perfectly matches the DFT calculations.

2.5 TRLFS spectroscopy and PARAFAC deconvolution

TRLFS measurements were performed using a Nd:YAG laser, at λ = 266 nm and a laser energy of 0.3 mJ. Samples were placed in a quartz cuvette. An average of 50 accumulations was collected and the baseline correction was performed with the software LabSpec 5 (Horiba). A 70 ns step size for 50 spectra was used. All measurements were done at 20°C using a controlled Peltier element (TC125 Temperature Control, Quantum Northwest). The static fluorescence spectra recorded after the initial delay of 70 µs at I = 0.75 mol kg^{-1} $NaClO_4$ are exemplarily shown in Fig. 4.

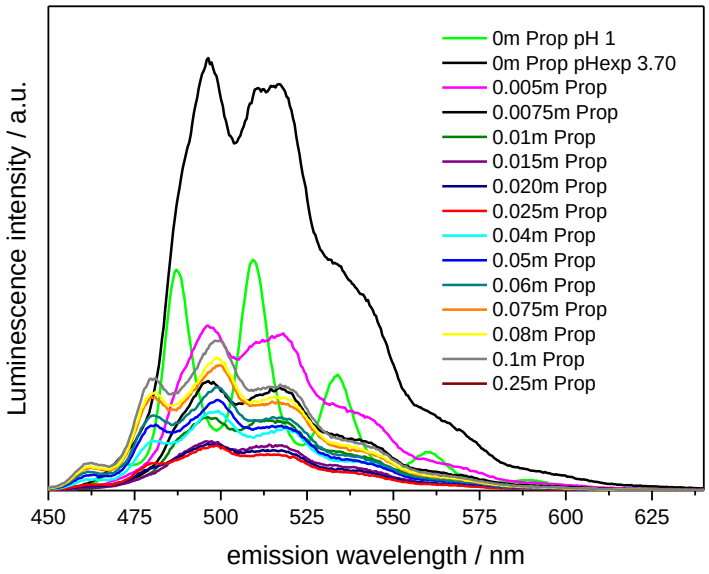

Fig. 4: Static TRLFS spectra of the U(VI) propionate system ([U(VI)] = 5×10^{-4} mol kg^{-1}, 0 to 0.25 mol kg^{-1} propionate, 0.75 mol kg^{-1} $NaClO_4$).

PARAFAC, coupled to a Newton-Raphson algorithm, was used to extract speciation information from the fluorescence data (Fig. 5). The extracted emission spectra of the five single components are shown in Fig. 5.

The 1st component corresponds to the uranyl UO_2^{2+} aquo ion, with peak maximum at 471, 486, 508, 532, 559 and 589 nm, in agreement with the literature (Drobot et al., 2015). The second can be attributed to the 1st hydrolyzed species of U(VI), i.e. UO_2OH^+, with peak maximum at 480, 496, 517, 541, 567 and 595 nm (Drobot et al., 2015). The three other components correspond then to the 1:1, 1:2 and 1:3 complexes. These five components can describe the fluorescence data observed in Fig. 4.

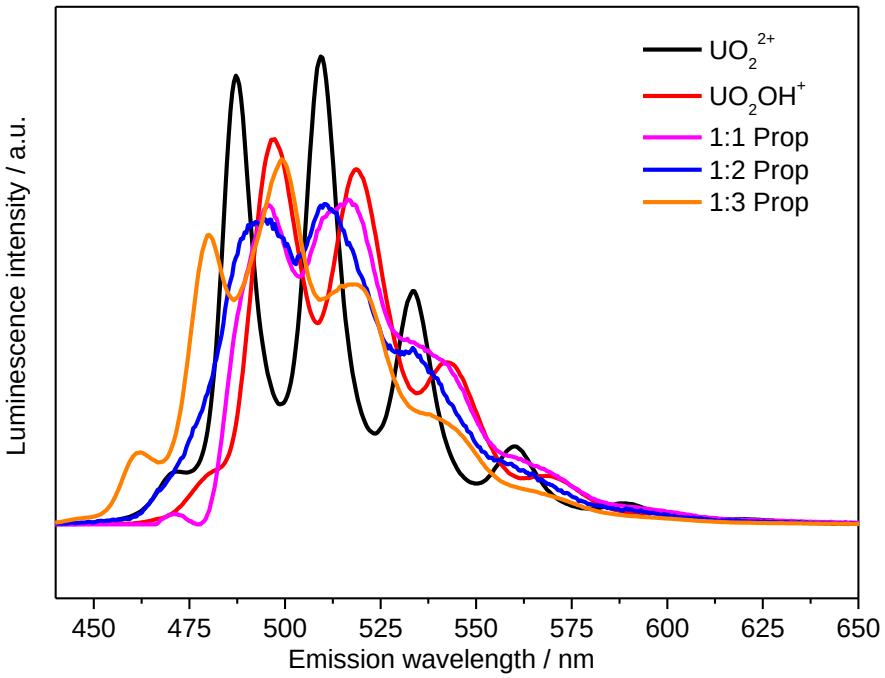

Fig. 5: Extracted emission spectra for 5 components of the U(VI) propionate system ([U(VI)] = 5×10^{-4} mol kg^{-1}, 0 to 0.25 mol kg^{-1} propionate, 0.75 mol kg^{-1} $NaClO_4$).

From the PARAFAC deconvolution of the fluorescence data, the following species distribution was obtained (Fig. 6).

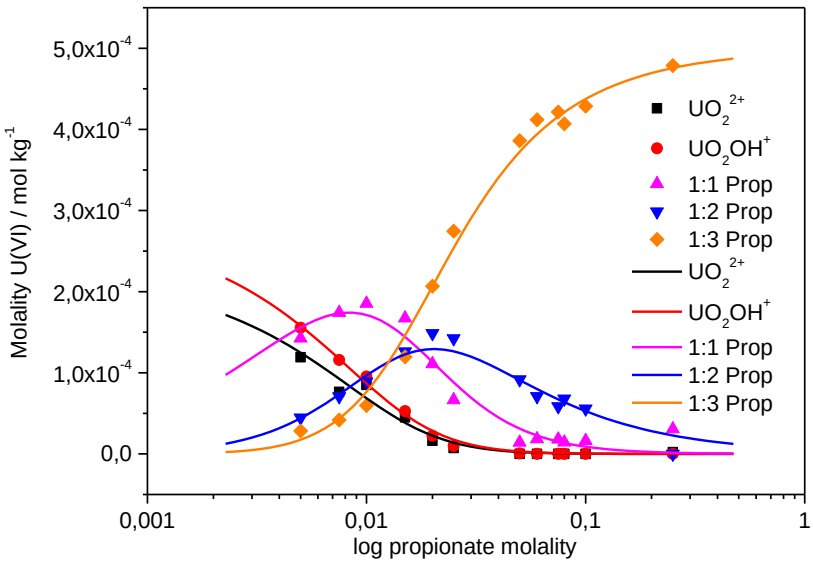

Fig. 6: Species distribution based on luminescence spectroscopy and PARAFAC deconvolution ([U(VI)] = 5×10^{-4} mol kg^{-1}, 0 to 0.25 mol kg^{-1} propionate, 0.75 mol kg^{-1} $NaClO_4$).

2.6 Determination of the complexation constants

The reactions leading to the formation of the three complexes and their equilibrium constants can be defined as follows:

$UO_2^{2+} + Prop^- \rightleftharpoons UO_2(Prop)^+$ (2.3)

$$\beta_1 = \frac{[UO_2Prop^+]}{[UO_2^{2+}][Prop^-]}$$

$UO_2^{2+} + 2\ Prop^- \rightleftharpoons UO_2(Prop)_2^0$ (2.4)

$$\beta_2 = \frac{[UO_2(Prop)_2]^0}{[UO_2^{2+}][Prop^-]^2}$$

$UO_2^{2+} + 3\ Prop^- \rightleftharpoons UO_2(Prop)_3^-$ (2.5)

$$\beta_3 = \frac{[UO_2(Prop)_3]^-}{[UO_2^{2+}][Prop^-]^3}$$

For each ionic strength, the speciation can be verified by slope analysis, by plotting log ($[UO_2(Prop)_n^{[2-n]+}]/[UO_2(Prop)_{n-1}^{[2-(n-1)]+}]$) as a function of log $[Prop^-]_{eq}$ (example for I = 0.75 mol kg^{-1} in Fig. 7).

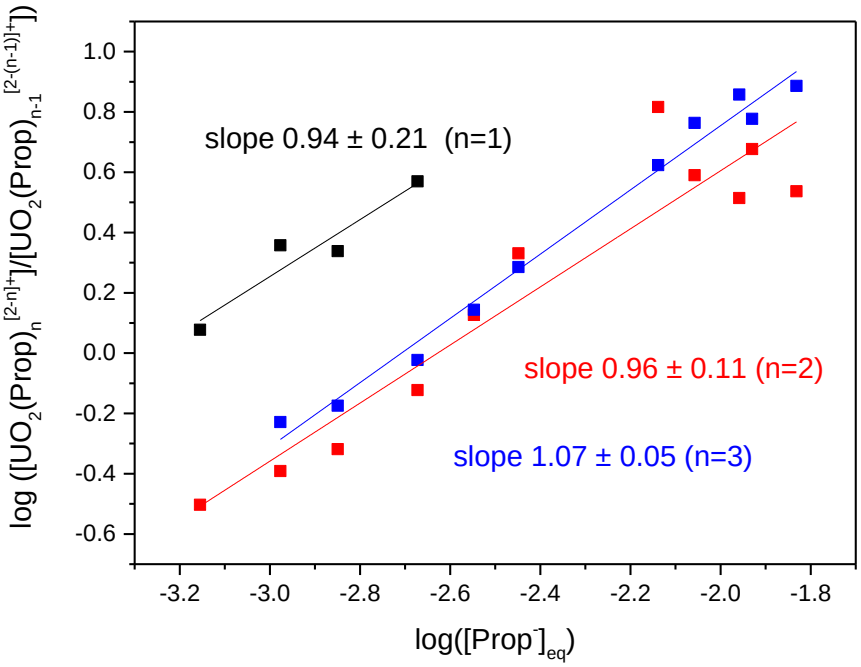

Fig. 7: Slope analyses for the stepwise formation of $UO_2(Prop)_n^{[2-n]+}$ complexes a n = 1, 2, 3 at 20°C and I = 0.75 mol kg^{-1} $NaClO_4$.

The slope of the linear correlations confirms the formation of the $UO_2(Prop)^+$, $UO_2(Prop)_2^0$ and $UO_2(Prop)_3^-$ complexes and their distribution as a function of the propionate concentration.

Based on the slope analysis, the following complexation constants were obtained (Table 3).

Table 3: Overall thermodynamic stability constants log β of the three U(VI)-propionate complexes at variable ionic strengths.

I (mol kg^{-1})	log β_1	log β_2	log β_3
0.75	3.30	5.93	8.67
2	2.89	5.69	8.80
4	2.51	5.76	7.85

The differences of the ionic strength dependencies of the log β values are connected with the charge of the complexes. For log β_1, all of the involved species (UO_2^{2+}, $Prop^-$, $UO_2(Prop)^+$) are charged. For log β_2, the $UO_2(Prop)_2^0$ complex has no charge. For log β_3, the complex is negatively charged $UO_2(Prop)_3^-$. Since $UO_2(Prop)_2^0$ is non-charged, the variation of its activity coefficient should be less pronounced than for a charged complex, i.e. $UO_2(Prop)^+$ and $UO_2(Prop)_3^-$. This is in good agreement with the data given in Table 3. Both the stability constants for the $UO_2(Prop)^+$ complex and the $UO_2(Prop)_3^-$ complexes change more with I than the $UO_2(Prop)_2^0$ complex. The differences in the two charged complexes are most likely related to the different interactions with the background electrolyte ($UO_2(Prop)^+$ interacts with ClO_4^-, $UO_2(Prop)_3^-$ interacts with Na^+) and to the different geometries of the complexes.

2.7 Extrapolation to zero ionic strength

The conditional stability constants, i.e. determined at specific ionic strength, can be extrapolated to zero ionic strength based on the Specific Interaction Theory (SIT) (Lemire et al., 2013). The relation between the conditional stability constant and the stability constant at zero ionic strength is given by the following equation:

$$\log_{10} {}^*\beta - \Delta z^2 D - n \log a(H_2O) = \log_{10} \beta^\circ - \Delta\varepsilon I \qquad (2.6)$$

$\log_{10} {}^*\beta$: conditional stability constant (at specific I)

$D = \frac{A\sqrt{I}}{1+Ba_j\sqrt{I}}$: the Debye-Hückel term

(A and B_{aj} are Debye-Hückel parameters taken from Lemire et al. (2013))

n = 0 for the 1:1, 1:2 and 1:3 complexes

$\log_{10} \beta^\circ$: stability constant at zero ionic strength

For the three reactions considered, $\Delta\varepsilon$ and Δz^2 are defined as follows:

$UO_2^{2+} + Prop^- \rightleftharpoons UO_2(Prop)^+$ (2.7)

$\Delta\varepsilon = \varepsilon(UO_2(Prop)^+;ClO_4^-) - \varepsilon(UO_2^{2+};ClO_4^-) - \varepsilon(Na^+;Prop^-)$; $\Delta z^2 = -4$

$UO_2^{2+} + 2\ Prop^- \rightleftharpoons UO_2(Prop)_2^0$ (2.8)

$\Delta\varepsilon = \varepsilon(UO_2(Prop)_2^0;ClO_4^-) - \varepsilon(UO_2^{2+};ClO_4^-) - 2\varepsilon(Na^+;Prop^-)$; $\Delta z^2 = -6$

$UO_2^{2+} + 3\ Prop^- \rightleftharpoons UO_2(Prop)_3^-$ (2.9)

$\Delta\varepsilon = \varepsilon(Na^+;UO_2(Prop)_3^-) - \varepsilon(UO_2^{2+};ClO_4^-) - 3\varepsilon(Na^+;Prop^-)$; $\Delta z^2 = -6$

$\varepsilon(UO_2^{2+};ClO_4^-) = 0.46$ (kg mol^{-1}) was taken from Lemire et al. (2013). No interaction coefficient is available for $\varepsilon(Na^+;Prop^-)$. Since ε(i,j) depends mostly on the charge of the ion (Skerencak et al., 2013), we used the analogy with $\varepsilon(Na^+;Acetat^-) = 0.08$ (kg mol^{-1}).

By plotting $\log_{10} {}^*\beta - \Delta z^2 D$ vs. the ionic strength, the slope and the intercept with the y-axis at $I = 0$ give $-\Delta\varepsilon$ and $\log_{10} \beta°$, respectively. The linear SIT regression plots for the experimental $\log \beta_1$, $\log \beta_2$ and $\log \beta_3$ values are shown in Fig. 8.

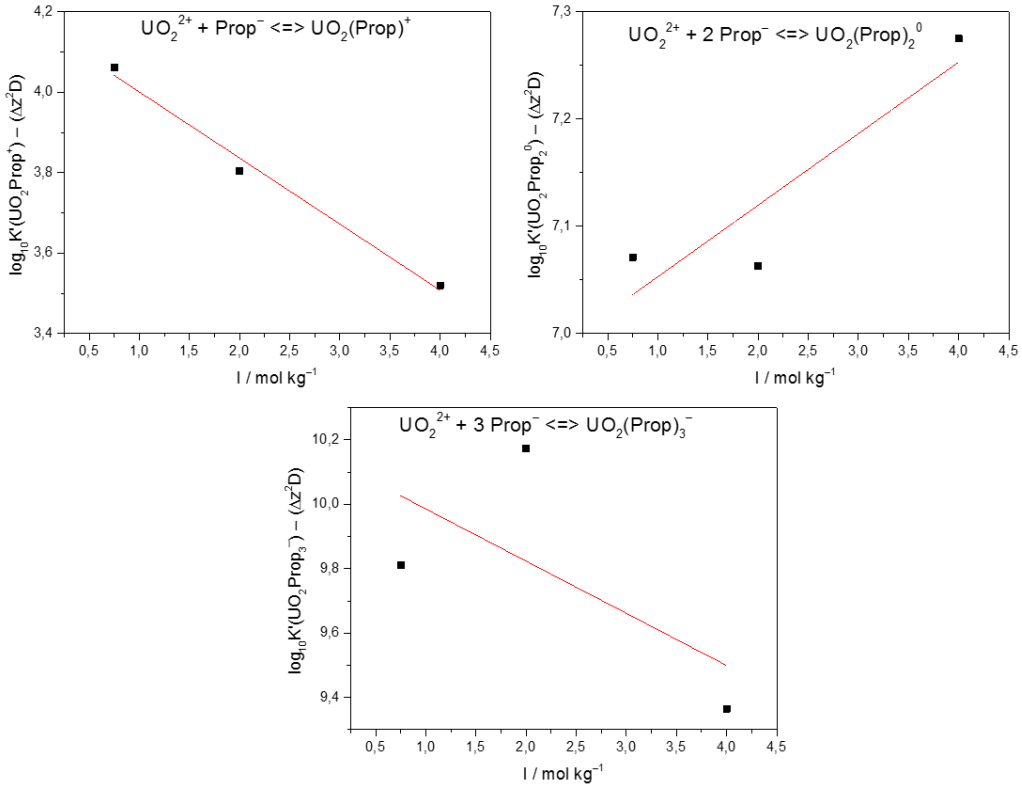

Fig. 8: Linear SIT regression plots for the first, second and third complexation constant of the U(VI) propionate system at 20°C.

The results, $\log_{10} \beta°$ and the different interaction coefficients ε(i,j) are shown in Table 4.

Table 4: Overall thermodynamic stability constants log β at I = 0 and the determined ε(i,j).

log $\beta_1°$	log $\beta_2°$	log $\beta_3°$
4.17	6.99	10.15
$\varepsilon(UO_2(Prop)^+;ClO_4^-)$	$\varepsilon(UO_2(Prop)_2^0;ClO_4^-)$	$\varepsilon(Na^+; UO_2(Prop)_3^-)$
0.70	0.55	0.86

Due to the lack of published data, our results cannot be directly compared. However, complexation constants at I = 0 are available for the U(VI)/acetate system. Sladkov (2013, 2014) found log $\beta_1°$ = 2.94 ± 0.08 (25°C) and log $\beta_2°$ = 5.50 ± 0.15 (25°C). Moskvin (1969) published log $\beta_3°$ = 7.25 (temperature not indicated). By comparing these data with our results from Table 4, it seems that the propionate ligand has a stronger affinity than acetate towards U(VI).

3 Interaction of radionuclides with microorganisms

One potential source of actinides (An) in the environment could be the accidental release from nuclear waste disposal sites. Microorganisms indigenous in potential host rocks are able to influence the speciation and therefore the mobility of An and their retardation both by direct and indirect pathways. They can as well affect the conditions in a geologic repository (e.g., by gas generation or canister corrosion). Currently salt, clay and granite are considered as potential host rocks for a nuclear waste disposal in Germany. Microorganisms are indigenous present in such subterranean environments and it was demonstrated that they can affect the speciation and hence the mobility of actinides (e.g., Lloyd and Gadd, 2011; Swanson et al., 2012; Lütke et al., 2013; Wouters et al., 2013; Moll et al., 2014). The Opalinus Clay layer of the Mont Terri Underground Rock Laboratory (Switzerland) is one potential host rock tested for nuclear waste disposal (Thury and Bossart, 1999). Recently, indigenous bacteria were isolated from Mont Terri Opalinus Clay and its interactions with uranium, europium and curium were investigated (Lütke et al., 2013; Moll et al., 2014). A couple of investigations (Panak and Nitsche, 2001; Neu et al., 2005; Moll et al., 2006; Renshaw et al., 2009; Ohnuki et al., 2009) documented the manifold impact of bacteria on the speciation of plutonium. Plutonium can coexist in different oxidation states under environmental conditions which makes interaction studies in biological systems challenging. Therefore, the interactions of the bacterial isolates from Mont Terri Opalinus Clay were investigated more in detail (cf. 3.1).

In salt rock, another potential host rock for nuclear waste disposal, in addition to bacteria and fungi, archaea are dominating the indigenous microbial community (McGenity et al., 2000; Stan-Lotter and Fendrihan, 2015) as shown in the Waste Isolation Pilot Plant in Carlsbad, New Mexico, USA (Swanson et al., 2012). To date, only a few studies have evaluated the interactions of halophilic microorganisms with uranium (Francis et al., 2000 and 2004) and other actinides (Gillow et al., 2000; Ozaki et al., 2004; Ams et al., 2013) at high ionic strength. Recently, an extremely halophilic archaeon namely *Halobacterium* (*Hbt*.) sp., putatively *noricense* (WIPP strain) was isolated from the WIPP site (Swanson et al., 2012). Its closest phylogenetic relative *Halobacterium noricense* DSM-15987 was originally isolated from a salt mine in Austria (Gruber et al., 2004). Within this project, first experiments were performed to study the adsorption of uranium(VI), europium(III), and curium(III) on the halophilic archaeon *Halobacterium noricense* DSM-15987 (cf. 3.2).

3.1 Interaction of Pu with bacterial isolates from Mont Terri Opalinus Clay

In this study, the unknown interactions between bacteria, isolated from Mont Terri Opalinus Clay core samples, namely *Sporomusa* sp. MT-2.99 and *Paenibacillus* sp. MT-2.2 cells and Pu were explored in aqueous solution under anaerobic conditions.

The Pu interaction experiments performed are the continuation of our first study with the Mont Terri Opalinus Clay bacterial isolates within the BMWi-project 02E10618 “Mikrobielle Diversität im Tongestein (Opalinus-Ton) und Wechselwirkung dominanter Mikroorganismen

mit Actiniden" (Moll et al., 2013). In Moll et al. (2013) we could only investigate the Pu interaction with *Sporomusa* sp. MT-2.99 cells at one pH value of 6.1 in 0.1 M $NaClO_4$ without adding an electron donor. These first experiments could be extended in order to get a more comprehensive overview of the interaction potential of our bacterial isolates namely *Sporomusa* sp. MT-2.99 and *Paenibacillus* sp. MT-2.2 towards Pu. The experiments can be divided in experiments without an electron donor where biosorption is favored and in experiments adding Na-pyruvate as an electron donor stimulating also bioreduction processes.

Experimental: Pu biosorption, solvent extraction

Sporomusa sp. MT-2.99 and *Paenibacillus* sp. MT-2.2 cells were cultured anaerobically in R2A medium at 30°C. Cells were harvested in the mid-exponential growth phase, washed and suspended in 0.9 % NaCl solution containing 10^{-4} M Na-pyruvate. The details of strain isolation, cultivation and characterization are summarized in (Moll et al., 2013).

The starting compound to obtain the ^{242}Pu stock solution was a green-brown powder of PuO_2 (AEA technology QSA GmbH) with the following composition: 0.009 % of Pu-238, 0.008 % Pu-239, 0.020 % Pu-240, 0.017 % Pu-241, 99.945 % Pu-242, and 0.001 % Pu-244. The problem is that this substance is chemically highly inert and dissolves extremely slowly in acids (Keller, 1971). We performed an oxidative dissolution of $^{242}PuO_2$ in HNO_3 in the presence of $AgNO_3$ and $K_2S_2O_8$. Finally, the ^{242}Pu(VI) stock solution in 3 M $HClO_4$ was prepared by electrolysis. Because of the low absorption coefficients of Pu(IV), Pu(V), and Pu(IV)-polymers (Keller, 1971; Wilson et al., 2005; Ockenden and Welch, 1956) and the low concentration of Pu in the solutions, the quantification of the different Pu oxidation states was performed by solvent extraction as described in (Moll et al., 2006). The extractions were performed rapidly and in parallel. All plutonium concentrations were measured by liquid scintillation counting (LSC) using a LS counter, Wallac system 1414 (Perkin Elmer). For this, defined sample volumes (50 to 300 µL) were mixed with 5 mL of Ultima Gold scintillation cocktail. The solvent extraction experiments demonstrated that the acidic Pu stock solution still contained, besides 70 % Pu(VI), 21 % Pu(IV)-polymers due to the synthesis procedure.

The pH was measured using an InLab Solids electrode (Mettler-Toledo, Giessen, Germany) calibrated with standard buffers and a pH meter (Microprocessor pH Meter pH 537, WTW, Weinheim, Germany). The pH was adjusted with a precision of 0.05 units. The pH adjustments were made with $HClO_4$ or NaOH both from Merck, Germany. The redox potential in blanks and cell suspensions was measured using a combination redox electrode (BlueLine 31 Rx from Schott, Germany) by applying the single point calibration using a redox buffer.

The adsorption of Pu onto the reaction vessel as source of error was investigated. Therefore after the Pu interaction experiments the reaction tubes were rinsed 3 times with Milli-Q water and then incubated for 2 days with 1 M $HClO_4$ to desorb Pu. Solutions where then analyzed with LSC regarding [Pu]. The determined loss of Pu was accounted for the calculation of, for instance, the amount of Pu bound per g dry biomass.

The Pu-bacteria interaction experiments were performed at [dry biomass] of 0.33 ± 0.01 $g_{dry\ weight}$/L and pH values of 3, 4, 6.1 and 7 under N_2 atmosphere at 25°C in 0.1 M $NaClO_4$ solution. $[^{242}Pu]_{initial}$ was varied between 0.2 and 110 mg/L. For the *Paenibacillus*-system selected pH values (4 and 6) were investigated. In the *Sporomusa*-system, Na-pyruvate as one potential electron donor was added in two concentrations (0.1 and 10 mM) at pH 6.1. At pH 4 only one Na-pyruvate concentration (10 mM) was added. For *Paenibacillus* sp. cells the influence of 10 mM Na-pyruvate on the time-dependent Pu oxidation state distribution was investigated at pH 6.1. The ^{242}Pu present in blank (no cells added), supernatant, and washed biomass suspension at pH 0 was analyzed using solvent extraction, and LSC as described in (Moll et al., 2006). Samples were taken after defined time steps. The separation of cells from the supernatant solution was performed by centrifugation (6000*g*).

Accumulation of plutonium (^{242}Pu) by *Sporomusa* sp. and *Paenibacillus* sp. as a function of pH and the initial Pu concentration under anaerobic conditions – no electron donor

The decrease of Pu concentration in the supernatant after contact with the cells of both strains is shown in Fig. 9.

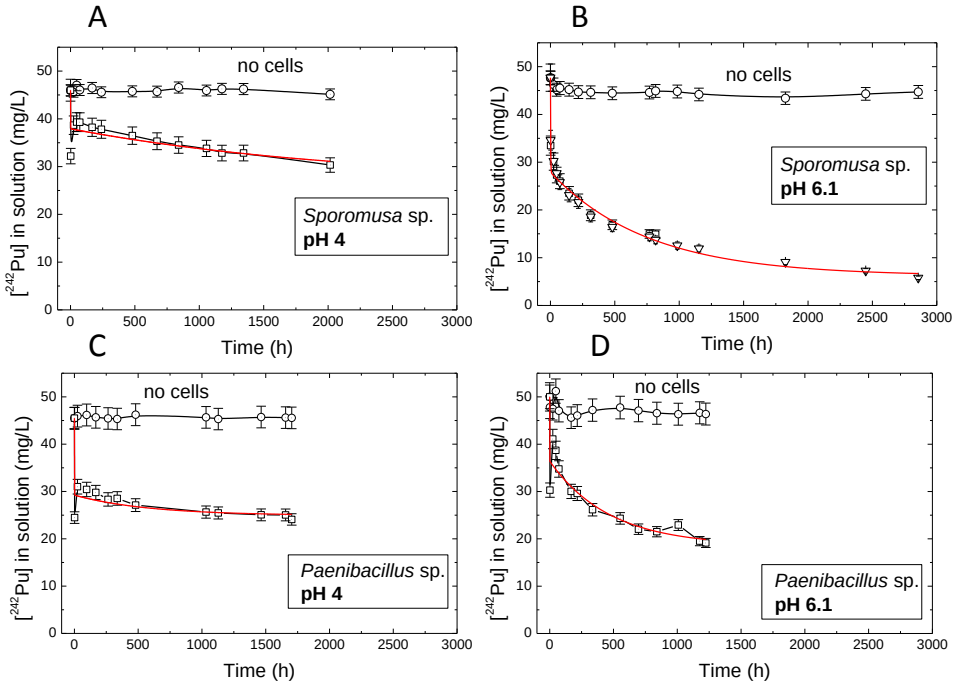

Fig. 9: Decrease of $[^{242}Pu]$ in solution at $[^{242}Pu]_{initial}$: 46 mg/L in 0.1 M $NaClO_4$ at pH 4 and 6.1 after contact with 0.33 $g_{dry\ weight}$/L of (A, B) *Sporomusa* sp. MT-2.99 and (C, D) *Paenibacillus* sp. MT-2.2. The red line represents the best fit of the experimental data.

In general, more Pu was removed at pH 6.1 compared with the results measured at pH 4.0. The time-dependent behavior of Pu in the supernatants was bi-exponential fitted ($y = y_0 + A_1\, e^{-(x/t1)} + A_2\, e^{-(x/t2)}$). The kinetic fits showed that the overall process consists of at least two parts: a fast process having a time frame of ~ 0.5 h (e.g., biosorption) and a much

slower process with a time frame of ~ 1000 h. We observed an increased amount of Pu at contact times > 300 h. This could be interpreted by a larger Pu binding capacity of the dead biomass. It seems that *Paenibacillus* has a slightly different strategy to avoid the stress caused by Pu. After 2 h of contact time (cf. Fig. 9 C, D) the cells released 40 % of this bound Pu. At incubation times ≥ 24 h an exponential decrease of the Pu concentration in solution was detected. This behavior was observed in all experiments performed as a function of the initial Pu concentration. A similar effect (but less pronounced) was observed in the *Sporomusa* sp. experiments at pH 4 at the two highest initial Pu concentrations (46 and 111 mg/L, Fig. 9 A).

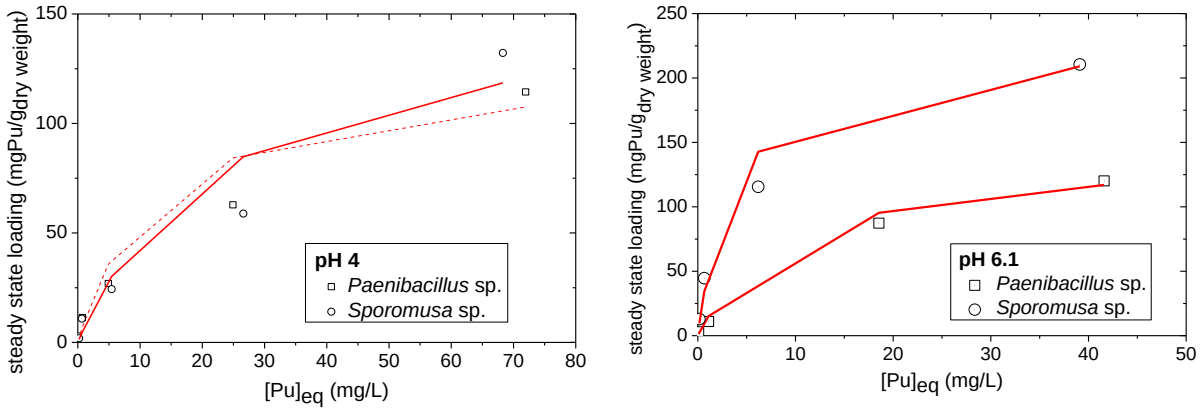

Fig. 10: Langmuir isotherms obtained in the *Sporomusa* sp. and the *Paenibacillus* sp. system at pH 4 and 6.1.

The biosorption of Pu on both strains was evaluated using the Langmuir absorption isotherm model. The application of the Langmuir-isotherm model in order to describe the biosorption of heavy metals in biological systems (e.g., biosorption of heavy metals on algae) was reported for instance in (Klimmek, 2003). The Langmuir constant b describes the affinity of the adsorbed metal to the bacterial surface (Kümmel and Worch, 1990; Atkins, 1998).

Table 5: Langmuir absorption isotherm data.

Strain	pH	a_m (mgPu/g)	b (L/mg)	R^2
Sporomusa sp.	4.0	160±46	0.043±0.011	0.730
	6.1	230±14	0.268±0.08	0.989
Paenibacillus sp.	4.0	130±21	0.081±0.04	0.892
	6.1	140±21	0.108±0.04	0.934

As depicted in Fig. 10 and Table 5 the Langmuir model could describe the experimental data with both strains and at both pH values with a reasonable quality. The sorption experiments showed that *Sporomusa* sp. cells are more effective in removing Pu from the surrounding solution. This effect is more pronounced at longer contact times. *Paenibacillus* sp. cells are accumulating less Pu. At pH 6.1 the maximal Pu loading on *Sporomusa* sp. cells was calculated to be 230 mgPu/g compared to 140 mgPu/g for *Paenibacillus* sp. cells. Panak and

Nitsche (2001) reported that aerobic soil bacteria accumulated ca. 45 mgPu/$g_{dry\ weight}$. This shows that *Sporomusa* sp. and also *Paenibacillus* sp. accumulated relatively high amounts of Pu.

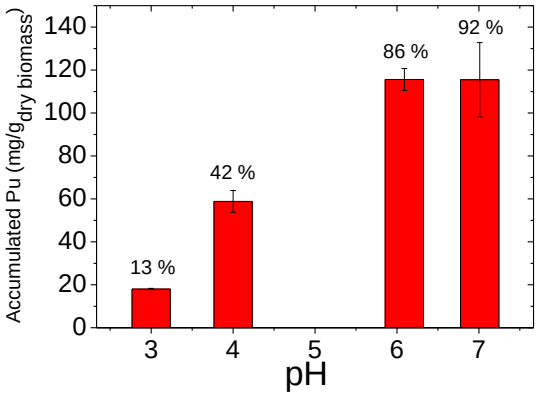

Fig. 11: Biosorption of Pu on *Sporomusa* sp. MT-2.99 at $[^{242}Pu]_{initial}$: 45 mg/L in 0.1 M $NaClO_4$ as a function of pH under steady state conditions.

Sporomusa sp. cells display a strong pH-dependent affinity for Pu (cf. Fig. 11). At pH 3, only 13 % of the initial Pu was accumulated whereas at pH 7, 90 % were associated with the biomass. The pH induced effect on the amount of biosorbed Pu was lower for *Paenibacillus* sp. cells.

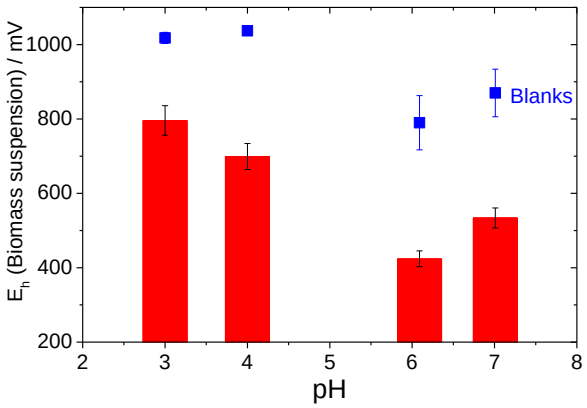

Fig. 12: Redox potentials in the *Sporomusa* sp. MT-2.99 system at $[^{242}Pu]_{initial}$: 45 mg/L in 0.1 M $NaClO_4$ as a function of pH under steady state conditions.

In the *Sporomusa* sp. system, the redox potential measurements indicated that the cells generated reducing conditions (cf. Fig. 12). The cell induced effect on the redox potential was highest at pH 6.1. Hence, the ability of the cells to decrease the redox potential seems to depend on the pH. At pH 6.1, in the blank sample at $t \geq 312$ h a redox potential of 790 ± 73 mV was measured. In the cell suspensions immediately a constant value of 331 ± 25 mV was reached. *Paenibacillus* sp. cells were less effective in minimizing the redox potential.

Desorption studies with 1 M $HClO_4$ showed that there was an incomplete Pu removal from the biomass. For both strains at $[Pu]_{initial}$ between 15 and 110 mg/L and independently of pH only 60 to 30 % of the Pu was released indicating irreversibly bound Pu.

Time-dependent Pu oxidation state distributions

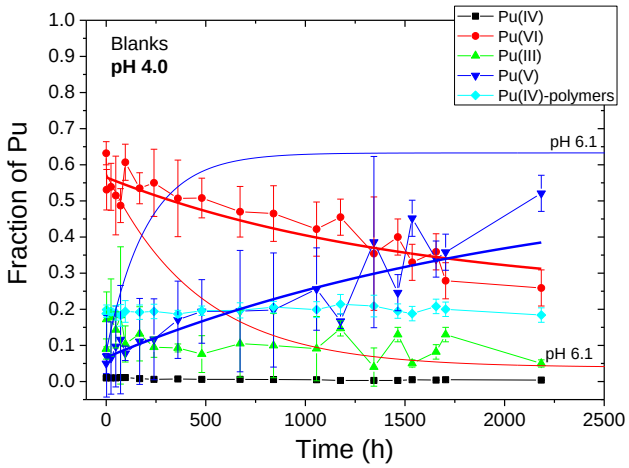

Fig. 13: ^{242}Pu oxidation state distributions in the blank samples determined by solvent extraction as a function of the incubation time ($[^{242}Pu]_{initial}$: 104±11 mg/L, 0.1 M $NaClO_4$, pH 4).

The blanks. The values depicted in Fig. 13 were averaged from three individual experimental runs. The relatively large errors of Pu(VI) and Pu(V) concentrations are the results of the averaging of the individual values from the different experimental runs. The error of the method is at largest 5 %. It reflects the temporally fluctuations of the abiotic reduction of Pu(VI) to Pu(V). In the beginning the dominating Pu species are Pu(VI), 58 ± 7 %, Pu(IV)-polymers, 19 ± 1 % and Pu(III), 13 ± 6 % (cf. Fig. 13). The time-dependent behavior of Pu(VI) and Pu(V) was mono-exponential fitted ($y = y_0 + A_1\, e^{-(x/t1)}$). By comparing the data at pH 6.1 with those at pH 4 one can conclude that the Pu redox chemistry is more reproducible at pH 4. The scattering of the data and hence the time-dependent decrease of Pu(VI) and the increase of Pu(V) is much less pronounced. The decrease of Pu(VI) at pH 6.1 is 3.2 times faster than at pH 4. The increase of Pu(V) at pH 6.1 is 3.3 times faster than at pH 4. It follows that a more acidic pH stabilizes Pu(VI). The Pu(IV)-polymer amount is with 19.6 ± 0.8 % constant within the investigated time range.

A significant change of the Pu oxidation state distributions was observed in the supernatants of both strains as shown in Fig. 14. At both pH values and for both strains a fast decrease of Pu(VI) combined with a fast increase of Pu(V) was observed. For a better comparison of the overall results the fitted Pu(VI) and Pu(V) concentrations measured at pH 6.1 were included in Fig. 14. At pH 6.1 in the *Sporomusa* sp. system the formation of Pu(V) in the supernatant is 48 times faster than in blank samples. The decrease of Pu(VI) in the supernatant is 28 times faster than in the blanks.

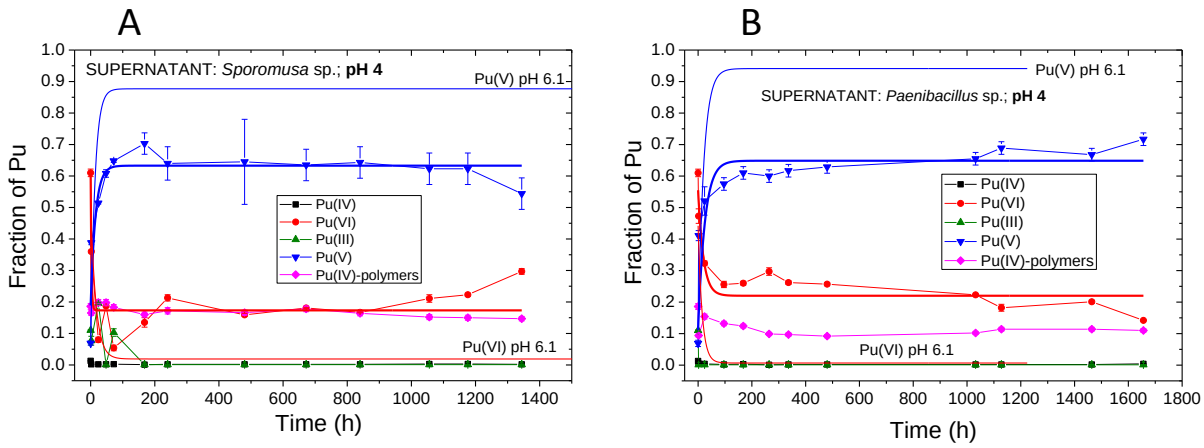

Fig. 14: ^{242}Pu oxidation state distributions in the supernatants after separation of the cells determined by solvent extraction as a function of time A) *Sporomusa* sp. and B) *Paenibacillus* sp. ([^{242}Pu]$_{initial}$: 111±2 mg/L, [dry biomass] 0.34 g/L, 0.1 M $NaClO_4$, pH 4).

At pH 6.1 in the *Paenibacillus* sp. system the formation of Pu(V) in the supernatant is only 30 times faster than in blank samples. The decrease of Pu(VI) in the supernatant is 31 times faster than in the blanks. The equilibrium concentration of Pu(V) in the supernatants of both strains is with ca. 90 % higher than in the blanks where 76 % were found. The difference between both strains is that in the *Sporomusa* sp. system the enrichment of Pu(V) in the supernatant was faster. At pH 4 in the *Sporomusa* sp. system the formation of Pu(V) in the supernatant is 144 times faster than in blank samples. The decrease of Pu(VI) in the supernatant is 626 times faster than in the blanks. The difference between both strains at pH 4 again is that in the *Sporomusa* sp. system the enrichment of Pu(V) (2 times) and the decrease of Pu(VI) (8 times) was faster compared to the *Paenibacillus* sp. system. The observed bioreduction process of Pu(VI) to Pu(V) by cells of *Sporomusa* sp. and *Paenibacillus* sp. is not yet fully understood. After the interaction the majority of the Pu(V) was detected in solution. We assume that this happens due to the comparable weak complexing properties of the PuO_2^+ ion which is related with a release from the cell envelope. Similar observations were made in the past (Panak and Nitsche, 2001; Moll et al., 2006; Moll et al., 2013). The formed Pu(V) is relatively stable after removing the cells from solution. At pH 6.1 for both strains the equilibrium concentration of the Pu(IV)-polymers was 6 % compared with 12.5 % found in the blanks. This suggests a pronounced biosorption of Pu(VI)-polymers on the biomass. At pH 4 similar results were observed for *Paenibacillus* sp. where 11 % Pu(IV)-polymers were measured in the supernatant compared with 20 % in the blanks. The average Pu(IV)-polymer concentration in the *Sporomusa* sp. supernatants was with 17 % higher showing a lower tendency to interact with cells.

Both strains showed no differences in the Pu-oxidation state distribution of the Pu associated on the biomass at pH 6.1 (cf. Fig. 15). The summary of all extraction data observed in the electron-donor free experiments with *Sporomusa* sp. and *Paenibacillus* sp. showed scattered concentration data of the individual plutonium oxidation states. However, a few trends can be seen.

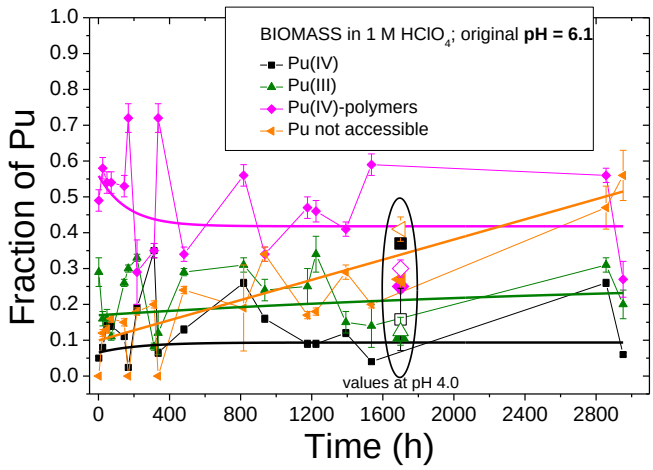

Fig. 15: ^{242}Pu oxidation state distributions in the biomass (*Sporomusa* sp. and P*aenibacillus* sp.) by solvent extraction over the time ([^{242}Pu]$_{initial}$: 15 to 110 mg/L, [dry biomass] 0.34 g/L, 0.1 M $NaClO_4$, pH 6.1 and 4).

The major oxidation state identified were Pu(IV)-polymers with an average amount of 42 %. The scattered data of Pu(IV)-polymers could be fitted to a mono-exponential decay function ($y = y_0 + A_1\ e^{-(x/t1)}$). The Pu(III) average amount of 27 % is clearly higher than found in the blanks and supernatant. There is a linear increase of Pu which was not accessible by the extraction technique. This plutonium could be masked for instance by an uptake in dead biomass. This amount of Pu can be also correlated with the amount of irreversibly bond Pu (*Sporomusa* sp.: 40-60 %; *Paenibacillus* sp.: ca. 30 %). The scattered values of Pu(IV) could be fitted to an exponential growth function ($y = y_0 + A_1\ e^{(x/t1)}$) giving an average concentration of 9 ± 2 %. This value is significantly higher compared to the findings in the blanks and supernatants of ca. 1 %. In general lower amounts of Pu(IV)-polymers, 34 %, were found at pH 4. This corresponds with higher concentrations of Pu(IV) (*Sporomusa* sp. are more effective in forming Pu(IV), 31 %, than *Paenibacillus* sp., 16 %). The other Pu oxidation states correspond well with the dependencies detected at pH 6.1.

Interaction of plutonium (^{242}Pu) with *Sporomusa* sp. and *Paenibacillus* sp. in the presence of an electron donor – 10 mM Na-pyruvate

The decrease of Pu concentration in the supernatant after contact with the cells of both strains applying 10 mM Na-pyruvate is shown in Fig. 16.

Sporomusa sp. system. At pH 4 the time-dependent behavior of Pu in the supernatants was bi-exponential fitted ($y = y_0 + A_1\ e^{-(x/t1)} + A_2\ e^{-(x/t2)}$) (cf. Fig. 16 A). The kinetic fits showed that the overall process consists of at least two parts: a fast process having a time frame of ~ 0.1 h (e.g., biosorption) and a much slower process with a time frame of ~ 120 h. We observed faster processes compared with the results at pH 6.1. At pH 6.1 the time-dependent decrease of Pu could be best fitted applying a mono-exponential decay law (cf. Fig. 16 B). This indicates one dominating step having a time frame of 8.3 h.

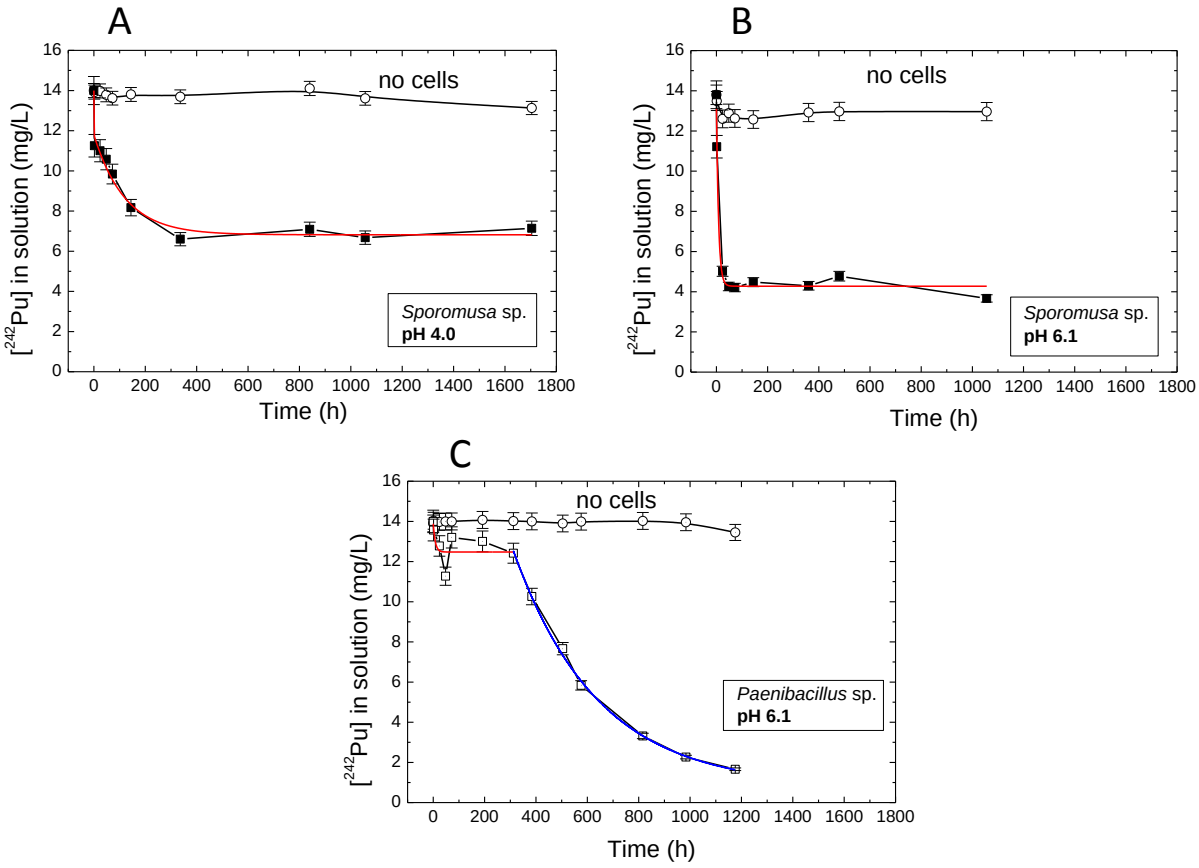

Fig. 16: Decrease of the [^{242}Pu] in solution at [^{242}Pu]$_{initial}$: 14 mg/L in 0.1 M $NaClO_4$ at pH 4 and 6.1 after contact with 0.34 g/L of (A, B) *Sporomusa* sp. MT-2.99 and (C) at pH 6.1 after contact with 0.22 g/L *Paenibacillus* sp. MT-2.2. The red and blue line represents the best fit of the experimental data.

Paenibacillus sp. system. The time-dependent decrease of the plutonium concentration in solution could only be fitted by dividing the time frame into two ranges and applying a mono-exponential law. Here the lack phase was longer compared to the 0.1 M $NaClO_4$ system (cf. Fig. 9 D). A continuous decrease of the plutonium in the cell surrounding solutions was observed first after 312 h of incubation. This underlines the finding in the 0.1 M $NaClO_4$ system except that the time frame is clearly longer than observed there with 24 h.

For *Sporomusa* sp. a comparison of the accumulated Pu in dependence of pH and Na-pyruvate concentration was done. The accumulated amount of Pu was calculated based on the fit of the Pu concentrations in solution. The results showed that with increasing Na-pyruvate concentration less Pu is associated on the biomass. Hence the cells displayed a higher affinity for Pu in the absence of an electron donor.

In the *Sporomusa* sp. system in contrast to the electron donor free experiments, we could measure that more than 80 % of the plutonium was released from the cells over the investigated time range at 10 mM Na-pyruvate at pH 6.1 (cf. Fig. 17).

Table 6: Pu loadings on *Sporomusa* sp. biomass at $[Pu]_{initial}$ = 14 mg/L.

Strain	pH	[Na-pyruvate] (mM)	Pu loading ($mgPu/g_{dry\ weight}$)
Sporomusa sp.	4.0	no	24.4
	4.0	10	20.5
	6.1	no	44.6
	6.1	0.1	41.9
	6.1	10	26.4

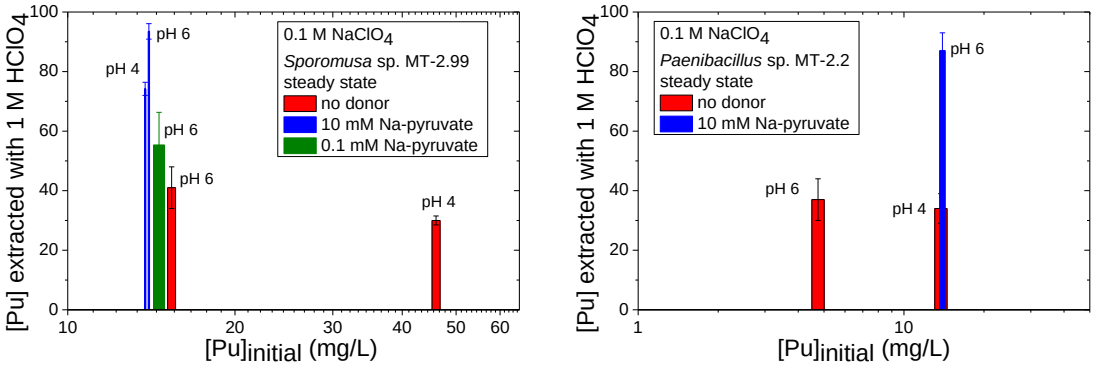

Fig. 17: Percentage of the cell bound Pu extracted from the biomass with 1 M $HClO_4$.

At pH 4.0 the value drops down to 74 %. However, this might indicate a dominant complexation/fixation of plutonium on functional groups located at the cell surface in the presence of 10 mM Na-pyruvate. Also for *Paenibacillus* sp. the majority (more than 80 %) of the plutonium could be dissolved from the cells pointing to a dominant surface complexation onto functionalities of the bacterial cell surface. In the case of *Sporomusa* sp. desorption experiments were performed as a function of the pyruvate concentration. The average amounts of extractable Pu from the cells at an initial Pu concentration of 14 mg/L were: 41 ± 7 % no donor, 55 ± 11 % 0.1 mM pyruvate, and 93 ± 3 % 10 mM pyruvate at pH 6. In the absence of an electron donor at pH 4 the average amount of extractable Pu from the biomass was in the same region (ca. 35 %) as observed for pH 6 for both strains. In the presence of 10 mM Na-pyruvate for both strains and independent of pH always more than 70 % of the Pu could be extracted from the biomass. It seems that increased concentrations of pyruvate increase also the contribution of a reversible surface complexation of Pu on the bacterial cell surface.

Between 2 and 144 h we measured lower redox potentials in the cell suspensions compared to the blanks at pH 4 (cf. Fig. 18). After 336 h similar redox potentials in blank and cell suspensions were measured. The average redox potential in blank solutions (144 to 1704 h) was 471 ± 18 mV. In the cell suspensions immediately a constant value of 477 ± 7 mV was reached. In the blank sample the redox potential drops slowly from 490 mV to 200 mV after 144 h of contact time and was than with 180 ± 18 mV nearly constant. In the cell suspensions immediately a drop in the redox potential to 284 mV was detected. Very quickly a constant value (24 to 1056 h) of 190 ± 10 mV was reached. After 360 h similar redox potentials

were measured in the blank and the cell suspensions. Both the pH and the Na-pyruvate are influencing the redox potential.

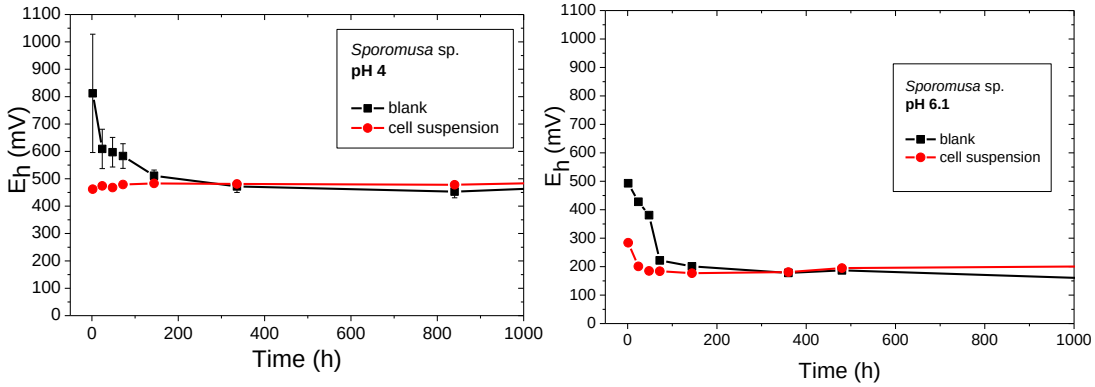

Fig. 18: Time-dependent redox potentials measured in the *Sporomusa* sp. system in the presence of 10 mM Na-pyruvate at pH 4 and pH 6.1 ($[Pu]_{initial}$ = 14 mg/L, 0.1 M $NaClO_4$).

Paenibacillus sp. cells are less effective in decreasing the redox potential in the presence of 10 mM Na-pyruvate (data not shown). To conclude, the cell induced effect on the redox potential is smaller in the presence of 10 mM Na-pyruvate.

Time-dependent Pu oxidation state distributions

Compared to the pyruvate-free system (cf. Fig. 13) a complicated Pu redox-chemistry was observed due to the reducing properties of pyruvate as depicted in Fig. 19.

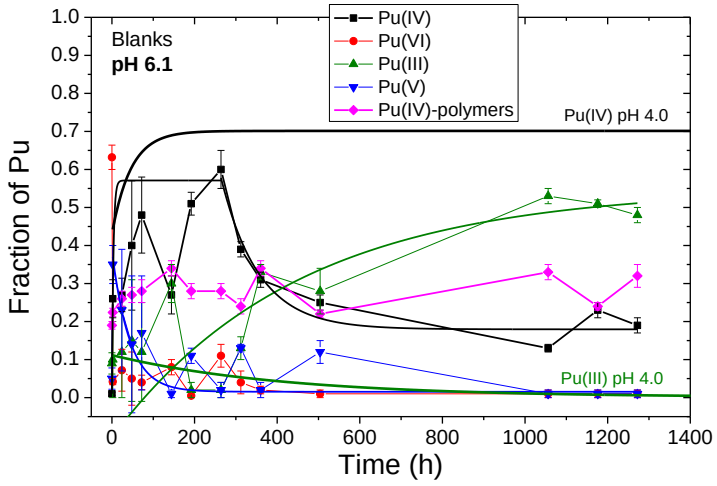

Fig. 19: ^{242}Pu oxidation state distributions in the blank samples determined by solvent extraction as a function of the incubation time ($[^{242}Pu]_{initial}$: 13.8±0.5 mg/L, 0.1 M $NaClO_4$, 10 mM Na-pyruvate, pH 6.1).

At pH 6.1 and 4 a fast abiotic reduction of Pu(VI) was observed. At pH 6.1 within the first 1.2 h the amount of Pu(VI) decreased from 61 to about 4 %. Whereas after 2 h almost no Pu(VI) could be detected at pH 4. At both pH values simultaneously Pu(V) and Pu(IV) increased to about 31 % (22 % at pH 4) and 22 % (45 % at pH 4), respectively. Due to the pH

of 6.1, we observed also an increase of Pu(IV)-polymers from 19 % in the beginning to about 34 % at the end of the experiment. This could be explained by a transfer of the formed Pu(IV) into Pu(IV)-polymers. At pH 4 the Pu(IV)-polymer fraction remained constant at 27.0 ± 2.9 %. Pu(V) was abiotically reduced to Pu(IV) due to the presence of pyruvate. Later on (t ≥ 144 h) we observed an increase of Pu(III) in combination with an decrease of Pu(IV) at pH 6.1. This might indicate a further reduction of Pu(IV) forming Pu(III). Hence to model the Pu(IV) behavior at pH 6 the data were split into two time ranges. First there was an exponential growth of Pu(IV) followed by an exponential decrease. In contrast at pH 4, there was an exponential growth of the Pu(IV) fraction with a steady state concentration of 70 % (major difference between both pH values). A further difference was the behavior of Pu(III). At pH 6.1 an exponential growth with an equilibrium concentration of 55 % was calculated. Whereas at pH 4 for Pu(III) an exponential decay with very low (0.1 %) equilibrium concentrations were found.

At the beginning at pH 6.1, the major oxidation states (complexed with pyruvate) interacting with the biomass are Pu(V) with 31 %, Pu(IV) with 22 %, and Pu(IV)-polymers with 23 %. At the beginning at pH 4, the major oxidation states (complexed with pyruvate) interacting with the biomass are Pu(IV) with 39 %, Pu(V) with 20 %, and Pu(IV)-polymers with 24 %.

Differences between the time-dependent Pu oxidation state distributions in the supernatant at pH 6.1 between both strains were detected (cf. Fig. 20).

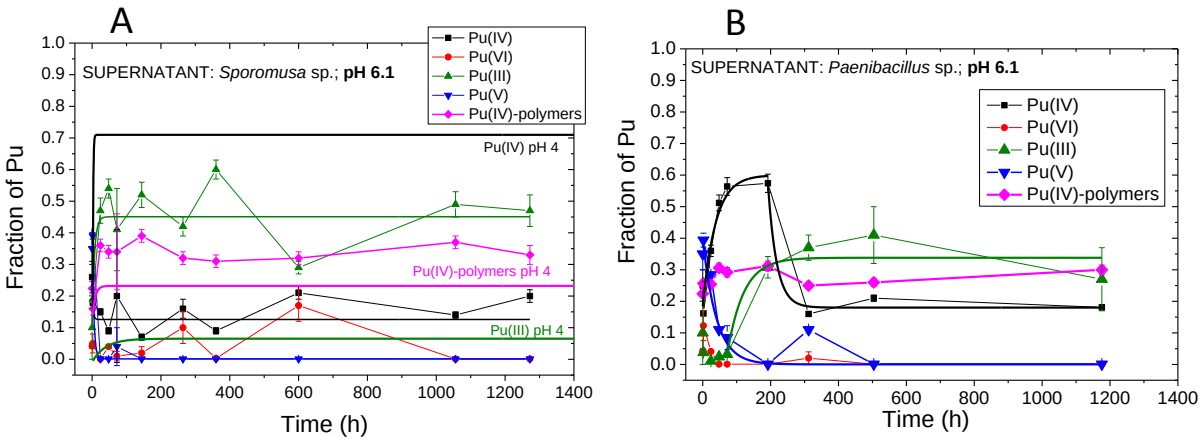

Fig. 20: ^{242}Pu oxidation state distributions in the supernatants after separation of the cells determined by solvent extraction as a function of time A) *Sporomusa* sp.: [dry biomass] 0.34 g/L at pH 4 and 6.1 and B) *Paenibacillus* sp.: [dry biomass] 0.22 g/L at pH 6.1 ($[^{242}Pu]_{initial}$: 14 mg/L, 0.1 M $NaClO_4$, 10 mM Na-pyruvate).

In the *Paenibacillus* experiment for the individual Pu oxidation states in the supernatants similar trends were observed as in the blanks. One reason could be the lower reducing properties of *Paenibacillus* sp. as indicated by the redox potential measurements compared to the *Sporomusa* sp. findings. At pH 6.1 the time-dependent behavior of Pu(III), Pu(IV), and Pu(V) was calculated with mono-exponential growth or decay functions except for Pu(IV) in the *Paenibacillus* experiment. The Pu(IV) data were split into two time ranges. First there was an mono-exponential growth followed by an exponential decrease of Pu(IV). At pH 6.1 in the

Sporomusa sp. system the formation of Pu(III) as the major oxidation state in the supernatant is 68 times faster than in blank samples. The decrease of Pu(IV) in the supernatant is 9 times faster than in the blanks. The decrease of Pu(V) is 35 times faster than in the blank samples. Under steady state conditions similar concentrations of Pu(III) (~50 %), Pu(IV) (~15 %), and Pu(V) (~1 %) were measured in blanks and the *Sporomusa* sp. supernatants. As a difference in the *Paenibacillus* sp. experiment slower processes than in the *Sporomusa* sp. supernatants were measured. At pH 6.1 Pu(III) was major Pu oxidation state in the blanks (55 %), the *Sporomusa* sp. supernatants (45 %), and the *Paenibacillus* sp. supernatants (34 %). At pH 4 in the *Sporomusa* sp. system a clear enrichment of Pu(IV) was observed. The main differences (influence of the cells) compared to the blanks are a faster increase of Pu(IV) (33 times), a slight increase of Pu(III) and slightly lower concentration of Pu(IV)-polymers (23.2 %). The equilibrium concentration of Pu(III) was with 6.5 % higher as in the blank (0.1 %).

The Pu oxidation state distributions of the Pu associated on the biomass under addition of 10 mM Na-pyruvate are summarized in Fig. 21.

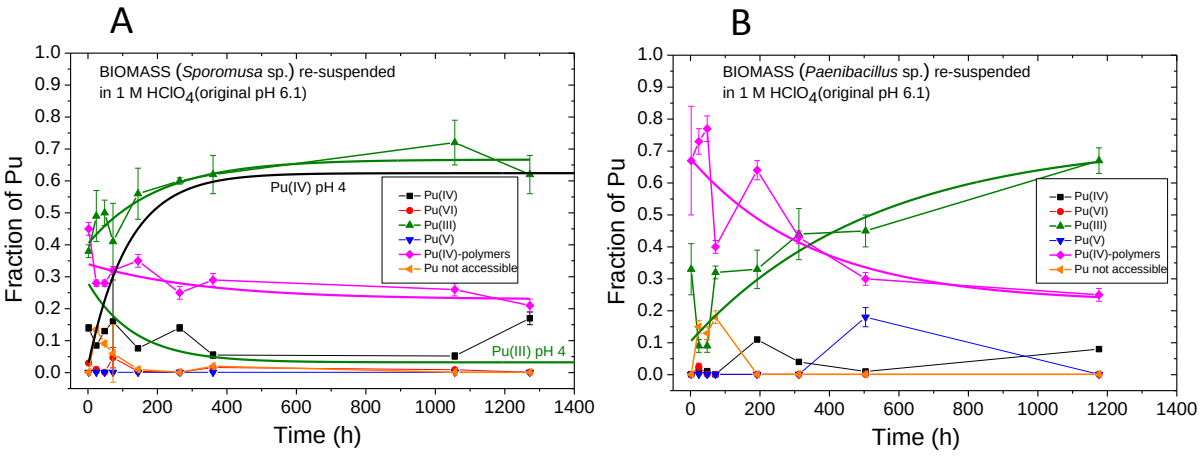

Fig. 21: ^{242}Pu oxidation state distributions in the biomass (*Sporomusa* sp. 0.34 g/L and P*aenibacillus* sp. 0.22 g/L) by solvent extraction over the time ([^{242}Pu]$_{initial}$: 14 mg/L, 0.1 M $NaClO_4$, 10 mM Na-pyruvate, pH 6.1 and 4 (only for *Sporomusa* sp.).

At pH 6.1 there was a clear enrichment of Pu(III) in the biomass in the presence of 10 mM Na-pyruvate (Fig. 21). Pu(IV)-polymers associated on biomass dominated in 0.1 M $NaClO_4$ (Fig. 15). The formation of Pu(III) was in the *Sporomusa* sp. system three times faster than in the *Paenibacillus* sp. system. In both cases similar steady state concentrations of 70 ± 4 % were observed. This amount is three times higher than in the electron donor free system. In the presence of Na-pyruvate, the Pu(IV)-polymer concentration in the biomass yielded lower steady state concentrations than in the electron donor free experiments. Therefore, we assume a transfer of Pu(IV)-polymers into Pu(III) promoted by pyruvate and surface functional groups of the cell surface. From the pyruvate concentration-dependent experiments one can conclude that 0.011 g/L pyruvate has a similar influence on the Pu redox chemistry as 0.33 g/L *Sporomusa* sp. MT-2.99 cells. For *Sporomusa* sp. the time-dependent behavior of the fractions Pu(V), Pu(VI), Pu not accessible, and Pu(IV)-polymers is comparable at both pH

values. The decrease of the Pu(IV)-polymer amount is approximately 4 times faster at pH 6.1 compared to pH 4. The equilibrium amount is with 23.5 % equal for both pH values. The main difference (as also observed in the blank and the supernatants) is an enrichment of Pu(IV) on the biomass at pH 4. Whereas at pH 6.1 Pu(III) was enriched.

Summary of the plutonium (^{242}Pu) interaction studies with *Sporomusa* sp. and *Paenibacillus* sp.

In this study, the interaction of Pu with two bacterial isolates, *Sporomusa* sp. and *Paenibacillus* sp., from Mont Terri Opalinus Clay was investigated in 0.1 M $NaClO_4$ as a function of the initial Pu concentration, the pH, and with and without adding Na-pyruvate as one potential electron donor. The decrease of the Pu concentration in the supernatants was bi-exponential fitted. The calculations showed that the overall process consists of at least two parts: a fast process having a time frame of ~ 0.5 h (e.g., biosorption) and a much slower process with a time frame of ~ 1000 h. In the electron donor containing system faster kinetics especially for the *Sporomusa* sp. were found. It seems that *Paenibacillus* has a slightly different strategy to avoid the stress caused by Pu. After 2 h of contact time the cells released 40 % of this bound Pu. At contact times ≥ 24 h an exponential decrease of the Pu concentration in solution was detected. This phase of the release of biosorbed Pu from the cells was prolonged in the presence of 10 mM Na-pyruvate. At pH 6.1 in the presence of 10 mM Na-pyruvate in the *Sporomusa* sp. system a mono-exponential decrease of Pu was found in the supernatant. The isolates displayed a strong pH-dependent affinity for Pu. Using the Langmuir model the maximal Pu loading at pH 6.1 on *Sporomusa* sp. and *Paenibacillus* sp., 230±14 and 140±21 mgPu/$g_{dry\ biomass}$, respectively, were calculated. This shows that *Sporomusa* sp. is more efficient in removing Pu from the surrounding solution. The maximal loadings are high compared to literature values (e.g., Panak and Nitsche, 2001). Desorption studies with 1 M $HClO_4$ showed that in the electron donor free samples only 60 to 40 % of the Pu was released indicating irreversibly bound Pu. In the presence of 10 mM Na-pyruvate more than 80 % of the Pu was released indicating a higher amount of reversible sorption reaction of Pu onto the cell surface. The redox potential measurements indicated that the cells generated reducing conditions. *Paenibacillus* sp. cells were less effective in minimizing the redox potential. The cell induced effect on the redox potential is smaller in the presence of 10 mM Na-pyruvate. In the pure $NaClO_4$ solutions a strong enrichment of Pu(V) in the supernatants was discovered. In the *Sporomusa* sp. system the formation of Pu(V) was 48 times faster than in blanks. In the *Paenibacillus* sp. system the enrichment of Pu(V) and the subsequent decrease of Pu(VI) was slower but still faster than in blanks. The Pu(V) was surprisingly stable in the bacterial suspensions. At pH 4 the enrichment of Pu(V) was less strong and also higher remaining Pu(VI) concentrations in the supernatants were measured. This might indicate a lower reducing impact of the cells at pH 4. No differences between both strains were observed regarding the Pu oxidation state distributions in the acidified biomass suspensions if no electron donor was previously added. The major Pu oxidation state was Pu(IV)-polymers with an average amount of 42 %. A change of the Pu oxidation state distributions in blanks, supernatants, and acidified biomass suspensions was observed in the presence of 10 mM Na-pyruvate. Also the pH influenced the Pu oxidation state distributions. At pH 6.1 for *Sporomusa* sp. an enrichment of Pu(III) was detected in the supernatant. This process was 68 times faster than in blanks. As a difference between both strains slower processes (Pu(III)

increase, Pu(IV)- and Pu(V) decrease) were measured in the *Paenibacillus* sp. system. At pH 6.1 Pu(III) was major Pu oxidation state in the blanks (55 %), the *Sporomusa* sp. supernatants (45 %), and the *Paenibacillus* sp. supernatants (34 %). At pH 4 in the *Sporomusa* sp. system a clear enrichment of Pu(IV) was observed. In contrast to the experiments in pure $NaClO_4$ solution, in the presence of 10 mM Na-pyruvate an enrichment of Pu(III) at pH 6.1 and of Pu(IV) at pH 4 was observed in the acidified biomass suspensions. This might indicate bio-reduction processes taking place. At pH 6.1 again the observed processes (decrease of Pu(IV)-polymers and increase of Pu(III)) were faster in the presence of *Sporomusa* sp. cells compared with *Paenibacillus* sp. cells. Hence, at a fixed concentration of Na-pyruvate of 10 mM the cell induced impact on the Pu oxidation state distributions depends on pH. To conclude, a moderate to strong impact of *Sporomusa* sp. and *Paenibacillus* sp. cells on the Pu speciation was observed. Differences in the Pu interaction process of both strains for instance depend on the presence or absence of an electron donor were detected.

3.2 Eu(III), Cm(III), and U(VI) interaction with the halophilic archaeon *Halobacterium noricense* (DSM-15987)

3.2.1 General remarks

Cultivation of Halobacterium noricense DSM-15987

The archaeon *Halobacterium noricense* DSM-15987 was ordered from the Leibniz Institute DSMZ-German Collection of Microorganisms and Cell cultures and cultivated in DSM-Medium 372 at 30°C. The strain was originally isolated from a salt mine in Austria (Gruber et al., 2004). The cells were grown up to exponential growth phase (OD_{600} of 0.5) for 4 days and harvested by centrifugation at 10.000 g for 10 min. To study the interactions of *Hbt*. *noricense* DSM-15987 with lanthanides and actinides, the cell pellet was washed three times and resuspended in 3 M NaCl solution. The biomass of the cell stock suspension was determined by measuring the OD_{600} which was then converted to the dry biomass.

Correction of the pH value at high ionic strength

Due to the high ionic strength the measured pH value corresponds not to the real hydrogen ion activity. For the microbiological studies the method described by (Ams et al., 2013) was used to correct the hydrogen ion concentration:

$$pC_{H+} = \text{pH measured} + K \quad (3.1)$$

There is a linear relationship between the ionic strength I and K, so that K can be calculated with the following equation.

$$K = (0.1868 \times I) - 0.073 \quad (3.2)$$

For a 3 M NaCl solution the measured pH value has to be corrected by the factor of 0.49.

3.2.2 Eu(III)/Cm(III)

The Eu(III)/Cm(III) experiments performed in the present project were planned as preliminary investigations to get a first insight on possible speciation changes of Eu(III)/Cm(III) in suspensions of the halophilic archaeon *Halobacterium noricense*. This organism requires high salt concentrations. Hence the speciation experiments using time-resolved laser-induced fluorescence spectroscopy (TRLFS) were performed in 3 M NaCl. Experiments were conducted at a fixed metal ([Eu] 30 µM, [Cm] 0.3 µM) and biomass concentration of 0.5 g/L as a function of pC_{H+}. The results will be compared with those measured in the presence of the bacterium *Sporomusa* sp. from Mont Terri Opalinus Clay (Moll et al., 2013; Moll et al., 2014). The investigations on the interaction of *Hbt. noricense* with Eu(III)/Cm(III) will be complemented by the HZDR Young Investigator Group MicroSalt.

In the past many spectroscopic investigations have demonstrated that the characteristic luminescence emission band of Cm^{3+} at 593.7 ± 0.1 nm is sensitive to changes in its first coordination sphere. The corresponding luminescence spectrum of Eu^{3+} is characterized by emission bands at 585-600 nm and 610-625 nm representing the magnetic dipole transition $^5D_0 \rightarrow {}^7F_1$ and the hypersensitive transition $^5D_0 \rightarrow {}^7F_2$, respectively (e.g., Plancque et al., 2003; Bünzli and Piguet, 2005; Heller et al., 2012). In contrast to curium, changes in the first coordination sphere of europium leads rather to a change in the intensity of the hypersensitive transition $^5D_0 \rightarrow {}^7F_2$ than in a wavelength shift of the emission maxima. Hence, this technique can be successfully used as a direct speciation method to explore Cm^{3+} and Eu^{3+} complex formation in the µM concentration range (e.g., Collins et al., 2011). Available experimental data until 2006 on the speciation of Cm(III) investigated by TRLFS were compiled by Edelstein et al. (2006). Compared to processes involving inorganic and organic ligands, little is known about the direct speciation of Cm(III) with halophilic microorganisms (e.g., Ozaki et al., 2004). Hitherto there is no literature source available on the Cm(III)/Eu(III) interaction with a *Halobacterium noricense* strain, whereof a phylogenetic closely related strain was isolated from the Waste Isolation Pilot Plant in Carlsbad, New Mexico, USA (Swanson et al., 2012).

Experimental: Preparation of Cm(III)/Eu(III) microbe solutions, TRLFS: experimental setup and evaluation of spectra

The cultivation of *Halobacterium noricense* DSM-15987 was already explained under 3.2.1.

A stock solution of the long-lived curium isotope ^{248}Cm (half-life: 3.4×10^5 years) was used. This solution had the following composition: 97.3 % ^{248}Cm, 2.6 % ^{246}Cm, 0.04 % ^{245}Cm, 0.02 % ^{247}Cm, and 0.009 % ^{244}Cm in 1.0 M $HClO_4$. $EuCl_3 \cdot 6H_2O$ (99.999 %) was purchased from Sigma. An Eu(III) stock solution, 0.01 M, was prepared by dissolving $EuCl_3$ in water. The exact concentration was determined by ICP-MS (Elan 6000, Perkin Elmer). The experiments were performed in a glove box under a N_2 atmosphere at 25°C. As a background electrolyte, analytical grade 3 M NaCl (Sigma-Aldrich, Germany) was used. To prevent the carbonate complexation of Cm(III) and Eu(III), carbonate-free water and NaOH solutions were used. The pH was measured using an InLab Solids combination pH puncture electrode (Mettler-Toledo, Giessen, Germany) calibrated with standard buffers. The pH was changed by

adding analytical grade NaOH or HCl with an accuracy of ± 0.05 units. The measured pH was corrected for 3 M NaCl by the factor 0.49 to get the real hydrogen ion activity pC_{H+} (cf. 3.2.1). For the Eu(III) measurements appropriate amounts of the concentrated cell suspension were centrifuged and the pellet was re-suspended in the corresponding blank solution with the required pC_{H+} containing 30 µM Eu in 3 M NaCl. Two series of experiments were performed at 30 µM Eu^{3+} and at [dry biomass] 0.5 g/L to explore its interaction behavior with *Hbt. noricense*, while varying the pC_{H+} between 4.0 and 8.0. In one run cells and supernatants were separated by centrifugation and analyzed for [Eu] by ICP-MS. Three series of experiments were performed at 0.3 µM Cm^{3+} and at [dry biomass] 0.5 g/L to explore its interaction behavior with *Hbt. noricense*, while varying the pC_{H+} between 4.0 and 8.0. All TRLFS spectra were measured after an equilibration time of 1 h. The pC_{H+}-dependent TRLFS spectra of the Cm(III)/Eu(III) containing *Hbt. noricense* suspensions will be discussed.

The time-resolved luminescence spectra were recorded using a unique pulsed flash lamp pumped Nd:YAG-OPO laser system (Powerlite Precision II 9020 laser equipped with a Green PANTHER EX OPO from Continuum, Santa Clara, CA, USA). The laser pulse energy, which was between 1.5 and 3.5 mJ was monitored using a photodiode. The luminescence spectra were detected using an optical multi-channel analyzer-system, consisting of an Oriel MS 257 monochromator and spectrograph with a 300 or 1200 line mm^{-1} grating and an Andor iStar ICCD camera (Lot-Oriel Group, Darmstadt, Germany). The Cm(III)/Eu(III) single luminescence emission spectra were recorded in the 570-650 nm (1200 line mm^{-1} grating with 0.2 nm resolution) range. The time-dependent luminescence spectra were detected in the 500-700 nm (300 line mm^{-1} grating) range. A constant time window of 1 ms length was applied, and due to the high absorption of the F-band usually observed in Cm^{3+} excitation spectra an excitation wavelength of 396 nm was used. For Eu(III) an excitation wavelength of 394 nm was used. The TRLFS setup has been described in detail elsewhere (Moll et al., 2008; Moll et al., 2014).

The spectra were base-line corrected; energy corrected and normalized using the OriginPro 8.6G (OriginLab Corporation, USA) code. The lifetime of luminescent species was obtained also with this software. In the case of Eu(III) normalization was applied only to the peak area of the $^5D_0 \rightarrow {}^7F_1$ band because the luminescence of this transition is a magnetic dipole and therefore not influenced by the chemical environment of the metal ion. In the case of Eu(III) the relative peak intensity ratio ($R_{E/M}$) was defined as:

$$R_{E/M} = I\,(^5D_0 \rightarrow {}^7F_2) \,/\, I\,(^5D_0 \rightarrow {}^7F_1) \qquad (3.3)$$

where I ($^5D_0 \rightarrow {}^7F_2$) and I ($^5D_0 \rightarrow {}^7F_1$) were calculated from the peak areas. The number of coordinated water molecules was calculated using the empirical equations given by Kimura et al. (1994; 1996; 1998):

$$nH_2O \pm 0.5 = 0.65 \times 1/\tau - 0.88 \text{ for Cm(III)} \qquad (3.4)$$

$$nH_2O \pm 0.5 = 1.07 \times 1/\tau - 0.62 \text{ for Eu(III)} \qquad (3.5)$$

where τ is the measured luminescence lifetime in ms. Luminescence data were analyzed with the factor analysis technique iterative transformation factor analysis (ITFA) to determine the number of acting species and their pH speciation. Applying factor analysis, the number of acting complexes can be estimated and the spectral mixtures can be decomposed into spectra of the acting complexes and their pH speciation. The application of ITFA to analyze spectroscopic date is summarized in (e.g., Rossberg et al., 2003; Lucks et al., 2012).

The *Hbt. noricense* Eu(III) system – TRLFS

Fig. 22 summarizes the amount of Eu(III) associated on the cells based on the ICP-MS analyses of the supernatants after separating the cells. We could detect a slightly pH-dependent biosorption of Eu(III) on *Hbt. noricense* cells. The affinity of *Hbt. noricense* cells to accumulate Eu(III) is relatively low after an incubation time of 1 h. There was an increase in Eu(III) sorption moving from pC_{H+} 4.1, 10 % sorbed to pC_{H+} 7.98, 40 % sorbed. The halophilic archaeon *Hbt. noricense* removed much less Eu(III) from the surrounding solution compared for instance with the Mont Terri Clay isolate *Sporomusa* sp. where independently of pH always ≥ 90 % of the Eu(III) was associated on the biomass (Moll et al., 2014).

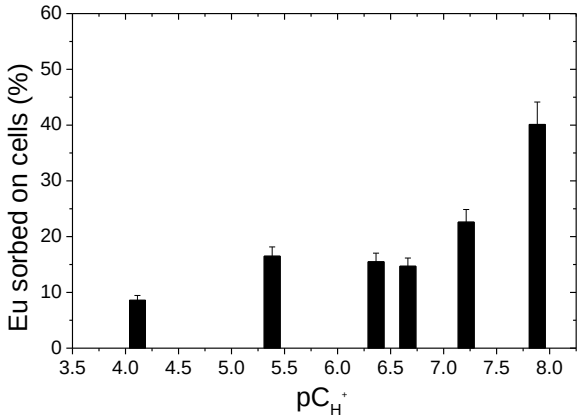

Fig. 22: Eu(III) association on *Halobacterium noricense* DSM-15987 after an incubation time of 1 h as a function of pC_{H+} ([Eu] 30 µM, [dry biomass] 0.5 g/L, 3 M NaCl).

Higher Eu(III) loadings were observed by increasing the incubation time to 48 h where than 55 %, 74 %, and 61 % of the Eu(III) was sorbed on the cells at pC_{H+} 4.5, 5.5 and 6.2, respectively. Ozaki et al. (2004) observed faster kinetics in their experiments between Eu(III) and for instance the halophilic archaeon *Halobacterium salinarum*. Already after 20 min of incubation time maximal loadings between 25 and 75 % were observed moving from pC_{H+} 3.7 to 5.7. As described later on for U(VI) also during the Eu(III) interaction experiments indications were found for an agglomeration of the cells especially at low and high pH in the presence of Eu(III) (stress response).

The luminescence spectrum of Eu^{3+} displays the changes upon cell addition and pC_{H+} change which points to complexation reactions of Eu(III) in *Hbt. noricense* suspensions (cf. Fig. 23 A).

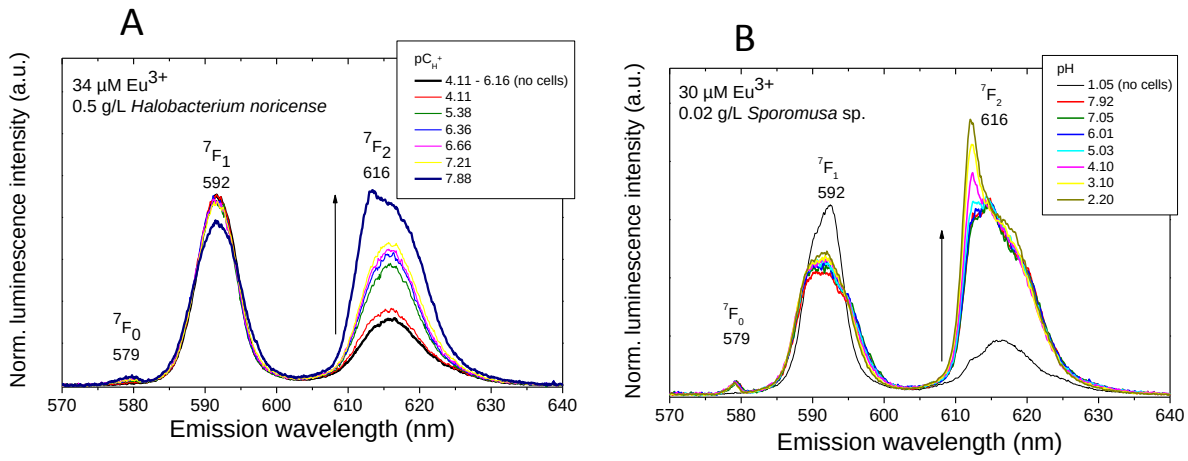

Fig. 23: Luminescence emission spectra of 32±3 µM Eu(III) as a function of pH/pC_{H+} after 1 h of contact time in (A) 3 M NaCl with 0.5 g/L *Hbt. noricense* DSM-15987 and in (B) 0.1 M $NaClO_4$ with 0.02 g/L *Sporomusa* sp. MT-2.99.

The intensity of the hypersensitive $^5D_0 \rightarrow {}^7F_2$ transition at about 616 nm increases (with increasing pH/pC_{H+}), the symmetry-forbidden $^5D_0 \rightarrow {}^7F_0$ transition at around 579 nm appears, and the luminescence decay changes to bi-exponential with prolonged lifetimes (cf. Table 7). The luminescence spectrum of the Eu^{3+} aqua ion is characterized by emission bands at 585-600 nm (magnetic dipole transition $^5D_0 \rightarrow {}^7F_1$) and 610-625 nm (hypersensitive transition $^5D_0 \rightarrow {}^7F_2$). The intensity ratio according to Eq. (3.3) of 0.54 and the measured lifetime of 112 ± 5 µs corresponding to 9 water molecules in its first coordination sphere are in agreement with the literature (e.g., Horrocks and Sudnick, 1979; Kimura et al., 1994; Kim et al., 1994; Moulin et al., 1999; Plancque et al., 2003; Heller et al., 2012; Barkleit et al., 2013). Even when it is proposed that the $^7F_1$ peak should not be influenced by complexation, we observed in cell suspensions slight variations in intensity combined with a broadening of this transition. The interaction of Eu^{3+} with *Hbt. noricense* cells is primarily pronounced in the $^7F_2$ peak. Based on the TRLFS spectra depicted in Fig. 23 we can conclude more intensive interactions of Eu(III) with *Sporomusa* sp. cells compared to the *Hbt. noricense* system. The changes in the $^7F_2$ transition are more pronounced (cf. Fig. 23 B). One main difference is also that *Sporomusa* sp. cells interact strongly with Eu(III) already at the acidic pH of 2.2.

Table 7: Spectroscopic properties of the identified Eu(III) species.

	Eu^{3+} (aq)	*Hbt. noricense* species 1	*Hbt. noricense* species 2
Emission (nm)			
$^7F_0$	-	579.7 (1.75)	578.9 (2.49)
$^7F_1$	591.2 (5.56)[a]	591.5 (5.56)	592.0 (8.28)
$^7F_2$	616.2 (9.18)	616.0 (7.69)	612.7 (3.48) 617.2 (9.54)
$R_{E/M}$[b]	0.54	1.21	1.96
Lifetime (µs)	112 ± 5	190 ± 42 **430 ± 52**	**190 ± 42** 430 ± 52

[a] Values in parentheses are full width at half-maximum; [b] Intensity ratio of the $^7F_2$ (electric dipole transition) over the $^7F_1$ (magnetic dipole transition) luminescence band.

In the *Hbt. noricense* system at $pC_{H+} \leq 5.4$ there are only weak changes visible in the TRLFS spectra coming from interactions between Eu(III) and *Hbt. noricense* (cf. Fig. 23 A). This might indicate that *Sporomusa* sp. can better cope with lower pH values than *Hbt. noricense*. Ozaki et al. (2004) reported strong Eu(III) interactions with *Hbt. Salinarum* at pH 3 (corresponds to pC_{H+} 3.7). Hence, *Hbt. salinarum* behaves differently at lower pH/pC_{H+}. The pC_{H+}-dependent effects in the TRLFS spectra are in agreement with the lifetime measurements. In all cell suspensions a bi-exponential luminescence decay behavior was measured. Within pC_{H+} 3.9 and 6.4 the short lifetime of ca. 108 µs can be assigned with the Eu^{3+} ion. Whereas the long lifetime of 430 µs measured at all pH values indicates a Eu(III) species either complexed with cell exudates or directly on functional groups of the cell envelope. From pC_{H+} 6.7 to 8.1 the shorter lifetime increased to an average value of 190 µs. This indicates a second distinct chemical environment contributing to the speciation of Eu(III) in the cell suspensions. These lifetimes correspond to 2.0 and 5.0, respectively, remaining water molecules in the Eu(III) first coordination sphere. By comparing our lifetime and later discussed speciation results with literature data on bacterial Eu^{3+} interaction studies (cf. Moll et al., 2013; Moll et al., 2014 and references therein), the longer lifetime can be assigned to Eu^{3+}–*Hbt. noricense* species 1, whereas the shorter lifetime corresponds to Eu^{3+}–*Hbt. noricense* species 2. That cell exudates from the halophilic archaeon could have an affinity for Eu(III) was reported in (Ozaki et al., 2004). From the relatively low amount of bound Eu(III) (cf. Fig. 22) and the measured effects by TRLFS (cf. Fig. 23 A) it is likely that *Hbt. noricense* cells secreted exudates. Based on the experimental findings presented it is not possible to distinguish between cell bound and ligand bound Eu(III).

Fig. 24 shows the Coordination-Environment diagram (CE diagram) for Eu(III) in *Hbt. noricense* suspensions. The CE diagram was constructed as described by Ozaki et al. (2002). The interpretation on the basis of the CE diagram implies that Eu(III) interacts with the coordination site characterized by the long lifetime in an inner-spherical complex (to compare with: phosphoryl sites: Eu^{3+}–*Sporomusa* sp. species 1).

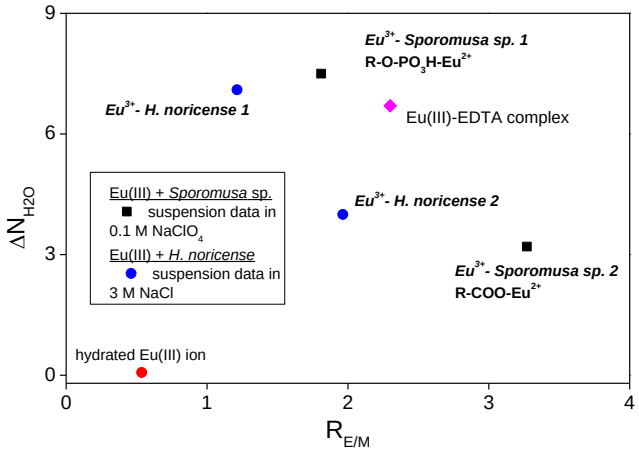

Fig. 24: CE diagram of Eu(III) in *Halobacterium noricense* DSM-15987 suspensions in comparison to the Eu(III)-*Sporomusa* sp. system (Moll et al., 2013; Moll et al., 2014).

The interaction with the coordination site characterized by the short lifetime combines both outer-spherical and inner-spherical properties (to compare with: carboxyl sites: Eu^{3+}–*Sporomusa* sp. species 2). Eu(III) associated on microbial phosphoryl sites are characterized by long luminescence lifetimes between 515 and 730 µs, whereas Eu(III) coordinated to carboxyl sites displayed luminescence lifetimes in the range of 98 to 255 µs (results summary in Moll et al., 2013 and 2014). The experimental results in comparison to the literature would suggest for Eu^{3+}–*Hbt. noricense* species 1 a coordination to phosphoryl sites and for Eu^{3+}–*Hbt. noricense* species 2 a coordination to carboxyl sites.

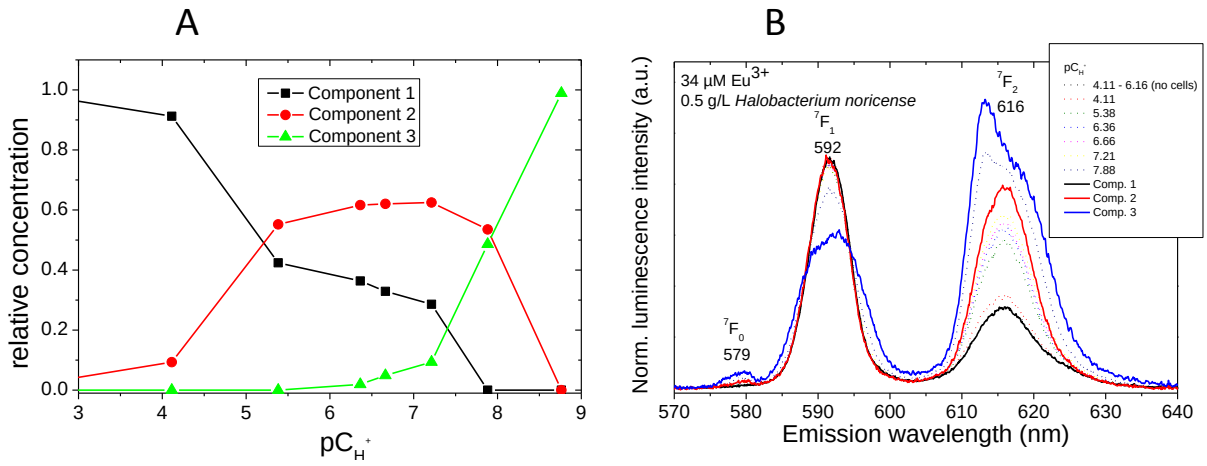

Fig. 25: ITFA results gained from the TRLFS spectra of the Eu(III)-*Hbt. noricense* system taken after 1 h of incubation time (Fig. 23 A). A: iterative target test (ITT) calculated species distribution of the components and B: ITFA extracted TRLFS component spectra (solid lines) and experimental data (dotted lines).

For a comprehensive evaluation of the spectral data set recorded throughout the whole pC_{H+} range, ITFA was applied to study the correlations between the observed changes in the luminescence spectra. As a first step, the principal component analysis (PCA) of the TRLFS spectra was performed. The eigenvalues which are a measure of the importance of a component rapidly drops down after the first 3 components. This inspection points out that the system contains three distinct components. As a second step, the VARIMAX rotation provided model-independent factor loadings which correlate with the assumption of three components and also with the later on calculated species distribution with ITT (cf. Fig. 25 A). For the ITT some relative concentrations or at least their minima and maxima in the spectral mixtures were used as constraints. The minima and maxima of the relative concentrations are supplied by the VARIMAX rotation. Component 1 can be assigned with the Eu^{3+} aquo ion. A significant influence of *Hbt. noricense* species on the Eu(III) speciation started at $pC_{H+} \geq 5.1$ and much later in pH units as observed in the Eu(III)-*Sporomusa* sp. system. Component 2 can be interpreted by interactions of Eu(III) with carboxyl groups, but phosphoryl groups may also participate. The influence of component 3 increased at $pC_{H+} \geq 7.1$. Component 3 could indicate interactions with a dissolved species what is in accordance with the percentage sorption data. A detailed characterization of aqueous Eu^{3+}–*Hbt. noricense* species based on the changes of the intrinsic luminescence of Eu^{3+} has not been reported before.

The *Hbt. noricense* Cm(III) system – TRLFS

The presented results allow a first insight in the pC_{H+}-dependent speciation of Cm(III) in cell suspensions of the halophilic archaeon *Hbt. noricense*.

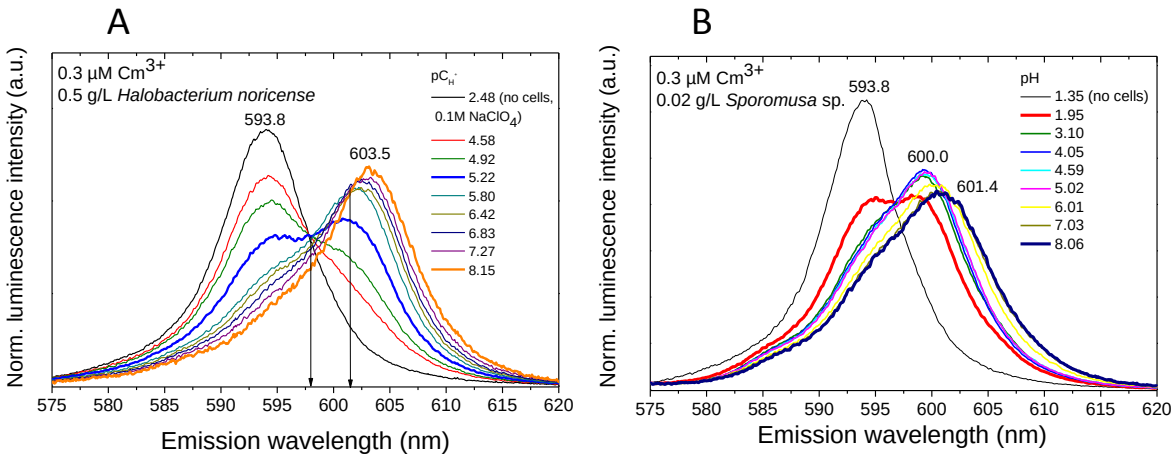

Fig. 26: Luminescence emission spectra of 0.3 µM Cm(III) as a function of pH/pC_{H+} taken after 1 h of incubation time in (A) 3 M NaCl with 0.5 g/L *Halobacterium noricense* DSM-15987 and in (B) 0.1 M $NaClO_4$ with 0.02 g/L *Sporomusa* sp. MT-2.99.

In agreement with our observations in the Eu(III)-*Hbt. noricense* system, a significant change in the luminescence spectra was first visible at $pC_{H+} \geq 5.1$ (cf. Fig. 26 A). *Sporomusa* sp. cells influenced strongly the luminescence spectra already at a low pH of 2 (Fig. 26 B). A stronger affinity of Cm(III) to the archaeon *Hbt. salinarum* was observed already at pC_{H+} 3.7 (Ozaki et al., 2004). This shows that both archaea behave different in the presence of Cm(III). For *Hbt. noricense* TRLFS investigations at pC_{H+} 3 are extremely difficult due to a fast agglomeration of cells. With increasing pH/pC_{H+} the intensity of the emission maximum at 593.8 nm (Cm^{3+}) decreases and simultaneously a second emission maximum increases at 602 nm (Cm(III)-*Hbt. noricense* 1). Within the investigated pC_{H+} range there is a continuous red shift of the emission maxima up to 603.5 nm indicating the occurrence of a second complex (Cm(III)-*Hbt. noricense* 2). There are two isosbestic points at 598 and 601.5 nm visible in Fig. 26 A underlining the assumption of two complex Cm(III) species besides the Cm^{3+} aquo ion in *Hbt. noricense* suspensions. The interaction of Cm(III) with *Hbt. noricense* cells and/or cell exudates resulted in more red shifted emission spectra compared to the *Sporomusa* sp. system (cf. Fig. 26).

In 3 M NaCl we observed with 70.3 µs a slightly longer lifetime for the Cm^{3+} aquo ion than 68 ± 4 µs reported in the literature for 0.1 M $NaClO_4$ systems (Edelstein et al., 2006). This could be explained by a reduced quenching caused by the O-H vibration due to the higher Cl^- concentration. Again in all cell suspensions a bi-exponential luminescence decay behavior was measured. The occurrence of two lifetimes suggests that two distinct chemical environments contribute to the total speciation of Cm(III) in the presence of the biomass. In the cell suspensions the short lifetime of 77 ± 6 µs shows the influence of the Cm^{3+} ion between pC_{H+} 4.1 and 5.1. However, the increase of 7 µs in comparison to the pure Cm^{3+} ion might

indicate the beginning influence of Cm(III)-*Hbt. noricense* species. The second longer lifetime of 328 ± 44 µs was measured over the whole pC_{H+} range and can be attributed to Cm(III)-*Hbt. noricense* 1. At pC_{H+} ≥ 5.1 the short lifetime increases to 129 ± 27 µs and can be assigned to Cm(III)-*Hbt. noricense* 2. These lifetimes correspond to 1.1 and 4.0, respectively, remaining water molecules in the Cm(III) first coordination sphere. By comparing our lifetime and later discussed speciation results with literature data on bacterial Cm^{3+} interaction studies (cf. Moll et al., 2013; Moll et al., 2014 and references therein), the longer lifetime can be assigned to Cm^{3+}–*Hbt. noricense* species 1, whereas the shorter lifetime corresponds to Cm^{3+}–*Hbt. noricense* species 2. Cm(III) associated on microbial phosphoryl sites are characterized by long luminescence lifetimes between 250 and 477 µs, whereas Cm(III) coordinated to carboxyl sites displayed shorter luminescence lifetimes in the range of 108 to 230 µs (results summary in Moll et al., 2013 and 2014). The experimental results in comparison to the literature would suggest for Cm^{3+}–*Hbt. noricense* species 1 a coordination to functional groups of the cell envelope (e.g. phosphoryl sites and carboxyl sites). Cm^{3+}–*Hbt. noricense* species 2 could be assigned to a solution species providing carboxyl sites (e.g. cell exudates). That cell exudates from halophilic archaea could have an affinity also for Cm(III) was reported in (Ozaki et al., 2004). Based on the experimental findings presented it is not possible to distinguish between cell bound and ligand bound Cm(III).

As described for the Eu(III) data, ITFA was applied to study the correlations between the observed changes in the luminescence spectra measured in the corresponding Cm(III) system. Again the PCA calculations of the TRLFS spectra pointed out that the system contains three distinct components. The VARIMAX rotation provided model-independent factor loadings which correlate with the assumption of three components and also with the later on calculated species distribution with ITT (cf. Fig. 27 A). For the ITT some relative concentrations or at least their minima and maxima in the spectral mixtures were used as constraints. The minima and maxima of the relative concentrations are supplied by the VARIMAX rotation.

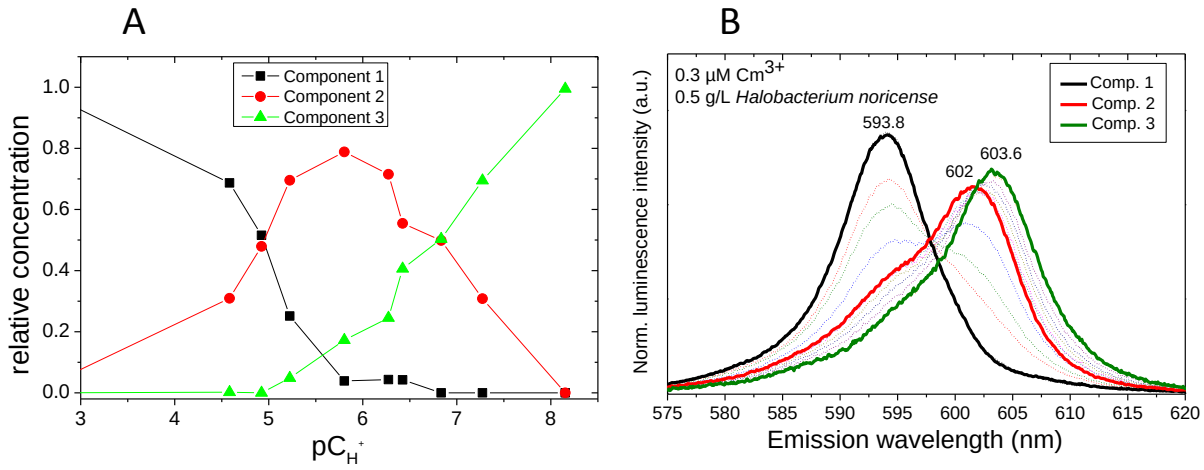

Fig. 27: ITFA results gained from the TRLFS spectra of the Cm(III)-*Hbt. noricense* DSM-15987 system (Fig. 26 A). A: iterative target test (ITT) calculated species distribution of the components and B: ITFA extracted TRLFS component spectra (solid lines) and experimental data (dotted lines).

Component 1 can be assigned with the Cm^{3+} aquo ion. A significant influence of *Hbt. noricense* species on the Cm speciation started at $pC_{H+} \geq 5.1$ and much later in pH units as observed in the Cm(III)-*Sporomusa* sp. system (cf. Fig. 26 B). Component 2 can be interpreted by interactions of Cm with functional groups of the cell envelope (Cm(III)-*Hbt. noricense* 1). The influence of component 3 increased at $pC_{H+} \geq 6.6$. Component 3 could indicate Cm(III) interactions with for instance carboxyl groups of released cell exudates (Cm(III)-*Hbt. noricense* 2). A detailed characterization of aqueous Cm^{3+}–*Hbt. noricense* species based on the changes of the intrinsic luminescence of Cm^{3+} has not been reported before.

The first TRLFS speciation analyses of Eu(III) and Cm(III) in *Hbt. noricense* suspensions revealed consistent results. Further investigations will focus on different aspects such as the kinetics, the analyses of supernatants and re-suspended cells in addition to the suspensions, and experiments as a function of biomass and Eu(III) concentration and will be performed by HZDR Young Investigator Group MicroSalt.

3.2.3 U(VI)

U(VI) biosorption by *Hbt*. *noricense* DSM-15987 was investigated in dependence on incubation time, initial U(VI) concentration and pC_{H+}. U(VI) sorption behavior over time was studied at 110 µM U(VI), pC_{H+} 6 over a time period of 0.5 up to 90 h. The U(VI) binding in dependence on initial U(VI) concentration (10-120 µM) was investigated at pC_{H+} 4 and 6. For all U(VI) experiments a stock solution of 80 mM in 0.1 M HCl was used. U(VI) accumulation experiments were carried out in 3 M NaCl (Carl Roth, Germany). The pC_{H+} adjustments were made with HCl or NaOH. The pC_{H+} was measured using an InLab Solids electrode (Mettler-Toledo, Giessen, Germany) calibrated with standard buffers and a pH meter (InoLab720, WTW, Weinheim, Germany). The pC_{H+} was adjusted with a precision of 0.05 units. For all these investigations the dry biomass was set to 0.5 $g_{dry\ weight}$/L. After contact of the cells with U(VI) for a certain time, the cells were separated by centrifugation 10000*g* for 10 min and Live/Dead staining was undertaken according to manufacturer's instructions (LIVE/DEAD® Bac Light™ Bacterial Viability Kit L7012, Molecular Probes). The supernatant was analyzed with Inductively Coupled Plasma Mass Spectrometry (ICP-MS) (Elan900, Perkin Elmer, Waltham, MA, USA) to determine how much uranium was bound to the cells. In selected samples the formed uranium-cell complexes were analyzed with time-resolved laser-induced fluorescence spectroscopy (TRLFS). For analysis a quadrupled (266 nm) Nd:YAG laser (Minilite, Continuum, San Jose, USA) with 0.3 mJ per 4 ns pulse were used and the slot was maximal opened (2238 mm). The measurements were performed at room temperature. Prior to the TRLFS measurement, the U(VI)-loaded cells were washed with 3 M NaCl at the appropriate pC_{H+} to remove loosely bound U(VI). In addition to the U(VI)-loaded cells also the corresponding supernatants were measured with TRLFS.

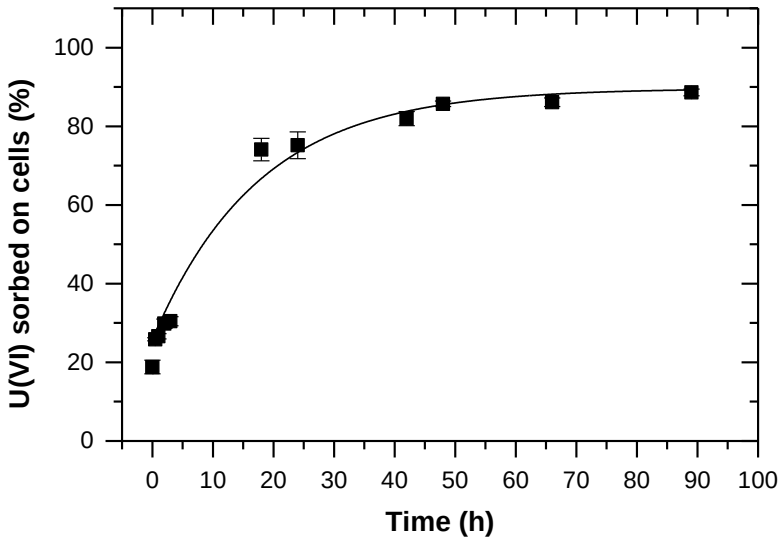

Fig. 28: Kinetic of U(VI) sorption on cells of *Hbt. noricense* (pC_{H+} 6, [U(VI)] = 110 µM, 0.5 $g_{dry\ weight}$/L, triplicate).

First insights into the interactions of *Hbt*. *noricense* with U(VI) can be gained by studying its time-dependent behavior. The sorption of U(VI) on *Hbt*. *noricense* cells during an incubation time of 0.5 up to 90 h is shown in Fig. 28 and can be described by a two-step process. At the beginning only a small part of the initial U(VI) (~35 %) is rapidly sorbed by the cells. The second slower step last up to 48 h, whereas finally 90 % of added uranium was bioassociated.

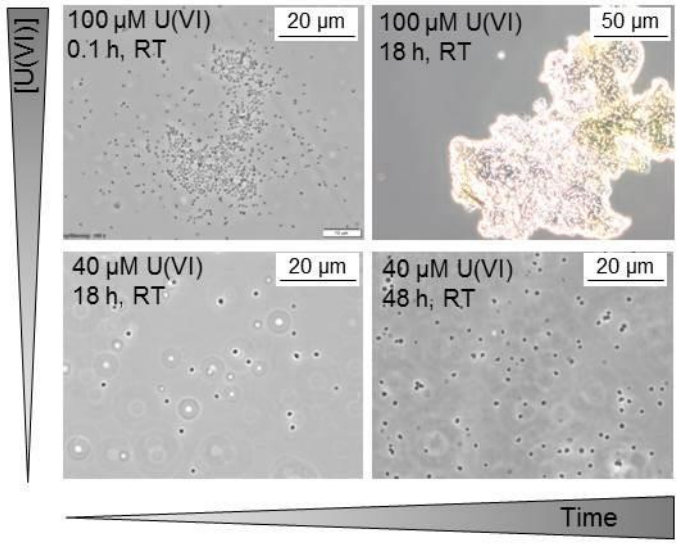

Fig. 29: Agglomeration of *Hbt. noricense* cells with increasing time and uranium concentration.

Another interesting observation is that with increasing incubation time as well as uranium concentration an agglomeration of the cells occurred (Fig. 29). A staining of cells with Bac Light™ Bacterial Viability Kit demonstrated that agglomerated cells were mostly alive whereas single cells were dead. A conclusion could be that this agglomeration process is a kind of

stress response to protect the cells themselves against environmental challenges. The formation of biofilms by other haloarchaea was just recently shown (Fröls et al., 2012).

The biosorption of U(VI) by *Hbt*. *noricense* cells depending on different initial U(VI) concentrations and two different pC_{H+} values (4 and 6) in 3 M NaCl after 48 h incubation time is shown in Fig. 30.

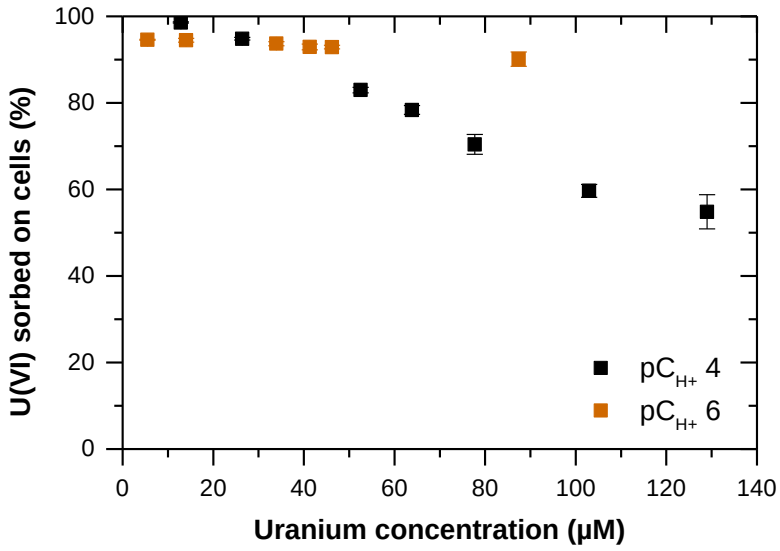

Fig. 30: Biosorption of uranium on cells of *Hbt. noricense* in dependence on pC_{H+} and U(VI) concentration (48 h incubation time, triplicate).

Hbt. noricense cells associate independent of the initial U(VI) concentration approximately 90 % of the added U(VI) at pC_{H+} 6, whereas the percentage sorption at pC_{H+} 4 decreases.

Furthermore, the supernatant and the washed cell suspension of selected samples were analyzed with TRLFS to characterize the binding of uranium to the cells. Despite the high quenching effect of chloride to uranium fluorescence a luminescence signal could be detected. One hypothesis of this phenomenon is the high quantum yield of some formed complexes. As shown in Fig. 31, uranium luminescence could be detected even at 3 M NaCl and binding kinetics could be documented over time. The further characterization of formed uranium-cell complexes will be performed by attenuated total reflection Fourier-transform infrared spectroscopy (ATR FT-IR) and also by microscopic investigations.

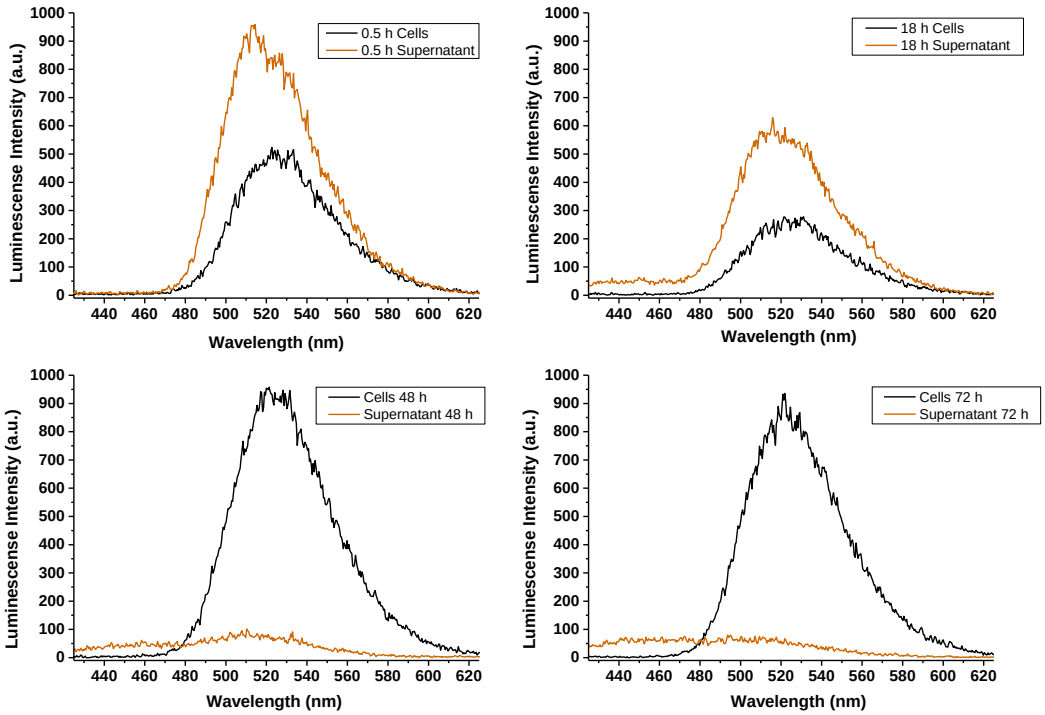

Fig. 31: By tracking the sorption process with TRLFS, increasing uranium intensity is detectable in the samples from the cell pellets (black), whereas the intensity decreases in the samples from the supernatant. After 48 h almost no uranium is detectable in the supernatant, everything is bioassociated.

The interactions of *Halobacterium noricense* DSM-15987 with uranium will be further investigated within the HZDR Young Investigator Group MicroSalt.

4 Dynamics of metal-humate complexation equilibria

4.1 Experimental

Materials. Non-radioactive chemicals and humic acid were purchased from Sigma-Aldrich (Germany). Another humic acid was isolated from surface water collected on the raised bog "Kleiner Kranichsee" (near Carlsfeld, Germany). Separation was carried out according to the recommendations of the International Humic Substances Society. Both humic materials were purified by repeated precipitation and redissolution with 0.1 M HCl and 0.1 M NaOH / 0.01 M NaF, respectively, followed by dialysis and lyophilization. [^{160}Tb]$TbCl_3$ (specific activity: ~ 1 GBq per mg Tb) was supplied by Radioisotope Centre Polatom (Poland).

Isotope exchange experiments. Stock solutions of 0.1 M $NaClO_4$ and of humic acid, $Tb(NO_3)_3$ as well as [^{160}Tb]$TbCl_3$ in 0.1 M $NaClO_4$, all adjusted to a pH of 4.0, were dispensed into 5 mL centrifuge tubes at variable amounts, giving a total volume of 4 mL. The component to be added finally after a pre-equilibration step was introduced in a small volume of 20 µL, keeping the concentrations of the other components virtually unchanged. Concentrations of humic acid and [^{160}Tb]Tb were fixed at 0.5 g L^{-1} and 1 nM, respectively. The solutions were rotated end-over-end during the equilibration steps. Wall adsorption was ascertained to be insignificant.

In a first series of experiments (illustrated in Fig. 32), humic acid was contacted with Tb (natural stable isotope ^{159}Tb) at a range of concentrations (0.3 mM - 2.4 mM), covering a binding isotherm up to the state of saturation. The systems were completed by adding a small amount of [^{160}Tb]Tb, either instantaneously or subsequently after different time periods of pre-equilibration.

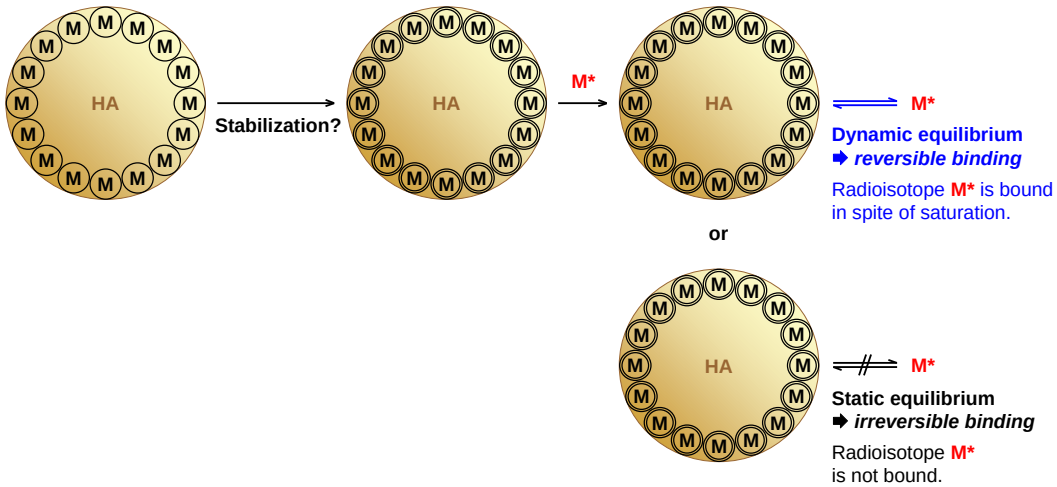

Fig. 32: Isotope exchange experiments for probing the equilibrium characteristics of metal-humate complexation (HA: humic acid, M: metal, M*: radioisotope), starting from the state of saturation.

Owing to the high metal loads, flocculation of humic colloids generates a solid-liquid system where adsorbed amounts of Tb can be determined by radiometric analysis of the supernatant

after centrifugation, presuming that ^{160}Tb represents total Tb. Flocculation was verified to be nearly complete by UV-vis spectrometry, using a Lambda 45 spectrophotometer (Perkin Elmer, USA). Concentrations of ^{160}Tb were determined by means of a gamma counter 1480 Wallac Wizard 3" (Perkin Elmer, USA).

In a modified procedure (Fig. 33), [^{160}Tb]Tb was introduced first, followed by saturation with non-radioactive ^{159}Tb after pre-equilibration for different periods of time. A fixed concentration within the plateau region of the binding isotherm (2 mM ^{159}Tb) was chosen in these experiments, and data were quantified referring to [^{160}Tb]Tb instead of total Tb. Humic-bound amounts of [^{160}Tb]Tb in the absence of ^{159}Tb were determined by ultrafiltration with Vivaspin 2 kDa centrifuge filters (Sartorius, Germany).

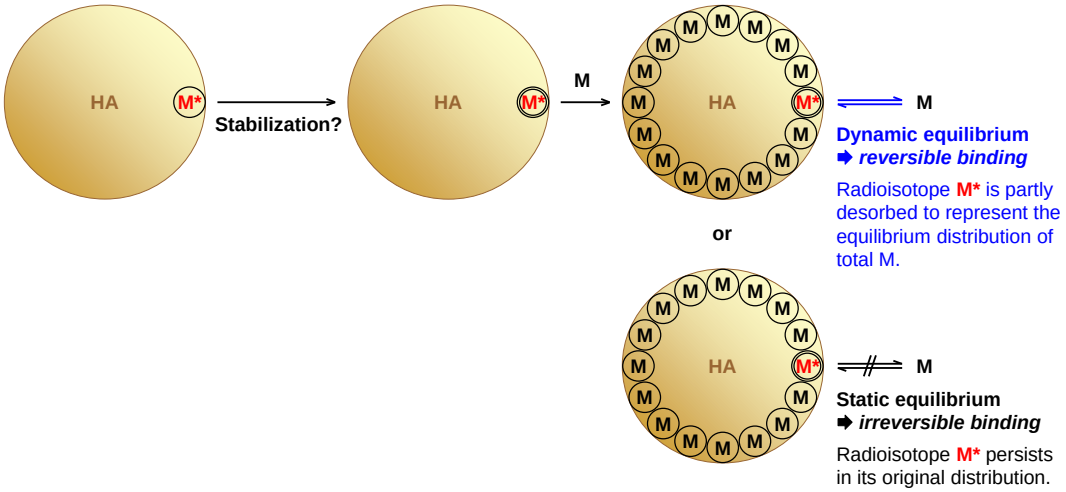

Fig. 33: Isotope exchange experiments in a reverse procedure, starting from a very low metal load with the radioisotope M*.

4.2 Results and discussion

Fig. 34 shows isotherms for binding of Tb to humic acid, obtained with ^{160}Tb as a radiotracer. The square symbols show the results of conventional experiments where the tracer was simultaneously added together with the bulk of non-radioactive Tb. At equilibrium concentrations higher than 1 mM, a plateau level is reached, indicating that more binding sites are not available under the given conditions. In a static equilibrium, where binding is simply "adhesion", all sites will be blocked in this state of saturation.

However, if the radiotracer is subsequently introduced after Tb and humic acid have already been pre-equilibrated (triangle symbols), coincident isotherms are obtained. The radioactive probe represents the solid-liquid distribution of total Tb, even though it encounters the state of maximum occupancy. It is thus evident that there is a permanent exchange between dissolved and humic-bound Tb; the tracer is involved a dynamic equilibrium. In additional tests, complete equilibration was also observed when reducing the time of contact with the radiotracer to 15 min instead of 1 day. This indication of a rapid isotope exchange is consistent with a spectroscopic study on Cm-humate complexation (Freyer et al., 2009).

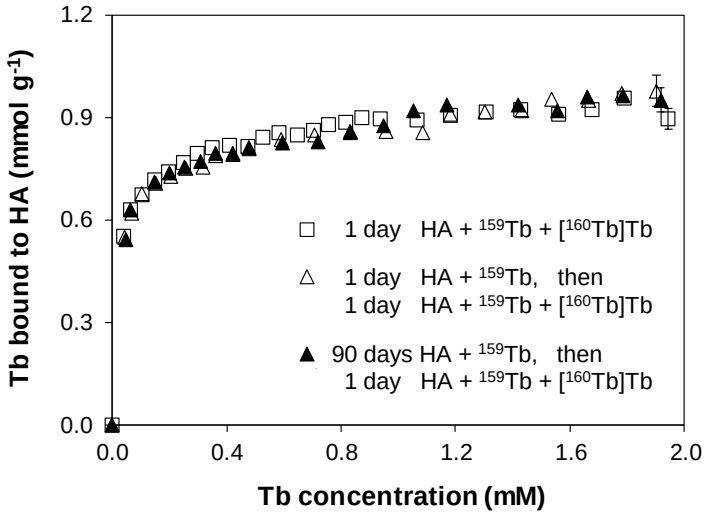

Fig. 34: Isotherms of adsorption of Tb(III) onto flocculated humic acid, obtained with ^{160}Tb(III) as a radiotracer, which was added simultaneously or subsequently after different times of pre-equilibration with non-radioactive ^{159}Tb(III) (1 nM [^{160}Tb]Tb, 0.5 g L^{-1} HA Aldrich, 0.1 M $NaClO_4$, pH 4.0).

Notably, there are no indications of stabilization processes, even after extended periods of pre-equilibration (90 days). Reported observations of increasing complex inertness refer to a similar or a shorter time frame. Metal loads were, however, far below saturation in these studies. An influence of concentration is conceivable since humic molecules comprise a multitude of binding sites with a broad affinity distribution (Tipping, 2002).

For this reason, the experimental approach was modified in that the sequence of introducing the isotopes was reversed: At first, humic acid was contacted with [^{160}Tb]Tb at a very low concentration. Subsequently, the large excess of ^{159}Tb was added at a concentration in the range of saturation. For representing the solid-liquid distribution of total Tb in a dynamic equilibrium, the radioisotope was expected to be partly desorbed since the bound fraction of total Tb is lower in the plateau region of the binding isotherm.

Fig. 35 shows the results of these experiments, conducted with two different humic materials. The upper equilibrium lines show their initial loads with [^{160}Tb]Tb prior to adding ^{159}Tb. The lower equilibrium lines show the amounts of bound [^{160}Tb]Tb representing the bound fraction of total Tb (virtually, ^{159}Tb) in the case of simultaneous addition. If the non-radioactive isotope is introduced later, desorption of the radiotracer is in fact initiated, striving towards the equilibrium state – however, at much lower rates compared to the equilibration process in the reverse procedure. Moreover, the rates proved to be dependent on the time of pre-equilibration with [^{160}Tb]Tb. Equilibrium is closely approached after 1 month of exchange for the shortest pre-equilibration times, whereas bound amounts are still far away from equilibrium after 3 months if more time is admitted for pre-equilibration. Evidently, desorption of the radiotracer is increasingly hindered. The existence of kinetic stabilization phenomena was thus substantiated. However, it appears that they are confined to the most reactive sites, occupied by the radiotracer.

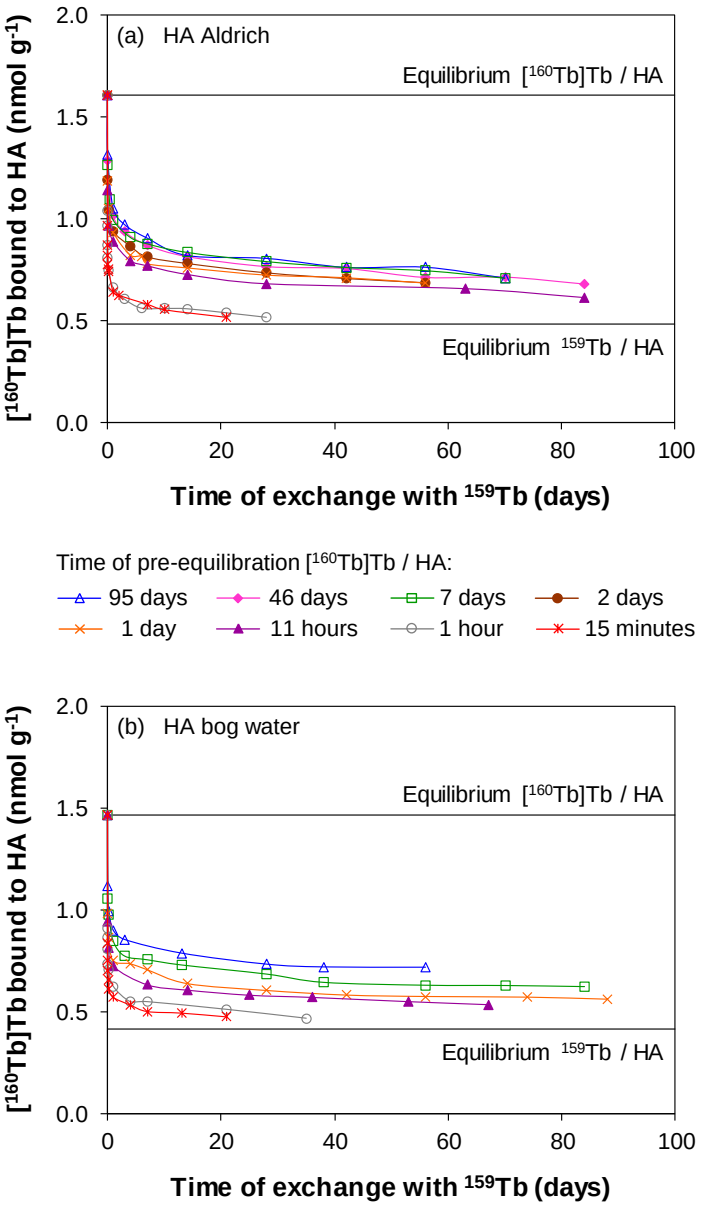

Fig. 35: Amount of [^{160}Tb]Tb(III) bound to humic acids after saturating with non-radioactive ^{159}Tb(III), shown as a function of exchange time for different times of pre-equilibration (1 nM [^{160}Tb]Tb, 2 mM ^{159}Tb, 0.5 g L^{-1} HA, 0.1 M $NaClO_4$, pH 4.0).

The time-dependent progress of this stabilization is shown in Fig. 36, where adsorbed amounts after a fixed time of exchange (1 h) are plotted as a function of pre-equilibration time. Changes are most pronounced in the first days, followed by a very minor trend over an extended time period. A similar time dependence was also reported for inertization effects in respect of complex dissociation (Cacheris and Choppin, 1987; Choppin and Clark, 1991; Rao et al., 1994; Lippold et al., 2012).

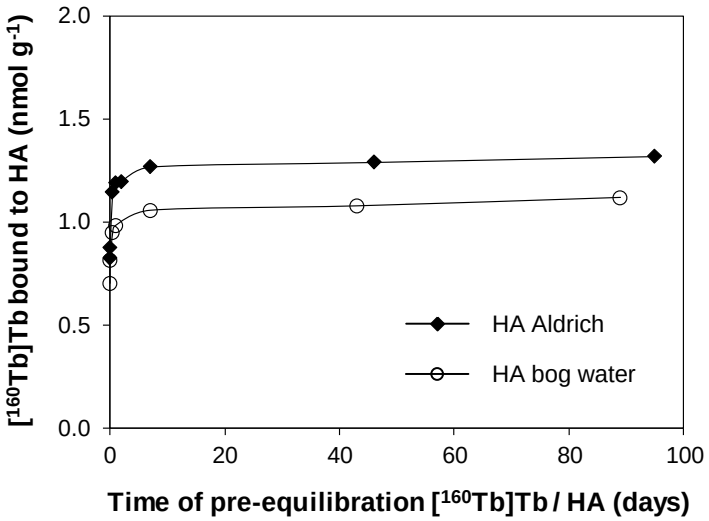

Fig. 36: Amount of [^{160}Tb]Tb(III) bound to humic acids after 1 h of exchange with ^{159}Tb(III), shown as a function of pre-equilibration time (conditions as in Fig. 35).

Aiming at an elucidation of the chemical background of this stabilization process, an attempt was made to detect structural changes in the microenvironment of the metal by means of time-resolved laser fluorescence spectroscopy, using Eu(III) as a (more sensitive) probe. However, significant time-dependent spectral changes could not be detected, probably because higher metal concentrations had to be applied to obtain sufficient fluorescence intensity.

For short pre-equilibration times, the kinetics of exchange (Fig. 35) is superimposed by the kinetics of stabilization (Fig. 36), resulting in a prolongation of the process. This interference can be neglected for longer times of pre-equilibration, and a kinetic analysis of the exchange process itself is possible. It can be shown that isotope exchange always follows first-order kinetics, regardless of the mechanism of the exchange reaction (Duffield and Calvin, 1946). For the system under study, the rate of approach to equilibrium is given by Eq. (4.1)

$$-\frac{\mathrm{d}c_{\mathrm{ads}}}{\mathrm{d}t} = k\left(c_{\mathrm{ads}} - c_{\mathrm{ads}}^{\mathrm{eq}}\right), \qquad (4.1)$$

where k is the rate constant, c_{ads} is the concentration of humic-bound [^{160}Tb]Tb at time t after saturation, and $c_{\mathrm{ads}}^{\mathrm{eq}}$ is its concentration at equilibrium. Integration yields Eq. (4.2) for the time course of isotope exchange

$$c_{\mathrm{ads}} = \left(c_{\mathrm{ads}}^{0} - c_{\mathrm{ads}}^{\mathrm{eq}}\right) e^{-kt} + c_{\mathrm{ads}}^{\mathrm{eq}}, \qquad (4.2)$$

where c_{ads}^{0} is the initial concentration of humic-bound [^{160}Tb]Tb. Fitting this monoexponential equation to the data was not successful, due to the very steep decrease for short times of exchange. In Eq. (4.3), the total amount of [^{160}Tb]Tb is split into a fast exchanging and a slowly exchanging component, characterized by the rate constants k_1 and k_2, respectively, with x denoting the fraction of the fast exchanging component.

$$c_{ads} = x \left(c_{ads}^{0} - c_{ads}^{eq}\right) e^{-k_1 t} + \left(1-x\right) \left(c_{ads}^{0} - c_{ads}^{eq}\right) e^{-k_2 t} + c_{ads}^{eq} \qquad (4.3)$$

Using this equation, the progress of exchange can be well described, as shown for an exemplary dataset in Fig. 37. Obviously, the very small fraction of sites occupied by [^{160}Tb]Tb (~ 1/10^{6}) is still heterogeneous with respect to exchange kinetics. Extrapolating the fit indicates that it takes about 2 years for a stabilized complex to arrive at equilibrium.

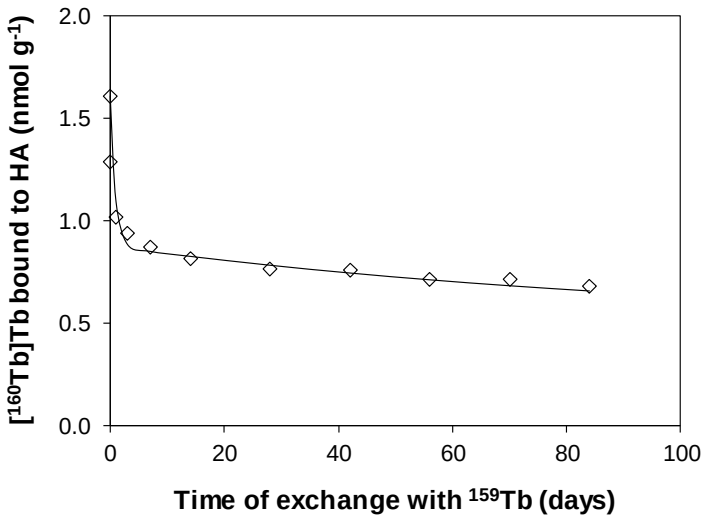

Fig. 37: Kinetic analysis of isotope exchange by fitting Eq. (4.3) (symbols: data set for HA Aldrich after 46 days of pre-equilibration, solid line: fitted curve calculated with the parameters k_1 = 1.20 d^{-1}, k_2 = 0.01 d^{-1}, x = 0.65).

Stabilization and slow kinetics as observed for the radiotracer will certainly affect humic-bound contaminant metals in geochemical systems since their concentrations are similarly low. A humic complex, loaded with trace amounts of metals and "aged" for some time, will not be in equilibrium with its aqueous surroundings if conditions change relatively fast, e.g., in case of rapid movement. To decide how to treat humic-bound metals in speciation and transport modeling, two aspects of the present findings are important: (I) The stabilization process does not continue endlessly but is virtually completed after a fairly short time period (Fig. 36). (II) Reversibility is not affected (Fig. 35). Whether humic-bound metals take part in interaction processes is a question of the time frame under consideration. Equilibration times of several years are still very short compared to the time scale to be covered in safety assessments for nuclear waste repositories. Nearly stagnant systems are to be considered, where steady equilibria may be assumed in spite of very slow kinetics. Under these conditions, metal exchange between humic carriers and mineral surfaces cannot be neglected in predictive transport calculations, and equilibrium constants are fully applicable.

5 Influence of higher salinities on the mobilization potential of high-molecular-weight organics towards Tb(III) and Eu(III)

5.1 Dispersion stability of fulvic acid in highly saline solutions (Na^+, Mg^{2+}, Ca^{2+})

Dissolved humic substances are dispersions of colloidal particles that are stabilized towards precipitation (flocculation) due to their negative surface charge. This stabilization is counteracted by cationic solutes. On the one hand, the dielectric properties of the aqueous medium are altered. On the other hand, the surface charge can be compensated by cation binding to acidic groups. The latter kind of destabilization applies to multivalent metal ions as well as protons. In contrast, monovalent metal ions are not directly bound to humic ligands. High-molecular-weight clay organics are, in some respect, comparable to fulvic acids. Different from humic acids, fulvic acids do not flocculate on protonation owing to their higher charge density. Ionic strengths of highly saline solutions, however, exceed the proton concentration even of concentrated acids. So far, nothing was known on colloidal stability of fulvic acids at salt concentrations close to saturation, as encountered in pore waters of Lower Cretaceous clay in Northern Germany. If flocculation occurs, humic-bound migration of radionuclides can be excluded. Specifying the conditions of such immobilization was the objective of this work package.

Two organic materials were chosen for these investigations: Suwannee River fulvic acid St. II standard material (International Humic Substances Society) and a fulvic acid isolated from surface water collected on the raised bog “Kleiner Kranichsee” (near Carlsfeld, Germany). Dispersion stability was examined on addition of NaCl, $MgCl_2$ and $CaCl_2$ as main electrolyte constituents of clay pore waters. Since co-operative effects by protonation are to be taken into account, investigations were performed at two different pH values; pH 5 and pH 7. The pH adjustment for stock solutions of the salts was carried out at a low salt concentration before the bulk amount was added to give the final concentration. Systems of 40 mg L^{-1} fulvic acid and variable amounts of NaCl, $MgCl_2$ and $CaCl_2$ (up to 4.9 M) were prepared in clear glass vials and were left to stand in the dark for 3 months. Flocculation was then evaluated by visual inspection.

No precipitation of fulvic acid was observed in any of these systems. It may be concluded that fulvic acid-like clay organics are not prone to flocculation even at very high salinities. Thus, the possibility of a mobilization of radionuclides by complexation with such material cannot be excluded and needs to be investigated for the special conditions of high electrolyte contents.

5.2 Effects of ionic strength and presence of fulvic acid on the adsorption of Tb^{3+} and Eu^{3+} onto Opalinus Clay

5.2.1 Experimental

5.2.1.1 Materials

^{160}Tb (half-life 72.3 d) was produced at the TRIGA Mark II reactor at the University of Mainz (Germany) and was used in the form of a stock solution of 10^{-4} M [^{160}Tb]terbium in 0.1 M $NaClO_4$. ^{152}Eu was purchased as a [^{152}Eu]$EuCl_3$ stock solution in 0.1 M HCl from Radioisotope Centre Polatom (Poland).

An Opalinus Clay sample (BHE-241) from the Mont Terri rock laboratory (Switzerland) was used as a 4.8 $g \cdot L^{-1}$ suspension. Characteristics of this material are given in Marquardt (2011) and Nagra (2002).

The fulvic acid was isolated from surface water collected on the moor *Kleiner Kranichsee* (near Carlsfeld, Germany). Purification was carried out according to the recommendations of the International Humic Substances Society (Aiken, 1985). The average molecular weight was determined to be 38 kDa by size exclusion chromatography, the total acidity was found to be 8.46 $meq \cdot g^{-1}$ by potentiometric titration.

All other chemicals were of analytical grade and used without further pretreatment. Solutions were prepared using ultrapure Milli-Q water. All experiments were carried out at ambient conditions.

5.2.1.2 Adsorption experiments

Variable amounts of NaCl, $CaCl_2$ or $MgCl_2$ in the range of 0 - 4 $mol \cdot L^{-1}$ were added to the clay suspension. The pH was adjusted to 5 or 7 by using HCl. Stock solutions of [^{160}Tb]terbium (for pH 5) or [^{152}Eu]europium (for pH 7) were added to yield a concentration of 10^{-6} M (42 $Bq \cdot mL^{-1}$ ^{160}Tb, 930 $Bq \cdot mL^{-1}$ ^{152}Eu). Fulvic acid solutions, adjusted to pH 5 or 7, were added to the clay suspension resulting in a concentration of 40 $mg \cdot L^{-1}$. After reaching equilibrium (24 h), the remaining [^{160}Tb]terbium or [^{152}Eu]europium concentration in the supernatant was determined after centrifugation (45 min at 7000 rpm), using a gamma counter WIZARD 3" (Perkin-Elmer, USA).

For measuring the adsorption of fulvic acid onto clay, ^{14}C-radiolabeled fulvic acid was prepared by azo-coupling with [^{14}C]aniline (Mansel and Kupsch, 2007). A detailed description of the procedure is given elsewhere (Lippold and Lippmann-Pipke, 2014). The [^{14}C]fulvic acid (40 $mg \cdot L^{-1}$; 150 $Bq \cdot mL^{-1}$) was added to the 4.8 $g \cdot L^{-1}$ clay suspension with variable amounts of NaCl, $CaCl_2$ or $MgCl_2$ (0 - 4 $mol \cdot L^{-1}$) at pH 5 and pH 7. After equilibration for 24 h and centrifugation, the remaining concentration of [^{14}C]fulvic acid was determined by liquid scintilla-

tion counting on a Tri-Carb 3110TR (Perkin-Elmer, USA), using Ultima Gold scintillation cocktail (Perkin-Elmer, USA).

5.2.1.3 Complexation experiments

Solutions of 40 mg·L^{-1} fulvic acid, 10^{-6} M [^{160}Tb]terbium (pH 5) or [^{152}Eu]europium (pH 7) and variable amounts of NaCl, $CaCl_2$ or $MgCl_2$ in a range of 0 - 4 mol·L^{-1} were shaken for an hour and then centrifuged (7000 rpm) with "Vivaspin 2" 2 kDa ultrafilters (Sartorius, Germany). The remaining [^{160}Tb]terbium or [^{152}Eu]europium concentration in the filtrate (non-complexed fraction) was determined with a gamma counter WIZARD 3" (Perkin-Elmer, USA).

5.2.2 Modeling adsorption in ternary systems

In order to predict the effect of ionic strength on the interactions in the ternary system of clay / metal / fulvic acid on the basis of the adsorption and complexation data in the constituent binary systems, a combined K_d approach was applied.

The solid-liquid distribution coefficient for metal adsorption $K_d^{M/S}$ (L·g^{-1}) is given by Eq. (5.1)

$$K_d^{M/S} = \frac{\Gamma_M}{c_M} \tag{5.1}$$

with Γ (mol·g^{-1}) denoting the amount of adsorbed metal M and c (mol·L^{-1}) denoting the concentration of free metal in solution.

Accordingly, the distribution coefficient for adsorption of fulvic acid $K_d^{FA/S}$ (L·g^{-1}) is equal to

$$K_d^{FA/S} = \frac{\Gamma_{FA}}{c_{FA}} \tag{5.2}$$

For simplicity, metal-fulvate complexation is likewise given as a distribution coefficient $K_d^{M/FA}$ (L·g^{-1}), calculated according to Eq. (5.3)

$$K_d^{M/FA} = \frac{c_{M-FA}}{c_M \, c_{FA}} \tag{5.3}$$

where $c_{M\text{-}FA}$ is the concentration of metal bound to fulvic acid.

According to the linear additive model, these distribution coefficients are independent of each other, and Eqs. (5.1) - (5.3) can be combined to Eq. (5.4) where K_d^{LAM} (L·g^{-1}) is the solid-liquid distribution coefficient of the metal (free and as fulvate complex) in the ternary system:

$$K_d^{LAM} = \frac{K_d^{M/S} + K_d^{FA/S} \, K_d^{M/FA}}{1 + K_d^{M/FA}} \tag{5.4}$$

5.2.3 Results

Fig. 38 shows the adsorption of Tb(III) (pH 5) and Eu(III) (pH 7) onto Opalinus Clay, represented as logarithmical solid-liquid distribution coefficient $K_d^{M/S}$ as a function of ionic strength. With increasing ionic strength *I* (up to almost saturated solutions, *I* = 4 M for NaCl, *I* = 12 M for $CaCl_2$ and $MgCl_2$), K_d values strongly decrease, most pronounced for the bivalent cations. At a pH of 5, metal adsorption is stronger suppressed than at pH 7, which is explained by the lower adsorption capacity of clay resulting from protonation.

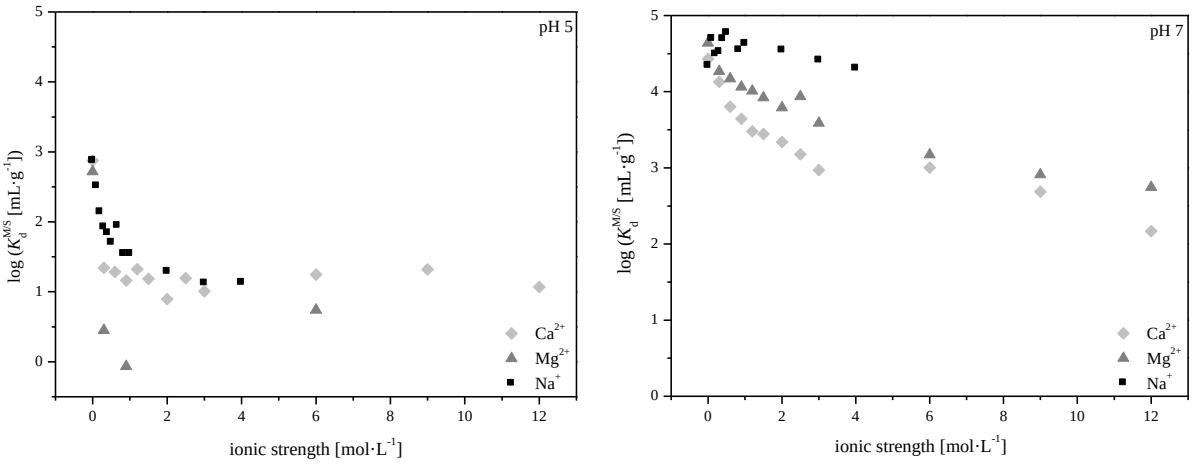

Fig. 38: Adsorption of Tb(III) (pH 5) and Eu(III) (pH 7) onto Opalinus Clay in the presence of NaCl, $CaCl_2$ and $MgCl_2$.

In Fig. 39, adsorption of fulvic acid at pH 5 and 7 in the presence of NaCl, $CaCl_2$ and $MgCl_2$ is shown as a function of ionic strength. Adsorbed amounts are relatively insensitive to increasing ionic strength. Adsorption of fulvic acid is slightly higher at pH 5 since repulsion by negative charge on fulvic acid and clay surface is reduced by protonation (Lippold and Lippmann-Pipke, 2009).

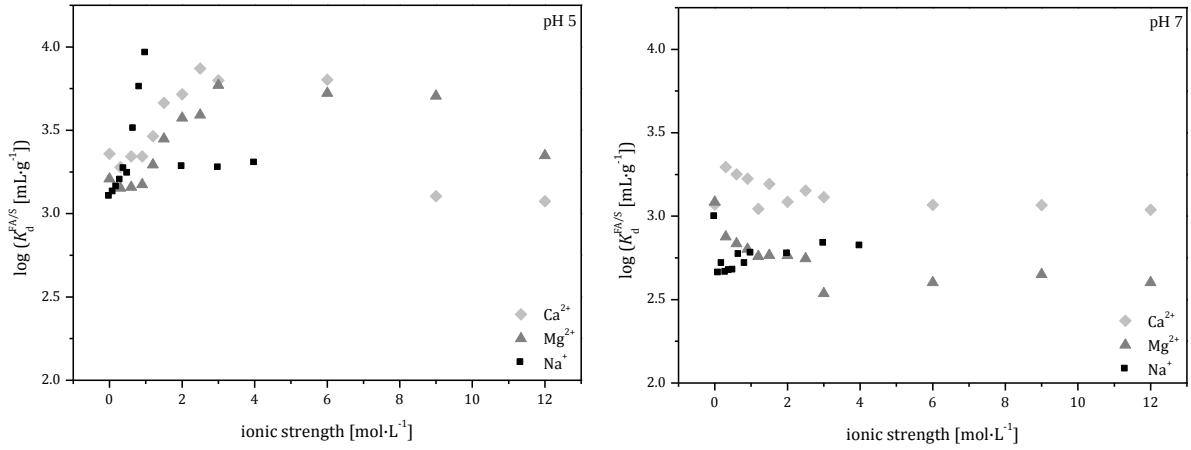

Fig. 39: Adsorption of fulvic acid onto Opalinus Clay at pH 5 and 7 in the presence of NaCl, $CaCl_2$ and $MgCl_2$.

The dependence of Tb(III)- or Eu(III)-fulvate complexation on ionic strength is shown in Fig. 40. For better comparison, these data are likewise given as distribution coefficients $K_{\mathrm{d}}^{\mathrm{M/FA}}$, considering the fulvic acid colloids as a pseudo solid phase. Complexation of Tb(III) and Eu(III) is strongly suppressed with increasing ionic strength and is significantly lower at pH 5 than at pH 7. The pH dependence is caused by the protonation of fulvic acid which leads to blocking of ligands (Lippold et al., 2005).

Again, the influence of ionic strength is higher for the bivalent cations Ca^{2+} and Mg^{2+}. Both show strong interference on complexation, which is explained by competition or shielding effects. More detailed investigations by mechanistic modeling to differentiate between these two influences are described in chapter 5.4.

To verify the accuracy of the separation of free and fulvic-bound metal via ultrafiltration, possible sources of experimental errors were taken into consideration. (I) The membrane of the ultrafilters may be transmissible for small fulvic acid molecules, pretending lower complexed fractions. (II) Tb or Eu may be adsorbed at the membrane, pretending higher complexed fractions. (III) A possible perturbation of the complexation equilibrium due to the up-concentration of fulvic acid during the filtration process may lead to changes in the results. Issues (I) and (II) proved to be insignificant in preliminary tests. Complexation was also investigated by time-resolved laser fluorescence spectroscopy (TRLFS) as an alternative method (cf. chapter 5.3.). Very similar results were obtained, showing that issue (III) is not important as well. The TRLFS studies have also shown that formation of chloro complexes for Tb(III) and Eu(III) at high ionic strength is negligible.

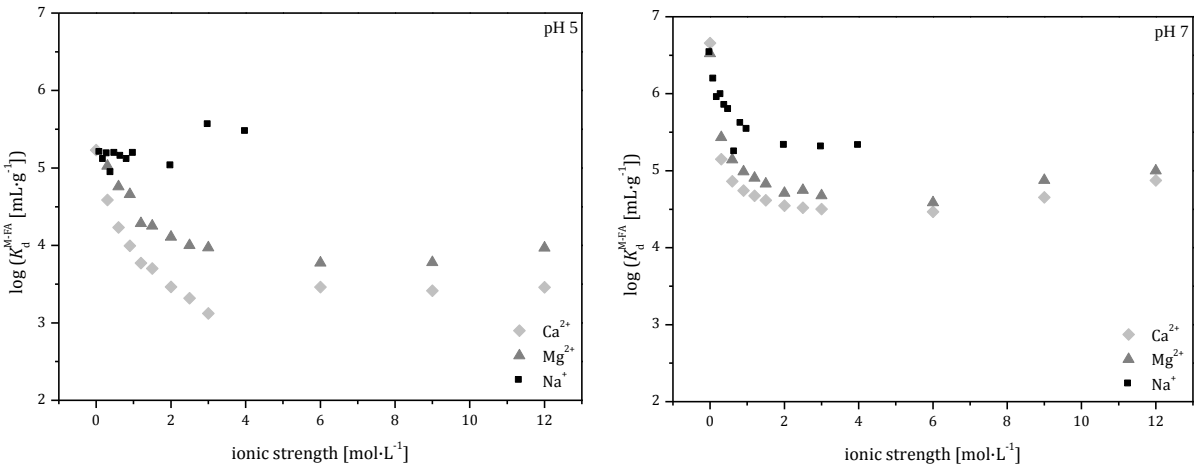

Fig. 40: Complexation of Tb(III) or Eu(III) with fulvic acid as a function of ionic strength at pH 5 and 7 in the presence of NaCl, $CaCl_2$ and $MgCl_2$.

Fig. 41 shows the adsorption of Tb(III) and Eu(III) on Opalinus Clay in the presence and absence of fulvic acid as a function of ionic strength for NaCl, $CaCl_2$ and $MgCl_2$. At pH 5, the presence of fulvic acid leads to increased adsorption of Tb(III) in general. In the case of $MgCl_2$, high ionic strength suppresses adsorption of Tb(III) on clay almost completely, whereas the ternary system with fulvic acid shows significant adsorption. Mineral-bound fulvic acid increases adsorption of metal ions at acidic conditions. With increasing ionic

strength, complexation is suppressed and leads to lower adsorbed amounts. At pH 7, the effect of fulvic acid is reversed: Metal adsorption is decreased compared to the system without fulvic acid. Obviously, this changeover is a consequence of the pH-dependent adsorption behavior of the organic carrier (cf. Fig. 39).

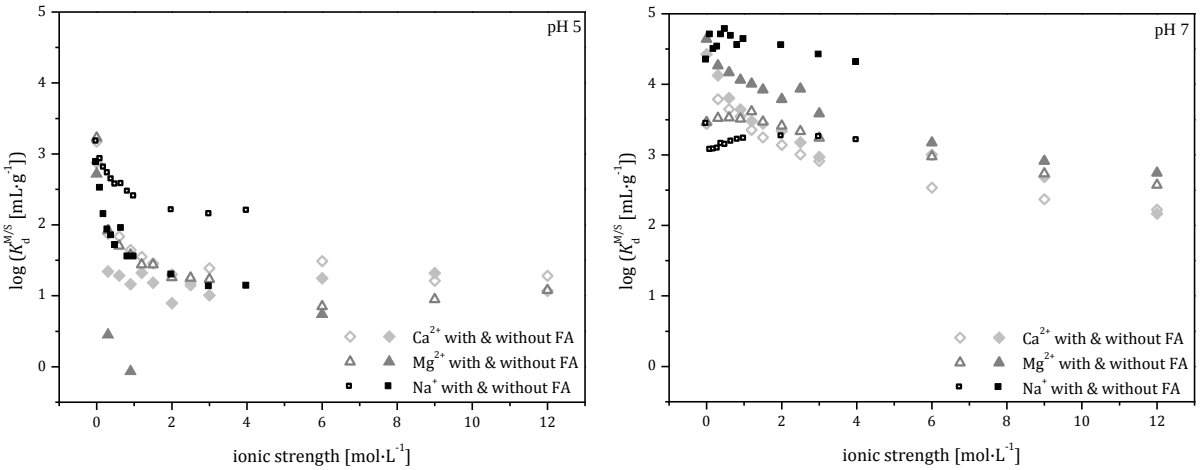

Fig. 41: Adsorption of Tb(III) (pH 5) and Eu(III) (pH 7) on Opalinus Clay in the presence (empty symbols) and absence (full symbols) of fulvic acid as a function of ionic strength for NaCl, $CaCl_2$ and $MgCl_2$ as electrolytes.

Fig. 42 shows the measured distribution coefficients for the co-adsorption of metal and metal-fulvate complex together with the corresponding K_d^{LAM} values calculated according to Eq. (5.4).

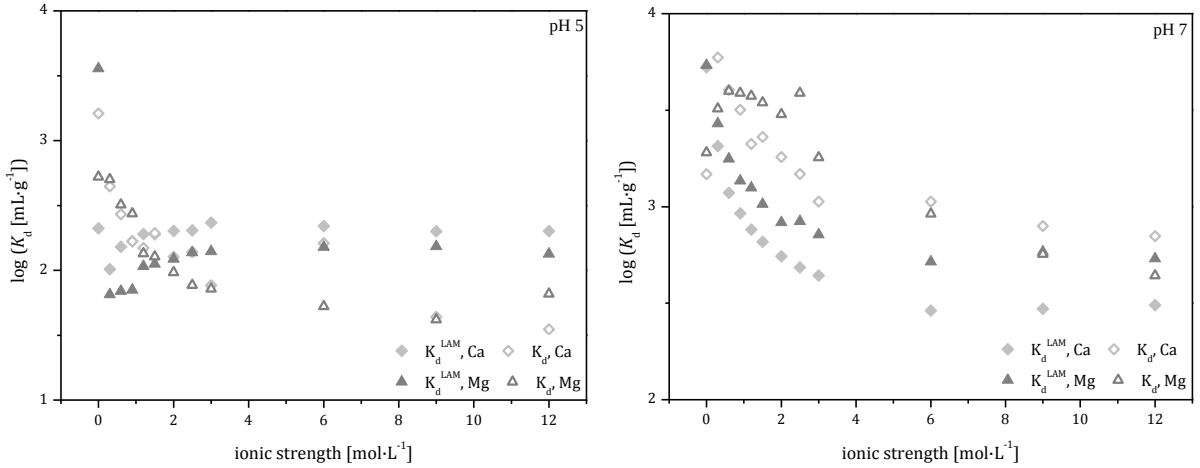

Fig. 42: Adsorption of Tb(III) (pH 5) and Eu(III) (pH 7) on Opalinus Clay in the presence of fulvic acid as a function of ionic strength for $CaCl_2$ and $MgCl_2$ as electrolytes. The full symbols show the calculated values according to the linear additive model (Eq. (5.4)).

The model reproduces the measured data for the bivalent cations quite well, especially for pH 7. Nonetheless, the prediction by the linear additive model leads to slightly lower (in case of pH 5) or higher (for pH 7) K_d values for the solid-liquid distribution ratio in the ternary system. Nonetheless, the predicted (i.e., not fitted!) modeled data show a similar trend as the

measured values. Overall, the additivity concept proved to be suitable for estimations on the effect of humic material on metal adsorption at variable solution conditions.

In summary, this study has shown that a mobilization of metals caused by humic matter is not enhanced by high ionic strength. On the contrary, a mitigating effect was evidenced, based on the fact that complexation is suppressed while adsorption of humic matter is hardly influenced. At low pH, adsorption of metals on a clay surface is increased by fulvic acid due to the formation of surface complexes of the type S-FA-M. Their presence has been proven by the applicability of the linear additive model. This approach is a simple method to reconstruct adsorption data, proving or disproving the additivity of the binary equilibria in the ternary system. It was found to be suitable for predicting trends in the co-adsorption of metals and fulvic acid in dependence on ionic strength, in part nearly quantitatively.

A main reason of deviations is that selectivities in complexation and adsorption within the polydisperse system of fulvic acid molecules are not taken into account. For instance, preferred adsorption of molecules with high metal loads would entail an underestimation by the model, since it operates with an averaged metal load, determined for the humic substance as a whole. Furthermore, a certain amount of ternary surface complexes of the kind S-M-FA may be present, which is not considered in this approach.

5.3 TRLFS studies of Eu-fulvate complexes at high ionic strength

5.3.1 Experimental

Multiple series of experiments were made to investigate the influence of high ionic strength on the complexation of fulvic acid with Eu^{3+} in detail. Variable amounts of NaCl, $CaCl_2$, $MgCl_2$, $AlCl_3$ or $GdCl_3$ (0 - 2 $mol \cdot L^{-1}$) were added to solutions of 40 $mg \cdot L^{-1}$ fulvic acid and 10^{-5} M Eu. The pH of the solutions was adjusted to 5. Time-resolved luminescence spectra were recorded using a pulsed flash lamp pumped Nd:YAG-OPO laser system (Powerlite Precision II 9020 laser equipped with a green PANTHER EX OPO from Continuum, Santa Clara, USA). The laser pulse energy, which was between 1.2 and 1.9 mJ, was monitored using a photodiode. Luminescence spectra were detected using an optical multi-channel analyzer-system, consisting of an Oriel MS 257 monochromator and spectrograph with a 300 or 1200 $lines \cdot mm^{-1}$ grating and an Andor iStar ICCD camera (Lot-Oriel Group, Darmstadt, Germany) (cf. Moll et al., 2014). The Eu(III) single luminescence emission spectra were recorded in a range of 570 - 640 nm (1200 $lines \cdot mm^{-1}$ grating) at an excitation wavelength of 394 nm. The time-dependent luminescence spectra were detected in the same range of wavelengths with a 300 $lines \cdot mm^{-1}$ grating. The spectra were base-line corrected, energy corrected and normalized using MATLAB R2015a (MathWorks GmbH, USA) and Origin 8.5 (OriginLab Corporation, USA).

The F1 and F2 bands were observed because these transitions are influenced by the chemical environment of the metal ion. The relative peak intensity ratios (F1:F2) were calculated

from the peak areas. The number of coordinated water molecules *n* was calculated using an empirical equation proposed by Kimura et al. (1996)

$$n(H_2O) = \frac{1.07}{\tau(Eu)} - 0.62 \qquad (5.5)$$

where τ is the measured luminescence lifetime (ms).

5.3.2 Results

As the emission spectra in Fig. 43 show, complexation of Eu with fulvic acid is highly suppressed at higher ionic strength. With increasing Ca^{2+} concentration, the F1 and F2 bands progressively converge to the spectrum of the Eu^{3+} aquo ion (black in Fig. 43).

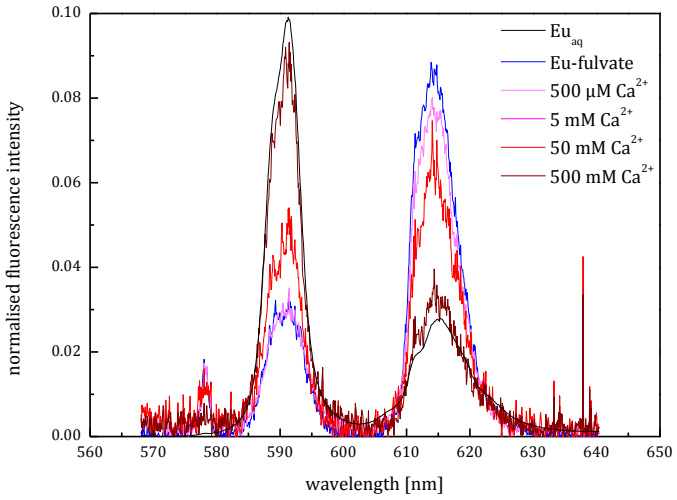

Fig. 43: Emission spectra of Eu-fulvate with different concentrations of $CaCl_2$. The spectrum in black represents the Eu^{3+} aquo ion, the spectrum in blue represents the Eu-fulvate complex without a background electrolyte.

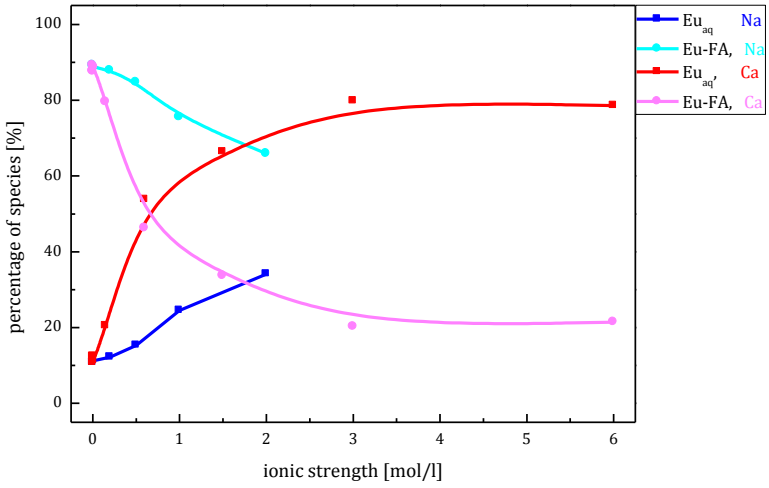

Fig. 44: Percentage of Eu species in solution as a function of ionic strength for Na^+ and Ca^{2+}. Light colors: fulvate species, dark colors: aquo species.

On the basis of this dependence, the species distribution of Eu can be calculated. Fig. 44 shows the percentages of Eu aquo and Eu-fulvate species depending on ionic strength.

As batch studies have shown before (Fig. 40), the percentage of Eu-fulvate decreases with increasing ionic strength. The TRLFS studies indicate that displaced Eu is present in the form of aquo species. By means of Eq. (5.5), it was found that at a concentration of 2 M NaCl or 50 mM $CaCl_2$, Eu is completely coordinated with water molecules and forms a $Eu(H_2O)_9$ complex.

At a fixed electrolyte concentration, different cations show very different spectral effects, as can be seen in Fig. 45. It is obvious that the influence of Na on complexation of Eu with fulvic acid is least. Even in the presence of 500 mM Na (Fig. 45, right), the spectrum is changed only slightly. The trivalent cations Al and Gd cause the most pronounced spectral changes. Already at a low electrolyte concentration of 500 µM, (Fig. 45, left), the spectra are close to that of the $Eu(H_2O)_9$ complex. This shows that the electrolyte cations differ greatly in their competing effects towards Eu. Binding sites are blocked by trivalent metals much more efficiently than by mono- and divalent cations.

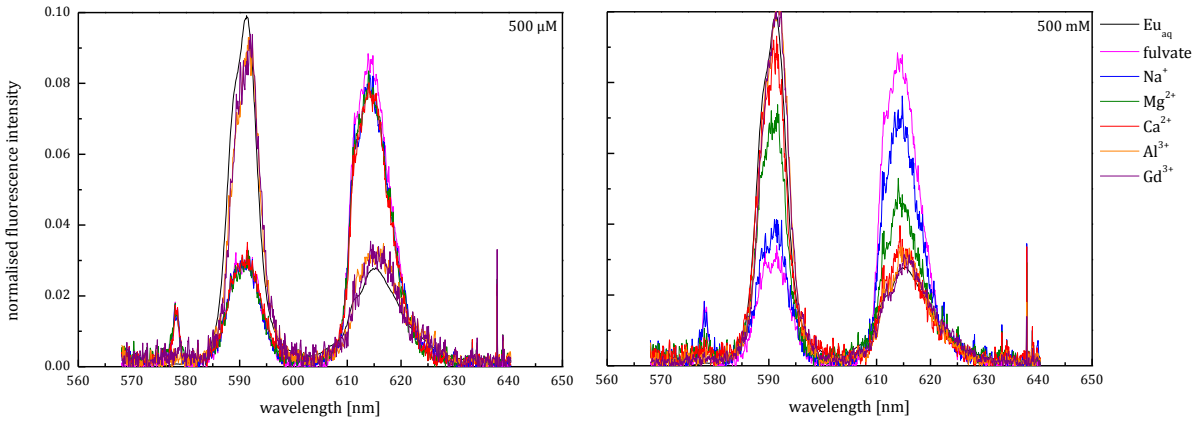

Fig. 45: Emission spectra of Eu-fulvate with 500 µM (left) and 500 mM (right) of Na^+, Mg^{2+}, Ca^{2+}, Al^{3+} or Gd^{3+}. The spectrum in black represents the Eu^{3+} aquo ion, the spectrum in magenta represents the Eu-fulvate complex without a background electrolyte.

The influence of the type of electrolyte anion was investigated as well and is shown in Fig. 46. The investigated counterions ClO_4^-, NO_3^- and Cl^- do not show a significant difference in their influence on the complexation of Eu with fulvic acid. The spectra are nearly identical for a defined concentration (1 mM and 200 mM). It is known that ClO_4^- ions, owing to their size, do not form complexes with Eu. Thus, it may be concluded that chloro complexes are not formed as well.

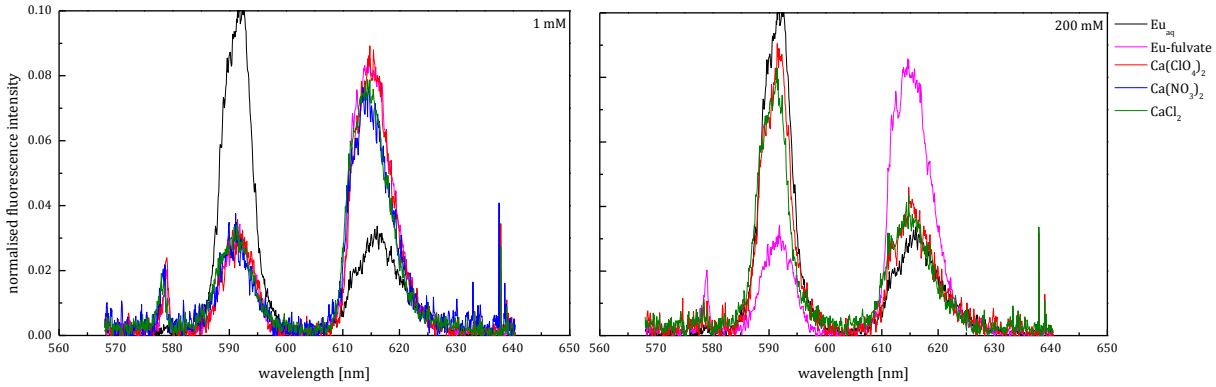

Fig. 46: Emission spectra of Eu-fulvate with 1 mM (left) and 200 mM (right) of ClO_4^-, NO_3^- or Cl^-. The spectrum in black represents the Eu^{3+} aquo ion, the spectrum in magenta represents the Eu-fulvate complex without a background electrolyte.

5.4 Modeling metal binding to fulvic acid

5.4.1 NICA-Donnan model

The NICA-Donnan model (Kinniburgh et al., 1996) describes cation binding to humic substances by specific interactions with functional groups as well as non-specific Coulomb interactions.

The NICA (non-ideal competitive adsorption) model (Koopal et al., 1994; Benedetti et al., 1995) is based on a continuous distribution of site affinities for protons and metal ions. The bimodal form for carboxylic and phenolic binding sites (type I and II, respectively) is given by Eq. (5.6)

$$Q_i = Q_{i,max}\,\theta_i = Q^{I}_{i,max}\,\theta^{I}_i + Q^{II}_{i,max}\,\theta^{II}_i = Q^{I}_{i,max}\,\frac{(\tilde{K}^{I}_i c_i)^{n^{I}_i}}{\sum_i (\tilde{K}^{I}_i c_i)^{n^{I}_i}}\,\frac{\{\sum_i (\tilde{K}^{I}_i c_i)^{n^{I}_i}\}^{p^{I}}}{1+\{\sum_i (\tilde{K}^{I}_i c_i)^{n^{I}_i}\}^{p^{I}}} + Q^{II}_{i,max}\,\frac{(\tilde{K}^{II}_i c_i)^{n^{II}_i}}{\sum_i (\tilde{K}^{II}_i c_i)^{n^{II}_i}}\,\frac{\{\sum_i (\tilde{K}^{II}_i c_i)^{n^{II}_i}\}^{p^{II}}}{1+\{\sum_i (\tilde{K}^{II}_i c_i)^{n^{II}_i}\}^{p^{II}}} \quad (5.6)$$

where Q describes the amount of a component i bound to the humic substance, Q_{max} is the number of binding sites, Θ is the degree of coverage, c is the concentration, $\widetilde{K_i}$ is the median equilibrium constant, p represents the width of the affinity distribution, and n is a parameter accounting for non-ideality with respect to component i.

Electrostatic effects are considered by using concentrations near binding sites rather than concentrations in the bulk solution. The up-concentration by the electric field is described by the Donnan model, assuming a gel-like phase with a uniform electric potential Ψ_D. Specific binding (Q_i) is calculated by Eq. (5.6), using enhanced concentrations c^D, which are given by Eq. (5.7):

$$c^{D}_{i} = c_i \exp(-z_i e \Psi_D / k T) \quad (5.7)$$

In this equation, c^D is the concentration of component i in the Donnan phase, z is the charge number of the ion, e is the elementary charge, k is the Boltzmann constant, and T is the absolute temperature.

Up-concentrated ions within the Donnan phase (in excess of the bulk concentration) are included in the total amount bound to the humic substance (non-specific binding):

$$Q^{D}_{i} = V_D (c^{D}_{i} - c_i) + Q_i \quad (5.8)$$

Q^D is the amount of component i enriched within the Donnan volume V_D by specific and non-specific binding. The Donnan volume is dependent on the ionic strength I. The following empirical relation holds:

$$\log V_D = B \log I - B - 1 \quad (5.9)$$

The parameter B is specific to the type of humic substance.

5.4.2 Results of modeling

NICA-Donnan parameters for binding of Eu, Na, Ca and Mg to a generalized fulvic acid were taken from (Milne et al., 2003). Measured data were modeled by fitting the parameters $\widetilde{K_1}$ and n in Eq. (5.6) for Tb and Eu by means of the speciation software ECOSAT 4.8 (Keizer and Van Riemsdijk, 2005) coupled with the parameter optimization program FIT. Results and adjusted parameters are shown in Fig. 47 and Table 8.

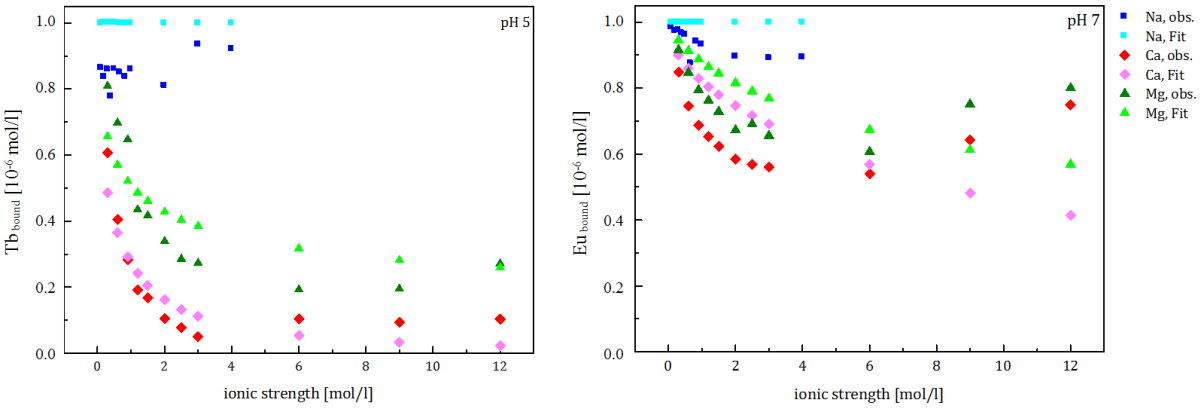

Fig. 47: Amount of Tb and Eu bound to fulvic acid at pH 5 and pH 7, respectively, plotted against ionic strength for NaCl, $CaCl_2$ and $MgCl_2$. Dark colors: experimental data, light colors: calculated data obtained with the NICA-Donnan model.

Table 8: NICA-Donnan parameters adjusted for Tb and Eu. All other parameters in Eqs. (5.6) - (5.9) were taken from Milne et al. (2003).

	log $\widetilde{K}^{I}$	log $\widetilde{K}^{II}$	n^{I}	n^{II}
Eu only (Milne et al., 2003)	-1.92	5.87	0.47	0.45
Eu with Na, pH 7	-1.91	5.87	0.50	0.49
Eu with Ca, pH 7	-1.92	5.87	3.07	4.17
Eu with Mg, pH 7	-1.61	5.29	0.44	0.93
Tb with Na, pH 5	-1.92	5.86	0.51	0.41
Tb with Ca, pH 5	-1.92	4.62	2.92	2.12
Tb with Mg, pH 5	-2.40	5.87	0.83	0.05

In general, the adjusted values for the equilibrium constants $\widetilde{K}^{I}$ and $\widetilde{K}^{II}$ show only moderate deviations from the generic parameters given by Milne et al. (2003), which were used as starting values for Eu as well as for Tb. From the fact that non-specific electrolyte effects at high ionic strengths are not yet considered adequately in these calculations, it may be inferred that the influence of the electrolyte cations is dominated by direct competition rather than shielding. This is, however, a tentative conclusion. More detailed studies including SIT and Pitzer parameters are pending.

6 Tc(VII)/Tc(IV) retention by iron(II)-containing minerals

Technetium-99 is a *β*-emitting fission product of uranium-235 and plutonium-239 with a long half-life (2.1×10^5 years) and a high content in radioactive waste (6 % of all fission products consist of Tc-99).

Under oxic conditions, Tc is present as pertechnetate (TcO_4^-, Tc(VII)), which is a highly soluble, aqueous species that is known not to sorb significantly on minerals or sediments. However, under anaerobic conditions and in the presence of a reducing agent, Tc(VII) is reduced to Tc(IV). Thereby, the Tc solubility decreases drastically due to precipitation of respective hydrolysis products of Tc(IV) (Peretyazhko et al., 2008, 2012; Kobayashi et al., 2013).

Iron(II)-containing minerals occur ubiquitously in nature and as corrosion products of carbon steel canisters used for storing radioactive waste. Iron(II)-minerals are characterized by redox reactivity and a high sorption capacity. Thus, they can control the environmental fate of radionuclides, for instance, Tc.

The objective of this study was to improve the understanding of Tc(VII)/Tc(IV) retention by iron(II)-containing minerals such as magnetite ($Fe^{II}Fe^{III}{}_2O_4$) and siderite ($Fe^{II}CO_3$). For this, batch sorption experiments were performed at room temperature under anoxic conditions and exclusion of CO_2 (glove box with N_2 atmosphere, O_2 <5 ppm), as function of pH, ionic strength of the background electrolyte (NaCl), contact time, and solid-to-liquid (S/L) ratio. In addition, ATR FT-IR and XAS spectroscopy were applied. For comparison, Tc retention on iron(III)-containing minerals hematite (α-Fe_2O_3) and maghemite (γ-Fe_2O_3) was studied.

6.1 Experimental

Materials

The mineral phases magnetite and siderite were prepared under inert gas conditions (glove-box, N_2 atmosphere, <10 ppm O_2) with degassed Milli-Q water.

Magnetite: 60 mL of a 6 M NH_4OH (p.a., Merck) solution was slowly added to 50 mL solution of 0.4 M $FeCl_2 \times 4H_2O$ (ReagentPlus 99 %, Sigma Aldrich) and 0.8 M $FeCl_3 \times 6H_2O$ (p.a., Merck) under vigorous stirring. Immediately a black precipitate was formed. The stirring of the solution was continued for 12 h. Then, the solid was separated by centrifugation (0.5 h, 4600*g*). Two batches of magnetite were synthesized. One part of the synthesized magnetite was washed two times with water and then, two times with 0.01 M NaCl (p.a., Merck). This material was stored as suspension in 0.01 M NaCl. The other part was washed four times with water and then, freeze-dried whereby a magnetite powder was obtained. The phase-purity and structure of the synthesized magnetite powder was characterized by X-ray diffraction (XRD) (mod. Bruker-AXS Diffractometer D8 with curved PG-secondary monochromator) and moreover, the specific surface area was determined applying the Brunauer-Emmet-Teller (BET) equation (mod. SA 3100, Beckman Coulter, Fullerton, USA).

Siderite: 100 mL of 0.8 M Na_2CO_3 (p.a., VWR) solution was slowly added (within 8 h by peristaltic pump) to 100 mL of 0.4 M $FeCl_2 \times 4H_2O$ (ReagentPlus 99 %, Sigma Aldrich) solution under vigorous stirring and purging with N_2. The formed pale solid was separated by centrifugation (0.5 h, 4600*g*) and washed with water. Then, the purified solid was washed three times with 0.1 M NaCl (p.a., Merck) and finally, equilibrated in 0.1 M NaCl. A detailed characterization of the siderite was not possible because of its pronounced oxidation-sensitivity. However, the characteristic light-grey color of the siderite suspended in solution, without any color change over time, is an indication of the chemical (redox) stability of the siderite batch.

Hematite, maghemite: The minerals hematite (>99 %, US Research Nanomaterials) and maghemite (>99 %, Alfa Aesar) were applied as obtained.

Batch sorption experiments

Calculated amounts of the minerals hematite and maghemite or calculated volumes of the magnetite and siderite stock suspensions (36.2 g/L and 54 g/L, respectively) were given in 15 mL centrifuge tubes (PP, Cellstar, Greiner Bio-One GmbH, Frickenhausen, Germany). After that, 10 mL of the background electrolyte (0.1 M or 1 M NaCl solution, which were prepared by dissolution of NaCl (p.a., Merck) in degassed Milli-Q water) were added. The pH values of the sample suspensions were measured applying a pH meter (mod. inoLab pH 720, WTW, Weilheim, Germany) with a SenTix® Mic pH microelectrode (WTW), calibrated using standard buffer solutions (WTW; pH= 4.006, 6.865, 9.180). If necessary, the pH values were adjusted by addition of small amounts of diluted HCl or NaOH (p.a., Merck; carbonate-free) solutions.
After pre-equilibration, the sorption experiment was started by adding an aliquot (5.55 µL) of the $^{99}TcO_4^-$ stock solution (1.81×10^{-2} M $^{99}TcO_4^-$; 1.125 MBq/mL) resulting in a Tc concentration of 1×10^{-5} M. Blank suspensions of the minerals in the background electrolytes without TcO_4^- were prepared and processed under the same conditions.
During pre-equilibration and sorption, the samples were continuously shaken on a horizontal shaker (mod. IKA Vibrax VXR basic). The pH values were measured/adjusted daily.
After the sorption experiments, the final pH values of the samples were determined. Moreover, for the experimental series with magnetite and siderite performed in 1 M NaCl background electrolyte as a function of pH, redox potentials (E_h) were monitored at selected pH values using a combined Pt/Ag/AgCl redox electrode (Schott, Mainz, Germany), calibrated using a standard redox buffer solution (WTW) at pH 7. The values were recorded after at least 1 h. The E_h values given in the paper correspond to the minima of the E_h evolution during the measurements and are corrected for the standard hydrogen potential (SHE).
With the exception of the siderite samples, the solid and liquid phases were separated by centrifugation (6800*g* for 2 h). To prevent the transport of the extremely oxidation-sensitive siderite samples to the centrifuge, standing outside the inert gas box, the siderite suspensions were filtered (0.2 µm, polyethersulfone, VWR International, Darmstadt, Germany) inside the glove box to separate the mineral from the sample solution.
The final Tc concentration in the supernatants was determined by liquid scintillation counting (LSC; mod. TriCarb 3100 TR, Perkin Elmer, Freiburg, Germany) using 1 mL supernatant and 15 mL Ultima Gold™ (Perkin Elmer) as scintillation cocktail.
A compilation of the various sorption series is given in Table 9. All sorption experiments were performed in duplicate.

Table 9: Summary of batch sorption experiments.

Mineral	Solid/solution ratio [g/L]	Contact time	pH value	Ionic strength [mol/L]
Hematite	1	18 d	4	0.1
Maghemite	1	18 d	4	0.1
Magnetite	0.1 – 1.5	2 d	4	0.1
	0.2	1 - 165 h	4	0.1
	0.2	2 d	4 - 12	0.1
	0.2	2 d	4 - 12	1
Siderite	0.2 - 0.5	0.5 - 150 h	8	0.1
	0.2	2 d	8 - 12	0.1
	0.2	2 d	8 - 12	1

ATR FT-IR spectroscopic sorption study

The Tc sorption onto hematite, maghemite and magnetite was studied by means of *in situ* ATR FT-IR spectroscopy. Although all sample preparation steps were performed in a glove box under N_2 atmosphere, the Tc sorption onto siderite could not be studied since a complete exclusion of oxygen during the FT-IR measurements was obviously not possible which led to a partial oxidation of iron(II) in the siderite mineral.

Infrared spectra were measured from 1000 to 800 cm^{-1} on a Bruker Vertex 70/v vacuum spectrometer, equipped with a Mercury Cadmium Telluride (MCT) detector. Spectral resolution was 4 cm^{-1} and spectra were averaged over 256 scans. A horizontal diamond crystal with nine internal reflections (DURA SamplIR II, Smiths Inc.) was used. The measurements were performed in D_2O to prevent an overlapping of the TcO_4^- band at about 900 cm^{-1} with the pronounced absorption band of H_2O at 1000 cm^{-1}.

For the *in situ* ATR FT-IR experiments a mineral film was prepared directly as stationary phase on the surface of the ATR diamond crystal. Then, the mineral film was conditioned by flushing with 0.1 M NaCl solution for 45 min using a flow cell (V = 200 µL) at a rate of 200 µL/min. Subsequently, the sorption reactions were induced by rinsing the stationary phase with the sample solution ($[TcO_4^-] = 5\times10^{-4}$ M; 0.1 M NaCl) for 60 min. Finally, the loaded mineral phase was flushed again with 0.1 M NaCl solution (45 min) in order to gain more information on the reversibility of the sorbed species.

XAS sample preparation and measurements

The XAS samples were prepared and processed analogous to the samples of the batch sorption experiments under N_2 atmosphere. 300 mg magnetite mineral and 5.55 mL siderite suspension, respectively, were added in 50 mL centrifuge tubes (PP). The volume was filled up to 40 mL with 0.1 M NaCl electrolyte and calculated amounts of the Tc stock solution. The solid-to-liquid ratio was 7.5 g/L. The Tc content, the pH values as well as the contact times were varied as specified in Table 10.

Table 10: Summary of XAS samples.

Sample	Mineral	Tc content [Bq/sample]	Solid/solution ratio [g/L]	Ionic strength [mol/L]	Contact time [d]	pH
Tc15-14	Magnetite	1265379	7.5	0.1	5	7.18
Tc15-15	Magnetite	631405	7.5	0.1	5	7.14
Tc15-16	Magnetite	159545	7.5	0.1	2	11.87
Tc15-17	Magnetite	633180	7.5	0.1	1	5.31
Tc15-18	Magnetite	183825	7.5	3.0	2	11.80
Tc15-19	Magnetite	631763	7.5	0.1	2	5.33
Tc15-20	Siderite	1263875	7.5	0.1	2	7.75
Tc15-21	Siderite	630847	7.5	0.1	2	7.82
Tc15-22	Siderite	1258953	7.5	0.1	2	11.83
Tc15-23	Siderite	633116	7.5	0.1	2	11.91

(The XAS data of Tc15-16 and Tc15-18 could finally not be evaluated since the surface loading was not high enough.)

After equilibration, the samples were centrifuged and the supernatants were removed. The remaining minerals were transferred as wet pastes into double confined sample holders (SH01C). Subsequently, the samples were shock frozen in liquid N_2. After that, the samples were transported to the Rossendorf Beamline at the European Synchrotron Radiation Facility (ESRF) in Grenoble, France. During the XAS measurements, the samples were kept at 15 K in a closed-cycle He cryostat. The spectra were acquired in fluorescence mode at the Tc *K*-edge (21044 eV). Energy of the Si(111) double-crystal monochromator was calibrated using a Mo foil (edge energy 20000 eV).

6.2 Results and discussion

6.2.1 Characterization of magnetite

Phase-purity and structure of the synthesized magnetite was checked by X-ray diffraction (XRD). The diffractograms recorded for the magnetite charges 1 and 2 are very similar (cf. Fig. 48). Only the diffractogram obtained for charge 1 shows a very slight 2θ-shift. Nevertheless, the reflexes correspond very well to the reflexes of a synthetic magnetite reference shown in red. This verifies a high phase-purity and a highly ordered crystal lattice of the synthesized magnetite charges.

The specific surface areas of the magnetite charges 1 and 2 were determined with 84.2 m^2/g and 86.3 m^2/g, respectively (cf. Table 11). This again shows, that the two magnetite charges are very similar. Thus, the comparability of the sorption series performed with the two charges is ensured.

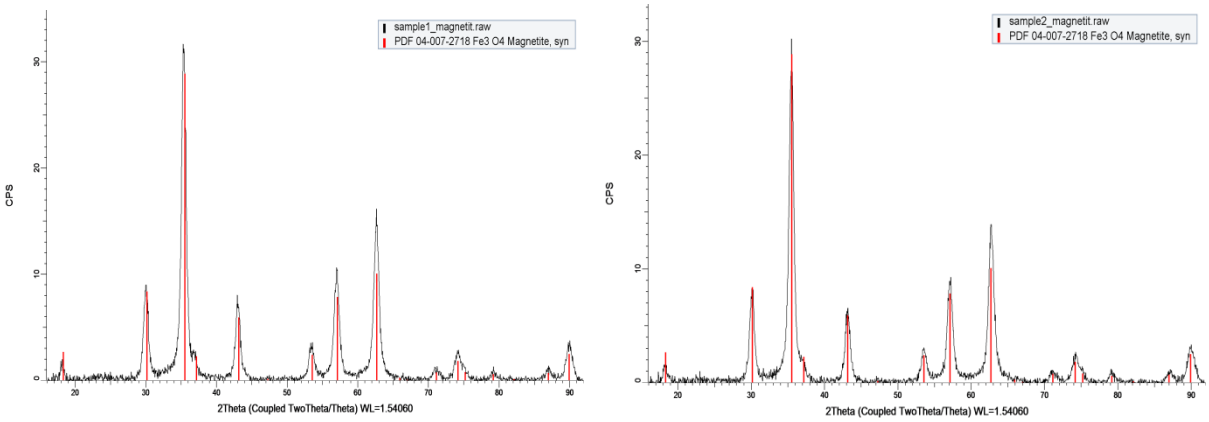

Fig. 48: Diffractograms of magnetite charges 1 and 2.

Table 11: Specific surface areas (BET) of magnetite charges 1 and 2.

	Charge 1 BET [m^2/g]	Charge 2 BET [m^2/g]
	85.1	86.3
	83.2	86.0
	84.2	86.6
Mean value	**84.2**	**86.3**

6.2.2 Batch sorption experiments

The objective of these experiments was the quantification of the retention behavior of various iron mineral phases towards pertechnetate.

Tc retention by hematite and maghemite

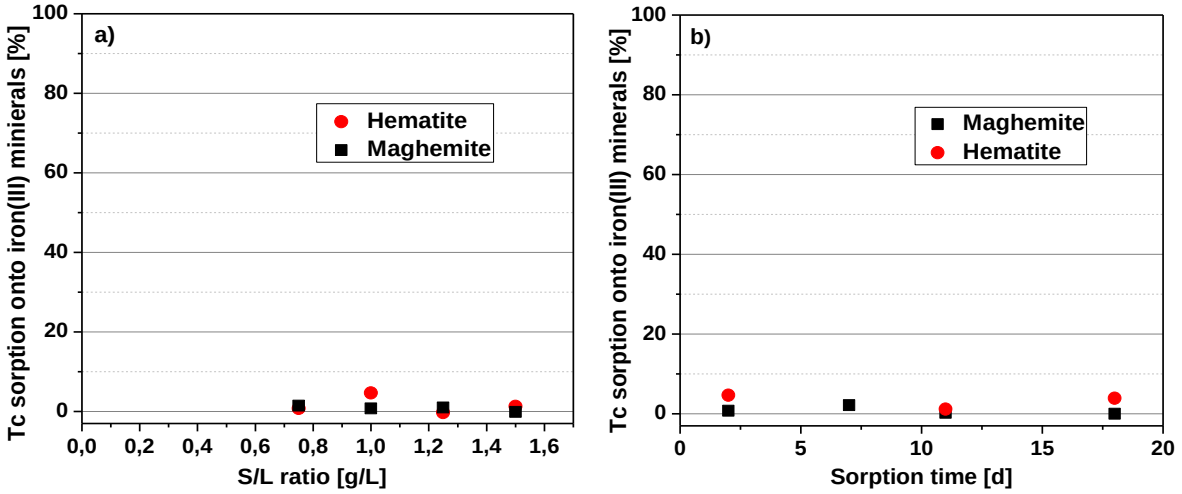

Fig. 49: Tc retention onto hematite and maghemite as function of a) S/L ratio ($[Tc(VII)]_{init}$ = 1×10^{-5} M, pH 4, 0.1 M NaCl, 2 d contact time) and b) contact time ($[Tc(VII)]_{init}$ = 1×10^{-5} M, pH 4, 0.1 M NaCl, S/L ratio: 1 g/L).

Fig. 49 shows that, independent of the S/L ratio, there is no Tc retention on the iron(III) oxides hematite and maghemite after 2 d contact time. Also for contact times of up to 18 d, shown for the samples with an S/L ratio of 1 g/L, no significant sorption of Tc, added as TcO_4^-, can be observed. These results correspond to the results of Peretyazkho et al. (2008).

Tc retention by magnetite and siderite

The iron(II) containing minerals magnetite and siderite show a retention behavior toward Tc completely different from that of maghemite and hematite. After addition of TcO_4^- to the siderite suspension equilibrated at pH 8.6, the Tc retention occurs almost instantly and completely, even at the small S/L ratio of 0.2 g/L (cf. Fig. 50). The Tc retention onto magnetite at pH 4 (Fig. 50), occurs slower and a maximum Tc retention of only 80 % is observed in this experiment.

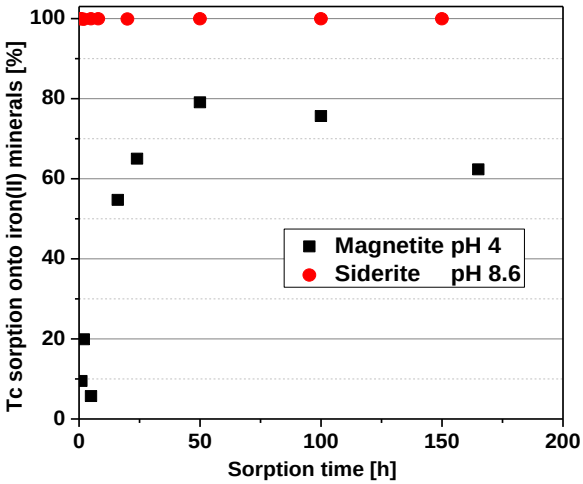

Fig. 50: Tc retention onto magnetite (pH 4) and siderite (pH 8.6) as function of contact time ($[Tc(VII)]_{init}$ = 1×10^{-5} M, S/L = 0.2 g/L, 0.1 M NaCl, N_2).

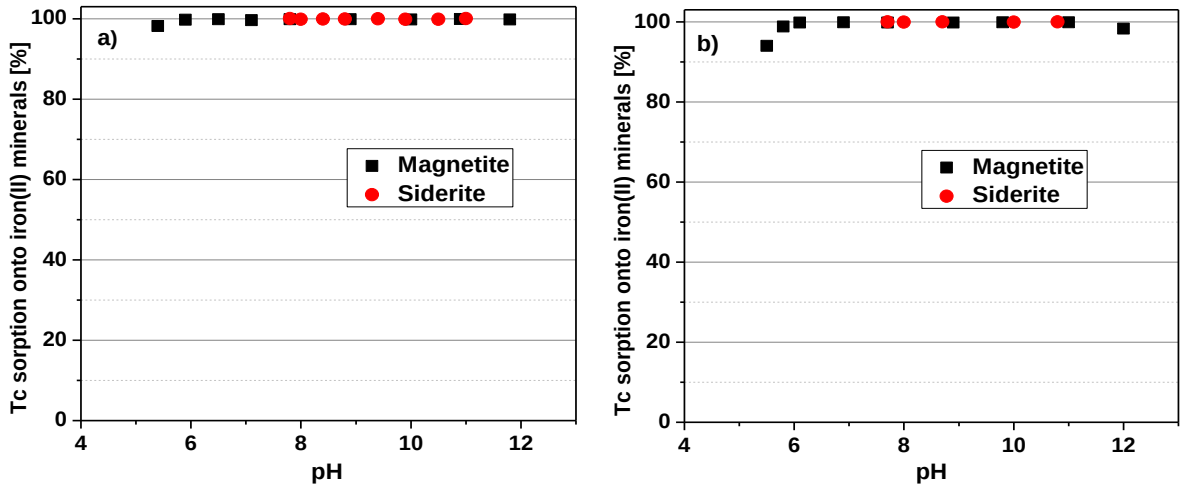

Fig. 51: Tc retention onto magnetite and siderite as function of pH value in a) 0.1 M NaCl and b) 1 M NaCl ($[Tc(VII]_{init}$ = 1×10^{-5} M, S/L = 0.2 g/L, N_2, 2 d contact time).

Fig. 51 shows the Tc retention onto magnetite and siderite as a function of pH value and ionic strength. In the case of siderite, independent of pH value and ionic strength, the Tc retention is almost complete. Magnetite also shows a very high Tc retention, only at pH values lower than 6 a slight decrease is observed. These results support results found by Kobayashi et al. (2013).

From the strong difference observed for the retention behavior of iron(II) and iron(III) minerals towards TcO_4^- it can be concluded that the immobilization of Tc in the case of iron(II) minerals is due to a reduction of Tc(VII) to Tc(IV). In order to estimate the potential for Tc reduction, redox potentials were measured in selected samples.

6.2.3 Redox potentials

Fig. 52 shows the E_h-pH diagram for Tc in aqueous solution, calculated for conditions applied in the sorption experiments (10 µM Tc, 1 M NaCl, 25°C). The calculation was performed with the geochemical speciation code „Geochemist's Workbench" (version 10.0.5) using the default data base „thermo.dat" (LLNL database). Here, the extended Debye-Hückel equation was applied, although only valid for low ionic strengths. However, the application of more adequate equations (SIT, Pitzer) was not possible due to the lack of thermodynamic data for technetium.

In Fig. 52, redox potentials of selected Tc/magnetite samples, monitored at the end of the sorption experiments, are shown as blue squares. They are near the borderline between Tc(VII) and Tc(IV). This means TcO_4^- can be reduced by magnetite. The redox potentials of Tc/siderite samples are even lower (cf. Fig. 53). This confirms the results of batch experiments where the Tc retention by siderite was found to be faster compared to magnetite.

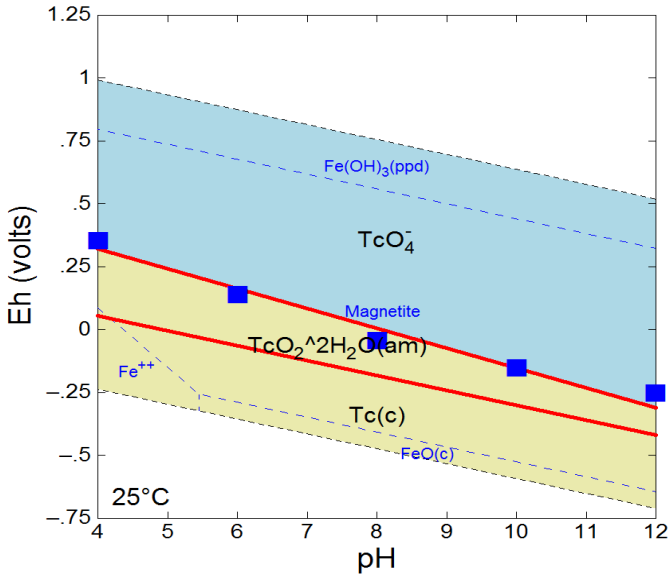

Fig. 52: Eh-pH diagram for Tc in 1 M NaCl (10 µM Tc, 25°C) calculated applying the extended Debye-Hückel equation. Redox potentials of selected Tc/magnetite samples monitored at the end of the sorption experiments are shown as blue squares.

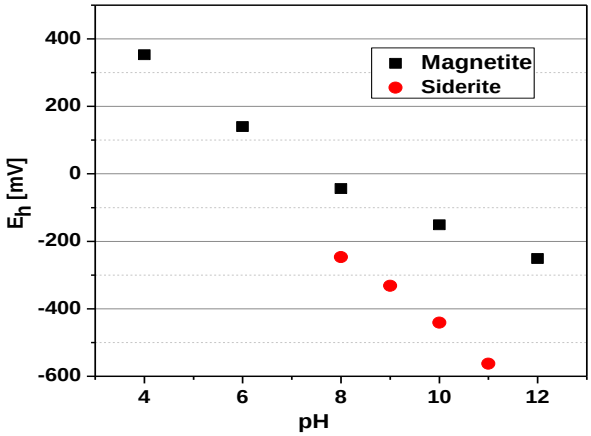

Fig. 53: Redox potentials of selected Tc/magnetite and Tc/siderite samples (1 M NaCl, 25°C).

For the identification of Tc species in aqueous solution as well as on the mineral phase *in situ* ATR FT-IR spectroscopy and X-ray absorption spectroscopy are applied.

6.2.4 ATR FT-IR spectroscopy

The IR spectrum of a pertechnetate reference sample shows that the absorption band of the pertechnetate ion in solution is found at about 908 cm^{-1} (Fig. 54).

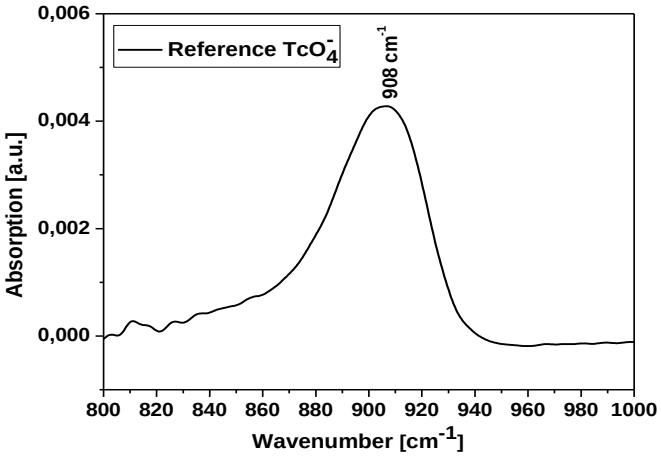

Fig. 54: Reference IR spectrum of pertechnetate ([Tc(VII] = 5×10^{-4} M, 0.1 M NaCl, 25°C).

The FT-IR spectra recorded during Tc(VII) sorption on magnetite, hematite and maghemite do not change with time, thus, for simplicity the spectra recorded after a contact time of 15 min are shown in Fig. 55. The Tc bands observed in these spectra are similar to the band of the aqueous TcO_4^- reference. No shifts are observed and no differences between iron(II) and iron(III) minerals are observed. This means, that during IR experiments only the aquatic, hardly sorbed TcO_4^- was observed. In the time frame of the *in situ* IR experiment, the signal of the Tc(VII) ion did not disappear indicating that the reduction to Tc(IV) occurs on a longer time scale.

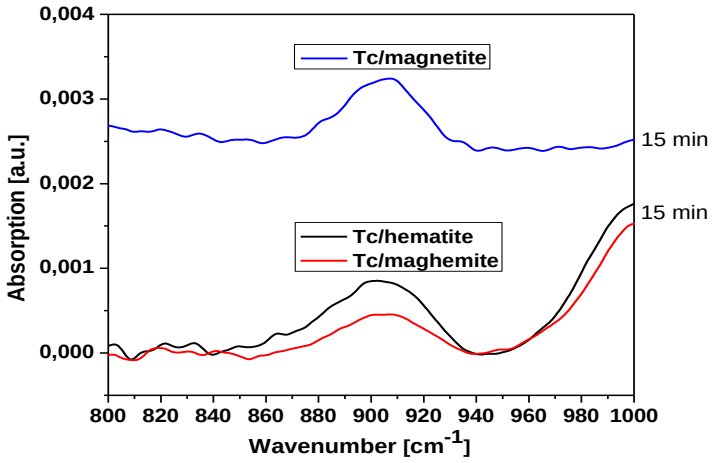

Fig. 55: *in situ* ATR FT-IR spectra of Tc(VII) sorption on magnetite, hematite and maghemite after a contact time of 15 min.

6.2.5 X-ray absorption spectroscopy

A first evaluation of the XAS data obtained for Tc/magnetite and Tc/siderite samples led to XANES spectra shown in Fig. 56 and Fig. 57. The XANES spectra, obtained for magnetite and siderite, are similar (absorption edge 21058 eV, no pre-edge) to each other, but differ from the XANES spectrum of TcO_4^-. This verifies that the immobilization of Tc onto these minerals is due to surface-mediated reduction of Tc(VII) to Tc(IV).

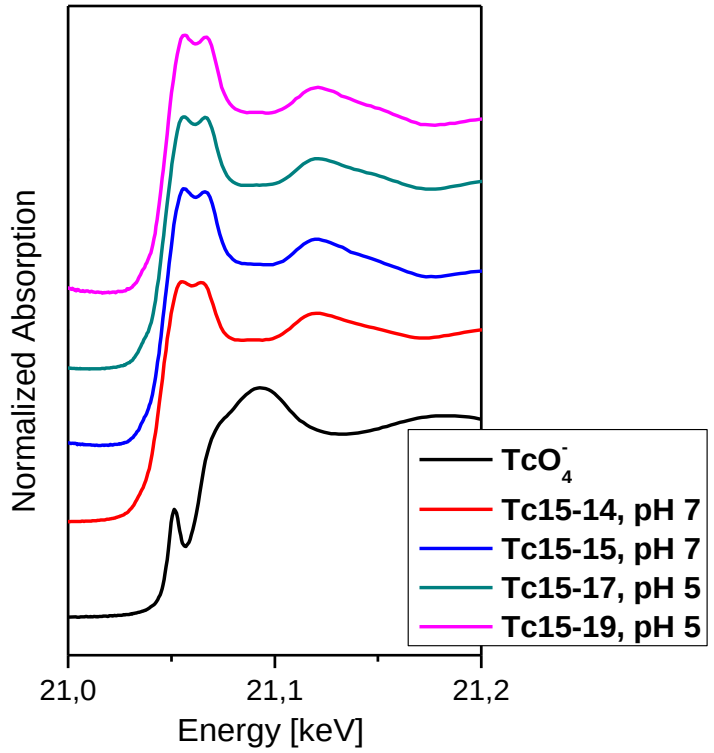

Fig. 56: Tc *K*-edge XANES spectra of Tc(VII) reacted with magnetite in comparison to a TcO_4^- reference spectrum (sample characteristics are given in Table 10).

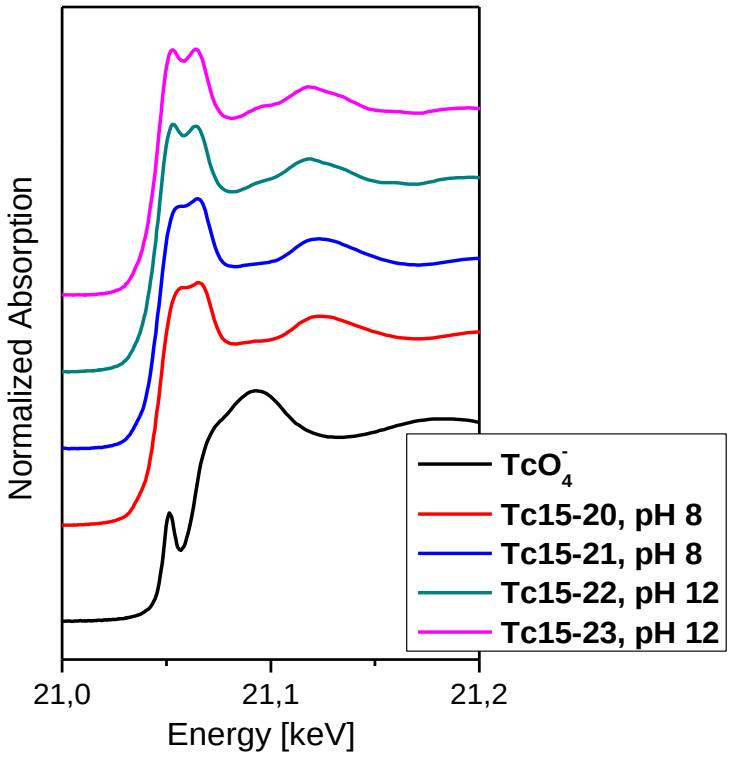

Fig. 57: Tc *K*-edge XANES spectra of Tc(VII) reacted with siderite in comparison to a TcO_4^- reference spectrum (sample characteristics are given in Table 10).

It can be concluded that both iron(II) minerals, occurring ubiquitously in nature and as corrosion products of carbon steel canisters used for storing radioactive waste, contribute effectively to the retention of Tc under repository conditions. This was found for a large pH range. An influence of ionic strength (0.1 or 1 M) was not observed.

7 U(VI) sorption on montmorillonite at high ionic strengths

In Germany, there are potentially two types of clay deposits that are eligible for high-level nuclear waste disposal: The Opalinus Clay of South Germany and Cretaceous clay sediments in North Germany. The latter exhibit ionic strengths of up to 4 mol L^{-1} in the groundwaters found in the relevant depths (Brewitz, 1982). Therefore, research into nuclear waste disposal in North German clays has to take these high ionic strengths into account.

For the safety case of a nuclear waste repository, thermodynamic data are needed that describe the interaction between radionuclide and host rock. Many studies have focused on the interaction between actinides with clay minerals or clay rock at low ionic strengths (Akcay and Kurtulmuş, 1995; Bradbury and Baeyens, 2002, 2005; Catalano and Brown, 2005; Chakraborty et al., 2010; Chisholm-Brause et al., 2001; Joseph et al., 2011, 2013a; Křepelová et al., 2006, 2007; Marques Fernandes et al., 2012; Meleshyn et al., 2009; Pabalan and Turner, 1996; Schmeide and Bernhard, 2010). Data and research for the behavior of radionuclides under the conditions found in North German clay is however still scarce.

Both ionic strength and pH have an influence on radionuclide speciation and sorption processes. In this chapter, this influence is investigated for U(VI) in detail, as spent fuel elements contain more than 90 % uranium. Furthermore, surface complexation modeling for the interaction of U(VI) with montmorillonite at high ionic strengths is presented. Surface complexation constants have been generated at high ionic strengths and these values have been extrapolated to zero ionic strength with the Specific Interaction of Ions Theory (SIT). The applicability of surface complexation constants generated in pure electrolytes to surface complexation in mixed electrolytes is shown.

7.1 Experimental

A Na-montmorillonite (SWy-2; Crook County, Wyoming, USA) was used as model clay mineral in this study. It was purified according to Poinssot et al. (1999) and Bradbury and Baeyens (2009). This purification consisted of sieving the clay to obtain the < 63 µm fraction, transforming the clay into its Na-form, a size separation to enrich the < 5 µm fraction, an acidification step to eliminate carbonates and hydroxides of low solubility and lastly a dialysis against Milli-Q water (until a residual conductivity of < 10 S cm^{-1} was achieved) and a freeze-drying step. The purified clay was then analyzed by X-ray diffraction (XRD) and, after digestion, inductively coupled plasma mass spectrometry (ICP-MS, ELAN 9000, Perkin Elmer, Waltham, MA) to obtain the phase composition and the elemental composition, respectively. Furthermore, N_2-BET (mod. Coulter SA 3100, Beckman Coulter, Fullerton, USA) and cation exchange capacity (CEC, $BaCl_2$ method according to Bain and Smith (1987)) measurements were performed. These methods yielded a specific surface area A_{sp} = (41.1 ± 0.8) m^2 g^{-1} and CEC of 85.0 $mmol_c$ $(100\ g)^{-1}$.

A U(VI) stock solution (5×10^{-4} mol L^{-1} $^{238}UO_2Cl_2$ in 0.01 mol L^{-1} HCl) was used for all experiments, with the exception of the determination of cation exchange and the U(VI) sorption isotherm in NaCl, for which a ^{233}U solution was employed (1.5×10^{-4} mol L^{-1} $^{233}UO_2Cl_2$ in 0.001 mol L^{-1} HCl). To prepare the background electrolyte, NaCl (p.a., > 99.5 %, Roth, Karlsruhe, Germany), $CaCl_2 \times 2\ H_2O$ (p.a., Merck) or $MgCl_2 \times 6\ H_2O$ (p.a., Merck) was dissolved in Milli-Q water (18 MΩ; mod. Milli-RO/Milli-Q-System, Millipore, Schwalbach, Germany). The pH values were adjusted with diluted HCl (Roth) and NaOH (p.a., Merck, Darmstadt, Germany). For experiments in absence of CO_2, NaOH prepared from carefully rinsed NaOH pellets (p.a., Roth) was used. The pH values were measured with laboratory pH meters (inoLab pH 720, WTW, Weilheim, Germany and pMX 3000/pH coupled with Multiplex 3000/pMX, WTW) with SenTix®Mic pH microelectrodes (WTW), calibrated with standard buffers at pH 1.679, 4.006, 6.865 (WTW) and 9.18 (Hanna Instruments, Woonsocket, Rhode Island, USA).

At high ionic strengths, the usage of pH as the negative decadic logarithm of the hydrogen ion activity is not feasible due to the strong dependency of activity on ionic strength. Instead, pH_c is used, the negative decadic logarithm of the molal hydrogen concentration. For practical measurement, a correction function that correlates the value displayed by the pH meter (pH_{exp}) with the pH_c is needed. This correction function can be approximated by a quadratic function. In this study, the approximation found by Altmaier et al. (2003, 2008) was used.

$$A_m = -0.0988 + 0.1715\ c_{m,NaCl} + 0.0013\ c_{m,NaCl}^2 \quad (7.1)$$

$$A_m = -0.1176 + 0.4308\ c_{m,CaCl_2} + 0.0096\ c_{m,CaCl_2}^2 \quad (7.2)$$

7.1.1 Batch sorption experiments

For the batch sorption experiments, 40 mg each of the purified montmorillonite were weighed into 15 mL PP centrifuge tubes (Cellstar, Greiner Bio-One GmbH, Frickenhausen, Germany). To the clay, calculated amounts of NaCl or $CaCl_2$ and/or $MgCl_2$ were weighed. Depending on the sample series, either the pure electrolytes were used or a mixed electrolyte consisting of 2.52 mol kg^{-1} NaCl, 0.12 mol kg^{-1} $CaCl_2$ and 0.048 mol kg^{-1} $MgCl_2$.

For the experiments under ambient conditions ($p_{CO2} = 1\times10^{-3.5}$ atm), 8.5 g of Milli-Q water were added. For samples above pH_c 7, calculated amounts of 1 mol L^{-1} $NaHCO_3$ (Merck) were added to achieve near-instant equilibrium with atmospheric CO_2. The samples were shaken continuously in an overhead shaker (mod. Reax 20, Heidolph, Schwabach, Germany). The samples were pre-equilibrated for 10 days (NaCl, $MgCl_2$), 4.5 weeks ($CaCl_2$) or 5 weeks (mixed electrolyte), during which pH_c was adjusted frequently until pH_c stability was reached. Then, Milli-Q water was added so that the samples contained 10 g of water each. After an additional pH_c adjustment, an aliquot of U(VI) stock solution was added to achieve the predetermined initial UO_2^{2+} concentration. For the batch sorption experiments in dependence on pH_c, this initial U(VI) was 1×10^{-6} mol kg^{-1}, while for the sorption isotherms the initial U(VI) concentration ranged from 1×10^{-5} mol kg^{-1} to 1×10^{-8} mol kg^{-1}. After four to seven days, during which the pH_c was continually adjusted, sorption was complete.

Samples that were to be equilibrated under CO_2-free conditions were transferred into a N_2-glove box, where 8.5 g of degassed Milli-Q water were added. The samples were loaded into an airproof shaking vessel and transferred to an overhead shaker. Pre-equilibration lasted 4.5 weeks with frequent pH adjustments until pH stability was reached, after which the samples were filled up to contain 10 g of water. After an additional pH adjustment, U(VI) stock solution was added to achieve the predetermined initial U(VI) concentration. Sorption was complete after one week, with frequent pH adjustments during this week.

When sorption was complete, the samples were centrifuged (Avanti J-20XP, Beckman Coulter, Brea, CA, 30 min, 4500 g) and then filtered (PES syringe filter, 0.2 µm, vwr, Radnor, PA) into new centrifuge tubes. Photon correlation spectroscopy (BI90, Brookhaven Instruments, Holtsville, NY) showed that this treatment was sufficient to remove colloids. Subsequently, the solution was acidified to 1 % HNO_3 and analyzed by ICP-MS. Alternatively, liquid scintillation chromatography (LSC, Wallac 1414WIN Spectral Low-Level α/β, Perkin Elmer) was used for several sample series. For LSC measurements, a scintillation cocktail suitable for high ionic strengths was used, namely Optiphase HiSafe 3 (Perkin Elmer). Analysis for Na and Ca was done by flame atomic absorption spectroscopy (F-AAS, AAS-4100, Perkin Elmer) to control the final ionic strength of the samples.

Under these conditions, batch sorption experiments in dependence on pH_c and ionic strength were performed (maximum pH_c and ionic strength range: pH_c 4 to 10, I = 0.1 to 9 mol kg^{-1}), as well as leaching experiments. Furthermore, the cation exchange coefficient for U(VI) in NaCl and $CaCl_2$ was determined at pH_c 2 at various ionic strengths. In the mixed electrolyte, the ionic strength was fixed and the experiments were conducted at pH_c 5.3, 6.5 and 8.5, with one sample series at pH_c 6.5 and 60°C.

Table 12 gives an overview of conditions of batch sorption experiments conducted for this study.

Table 12: Overview of conditions of batch sorption experiments conducted for this study.

Background electrolyte	Type of experiment	I / mol kg^{-1}	$c_{m,U(VI),ini}$ / mol kg^{-1}	Atmosphere	pH_c	Sorption time / d	Equilibration time / weeks
NaCl	I/pH_c dependence	0.3 / 1 / 3	1×10^{-6}	N_2	5–9	7	4.5
		0.1 / 0.3 / 1 / 2 / 3		CO_2	4–9	5	1.5
	Cation exchange	0.3 / 1 / 3			2	4	1
	Sorption kinetic	2			5.3	0.5 h – 7d	1.5
	Sorption isotherm	2	1×10^{-5} to 1×10^{-8}	N_2	5.3	7	4.5
$CaCl_2$	I/pH_c dependence	0.3 / 1 / 3	1×10^{-6}	N_2	5–9	7	4.5
		0.3 / 1 / 3 / 9		CO_2	4–9	5	4.5
		0.3 / 1 / 3 / 6 / 9			4–10	7	1.5
	Cation exchange (1st series)	0.3 / 1 / 3			2	4	1
	Cation exchange (2nd series)						
	Sorption isotherm	2	1×10^{-5} to 1×10^{-8}	N_2	5.3	7	4.5
$MgCl_2$	I/pH_c dependence	3 / 6 / 9	1×10^{-6}	CO_2	4–9	5	1.5
Mixed electrolyte	Isotherms (23°C)	3	1×10^{-5} to 1×10^{-7}	N_2	5.3 / 6.5 / 8.5	7	5
	Isotherm (60°C)						
	pH dependency		1×10^{-6}				
	Mineral batch comparison				6.5		17.5

7.1.2 IR and TRLFS spectroscopy

To investigate sorption on a molecular level, *in situ* attenuated total reflection Fourier-transform infrared spectroscopy (ATR FT-IR) and time-resolved laser-induced fluorescence spectroscopy (TRLFS) experiments were performed.

The IR measurements are based on the principle of reaction-induced difference spectroscopy. IR single beam spectra of a mineral film (stationary phase) are continuously recorded while it is rinsed by a flushing blank solution for equilibration and subsequent actinide solution for induced sorption (mobile phase). Since the acquisition time of each spectrum is about 30 seconds, the progress of the sorption process can be monitored with a time resolution in the sub-minute time range. This procedure allows the detection of spectral features showing very small absorption changes. A montmorillonite film was deposited on the ATR crystal from a suspension which was pre-equilibrated in a dilute NaCl solution for a week ($^{S}/_{L}$ = 2.5 g L^{-1}). To this end, the suspension was pipetted with intermittent drying steps until a film thickness of about 1 mg cm^{-2} was reached. In the first step of the online monitoring of the surface reaction, the conditioning of the mineral surface was performed. The montmorillonite film was equilibrated with an inactive solution that otherwise shares the same properties as the active solution in the sorption step. In this case, the solution had a corrected pH of 6.8 and an ionic strength of 3 M and 0.3 M respectively. To increase the signal-noise ratio, D_2O was used instead of H_2O. The experiment was performed under exclusion of CO_2 in a N_2 atmosphere. The velocity of the solution that is pumped through the used flow cell was 0.2 mL min^{-1}. For the sorption step, the inactive solution is replaced with a solution containing 2×10^{-5} M U(VI). The concentration of 2×10^{-5} M U(VI) ensures that a decent signal-noise ratio can be achieved while operating at a concentration where U(VI) speciation in solution is still reasonably similar to solutions with 1×10^{-6} M U(VI). Difference spectra of the sorption reaction are calculated from single beam spectra at the end of the conditioning stage and at distinct time intervals during the sorption stage. When the sorption step is deemed complete, the mineral is once again contacted with inactive solution in a flushing step to determine whether a surface complex is flushed out.

The TRLFS experiments were performed under cryogenic conditions at 153 K. The samples were prepared as described in section 7.1.1. To determine the U(VI) speciation in solution, the samples were prepared without mineral and after pH stability was reached after U(VI) was added to the solution, an aliquot of solution was filled in a plastic cuvette and frozen at 255 K. Directly before the measurement, the samples were cooled further down with liquid nitrogen. They were then placed in a sample holder that was placed inside a cryogenic cooling system (KGW Isotherm, Karlsruhe, Germany). Laser pulses with a wavelength of 266 nm and an average energy of 3 mJ (Minilite high-energy solid-state laser; Continuum, Santa Clara, CA) were used for the excitation of the samples. The spectra were recorded in the wavelength range of 371 to 670 nm with an iHR550 spectrograph (HORIBA Jobin Yvon, Edison, NJ) and an ICCD camera (HORIBA Jobin Yvon), using delay times of up to 9.5 ms.

7.1.3 Surface complexation modeling

Surface complexation modeling was performed using the two-site protolysis non-electrostatic surface complexation and cation exchange (2SPNE SC/CE) model. Aqueous geochemistry modeling was performed with PHREEQC v3.1.2 (Parkhurst and Appelo, 2013), which was coupled with the model-independent parameter estimation program PEST v13.0 (Doherty and Hunt, 2010). The database employed was the NEA thermodynamic database (Guillaumont et al., 2003) to which the complexation constants for $Ca_2UO_2(CO_3)_3(aq)$ and $CaUO_2(CO_3)_3^{2-}$ were added (Bernhard et al., 2001; Dong and Brooks, 2006). Due to the high ionic strengths in the experiments, the Specific Interaction of Ions Theory was applied (Guggenheim and Turgeon, 1955).

The 2SPNE SC/CE model describes the interaction of aqueous metal ions with the surface of a mineral (for a detailed description of the model see Bradbury and Baeyens (1997, 1999, 2002). It is a non-electrostatic model and therefore does not take any electrostatic interactions on the surface into account. The 2SPNE SC/CE model takes cation exchange and reactions between ions and surface groups into account. Cation exchange reactions

$$z_B\, A - clay + z_A\, B^{z_B+} \leftrightarrow z_A\, B - clay + z_B\, A^{z_A+} \tag{7.3}$$

and inner-sphere surface reactions of the general form

$$\equiv SOH + Me^{+} \leftrightarrow \equiv SOMe \quad + H^{+} \tag{7.4}$$

are defined in this model.

For the cation exchange reaction, the Gaines-Thomas convention was used to model cation exchange (Gaines and Thomas, 1953). This convention uses the equivalent fraction N_i of the exchangeable cation – which is the amount of sorbed cation expressed in equivalents divided by the cation exchange capacity – to express the activity of the exchange species. This leads to the following equation for the selectivity coefficient:

$${}^{B}_{A}K_c = \frac{N_B^{z_A}}{N_A^{z_B}} \times \frac{c_A^{z_B}}{c_B^{z_A}} \tag{7.5}$$

The 2SPNE SC/CE model uses several types of surface sites: Two weak sites W1 and W2 and one type of strong surface sites S. The model describes metal binding to the S and W1 sites. The weak sites are more abundant than the strong surface sites, but they have a much lower affinity towards metal cations than the strong surface sites. For trace metal sorption this means that the cations will only bind to the weak sites once the strong sites are beginning to get saturated.

The cation exchange and surface complexation reactions are combined to describe the experimental results. Furthermore, site capacities and surface site protolysis constants are fed

into the model. As non-adjustable parameters, the values for the site capacities and surface site protolysis constants that were derived by Bradbury and Baeyens are used in this work.

At high ionic strength, the Specific Interaction of Ions Theory (SIT) is commonly employed to correct the ion activity:

$$\log k^0 = \log k - \sum_i \nu_i Z_i^2 \frac{A\sqrt{I_m}}{1+1.5\sqrt{I_m}} + \sum_k \varepsilon(i,k) m_k \quad (7.6)$$

This can be linearized to

$$\log k - \Delta Z^2 D = \log k^0 - m\Delta\varepsilon \quad (7.7)$$

with A = 0.5100 $kg^{0.5}$ $mol^{-0.5}$. Values for ε are tabulated and can be found in Grenthe et al. (1992).

The workflow to obtain the thermodynamic parameters was as follows: Cation exchange, which was determined in a separate experiment, is modeled in a first step and then kept constant for the rest of the calculations. Then, all data points from experiments in dependence on pH were included in the model. In this work, they were included as equilibrium concentrations of U(VI). These equilibrium concentrations span three orders of magnitude, which is why they were weighted to normalize them to a value of 1. For the background electrolyte concentration, the experimentally determined values for each data point were used. For each background electrolyte and ionic strength, a separate set of log k values is calculated in an iterative process. The surface complexation constants are then extrapolated to zero ionic strength, which yields log k^0 for each surface reaction.

7.2 NaCl and $CaCl_2$ systems

7.2.1 U(VI) speciation in NaCl and $CaCl_2$

The calculated U(VI) speciation in NaCl and $CaCl_2$ solutions with an ionic strength of 3 mol kg^{-1} is shown in Fig. 58 and Fig. 59. According to these calculations, the uranyl cation and uranyl chlorides are the dominant species up to pH_c 5.5. In absence of CO_2 in both electrolytes, U(VI) forms various uranyl hydroxide species above pH_c 5.5. In presence of CO_2 in NaCl, uranyl hydroxides have a much lower influence on U(VI) speciation and uranyl carbonates dominate the speciation in the circumneutral and alkaline pH_c range. While in NaCl, $(UO_2)_2(CO_3)(OH)_3^-$ and $UO_2(CO_3)_3^{4-}$ dominate the range between pH_c 6.5 and 8.5, U(VI) in $CaCl_2$ forms the $Ca_2UO_2(CO_3)_3(aq)$ complex. Furthermore, due to the formation of $CaCO_3$ precipitates, with increasing pH the carbonate content in solution becomes small enough that uranyl hydroxides become once again the dominant U(VI) species by pH_c 8.5.

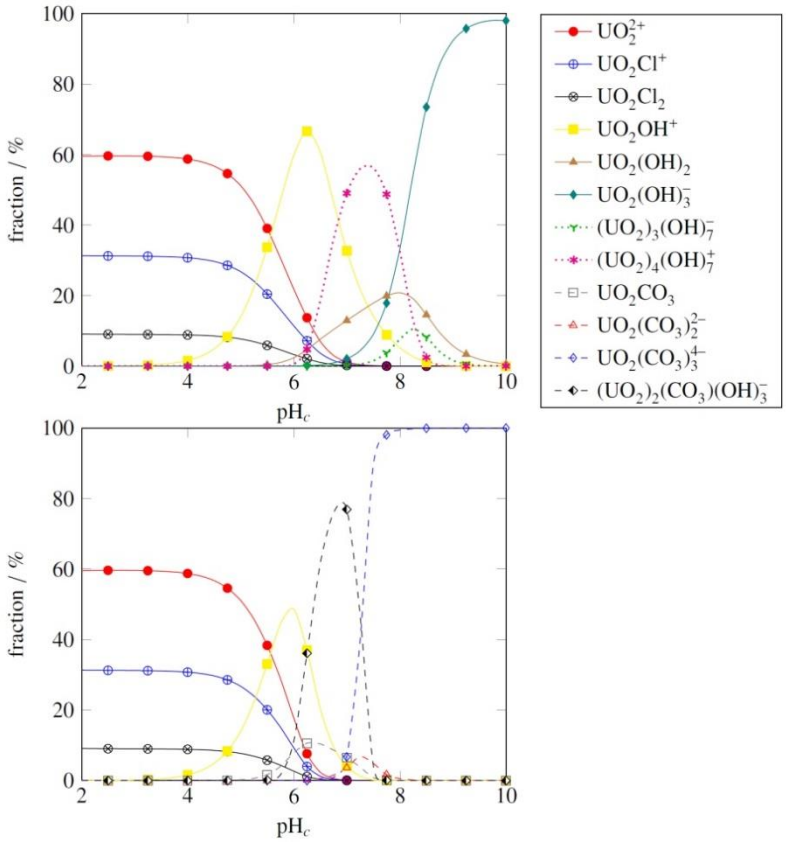

Fig. 58: Calculated U(VI) speciation in 3 mol kg^{-1} NaCl in absence (upper picture) and presence (lower picture) of CO_2 ($c_{U(VI)}$ = 1×10^{-6} mol kg^{-1}).

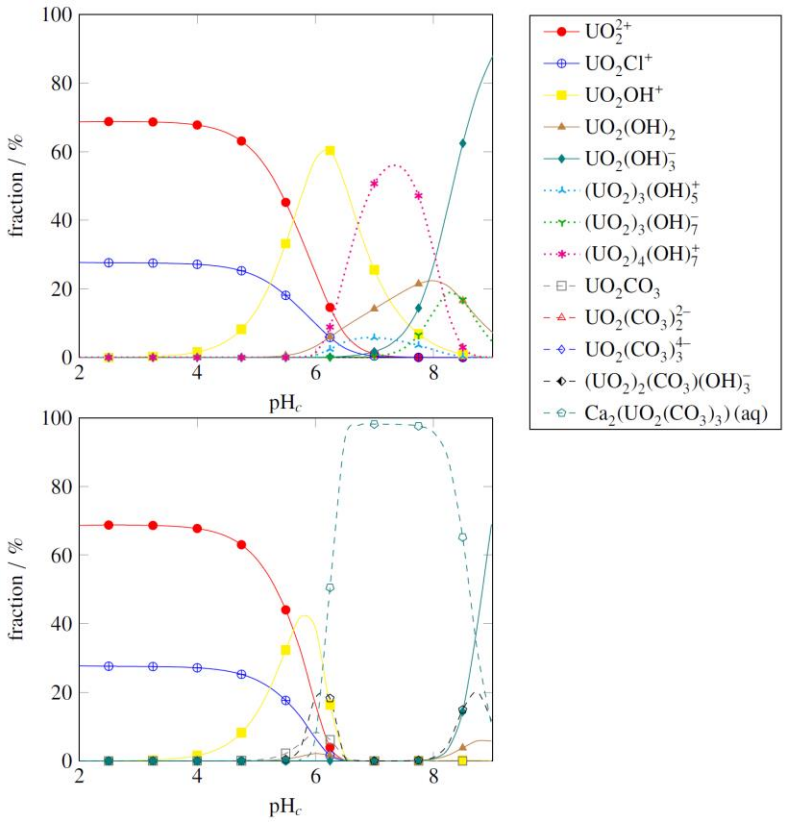

Fig. 59: Calculated U(VI) speciation in 1 mol kg^{-1} $CaCl_2$ in absence (upper picture) and presence (lower picture) of CO_2 ($c_{U(VI)}$ = 1×10^{-6} mol kg^{-1}).

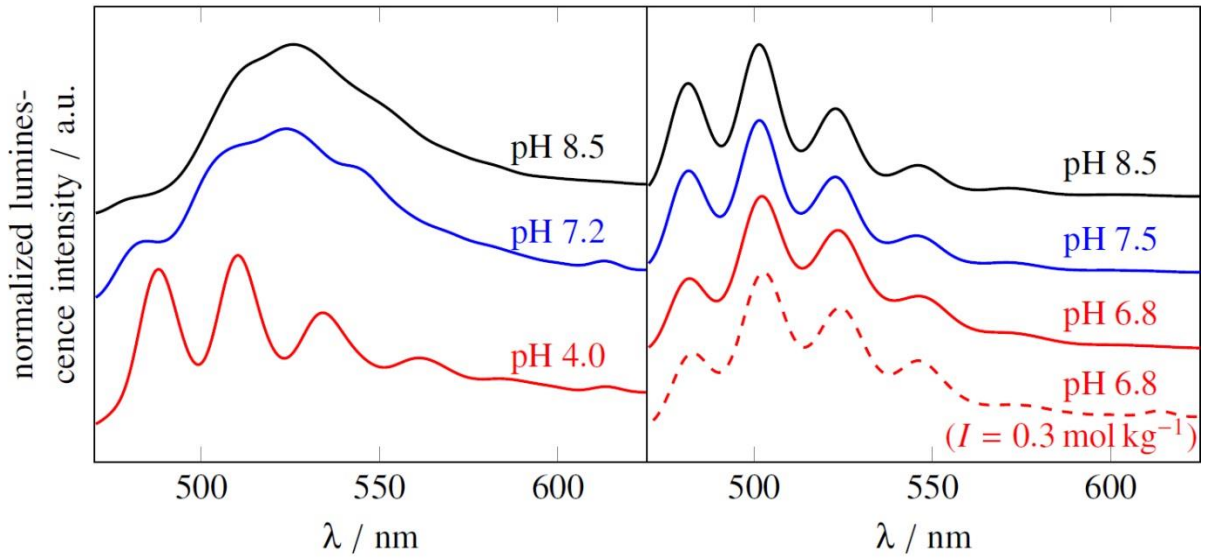

Fig. 60: TRLFS spectra of U(VI) ($c_{m,U(VI)}$ = 1×10^{-6} mol kg^{-1}) in 3 mol kg^{-1} NaCl in depedence on pH. Left picture: absence of CO_2, right picture: presence of CO_2.

Table 13: Luminescence properties of the spectra measured in absence of CO_2.

pH	Aqueous species	Emission bands / nm (±0.5 nm)				τ / µs	T / K
4.0	UO_2^{2+}	487.6	509.8	533.4	561.2	292 ± 53	153
7.2	$(UO_2)_3(OH)_7^-$ or $(UO_2)_4(OH)_7^+$	502.4	523.7	545.5	---	368 ± 48	153
8.5	$(UO_2)_3(OH)_7^-$ or $(UO_2)_4(OH)_7^+$	510.3	525.6	552.9	---	96 ± 11	153

Table 14: Luminescence properties of the spectra measured in presence of CO_2.

Sample	Aqueous species	Emission bands / nm (±0.5 nm)				τ / µs	T / K
6.8 (0.3 m)	UO_2CO_3	481.6	502.4	524.6	546.4	486 ± 107	153
6.8	⇩	481.1	502.0	523.7	547.8	603 ± 32	153
7.5		481.1	501.5	523.2	546.4	731 ± 11	153
8.5	$UO_2(CO_3)_3^{4-}$	481.1	501.5	523.2	546.4	801 ± 11	153

Cryogenic TRLFS measurements (cf. Fig. 60, Table 13, Table 14) in 3 mol kg^{-1} NaCl show that at pH_c 4, the free uranyl cation is indeed the dominant U(VI) species. In absence of CO_2, spectra at pH_c 7.2 and 8.5 were interpreted to indicate the presence of $(UO_2)_3(OH)_7^-$ or $(UO_2)_4(OH)_7^+$, which is in reasonably good agreement with the calculated speciation. Measurements at higher pH values were not successful. In presence of CO_2, UO_2CO_3 is the dominant species at pH_c 6.8 in a sample prepared at I = 0.3 mol kg^{-1}. At pH_c 6.8 and 7.5 in

3 mol kg^{-1} NaCl, a mixture of UO_2CO_3 and $UO_2(CO_3)_3^{4-}$ can be found, with $UO_2(CO_3)_3^{4-}$ becoming the sole U(VI) species in evidence at pH_c 8.5, as evidenced by the increase in lifetime with increasing pH_c. No evidence for $(UO_2)_2(CO_3)(OH)_3^-$ could be found in this experiment.

7.2.2 Sorption kinetics

To verify that the chosen sorption time of 5 to 7 days is sufficiently long, an experiment into the U(VI) sorption kinetic was conducted at pH_c 5.3 and 2 mol kg^{-1} NaCl. Sorption has reached >95 % after half an hour and within 4 hours, sorption was stable (Fig. 61).

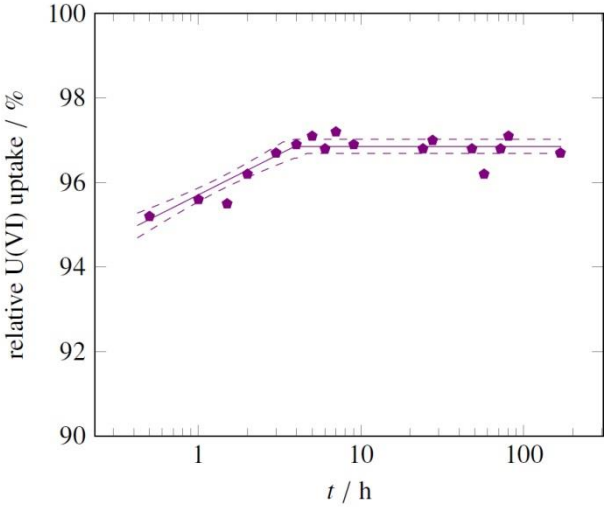

Fig. 61: U(VI) sorption kinetic in NaCl.

7.2.3 Cation exchange

In both NaCl and $CaCl_2$, cation exchange was determined at pH_c 2 to ensure that UO_2^{2+}, which is susceptible to ionic strength, was the only U(VI) species in solution (cf. Fig. 62).

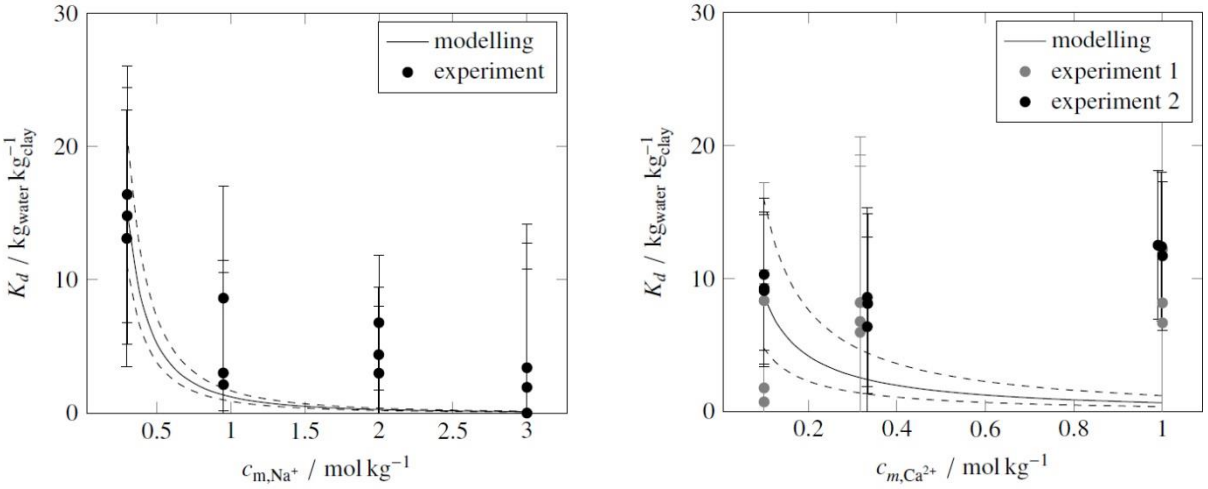

Fig. 62: Cation exchange of U(VI) in NaCl and $CaCl_2$ in dependence on ionic strength.

In NaCl, a logarithmic cation exchange coefficient for the exchange of UO_2^{2+} against Na^+ of 0.55 ± 0.14 was determined, which is within the expected range for divalent cations. In $CaCl_2$, the logarithmic coefficient for the exchange of UO_2^{2+} against Ca^{2+} was found to be 0.33 ± 0.23, which is higher than expected for an exchange of one divalent cation exchange against another divalent cation. However, a second experiment confirmed this value.

Due to measurement constraints, the selectivity coefficients have broad error margins, but at high ionic strengths cation exchange does not exert a great influence, therefore the selectivity coefficients were deemed usable.

7.2.4 Sorption in dependence on pH value and ionic strength

U(VI) sorption on montmorillonite shows a marked dependence on pH and CO_2 presence (cf. Fig. 63 and Fig. 64). In absence of CO_2, the sorption curves in NaCl and $CaCl_2$ look similar, with U(VI) sorption in $CaCl_2$ being 0.5 to 1 log K_d units lower than in NaCl. The maximum U(VI) uptake in NaCl is >99.5 %, while in $CaCl_2$ it is >98.5 %.

In both systems, a small influence of ionic strength below pH_c 5 can be observed, which is caused by the ionic strength dependence of cation exchange. In NaCl, the U(VI) uptake is significantly higher for I > 1 mol kg^{-1} than for lower ionic strengths at the sorption maximum both in absence and presence of CO_2. At pH_c 9 and 10 however, no difference in U(VI) sorption can be observed for the different ionic strengths. Larger error margins in the sorption values in the $CaCl_2$ do not make a similar conclusion possible.

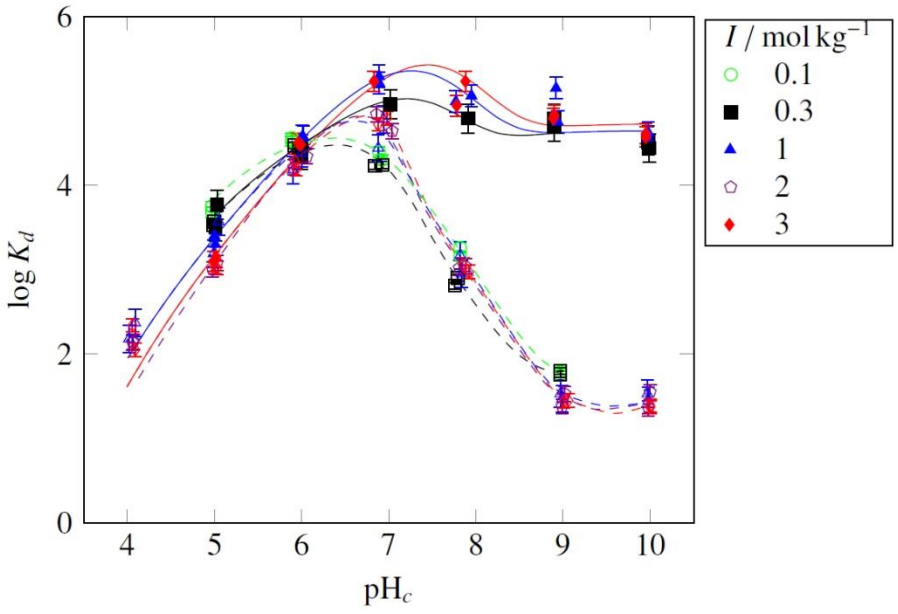

Fig. 63: U(VI) sorption in NaCl in dependence on pH and ionic strength in absence (closed symbols) and presence (open symbols) of CO_2.

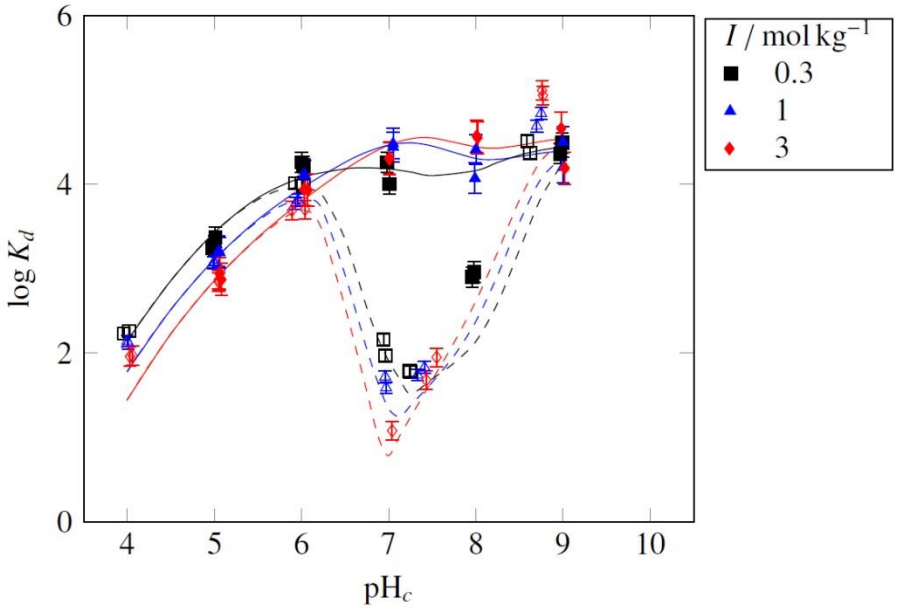

Fig. 64: U(VI) sorption in $CaCl_2$ in dependence on pH and ionic strength in absence (closed symbols) and presence (open symbols) of CO_2. (Data points at pH_c 8 at I = 0.3 mol kg^{-1} were excluded from the fit due to carbonate content in the sample. Carbonate concentration could not be determined experimentally but was modeled to 2.1×10^{-5} mol kg^{-1}.)

Additionally to the experiments in dependence on pH, U(VI) sorption isotherms at pH_c 5.3 and at an ionic strength of 2 mol kg^{-1} have been produced (cf. Fig. 65). These have been fitted with the linearized Freundlich equation.

$$\log a_{eq} = n_F \times \log c_{m,eq} + \log k_F \qquad (7.8)$$

The U(VI) sorption isotherm in NaCl was fitted to log k_F = 1.51 ± 0.14 and n_F = 0.709 ± 0.018, while the U(VI) sorption isotherm in $CaCl_2$ was fitted to log k_F = 1.56 ± 0.13 and n_F = 0.748 ± 0.017.

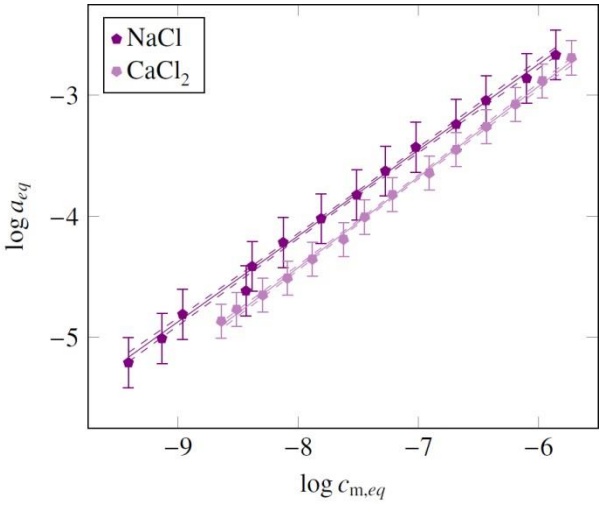

Fig. 65: U(VI) sorption isotherm at I = 2 mol kg^{-1} and pH 5.3.

In the U(VI) sorption experiments in dependence on pH and ionic strength in pure $MgCl_2$, U(VI) uptake was governed by (co-)precipitation with magnesium and silicon compounds of low solubility. The apparent log K_d values in this system averaged at 3.5 ± 1 for pH_c 5.5 to 9 (cf. Fig. 66).

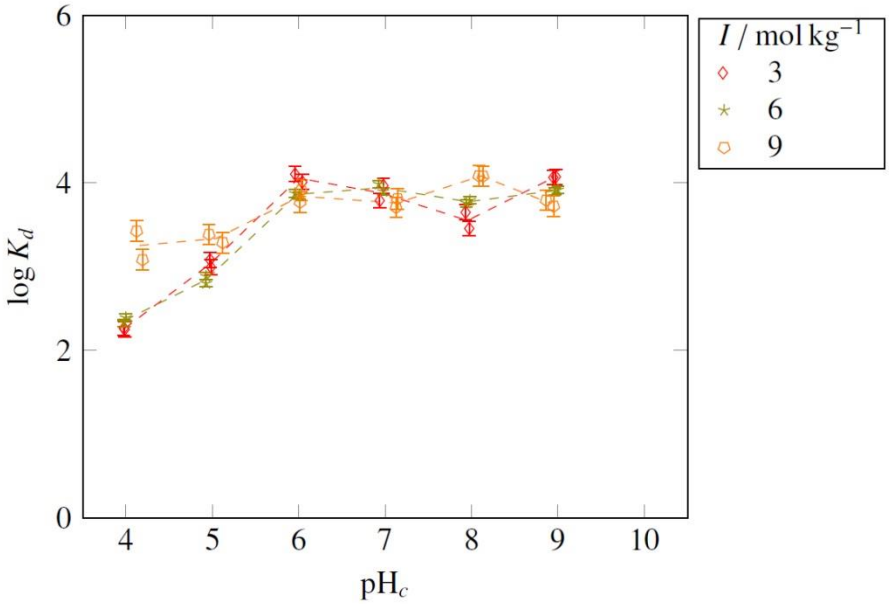

Fig. 66: U(VI) sorption on montmorillonite in $MgCl_2$ in presence of CO_2. Points connected for clarity.

TRLFS spectra of sorption samples showed a signal noise ratio that prevented interpretation.

7.2.5 ATR FT-IR measurements

Fig. 67 (left) illustrates the course of an ATR FT-IR *in situ* sorption experiment at a total U(VI) concentration of 20 µM at an ionic strength of 3 M NaCl and pH 6.8 in D_2O in N_2 atmosphere. The spectrum referred to as “Conditioning” reflects the equilibrium state of the montmorillonite mineral film after flushing it with the blank solution for 60 minutes (Fig. 67, left, lower red trace). Small absorption changes are observed in the spectral region from 1150 to 1000 cm^{-1} most likely attributed to vibrational modes of the mineral. The bands possibly result from a slight instability of the clay film, presumably due to out-flushing of some few clay platelets. The pattern is observed similarly during the whole experiment. The transmission spectra taken from the dried film before and after the experiment (not shown) confirms only very small deviations in band intensities, indicating that wash-out must be insignificant low.

The ATR FT-IR difference spectra calculated from the spectra recorded at the end of the conditioning step and after 5, 10, 15, 30, 60 and 120 minutes of the induction of U(VI) sorption are denoted as “Sorption” spectra in Fig. 67 (left, middle black traces). Clearly, a broad positive band is observed around 900 cm^{-1}, corresponding to the ν_3 antisymmetric stretching mode of the uranyl cation. The time-resolved spectra are characterized by an increasing band amplitude reflecting U(VI) accumulation on the mineral’s surface with ongoing sorption time. The free uranyl cation in solution shows an absorption band of the ν_3 mode at 961 cm^{-1}

(Quilès and Burneau, 2000). Upon complexation in solution, e.g. with inorganic ions or at mineral-water interfaces, the v_3 mode shifts to lower wavenumbers because of a decrease of the U=O force constant. Under the conditions chosen for this experiment, $(UO_2)_3(OH)_5^+$ is predicted to be the dominant uranyl species in solution (see section 7.2.1), characterized by an absorption band at 923 cm^{-1} (Quilès and Burneau, 2000). At a reduced total U(VI) concentration of 20 µM recently the formation of a monomeric species was proposed with a very similar spectral response of v_3 at 922 cm^{-1} (Müller, 2008). During the U(VI) sorption process onto montmorillonite, a very broad band of v_3 emerges with a maximum at 910 cm^{-1} and a distinct shoulder at 900 cm^{-1} possibly indicating the presence of more than one surface species. The shift of more than 10 cm^{-1} in comparison to the predicted species in solution points to the formation of an inner-sphere uranyl species on the montmorillonite surface. The *in situ* vibrational data of U(VI) sorbed onto other oxides of Al and Ti serves as references showing similar shifts of the v_3 mode under identical U(VI) concentrations (Müller et al., 2012, 2013). A coordination of the actinyl ion by physisorption (electrostatic attraction) is not expected to shift the absorption frequency to such an extent (Lefèvre, 2004).

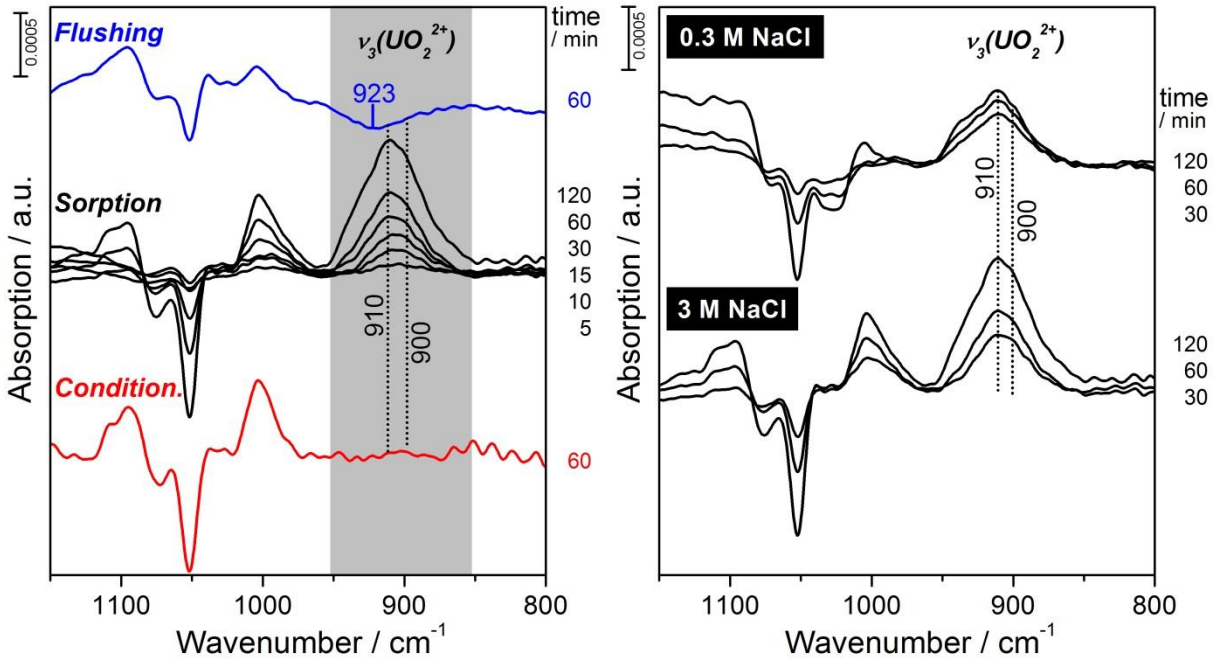

Fig. 67: ATR FT-IR study of U(VI) sorption on montmorillonite at the sorption maximum in absence of CO_2 in D_2O ($c_{U(VI)}$ = 2×10^{-5} mol kg^{-1}, pH 6.8). Left picture: *in situ* spectra in 3 M NaCl. Right picture: comparison of U(VI) uptake in 0.3 and 3 M NaCl.

Subsequent to sorption, “Flushing” of the montmorillonite film with blank solution was performed in order to potentially provide information on surface species, which can be easily removed. The difference spectrum, shown in Fig. 67 (left, upper blue trace) was calculated from the spectra recorded at the end of the sorption step and after 60 minutes of flushing. No further changes in the spectra are observed after prolonged flushing. The absence of a negative band of v_3 around 910 cm^{-1} indicates that none of the sorbed species are easily removed by flushing the mineral with the blank solution and therefore strengthens the assumption of the formation of an inner-sphere sorption complex. The tentatively labeled very small nega-

tive band located at 923 cm^{-1} can be explained by flushing of remaining aqueous complexes from the pores of the mineral film.

In order to check the impact of ionic strength on the U(VI) sorption complex the experiment was repeated using 0.3 M NaCl in solutions of conditioning and sorption. A comparison of the calculated ATR FT-IR difference spectra of the sorption stage is shown in Fig. 67 (right). The spectral signal seems to be identical, indicating the formation of equal sorption complexes. However, the intensity of the v_3 related band at 910 cm^{-1} is found to be slightly higher at increased ionic strength, confirming the findings from batch sorption studies.

Experiments in 3 M NaCl in presence of CO_2 and in 1 M $CaCl_2$ showed a signal-noise ratio that prevented meaningful interpretation of the spectra.

7.2.6 Surface complexation modeling

The 2SPNE SC/CE model uses up to 10 parameters to describe U(VI) sorption on clays - cation exchange, 4 surface complexes on strong sorption sites in absence of CO_2, 2 surface complexes on weak sorption sites in absence of CO_2 and, in presence of CO_2, three further sorption complexes that contain carbonate, one of which is bound at a weak sorption site (Marques Fernandez et al., 2012). To render the calculations for the surface complexation model more robust, a reduction of the numbers of parameters was attempted in this work.

Exemplary for the total ionic strength range studied, the modeling of the U(VI) sorption on montmorillonite is shown for 3 mol kg^{-1} NaCl and $CaCl_2$ in Fig. 68 and Fig. 69, respectively. At pH_c 4, innersphere sorption is already the dominant sorption mechanism in both systems. The $\equiv S^SOUO_2^+$ surface complex (k1 in Fig. 68 and Fig. 69) is the predominant sorption complex until pH_c 5.5. In absence of CO_2, the sorption maximum around pH_c 7, $\equiv S^SOUO_2OH$ (k2) contributes most to the overall U(VI) uptake in both systems. Above pH_c 8, sorption is determined by the $\equiv S^SOUO_2(OH)_3^{2-}$ (k3) surface complex. In contrast to Bradbury and Baeyens (2005), neither $\equiv S^SOUO_2(OH)_2^-$ nor any U(VI) surface complexes on weak sites could be fitted to the experimental data, as these would have greatly increased the error margins of the fit or rendered the parameter estimation calculations unstable.

In presence of CO_2, marked differences between the NaCl and $CaCl_2$ systems are apparent. In the NaCl system, U(VI) speciation above pH_c 6.5 is dominated by uranyl carbonate complexes. Therefore, U(VI) sorption in NaCl in presence of CO_2 decreases above pH_c 7. $\equiv S^SOUO_2(CO_3)_2^{3-}$ (k4) is the predominant U(VI) sorption complex in the alkaline pH range until pH_c 9. To be able to describe U(VI) sorption until pH_c 10, the $\equiv S^SOUO_2(CO_3)_3^{5-}$ surface complex (k5) was added to the model, as proposed by Bachmaf and Merkel (2011). This addition widens the error margins of the overall sorption curve; this could be rectified by the inclusion of experimental data points above pH_c 10. In contrast to Marques Fernandes et al. (2012), no changes to the uranyl carbonate complexation constants in Guillaumont et al. (2003) was necessary to achieve a better fit between experimental data and model for U(VI) in presence of CO_2. Similar to the modeling performed in absence of CO_2, no surface complexes on weak surface sites were included in the calculations.

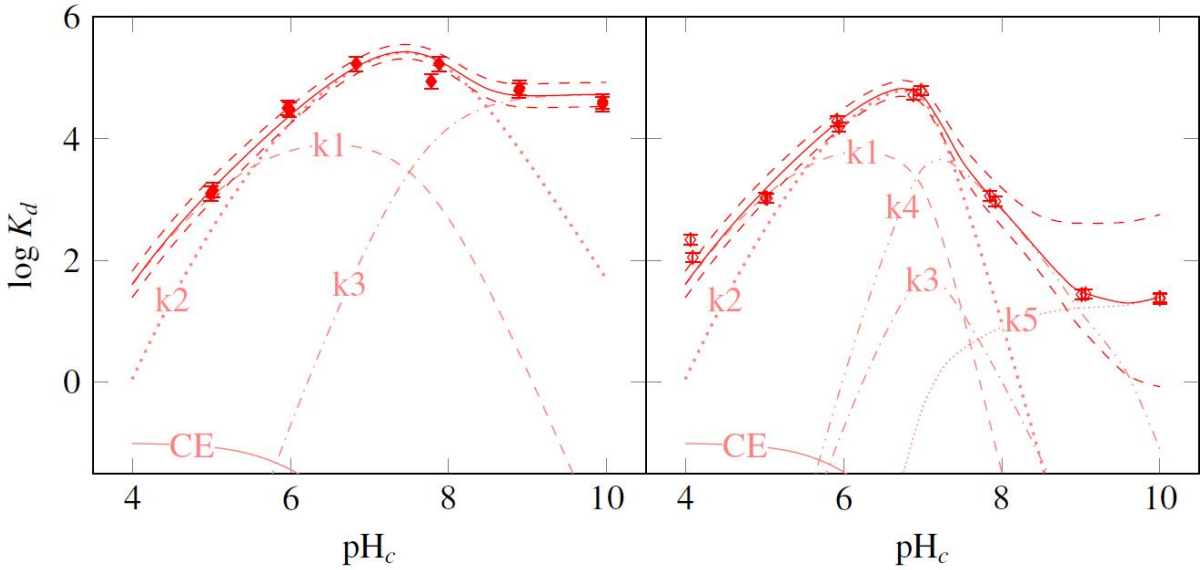

Fig. 68: U(VI) sorption in 3 mol kg^{-1} NaCl in absence (left) and presence (right) of CO_2 with contribution of U(VI) surface complexes to overall sorption.

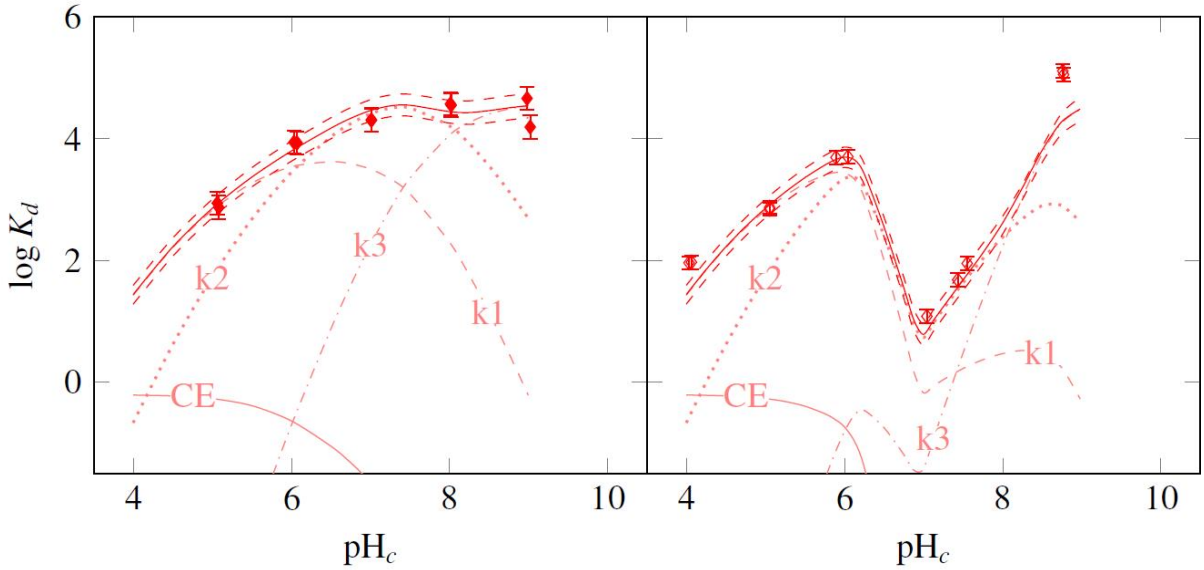

Fig. 69: U(VI) sorption in 3 mol kg^{-1} $CaCl_2$ in absence (left) and presence (right) of CO_2 with contribution of U(VI) surface complexes to overall sorption.

In the $CaCl_2$ system, a steep decrease in sorption can be observed above pH$_c$ 6. The $Ca_2UO_2(CO_3)_3$(aq) complex dominates the U(VI) speciation from pH$_c$ 6.5 to 8.5, which greatly reduces U(VI) sorption as compared to the NaCl system. Above pH$_c$ 7 however, a decrease in carbonate content in solution due to $CaCO_3$ precipitation is responsible for the dominance of uranyl hydroxides in solution at this point. Therefore, after a sorption minimum at pH$_c$ 7, U(VI) uptake increases again. At ionic strengths of 0.3 and 1 mol kg^{-1}, $\equiv S^SOUO_2(CO_3)_2^{3-}$ contributes to the overall U(VI) uptake, while at an ionic strength of 3 mol kg^{-1} no uranyl carbonate complex could be modeled to the experimental data. Data points at pH$_c$ 9 were excluded from the modeling, as they show an increased sorption as compared to the sorption

curves in $CaCl_2$ in absence of CO_2. Due to the high salt content in the samples, no experimental determination of a reason for this behavior was possible, however it is likely that either coprecipitation with $CaCO_3$ or the formation of U(VI) precipitates play a role.

In fact, in $CaCl_2$ a dependence on pre-equilibration time could be observed. A sample series with a pre-equilibration time of 1.5 weeks had a U(VI) uptake that in the acidic pH range was one order or magnitude higher than for the sample series that was pre-equilibrated for 4.5 weeks. Furthermore, the sample series with the shorter pre-equilibration time showed a marked difference in U(VI) uptake between the different ionic strengths in the alkaline pH range, with U(VI) uptake increasing with ionic strength (see Fig. 70). In NaCl however, sample series could be replicated regardless of differences in contact time between clay and electrolyte. Furthermore, there are no interaction parameters between uranyl carbonates and Ca^{2+} tabulated. Modeling of U(VI) interaction with montmorillonite in $CaCl_2$ in presence of CO_2 is therefore less accurate than in NaCl because of the assumption that these interactions are small enough to be ignored for the calculation.

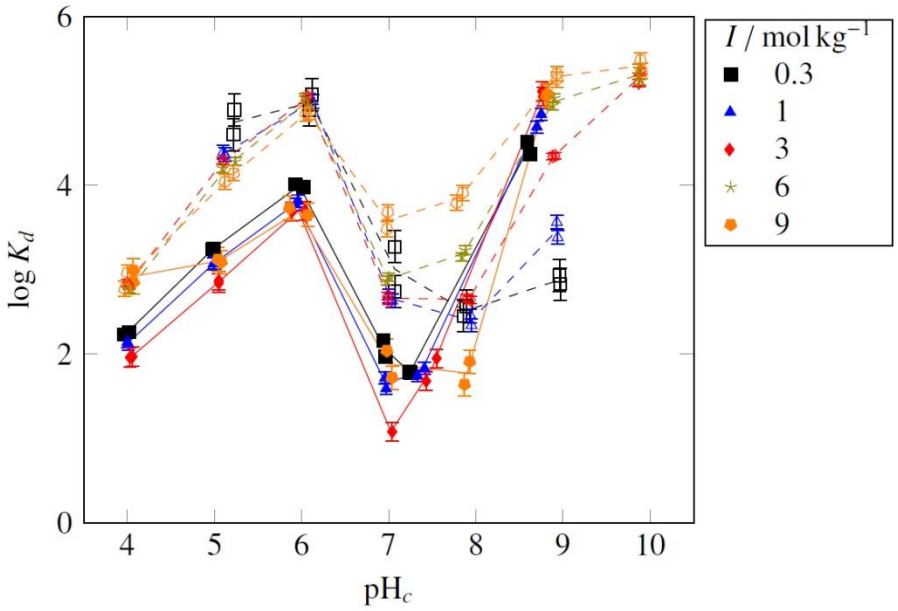

Fig. 70: U(VI) sorption in $CaCl_2$ in presence of CO_2. Open symbols: Pre-equilibration time 1.5 weeks, closed symbols: 4.5 weeks. Points connected for clarity.

7.2.7 Extrapolation to zero ionic strength

The batch sorption experiments, performed in NaCl and $CaCl_2$, yielded surface complexation constants in dependence on ionic strength (Fig. 71). These were extrapolated to zero ionic strength with the SIT approach. For the extrapolation to zero ionic strength, the log *k* values derived in the ionic strength-dependent surface complexation calculations are plotted against ionic strength. Except for log k^0, all parameters are known.

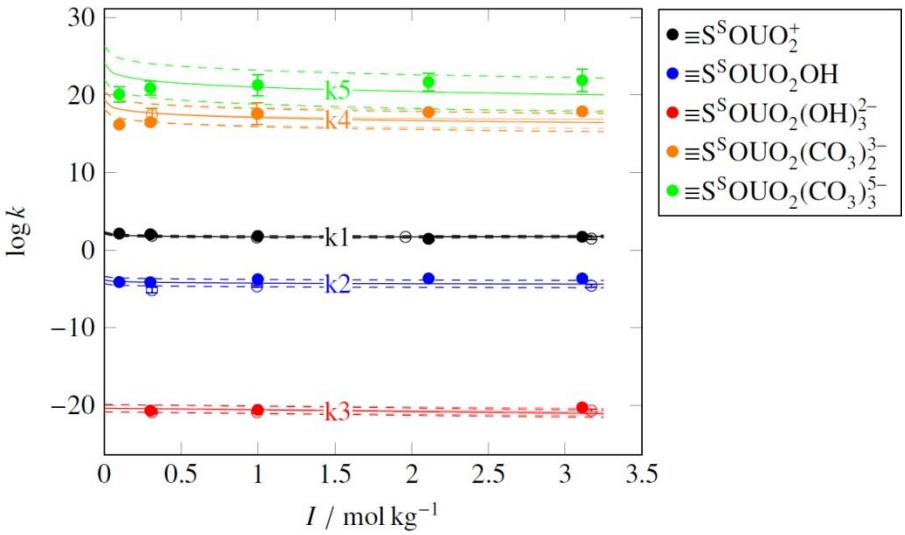

Fig. 71: Extrapolation of surface complexation constants in NaCl and $CaCl_2$ to I = 0. Closed symbols: log k in NaCl, open symbols: log k in $CaCl_2$.

The surface complexation constants for NaCl and $CaCl_2$ were at first extrapolated separately, however statistical analysis showed that with 95 % confidence they belong to the same population. Therefore, they were extrapolated to a single log k^0, valid for U(VI) sorption in both NaCl and $CaCl_2$. Table 15 shows the resulting values for log k^0 for each surface complex.

Table 15: Surface complexation constants in NaCl and $CaCl_2$ at I = 0.

	Surface complex	log k^0
k1	$\equiv S^SOUO_2^+$	2.24 ± 0.13
k2	$\equiv S^SOUO_2OH$	-3.84 ± 0.47
k3	$\equiv S^SOUO_2(OH)_3^{2-}$	-20.4 ± 0.5
k4	$\equiv S^SOUO_2(CO_3)_2^{3-}$	19.4 ± 1.2
k5	$\equiv S^SOUO_2(CO_3)_3^{5-}$	24.2 ± 2.2

7.3 Mixed electrolyte

To investigate the interactions of U(VI) with montmorillonite in an electrolyte that is closer to the composition of natural groundwater, a mixed electrolyte was employed. This electrolyte consists of 2.52 mol kg^{-1} NaCl, 0.12 mol kg^{-1} $CaCl_2$ and 0.048 mol kg^{-1} $MgCl_2$. The composition of this electrolyte was derived from the groundwater composition in the Konrad mine in Lower Saxony in a depth of 480 m, for which measurements that were taken over the space of twenty years can be found in Brewitz (1982).

7.3.1 U(VI) speciation in mixed electrolyte

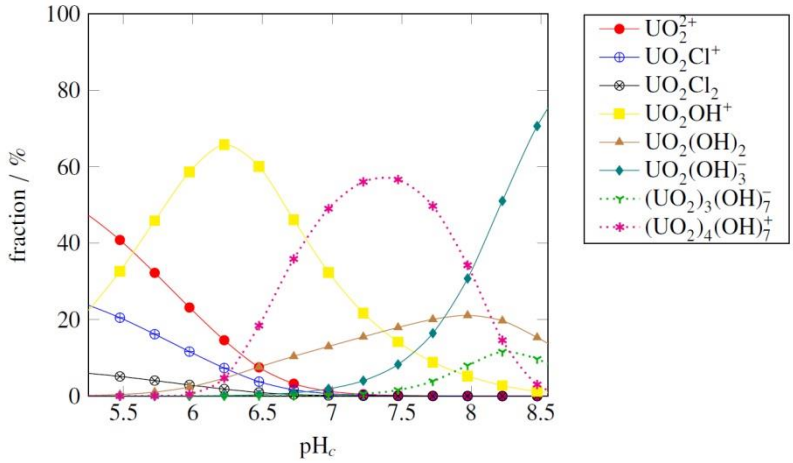

Fig. 72: Calculated U(VI) speciation in mixed electrolyte in absence of CO_2 ($c_{U(VI)}$ = 1×10^{-6} mol kg^{-1}).

As shown in Fig. 72, U(VI) speciation in the mixed electrolyte at pH_c 5.3 is dominated by the free uranyl cation with a contribution of almost 50 %. Additionally, UO_2OH^+ and UO_2Cl^+ each contribute with slightly over 20 % to the U(VI) speciation. At pH_c 6.5, half the U(VI) is found in form of UO_2OH^+, with $(UO_2)_4(OH)_7^+$ contributing just under 20 % to the U(VI) speciation. At pH_c 8.5, the largest fraction of U(VI) with about 75 % is found in the $UO_2(OH)_3^-$ complex.

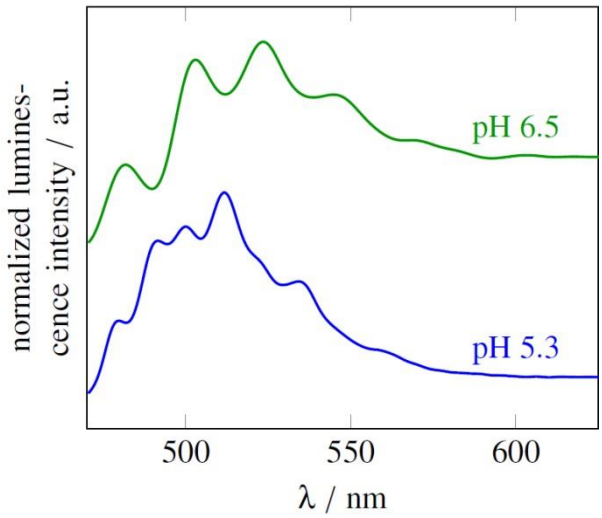

Fig. 73: TRLFS spectra of U(VI) ($c_{m,U(VI)}$ = 1×10^{-6} mol kg^{-1}) in mixed electrolyte in depedence on pH in absence of CO_2.

TRLFS measurements in the mixed electrolyte at $c_{m,U(VI)}$ = 1×10^{-6} mol kg^{-1} show that at pH_c 5.3 there is evidence for the formation of uranyl chloro species in solution (Fig. 73, Table 16). At pH_c 6.5, uranyl hydroxide is the dominant U(VI) complex, in good accordance with the calculated U(VI) speciation in solution. Measurements at pH_c 8.5 were not successful.

Table 16: Luminescence properties of the spectra measured in mixed electrolyte.

pH	Species	Emission bands / nm (±0.5 nm)				τ / µs	T / K
5.3	UO_2Cl_x species	489.9	500.0	511.7	535.7	338 ± 12	153
6.5	UO_2OH^+	---	501.5	523.2	547.3	43 ± 19	153

7.3.2 Sorption in dependence on U(VI) concentration and pH value

Three U(VI) sorption isotherms at 23°C and at pH_c 5.3, 6.5 and 8.5 have been determined as well as one isotherm at a temperature of 60°C at pH_c 6.5. Additionally, one series of U(VI) sorption samples at pH_c 5.3, 6.5 and 8.5 with $c_{m,U(VI),ini}$ = 1×10^{-6} mol kg^{-1} and furthermore, one experiment that compared U(VI) uptake on different clay minerals under the same experimental conditions. All experiments in the mixed electrolyte were performed in absence of CO_2.

The sorption isotherms were fitted with the linearized Freundlich isotherm (see Fig. 74 and Table 17).

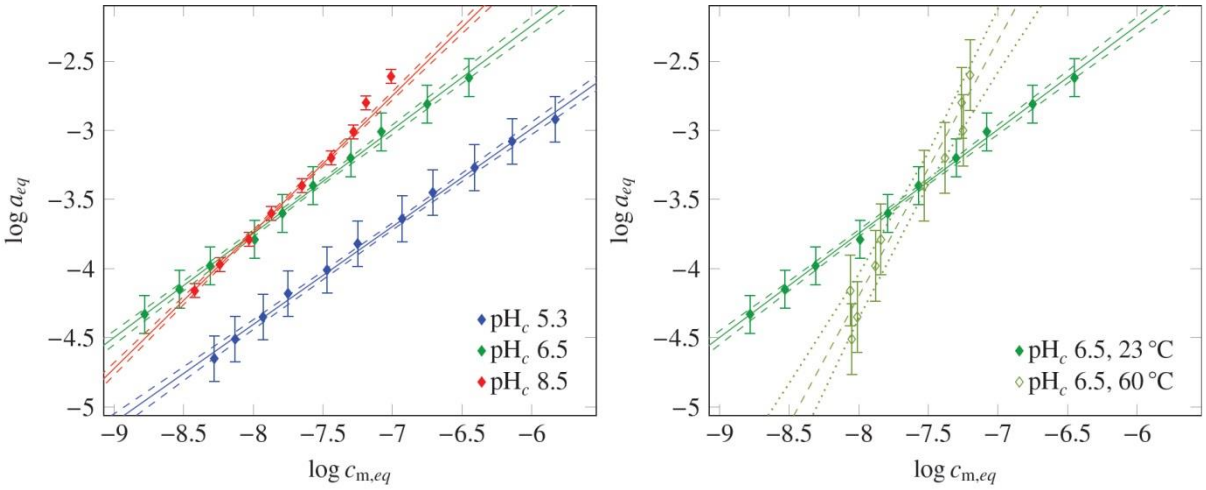

Fig. 74: U(VI) sorption isotherms in mixed electrolyte in absence of CO_2.

Table 17: Freundlich coefficients of U(VI) sorption isotherms in mixed electrolytes.

Isotherm	log k_F	n_F
pH_c 5.3, 25°C	1.26 ± 0.23	0.708 ± 0.031
pH_c 6.5, 25°C	2.27 ± 0.25	0.752 ± 0.032
pH_c 8.5, 25°C	4.16 ± 0.25	0.987 ± 0.031
pH_c 6.5, 60°C	10.6 ± 2.4	1.85 ± 0.31

The U(VI) uptake at pH_c 5.3 is slightly lower but shows otherwise the same characteristics as the isotherm in pure NaCl. U(VI) sorption at pH_c 6.5 and 8.5 is considerably higher. For the two highest initial U(VI) concentrations, 1×10^{-5} mol kg^{-1} and 6.3×10^{-6} mol kg^{-1}, at pH_c 8.5, a U(VI) uptake that lies above the level predicted by the Freundlich isotherm is observed. Thermodynamic calculations show that it is likely that U(VI) precipitates begin to form at this point. The comparison between U(VI) uptake at 60°C and 23°C shows a strong contrast. The slope of the sorption isotherm is much steeper at 60°C. At an initial U(VI) concentration of 1.6×10^{-6} mol kg^{-1}, data points in both sample series show a practically identical log K_d value, however, above and below this concentration, the amount of U(VI) sorbed at the different temperatures quickly diverges. This means that at U(VI) equilibrium concentrations in solution below 2.6×10^{-8} mol kg^{-1}, sorption is considerably higher at 25°C than at 60°C, while above this equilibrium concentration, U(VI) uptake at 60°C is increased over U(VI) uptake at 25°C.

A comparison between U(VI) sorption on different clay minerals as well as a comparison of U(VI) sorption on montmorillonite in different experimental setups at pH_c 6.5 shows no significant differences between the samples (see Fig. 75).

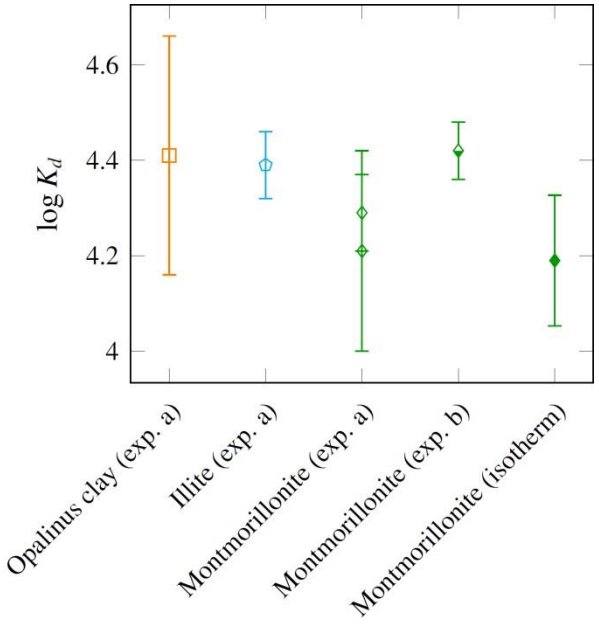

Fig. 75: Comparison of U(VI) sorption on different minerals in mixed electrolyte at 23°C and pH_c 6.5 in absence of CO_2. Experiment (a): 4 months equilibration time, experiment (b) and isotherm: 6 weeks pre-equilibration time.

The sample series with Opalinus Clay, illite and two different batches of montmorillonite, termed experiment (a) in Fig. 75, was pre-equilibrated for 4 months. It has to be noted that for pH adjustments of the Opalinus Clay samples, much greater amounts of acid than for the other samples were necessary to achieve pH_c 6.5 and small amounts of gas bubbles formed in the electrolyte solution. This points towards a dissolution of a part of the calcite content of the Opalinus Clay. Experiment (b) used the same conditions as the U(VI) sorption isotherm, however the isotherm experiments were conducted by a another operator. Differences be-

tween the results in the experiments which used montmorillonite as mineral can be attributed to differences in electrolyte concentration brought on by crystallization of salts and evaporation of water during the pH adjustments.

7.3.3 Surface complexation modeling

For surface complexation modeling in the mixed electrolytes, two approaches were used: The direct fit of surface complexation constants on the experimental data and the calculation of sorption curves with the data that were derived in the pure electrolytes as described in sections 7.2.6 and 7.2.7. For the latter approach, the log k^0 values were used to calculate theoretical surface complexation constants that correspond to the composition and ionic strength of the mixed electrolyte.

The first approach of a direct fit to generate surface complexation constants for the mixed electrolyte system gave the surface complexation constants in the middle column in Table 18.

Table 18: Surface complexation constants for modeling U(VI) sorption isotherms in the mixed electrolyte.

Surface complex	log *k* (fit)	log *k* (calculated)
$\equiv S^S OUO_2^+$	1.70 ± 0.06	1.75 ± 0.13
$\equiv S^S OUO_2OH$	-4.48 ± 0.10	-4.37 ± 0.47
$\equiv S^S OUO_2(OH)_3^{2-}$	-20.8 ± 0.1	-21.0 ± 0.5

According to the surface complexation calculations, at pH_c 5.3 $\equiv S^S OUO_2^+$ is the dominant complex with a fraction of 92 %. $\equiv S^S OUO_2OH$ accounts for 8 % of the U(VI) uptake, while $\equiv S^S OUO_2(OH)_3^{2-}$ plays no role at this pH value. At pH_c 6.5, 55 % of U(VI) is found in the form of $\equiv S^S OUO_2OH$, while $\equiv S^S OUO_2^+$ binds 45 % of the uranium present. At pH_c 8.5, most uranium is found in the $\equiv S^S OUO_2(OH)_3^{2-}$ complex (65 %), with $\equiv S^S OUO_2OH$ making up the remaining 35 %.

This approach generates a fit for the data that is very precise. However, as mentioned in the discussion of the Freundlich fit, it is likely that the formation of precipitates plays a role in the uptake of uranium from the solution. The sample series at pH_c 8.5 has a silicon content in solution of on average 3×10^{-5} mol kg^{-1}, while the average silicon content in a leaching series in a NaCl solution of the same ionic strength lies about one order of magnitude higher. The surface complexation modeling as presented in Fig. 76 was done without the inclusion of any precipitates including U(VI) as it is likely that after one week of U(VI) being in contact with the clay and the solution the system is not yet in thermodynamic equilibrium with any U(VI) precipitates.

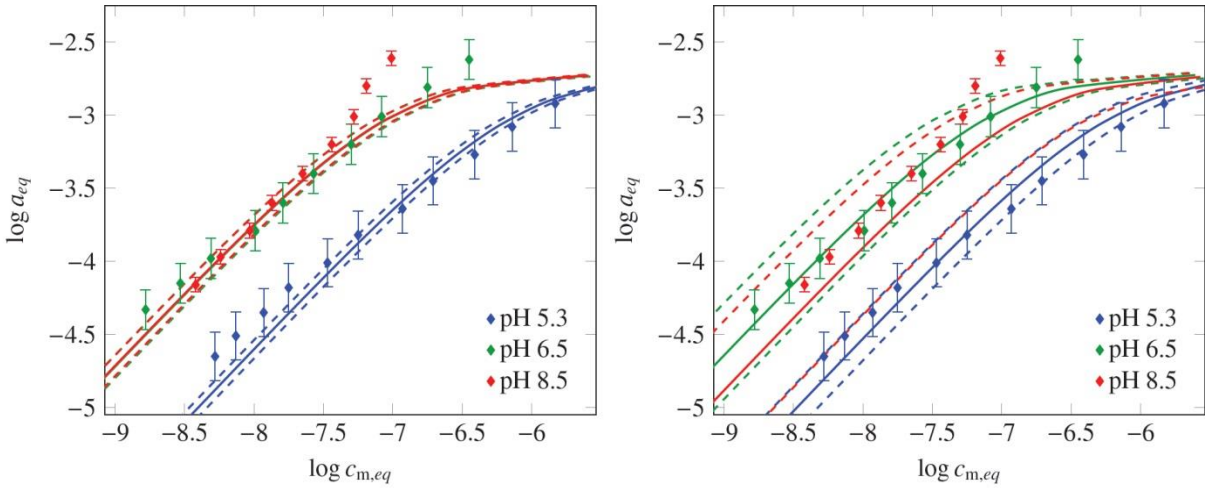

Fig. 76: Surface complexation modeling of U(VI) sorption isotherms in mixed electrolyte (absence of CO_2). Left picture: Fit on isotherm data. Right picture: Use of surface complexation constants generated in pure electrolytes and calculated to composition and ionic strength of the mixed electrolyte.

To check the applicability of the surface complexation constants derived in section 7.2 to mixtures of different electrolytes, the log k^0 values derived in section 7.2.7 were used to calculate log k values for the composition and ionic strength of the mixed electrolyte (see third column Table 18). These were then used to calculate U(VI) sorption isotherms, as pictured in Fig. 76 (right picture). The calculated sorption isotherms for pH_c 5.3 and 6.5 are accurate though they are less precise than the direct fit of the experimental data. For pH_c 5.3, the error margins of the sorption isotherm calculated from the parameters derived in the pure electrolytes are about the same size as the experimental error margins. The error margins of the sorption isotherm at pH_c 6.5 are twice the size of the experimental error. At pH_c 8.5, the discrepancy between the error margins of the calculation and the experiment is even larger and furthermore, while all experimental data lie within the error margin of the calculated isotherm, the calculated sorption isotherm slightly underestimates the actual U(VI) uptake. Nevertheless, this comparison shows that it is in fact possible to use surface complexation constants derived in single electrolytes to describe U(VI) sorption in a mixed electrolyte.

Fig. 77 plots the results of several sample series with different operators and/or experimental setups in dependence on pH_c. Due to crystallization and evaporation processes, the samples from different series showed differences in ionic strength at the conclusion of the experiments, which causes differences in U(VI) uptake. Therefore, the calculated sorption curve that was derived from the isotherm data can only be expected to fit the data from this experiment over the whole pH range. The sorption curve that was calculated from the fit in pure electrolyte was calculated for the average solution composition of all data points presented in this figure, and due to its wider error margins manages to describe all data points.

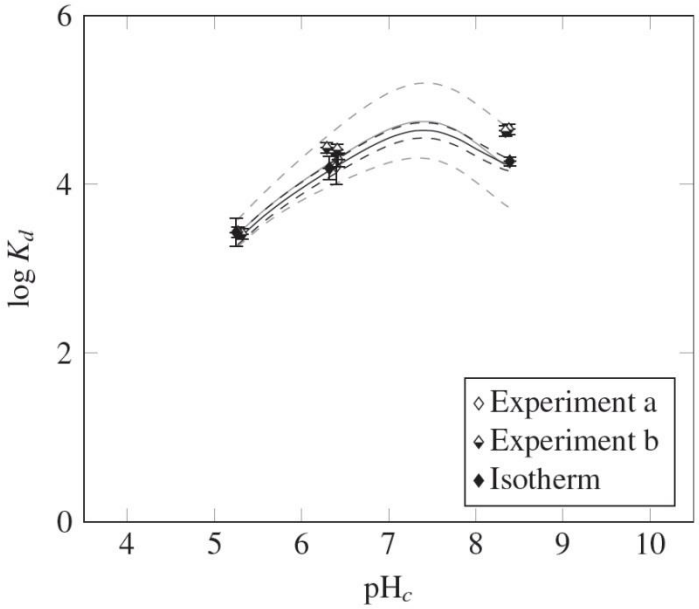

Fig. 77: Comparison of results of different U(VI) sorption experiments on montmorillonite in mixed electrolyte at $c_{U(VI)} = 1\times10^{-6}$ mol kg^{-1}. Experiment (a): 4 months equilibration time, experiment (b) and isotherm: 6 weeks pre-equilibration time. Solid line: Fit on isotherm data. Shaded line: Use of surface complexation constants generated in pure electrolyte and calculated to average ionic strength and composition of the mixed electrolyte after the end of the experiments.

7.4 Conclusions

It can be concluded that at environmentally relevant pH values, ionic strength does not exert an adverse influence in the conditions investigated. In absence of CO_2, U(VI) uptake is consistently above 95 % for $pH_c > 6$ in all investigated systems. In presence of CO_2, a reduction of U(VI) uptake occurs in the alkaline pH range, and in presence of calcium ions, U(VI) will be mobilized due to formation of the $Ca_2UO_2(CO_3)_3$(aq) complex. Whether an elevated temperature leads to an increase or a decrease of U(VI) uptake depends on the U(VI) concentration in solution, with a higher uptake promoted by higher U(VI) concentrations.

The 2SPNE SC/CE model was successfully applied to high ionic strengths. A decrease in the number of parameters led to a more robust surface complexation calculation. The surface complexation constants that were generated at different ionic strengths were extrapolated for a common log k^0 for both the NaCl and $CaCl_2$ systems. These values were then successfully used to calculate sorption isotherms in a mixed electrolyte that consists of the main ions found in groundwaters in North Germany.

8 Diffusion of U(VI) in Opalinus Clay in the absence and presence of citric acid

Uranium represents the main mass fraction of spent nuclear fuel planned to be stored in high-level nuclear waste repositories in deep geologic formations. It represents a serious radiotoxic and chemotoxic hazard (Bleise et al., 2003). Current performance assessment models predict the waste container rupture and release of radionuclides after 10^5 years (Jové Colón et al., 2014). Under present repository conditions, the initial stored immobile U(IV)O_2 will be partly oxidized to more mobile U(VI) species (Thoenen, 2014).

After passing barriers such as the waste container and the backfill material, U(VI) will interact with the repository host rock. Opalinus Clay (OPA) is one representative clay host rock internationally investigated (Nagra, 2002). Due to its high density and low porosity the migration of waste-released radionuclides, such as uranium, through this clay rock, is governed by molecular diffusion. Wu et al. (2009) investigated the diffusion and sorption of Np(V) in/onto OPA and Bauer et al. (2006) the Pu diffusion in OPA. Recently, the U(VI) diffusion in OPA and the influence of humic acid and elevated temperature on it was reported by Joseph et al. (2013b). No significant effect of humic acid and a temperature of 60°C on the diffusion parameter values of the dominating aqueous U(VI) species, $Ca_2UO_2(CO_3)_3(aq)$, was found. However, a change of U(VI) speciation was observed at elevated temperature resulting in the partly formation of particles. For the Np(V) diffusion in OPA only a slight influence of humic acid was detected by Fröhlich et al. (2013).

Notably, the nuclear waste contains a substantial amount of organic compounds (IAEA, 2004). One low molecular weight representative used for decontamination is citric acid. In the past, its complexation behavior with U(IV) and U(VI) was thoroughly studied in inert background electrolytes as summarized in Hummel et al. (2005). Under repository conditions, water with much more complex composition will be present (e.g., OPA pore water). This can significantly influence the uranium speciation. Recent studies were focused on the investigation of the U(VI) complexation with citric acid in the presence of calcium ions (Steudtner et al., 2012). At pH 6, the formation of a new species, $Ca(UO_2)_2(cit)_2(aq)$, is described. Furthermore, Steudtner (2010) investigated the uranium / citric acid system in the absence and presence of light under aerobic and anaerobic conditions. He showed that the system acts very light-sensitive, citric acid is able to reduce U(VI) to U(IV).

The influence of citric acid on the U(VI) sorption onto OPA was studied by Schmeide and Joseph (2012) among other organic ligands. Due to the formation of U(VI)-citric acid complexes in solution the U(VI) sorption to OPA decreases with increasing citric acid concentration. The sorption and diffusion of organic acids, in particular, EDTA, isosaccharinate, phthalate, and oxalic acid, with Callovo-Oxfordian Clay was investigated by Dagnelie et al. (2014). They obtained diffusion coefficients which are lower than values for tritiated water (HTO) diffusion but in the same order of magnitude as anions (Cl^-, I^-, SO_4^{2-}). The organic acids showed a higher affinity towards the clay rock than usual anions. Diffusion studies with small organic compounds were performed by Wu et al. (2015). They observed that EDTA, oxalic acid and hydrazine have no influence on ^{125}I diffusion in bentonite. Staunton et al. (1990) studied the

Np(V) sorption and diffusion with montmorillonite, kaolinite, and illite as a function of background electrolyte and organic ligand (EDTA, citrate, and humic acid). They found that the diffusion coefficients are higher in Na-conditioned clays than in Ca-conditioned clays. The addition of small organic ligands, such as EDTA and citrate, leads to a decrease of the diffusion coefficient in the case of montmorillonite but an increase in the case of kaolinite.

In the present work, the diffusion of HTO, ^{233}U(VI), and citric acid in OPA was investigated under anaerobic conditions under exclusion of light. HTO diffusion experiments were used to determine values for the transport porosity (ε) in the clay samples. The U(VI) diffusion was studied in the absence and presence of citric acid for a duration of three months. To study the U(VI) speciation in solution as a function of time UV-vis spectroscopy was applied. The outcome of this work will be published in Joseph and Schmeide (in preparation).

8.1 Materials and methods

8.1.1 Materials

OPA bore cores from the Mont Terri underground rock laboratory in Switzerland were taken by the Federal Institute for Geosciences and Natural Resources (BGR) and stored under argon atmosphere. The preparation of the OPA bore core samples for the diffusion experiments (length: 11 mm, diameter: 25.5 mm) was performed at the Karlsruhe Institute of Technology – Institute for Nuclear Waste Disposal (KIT–INE). Thereby, only the inner part of the bore core was used for sample preparation. The mineralogy of OPA can be found elsewhere (Nagra, 2002).

Synthetic OPA pore water (pH 7.6 (Pearson, 1998); cf. Table 19) was prepared in Milli-Q water (18 MΩ; mod. Milli-RO/Milli-Q-System, Millipore, Schwalbach, Germany) and used as background electrolyte in all diffusion experiments. Its true ionic strength (I_t) of 0.36 M was calculated using the speciation code EQ3/6 (Wolery, 1992).

Table 19: Composition of OPA pore water according to Pearson (1998).

Ion	M
Na^+	2.4×10^{-1}
K^+	1.6×10^{-3}
Mg^{2+}	1.7×10^{-2}
Ca^{2+}	2.6×10^{-2}
Sr^{2+}	5.1×10^{-4}
Cl^-	3.0×10^{-1}
SO_4^{2-}	1.4×10^{-2}
CO_3^{2-}/HCO_3^-	4.8×10^{-4}
I_t [a]	0.36

To avoid bacterial growth during the diffusion experiment, 1×10^{-3} M NaN_3 (extra pure, Merck, Darmstadt, Germany) was added to the pore water.

A $^{233}U(VI)$ stock solution was used for the diffusion experiments. For that, a solution of $^{233}UO_2(NO_3)_2$ was acquired (Eckert & Ziegler, Valencia, CA, USA) and dried up. After adding the threefold molar quantity of 0.01 M $NaHCO_3$ (p.a., Merck) to form $^{233}UO_2(CO_3)_3^{4-}$ as precursor, a surplus of 0.1 M HCl (p.a., Merck) was added and $^{233}UO_2Cl_2$ was formed. The specific activity of the $^{233}U(VI)$ stock solution determined with liquid scintillation counting (LSC; mod. TriCarb 3100 TR, Perkin Elmer, Freiburg, Germany) using Ultima Gold (Perkin Elmer) as scintillation cocktail amounted to 13.4 kBq/mL (1.7×10^{-4} M $^{233}UO_2Cl_2$). For UV-vis spectroscopy a $^{238}U(VI)$ stock solution was used (0.1 M $^{238}UO_2Cl_2$). For the studies with citric acid, a mixture of unlabeled and ^{14}C-labeled citric acid (9.43×10^{-4} M; 1.85×10^{6} Bq) was prepared. For this, the unlabeled and ^{14}C-labeled citric acid were dissolved in Milli-Q water and mixed in the ratio 21000 : 1. Subsequently, the pH of the mixture was adjusted to pH 5 using 2 M NaOH (*p.a.*, Roth, Karlsruhe, Germany) which resulted in a citric acid stock solution of 0.17 M (29 kBq/mL). The solution was stored under exclusion of light.

8.1.2 Experimental set-up

The details of the diffusion cells applied in the experiments can be found in literature (Van Loon et al., 2003a). Two identical diffusion cells were conditioned at room temperature under inert gas atmosphere (N_2). Each OPA bore core sample was placed in the cells between two stainless steel filter plates (length: 1.55 mm, diameter: 25.5 mm, ε: 0.3, bulk density: 5000 kg/m^3; 316L, pore diameter: 0.01 mm; MOTT industrial division, Farmington, USA). The confining pressure on each sample was 5 MPa. The experimental set-up used for the experiments is presented in Fig. 78.

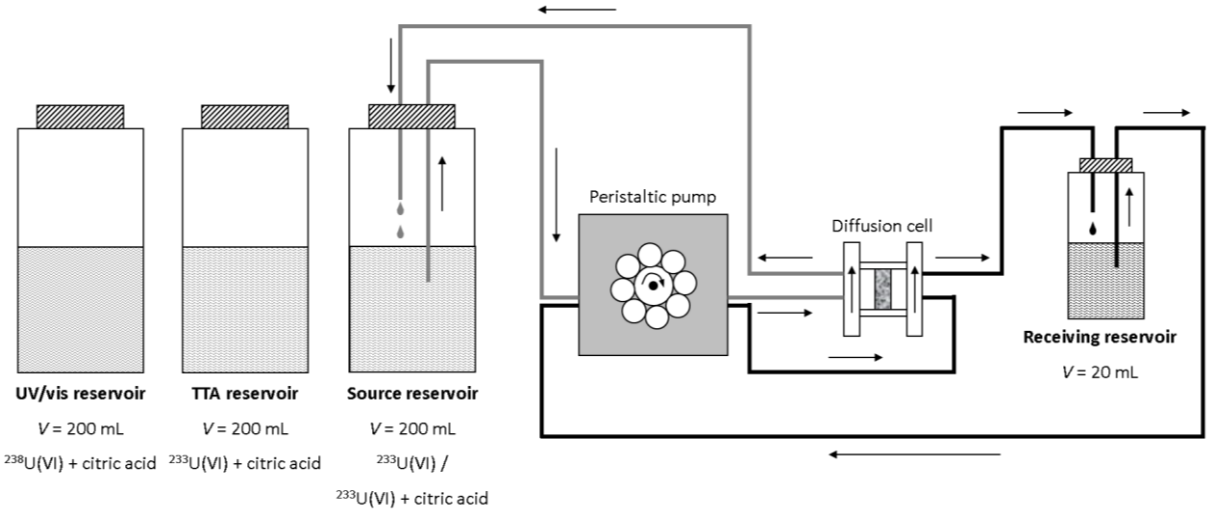

Fig. 78: Experimental set-up used to investigate the U(VI) diffusion in the absence and presence of citric acid (based on (Van Loon et al., 2003a)).

During the studies, care was taken to exclude light from the experiment. Each diffusion cell was coupled with a peristaltic pump (mod. Ecoline, Ismatec, IDEX Health & Science, Glattbrugg, Switzerland) and a source and receiving reservoir filled with 200 mL and 20 mL synthetic OPA pore water, respectively. 250 mL and 25 mL PTFE bottles (vwr collection, Darmstadt, Germany) served as reservoirs. As connection between reservoirs and cells dark-colored tubing was used (pump tubing: Fluran® F-5500-A, Saint-Gobain, Courbevoie, France; reservoir tubing: PTFE-EX, Bohlender GmbH, Grünsfeld, Germany).

The solutions circulated through the end plates of the cells in order to saturate the clay samples. The saturation time was three weeks. After this time the pressure was constant indicating that the samples were hydrostatically in equilibrium. Subsequently, the solutions were replaced by fresh ones, whereby the source reservoir contained the tracer.

At first, HTO through- and out-diffusion experiments were performed as described by Van Loon et al. (2003a) in order to determine values for the porosity (ε) of the clay samples (c_0(HTO) = 1000 Bq/mL). Subsequently, the ^{233}U(VI) in-diffusion in the absence (Cell 1) and presence of citric acid (Cell 2) was studied (c(^{233}U(VI)) = 1×10^{-6} M, c(citric acid) = 1×10^{-3} M). The pH value in the reservoirs was not adjusted, but monitored using a laboratory pH meter (mod. inoLab pH 720, WTW, Weilheim, Germany), equipped with a SenTix Mic pH microelectrode (WTW), and calibrated using standard buffers pH 7 and 9 (WTW).

Since the mixture of U(VI) and citric acid represents a light-sensitive redox system, two additional separate reservoirs, each containing 200 mL OPA pore water, were prepared to monitor possible redox reactions during the experiment. One reservoir contained 1×10^{-6} M ^{233}U(VI) and 1×10^{-3} M citric acid. Here, with respect to a possible reduction of U(VI) to U(IV) in distinct time steps an aliquot of the solution was taken and analyzed by solvent extraction using thenoyltrifluoroacetone (TTA; *p.a.*, Fluka/Sigma–Aldrich, Steinheim, Germany) according to Bertrand and Choppin (1982). The second reservoir contained 1×10^{-4} M ^{238}U(VI) and 1×10^{-3} M citric acid. Aliquots of this solution were regularly analyzed by UV-vis spectroscopy (mod. Cary 500, Varian Inc., Palo Alto, CA, USA; mod. Lambda 900, Perkin Elmer). To distinguish between the different reservoirs used in this study, the following designations were used: Cell 1, Cell 2, TTA, and UV-vis.

The redox potential of all four 200 mL reservoirs was regularly measured using a BlueLine 31 RX redox electrode (SI Analytics GmbH, Mainz, Germany). Additionally, the reservoir solutions were investigated for colloids and for the size of the colloidal particles by photon correlation spectroscopy (PCS; mod. BI-90, Brookhaven Instruments, USA). A detailed description of the instruments and the procedure is given in Dreissig et al. (2011).

After 3 months, the diffusion experiments were stopped and the clay samples were extruded from the cells. Using the abrasive peeling technique (Van Loon and Eikenberg, 2005), U(VI) and citric acid diffusion profiles were determined. The peeled layers were extracted with 1 M HNO_3 (*p.a.*, Roth). This method was already applied in former experiments (Joseph et al., 2013b; Sachs et al., 2007). The tracer concentrations in the extracts were determined by LSC.

The reservoir solutions tracered with $^{233}U(VI)$, $^{238}U(VI)$, and citric acid were analyzed for Na, K, Sr, Ba, Al, Si, Mn, and U by inductively coupled plasma – mass spectrometry (ICP-MS; mod. ELAN 9000, Perkin Elmer, Boston, USA), for Mg and Ca by atomic absorption spectroscopy (AAS; mod. AAS-4100, Perkin Elmer), and for SO_4^{2-} and Cl^- by ion chromatography (IC; mod. IC separation center 733, Metrohm, Herisau, Switzerland). The total inorganic carbon content (TIC) was determined using the multi N/C 2100 analyzer (Analytik Jena, Jena, Germany) as difference of the total carbon (TC) and the total organic carbon (TOC). Based on the TIC results, the CO_3^{2-}/HCO_3^- concentration in the reservoirs were re-adjusted to the value given in Table 19 before the start of the experiment. Fe and P were determined, too, but were always below the ICP-MS detection limit.

8.1.3 Theoretical background

All diffusing species were assumed to migrate via molecular diffusion through OPA. The theoretical background of molecular diffusion has been described previously, e.g., by Crank (1975) and Van Loon et al. (2003b). For the determination of the diffusion parameters, a one-dimensional model composed of source reservoir, filter, OPA bore core sample, filter, and receiving reservoir was applied as described by Jakob et al. (2009). The OPA sample and the filters were considered as homogeneous each with a single value for the transport porosity.

The diffusion process through a porous medium is defined by Fick's first law:

$$J = -D_e \cdot \frac{\partial c}{\partial x} \tag{8.1}$$

where J [mol/(m^2·s)] is the diffusive flux of a solute, c [mol/m^3] represents the decay corrected tracer concentration in the mobile phase, and x [m] is the spatial coordinate. The change of concentration with time, t [s], is expressed by Fick's second law:

$$\frac{\partial c}{\partial t} = D_a \cdot \frac{\partial^2 c}{\partial x^2} \tag{8.2}$$

Thereby, D_a [m^2/s] denotes the apparent diffusion coefficient. Both diffusion coefficients are linked by the rock capacity factor α [–] according to:

$$D_a = \frac{D_e}{\alpha} \tag{8.3}$$

The rock capacity factor is defined as:

$$\alpha = \varepsilon_{eff} + \rho \cdot K_d \tag{8.4}$$

where ρ [kg/m^3] is the dry bulk density and K_d [m^3/kg] the sorption distribution coefficient. For non-sorbing tracers such as HTO with K_d = 0, it is assumed that α is equal to ε_{eff}. In contrast to D_e, D_a considers the tracer sorption to the clay.

For HTO, D_e and α were determined by modeling the through-diffusion flux of HTO monitored in the receiving reservoir as a function of time. For ^{233}U(VI) and citric acid, the values for the diffusion parameters (D_e, α, ε, K_d) were determined by fitting the experimental tracer distribution profiles in the clay.

The clay samples as well as the filters were initially free of tracer. For all diffusing tracers investigated the model boundary condition for the source reservoir concentration was as follows:

$$c(x = 0, t > 0) = f_0(t) \quad (8.5)$$

For the boundary conditions of the receiving reservoir two possible descriptions were applied:

$$c(x = L, t > 0) = f_L(t) \text{ and} \quad (8.6)$$

$$c(x = L, t > 0) = 0, \quad (8.7)$$

whereby L [m] describes the thickness of the system filter/clay/filter. Condition (8.6) was only applied for tracers detected in the receiving reservoir, that means, HTO. For ^{233}U(VI) and citric acid, where no tracer breakthrough could be observed, condition (8.7) was applied. According to (Jakob et al., 2009) continuity regarding tracer flow [mol/s] at the interfaces of filters and clay was considered in the model.

All experimental results were evaluated using the commercial software COMSOL Multiphysics® 4.2a (COMSOL, 2011).

The experimental uncertainties of the values of the diffusive HTO flux and the accumulated diffused HTO activity in the receiving reservoir solution resulted from the uncertainty of the parameters required to calculate these values (cf. Van Loon and Soler (2004)). To analyze the HTO through-diffusion, the COMSOL Optimization Module was applied. A least square fit was performed using the Levenberg-Marquardt algorithm to determine best fit values for the diffusion parameters. The uncertainty of D_e and ε was estimated by fitting the upper and the lower boundaries covered by the uncertainties of the experimental fluxes.

In the case of ^{233}U(VI) and citric acid diffusion profiles, the experimental uncertainty of the diffusion depth was given by the average of the individual distance measurement at four points of the clay sample. The uncertainties of the D_e and K_d values were estimated by fitting the upper and lower boundaries of the diffusion profile. Both D_e and K_d were varied in such a way that 90 % of the experimental values were covered by the envelope curves.

8.1.4 Filter diffusion parameters

For fitting the clay diffusion parameters, the diffusion characteristics of the adjacent stainless steel filter plates for HTO, U(VI), and citric acid had to be included in the model, because they could have influenced the retardation and migration of the tracer. In the case of HTO,

the filter K_d value was assumed to be 0. The corresponding filter D_e value, D_f, was 2.3×10^{-10} m^2/s (Glaus et al., 2008).

In contrast to HTO, for $^{233}U(VI)$ and citric acid an interaction of the tracers with the filters was assumed. The respective filter K_d values were obtained by extraction experiments. Subsequently after the clay diffusion experiment $^{233}U(VI)$ and citric acid were extracted from the filter plates by 1 M HNO_3. After shaking for 7 days, the extracts were analyzed by LSC. The resulting K_d values were $K_d(U(VI)) = 7.91\times10^{-4}$ m^3/kg in the absence of citric acid and $K_d(U(VI)) = 1\times10^{-3}$ m^3/kg in the presence of citric acid, and $K_d(\text{citric acid}) = 9\times10^{-5}$ m^3/kg. Values for D_f of U(VI) and citric acid were taken from the literature. D_f of $Ca_2UO_2(CO_3)_3(aq)$, the dominating U(VI) species in OPA pore water (Joseph et al., 2011), was taken from (Joseph et al., 2013b) and amounted to 3.5×10^{-11} m^2/s. If the diffusion coefficient of a diffusing species in bulk water, D_w [m^2/s], is known, D_f can be estimated by $D_f = D_w/10$ (Glaus et al., 2008). For citric acid at pH 4, D_w values around 0.7×10^{-9} m^2/s were reported (Laguerie et al., 1976; Liu et al., 2004). Therefore, a D_f value of 7×10^{-11} m^2/s was used.

8.2 Results and discussion

8.2.1 HTO diffusion in Opalinus Clay

The results obtained by fitting the experimentally determined diffusive flux of HTO in the respective receiving reservoir solution are presented in Table 20. As shown, the data are in reasonably good agreement with literature values. Small differences can be attributed to the different OPA bore cores used in the experiment.

Table 20: Diffusion parameters determined by HTO diffusion experiments through OPA.

	Cell 1	Cell 2	(Van Loon and Soler, 2004)
c_0 / Bq/mL	986 ± 3	990 ± 107	1217 ± 83
D_e / × 10^{-11} m^2/s	1.67 ± 0.12	1.33 ± 0.11	1.21 ± 0.08
ε / –	0.10 ± 0.01	0.10 ± 0.005	0.09 ± 0.02

The obtained ε values were included in the COMSOL model used for fitting the U(VI) and citric acid diffusion depth profiles.

8.2.2 Aqueous U(VI) and citric acid speciation

To interpret the obtained diffusion profiles of U(VI) and citric acid in OPA, the diffusing species have to be known. As discussed previously (Joseph et al., 2011), the U(VI) speciation in OPA pore water is dominated by the neutral $Ca_2UO_2(CO_3)_3(aq)$ complex to almost 100 %. In respective diffusion experiments, this species was assumed to be the main diffusing species in the system (Joseph et al., 2013b).

In the present study, the U(VI) speciation in the absence and presence of citric acid as well as the citric acid speciation in the presence of U(VI) in the source reservoir solutions were calculated using the speciation code EQ3/6 (Wolery, 1992) considering the thermodynamic data compiled in Guillaumont et al. (2003), Bernhard et al. (2001), Lee et al. (2015), Hummel et al. (2005), and Steudtner et al. (2012). In the model, the present cation and anion concentration of the dissolved salts as well as the concentration of U(VI) and citric acid, the pH, and the redox potential in the source reservoir solutions were included. The conditions and the resulting species distributions in the beginning of the experiment are summarized in Table 21 for the solutions of the reservoirs Cell 1, Cell 2, TTA, and UV-vis.

Table 21: Conditions present in the solutions of reservoirs Cell 1, Cell 2, TTA, and UV-vis at the *beginning* of the diffusion experiment as well as the corresponding U(VI) speciation in the solution.

	Cell 1	Cell 2	TTA	UV-vis
c(U(VI)) / M	9.85×10^{-7}	9.84×10^{-7}	9.98×10^{-7}	1.08×10^{-4} [a]
c(citric acid) / M	-	9.92×10^{-4}	1.01×10^{-3}	9.99×10^{-4}
Na / M [a]	2.31×10^{-1}	2.37×10^{-1}	2.37×10^{-1}	2.30×10^{-1}
K / M [a]	1.98×10^{-3}	2.21×10^{-3}	2.49×10^{-3}	2.23×10^{-3}
Mg / M [b]	1.65×10^{-2}	1.65×10^{-2}	1.67×10^{-2}	1.61×10^{-2}
Ca / M [b]	2.62×10^{-2}	2.59×10^{-2}	2.57×10^{-2}	2.57×10^{-2}
Sr / M [a]	4.96×10^{-4}	4.91×10^{-4}	4.88×10^{-4}	4.85×10^{-4}
Ba / M [a]	6.68×10^{-8}	1.25×10^{-7}	8.59×10^{-8}	7.04×10^{-8}
Al / M [a]	8.78×10^{-7}	9.01×10^{-7}	7.78×10^{-7}	3.74×10^{-7}
Si / M [a]	3.63×10^{-6}	6.41×10^{-6}	5.95×10^{-6}	4.49×10^{-6}
Mn / M [a]	3.49×10^{-8}	3.28×10^{-8}	2.86×10^{-8}	3.24×10^{-8}
Cl^- / M [c]	2.85×10^{-1}	2.93×10^{-1}	2.96×10^{-1}	2.85×10^{-1}
SO_4^{2-} / M [c]	1.37×10^{-2}	1.42×10^{-2}	1.38×10^{-2}	1.37×10^{-2}
CO_3^{2-}/HCO_3^- / M [d]	4.80×10^{-4}	5.20×10^{-4}	4.60×10^{-4}	4.77×10^{-4}
pH	8.46	8.47	8.46	8.39
E_h / mV	390	340	275	270
U(VI) speciation (aqueous species accounting for 99 % or more)				
$Ca_2UO_2(CO_3)_3(aq)$	97.91	97.77	97.72	96.28
$UO_2(CO_3)_3^{4-}$	0.66	0.77	0.79	0.75
$MgUO_2(CO_3)_3^{2-}$	0.63	0.67	0.69	0.65
$(UO_2)_2CO_3(OH)_3^-$				1.4
Citric acid speciation (aqueous species accounting for 99 % or more)				
$Ca(cit)^-$	-	60.41	59.92	60.60
$Mg(cit)^-$	-	37.10	37.58	36.91
Cit^{3-}	-	2.48	2.49	2.48

[a] ICP-MS (error: ±10 %), [b] AAS (error: ±2 %), [c] IC (error: 3-10 %), [d] TC-TOC (error: ±3 %)

The diffusion experiments were conducted for 3 months. At the end of the experiment the conditions in the source reservoir solutions were measured again and the speciation was calculated (cf. Table 22).

Table 22: Conditions present in the solutions of reservoirs Cell 1, Cell 2, TTA, and UV-vis at the *end* of the diffusion experiment as well as the corresponding U(VI) speciation in the solution.

	Cell 1	Cell 2	TTA	UV-vis
c(U(VI)) / M	9.00×10^{-7}	8.61×10^{-7}	1.03×10^{-6}	5.80×10^{-5} [a]
c(citric acid) / M	-	9.19×10^{-4}	9.66×10^{-4}	8.84×10^{-4}
Na / M [a]	2.52×10^{-1}	2.57×10^{-1}	2.57×10^{-1}	2.50×10^{-1}
K / M [a]	2.46×10^{-3}	4.25×10^{-3}	3.48×10^{-3}	2.84×10^{-3}
Mg / M [b]	1.80×10^{-2}	1.78×10^{-2}	1.78×10^{-2}	1.74×10^{-2}
Ca / M [b]	2.82×10^{-2}	2.82×10^{-2}	2.82×10^{-2}	2.82×10^{-2}
Sr / M [a]	5.07×10^{-4}	5.14×10^{-4}	5.15×10^{-4}	5.04×10^{-4}
Ba / M [a]	1.38×10^{-7}	1.66×10^{-7}	1.22×10^{-7}	8.16×10^{-8}
Al / M [a]	1.03×10^{-6}	2.04×10^{-6}	1.03×10^{-6}	6.86×10^{-7}
Si / M [a]	2.32×10^{-5}	2.62×10^{-5}	1.13×10^{-5}	5.98×10^{-6}
Mn / M [a]	1.65×10^{-6}	7.55×10^{-7}	1.18×10^{-7}	1.29×10^{-7}
Cl^- / M [c]	2.91×10^{-1}	3.10×10^{-1}	2.99×10^{-1}	2.88×10^{-1}
SO_4^{2-} / M [c]	1.49×10^{-2}	1.41×10^{-2}	1.31×10^{-2}	1.25×10^{-2}
CO_3^{2-}/HCO_3^- / M [d]	2.62×10^{-4}	3.23×10^{-4}	3.62×10^{-4}	4.70×10^{-4}
pH	8.81	9.09	9.06	8.92
E_h / mV	250	210	230	140
U(VI) speciation (aqueous species accounting for 99 % or more)				
$Ca_2UO_2(CO_3)_3(aq)$	98.02	97.93	97.98	98.03
$UO_2(CO_3)_3^{4-}$	0.63	0.69	0.66	0.63
$MgUO_2(CO_3)_3^{2-}$	0.60	0.62	0.61	0.59
Citric acid speciation (aqueous species accounting for 99 % or more)				
$Ca(cit)^-$	-	60.66	60.62	61.05
$Mg(cit)^-$	-	36.98	37.07	36.68
Cit^{3-}	-	2.36	2.30	2.27

[a] ICP-MS (error: ±10 %), [b] AAS (error: ±2 %), [c] IC (error: 3-10 %), [d] TC-TOC (error: ±3 %)

The comparison of the speciation in the beginning and at the end of the experiment showed that, based on the currently available data for U(VI) and citric acid, the $Ca_2UO_2(CO_3)_3(aq)$ complex should be the main diffusing U(VI) species in the absence and presence of citric acid. In the case of citric acid, $Ca(cit)^-$ was calculated to dominate the speciation in solution.

The decrease of the U(VI) and citric acid concentration in the solution of Cell 1 and Cell 2 was due to the diffusion of species into the clay. In the TTA reservoir solution no significant change in U(VI) and citric acid concentration was observed. In contrast, the U(VI) and citric acid concentration in the UV-vis reservoir solution decreased by about 50 % and by about

10 %, respectively, during the experiment. Since no diffusion cell was connected to this reservoir solution a U(VI) precipitation with citric acid involvement can be assumed.

Compared to the three reservoirs with low U(VI) concentration, the UV-vis reservoir showed the largest variance in redox potential (cf. Fig. 79). Based on these observations it can be assumed that instead of a U(VI) precipitation a reduction to U(IV) with subsequent precipitation occurs in the reservoir, probably caused by the citric acid. Perhaps, the about two orders of magnitude higher U(VI) concentration was more sensitive towards reduction than the lower U(VI) concentration in the reservoirs Cell 1, Cell 2, and TTA. However, the precipitation was not entire; the majority of uranium was still in solution (cf. Table 22).

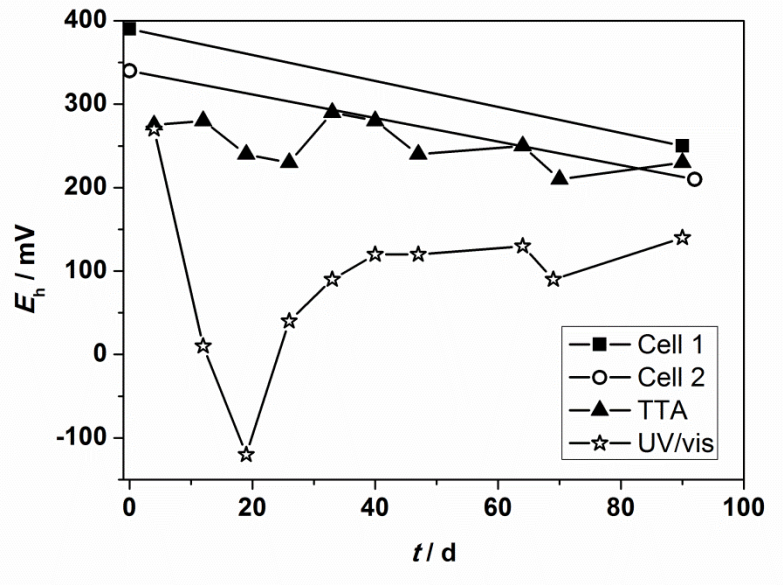

Fig. 79**:** Redox potential as a function of time determined in the solutions of reservoir Cell 1, Cell 2, TTA, and UV-vis. Lines were drawn for visual reasons.

In addition to redox potential measurements, the redox state of uranium was determined by TTA solvent extraction using aliquots of the reservoir solutions of Cell 1, Cell 2, and TTA. No reduction of U(VI) to U(IV) was detected in all samples taken within the three months. This supported the results of the redox potential measurement, that uranium was stable in the hexavalent oxidation state in these solutions.

The solution of the UV-vis reservoir was regularly analyzed by UV-vis spectroscopy. The spectra are presented in Fig. 80.

In the beginning of the experiment the spectrum of the solution was similar to the spectrum of the $(UO_2)_3(cit)_3(OH)_3^{8-}$ complex (Steudtner et al., 2012). This observation indicated the presence of a U(VI)-citric acid species in the beginning of the experiment which was in contrast to the results of the speciation calculation (cf. Table 21). It seems that based on the current knowledge of U(VI)-citric acid species the present experimental speciation is not described correctly. Species containing U(VI) and citric acid which may form under the investigated environmentally relevant conditions are not reported yet. Felipe-Sotelo et al. (2015) investigated

to solubility of U(IV)/U(VI) in the presence of citric acid at higher pH values in saturated $Ca(OH)_2$ solution. They observe a 3-4 orders of magnitude higher solubility of uranium than in the absence of citric acid. Thermodynamic modeling underestimates the solubility since thermodynamic constants of these conditions are missing. They assume that soluble metal-citrate-OH complexes stabilized by Ca^{2+} are formed.

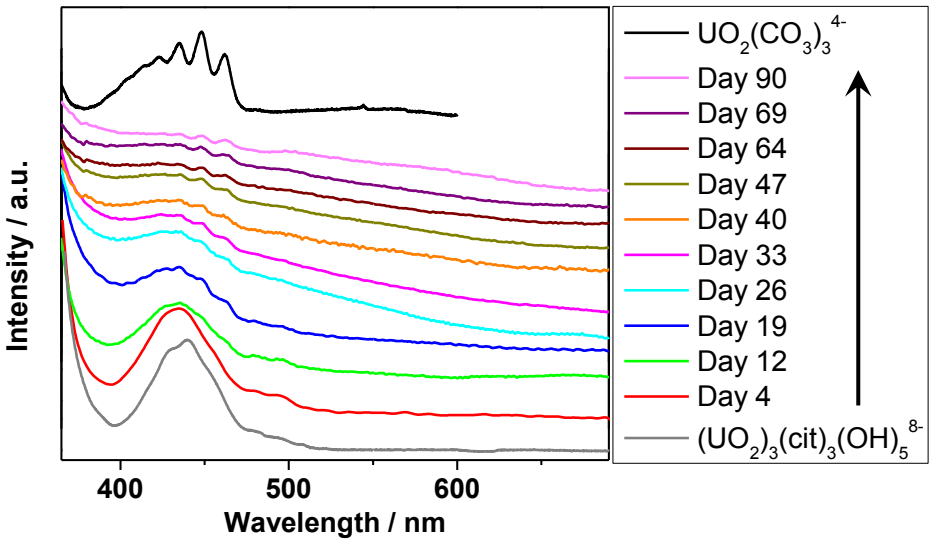

Fig. 80: UV-vis spectra of the UV-vis reservoir solution as a function of time. Spectra of $UO_2(CO_3)_3^{4-}$ and $(UO_2)_3(cit)_3(OH)_5^{8-}$ provided by Steudtner et al. (2012).

The UV-vis spectra changed within 12 and 19 days which was in agreement with the largest variation in redox potential (cf. Fig. 79) and can be attributed to the assumed partly reduction of U(VI) to U(IV). At the end of the experiment the UV-vis spectrum showed a slightly smaller intensity which can be due to the lower U(VI) concentration in solution and/or a change of the extinction coefficient associated to a change in speciation. The shape of the spectrum was similar to the spectrum of $UO_2(CO_3)_3^{4-}$. That indicates that after the reaction of the U(VI)-citric acid species with possible U(IV) precipitation, the remaining U(VI) seems to form a carbonates species, probably $Ca_2UO_2(CO_3)_3(aq)$, which would be in agreement with the U(VI) speciation calculated.

PCS measurements showed the absence of colloids in the solutions of the reservoirs TTA and UV-vis. Contrary, colloids were detected in the source reservoir solution of Cell 1 and Cell 2. Probably, mineral particles were released from the clay during the diffusion experiment.

8.2.3 Influence of citric acid on the diffusion of U(VI) in Opalinus Clay

At the end of the diffusion experiment, depth profiles of $^{233}U(VI)$ in OPA in the absence and presence of citric acid were determined (cf. Fig. 81). Within the three months neither $^{233}U(VI)$ nor citric acid were detected in the receiving reservoir solution.

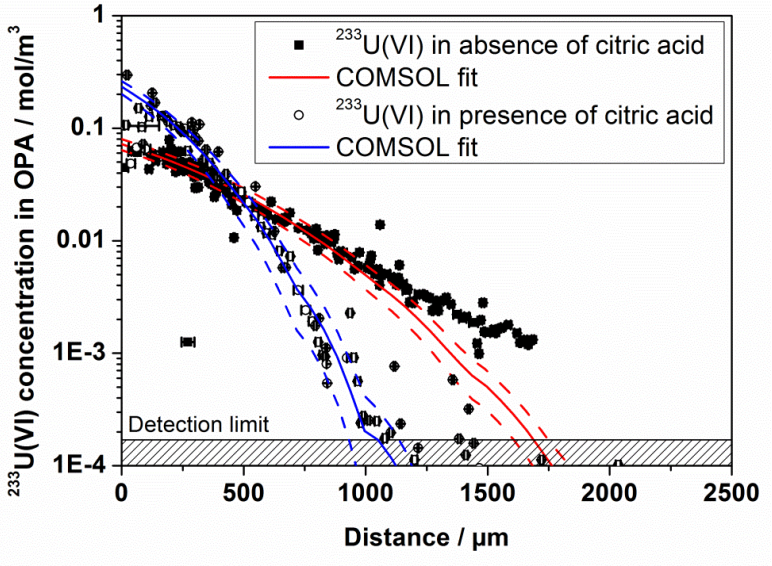

Fig. 81: Concentration profiles of ^{233}U(VI) in the absence (filled symbols) and presence (open symbols) of citric acid.

The comparison of the profiles shows that in the presence of citric acid more ^{233}U(VI) was detected at the boundary of the clay sample pointing to a much stronger sorption of ^{233}U(VI) on the clay. In addition, ^{233}U(VI) diffusion was less deep in the clay (about 1 mm) than in the absence of citric acid (about 1.75 mm). These observations indicate the presence of different diffusing species in the absence and presence of citric acid. Furthermore, the data of the ^{233}U(VI) profile in the presence of citric acid scatter close to the OPA boundary. A small fraction of a different U(VI) species could have been formed, perhaps reaction products. As discussed in section 8.2.2, although it was observed only in the UV-vis reservoir solution a reaction of the main diffusing species in the solution of Cell 2 during the three-month experiment cannot be excluded. Another reason for this data scattering could be the preparation method. The observed behavior of the profiles is contrary to the results of the speciation calculations (Table 21 and Table 22) where in the absence as well as presence of citric acid $Ca_2UO_2(CO_3)_3$(aq) was identified as dominant U(VI) species in solution and assumed to be the main diffusing species in the diffusion experiment. It seems, that in addition to the U(VI) speciation of the UV-vis reservoir solution also the U(VI) speciation in the solutions of the reservoirs Cell 2 and TTA are incorrect. Based on the diffusion results there should be another species diffuse through the clay than $Ca_2UO_2(CO_3)_3$(aq). This discrepancy represents a further example of missing thermodynamic data of U(VI)-citric acid species for the present conditions.

Under consideration of the boundary conditions, the experimental profile data were fitted with COMSOL by variation of D_e and K_d. The diffusion parameter values obtained for ^{233}U(VI) in the absence and presence of citric acid are summarized in Table 23. In the model, the transport porosity of U(VI) and citric acid equaled ε(HTO), although it appears likely that ε(U(VI) and ε(citric acid) are smaller than for HTO. Given their relatively large size, the dominant U(VI) and citric acid species may not have access to the interlayers of the smectite fraction of OPA. However, Joseph et al. (2013b) have been discussed previously that the choice

of ε_{eff} has no significant impact on the modeled U(VI) diffusion parameters, since the U(VI) sorption onto the clay is dominating (cf. Eq. (8.4): $\rho \cdot K_d >> \varepsilon_{eff}$).

Table 23: Parameter values for the ^{233}U(VI) diffusion in OPA in the absence and presence citric acid.

	Cell 1: ^{233}U(VI) in the absence of citric acid	^{233}U(VI) [b]	Cell 2: ^{233}U(VI) in the presence of citric acid
t / d	90	89	91
ρ / kg/m^3	2364	2424	2357
ε / – [a]	0.10 ± 0.01	0.16 ± 0.01	0.10 ± 0.005
K_d / m^3/kg	0.038 ± 0.005	0.025 ± 0.003	0.15 ± 0.03
α / –	90 ± 12	61 ± 7	354 ± 70
D_e / × 10^{-12} m^2/s	1.9 ± 0.4	1.9 ± 0.4	2.3 ± 0.8
D_a / × 10^{-14} m^2/s	2.1 ± 0.2	3.1 ± 0.3	0.65 ± 0.1

[a] Determined by HTO through-diffusion.

[b] Determined by diffusion experiments (Joseph et al., 2013b).

The comparison of the results from Cell 1 with literature data (Joseph et al., 2013b) shows that the literature D_e value determined under similar conditions could be confirmed by this experiment. This indicates that the same diffusing U(VI) species was present in both diffusion experiments, probably $Ca_2UO_2(CO_3)_3$(aq). However, in the present study the determined K_d value was slightly larger than the reported value which can be attributed to differences in the clay batch used in the diffusion cells. This batch had also a smaller porosity than the literature sample which can have an effect on K_d.

As discussed, in the presence of citric acid a U(VI)-citric acid species may be formed in solution which seemed to be the main diffusing species in Cell 2. Based on the modeling results, this species sorbed stronger onto OPA than $Ca_2UO_2(CO_3)_3$(aq). The K_d increased by one order of magnitude. This is in contrast to previous findings where the influence of citric acid on the U(VI) sorption to OPA was investigated by batch sorption experiments (Schmeide and Joseph, 2012). There, a significant decrease of the K_d value of U(VI) was observed with increasing citric acid concentration. At a citric acid concentration of 1×10^{-3} M the K_d value decreased from about 0.025 m^3/kg to about 0.0045 m^3/kg. This was explained by the formation of very stable aqueous U(VI)-citric acid complexes with probable smaller sorption affinity towards OPA than the $Ca_2UO_2(CO_3)_3$(aq) complex. A reduction of U(VI) to U(IV) was not detected in the batch sorption experiments. These contradictory observations point to the presence of different uranium species in the batch sorption and diffusion experiments. Although it was not found in the source reservoir solution by solvent extraction U(VI) could have been reduced to U(IV) directly on the clay surface. A similar behavior was observed for the Np(V) / OPA system (Wu et al., 2009). Without the probable catalyzing effect of citric acid, a one order of magnitude higher K_d value was obtained by Np(V) diffusion experiments than by Np(V) batch sorption experiments. It was assumed that Np(V) was partly reduced to Np(IV) in OPA. It can be assumed that the formation of $Ca_2UO_2(CO_3)_3$(aq) stabilized U(VI) against reduction by OPA, but as the U(VI) species changed due to the influence of citric acid, U(VI) may have become more vulnerable for reduction.

Under consideration of the uncertainties the D_e value of the species formed in the presence of citric acid was comparable to the D_e value of $Ca_2UO_2(CO_3)_3(aq)$. The combination of similar D_e and increased K_d led to an one order of magnitude decreased D_a value for the assumed U(VI)-citric acid species compared to the D_a value of U(VI) in the absence of citric acid. That means, the formed uranium species was stronger retarded by OPA than $Ca_2UO_2(CO_3)_3(aq)$. Citric acid had a significant influence on the retention of U(VI) in OPA.

8.2.4 Diffusion of citric acid in Opalinus Clay

In addition to the profiles of U(VI), the diffusion profile of citric acid in the OPA sample of Cell 2 was studied. The experimental and model profile data are presented in Fig. 82.

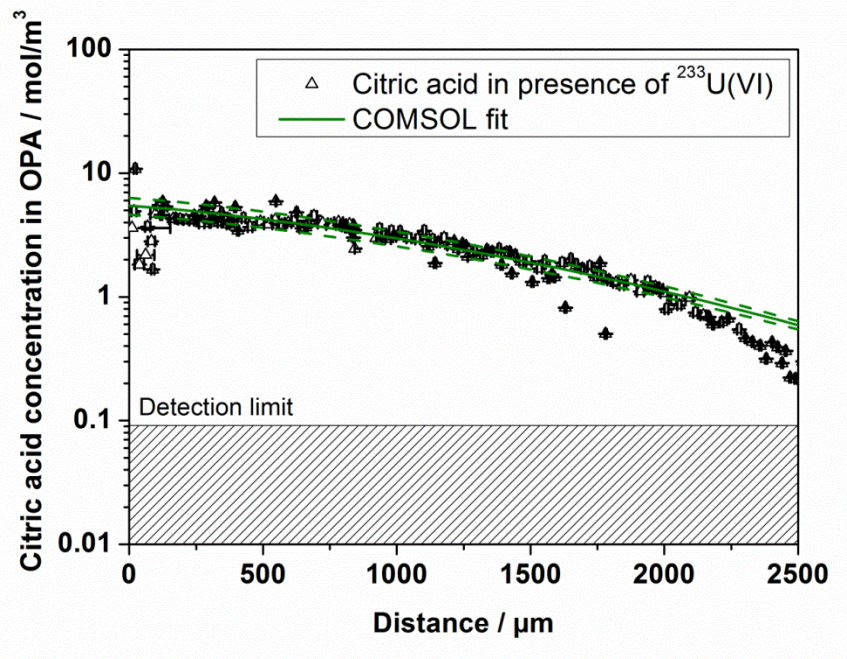

Fig. 82: Concentration profile of citric acid in the presence of $^{233}U(VI)$.

In the main part of the OPA sample only one profile can be seen assuming that there was only one main citric acid species diffusing through the clay. Based on the species distribution shown in Table 21 and Table 22, this could be $Ca(cit)^-$. A small fraction of citric acid should be associated to $^{233}U(VI)$ which diffused only about 1 mm deep into the clay (cf. Fig. 81). However, since the concentration of $Ca(cit)^-$ is about three orders of magnitude higher than any U(VI)-citric acid complex which may have formed, the $Ca(cit)^-$ profile superimposes any other profile. As seen in the U(VI) profile in the presence of citric acid at the boundary of the OPA sample the data scattering was quite large. Since this was observed for different species in Cell 2 in different concentration ranges the scattering could be attributed to the preparation method. However, citric acid is a strong complexation agent which also complexes ions from the mineral itself, in that way it can dissolve the clay and can alter the mineral surface with time (Huang and Keller, 1971). Although over the course of the diffusion experiment the concentration of clay released ions did not significantly increase in the source reservoir solutions (cf. Table 21 and Table 22) an alteration of the OPA surface within the first

100 µm of the OPA sample cannot be excluded due to the contact with citric acid. This would lead to a weaker sorption of the diffusing species at the boundary of the clay sample and would explain the data scattering at this diffusion depth.

The diffusion parameter values for citric acid obtained by COMSOL modeling are summarized in Table 24. For comparison literature data for the humic acid diffusion through OPA in the presence of U(VI) (Joseph et al., 2013b) are shown, too.

Table 24: Parameter values for the citric acid and humic acid diffusion in OPA in the presence ^{233}U(VI).

	Cell 2: Citric acid in the presence of ^{233}U(VI)	Small humic acid colloids [b]
t / d	91	87
ρ / kg/m^3	2357	2392
ε / – [a]	0.10 ± 0.005	0.15 ± 0.01
K_d / m^3/kg	0.0025 ± 0.0004	0.002 ± 0.0005
α / –	6 ± 1	5 ± 1.2
D_e / × 10^{-13} m^2/s	9 ± 1	4 ± 2.5
D_a / × 10^{-14} m^2/s	15 ± 1	8 ± 3

[a] Determined by HTO through-diffusion.

[b] Determined by diffusion experiments (Joseph et al., 2013b).

Citric acid sorbed relatively weakly onto OPA. The K_d value was about one and two orders of magnitude smaller than the K_d value of $Ca_2UO_2(CO_3)_3$(aq) and the sorbed U(VI)-citric acid species (cf. Table 23), respectively, but comparable to the sorption strength of small humic acids. Probably, the negative charge of the main diffusing species, Ca(cit)$^-$, led to electrostatic repulsion from the negatively charged clay surface. The D_e value of the main diffusing citric acid species was smaller than the D_e value of the respective diffusing U(VI) species in Cell 1 and 2, but was slightly higher than the D_e value for small humic acid colloids. Both competing effects, sorption and migration, led to an increased D_a value for the predominantly diffusing citric acid species compared to the D_a values of U(VI) in the absence and presence of citric acid and of small humic acid colloids. Dagnelie et al. (2014) obtained one order of magnitude higher D_a values for the diffusion of EDTA ($D_a = 3.5\times10^{-12}$ m^2/s) and oxalic acid ($D_a = 1.9\times10^{-12}$ m^2/s) through Callovo-Oxfordian Clay.

In contrast to small humic acid colloids, citric acid was not detected in the receiving reservoir of Cell 2 within three months of diffusion. Since humic acid colloids have no distinct size but a molecular size distribution, probably, smaller colloids than the main fraction of small humic acid colloids diffused through the OPA sample. However, in the case of citric acid, modeling based on the fitted diffusion parameters showed that a detectable amount of citric acid in the receiving reservoir solution can be expected after 250 days of diffusion time.

8.2.5 Conclusions

In this study the HTO and U(VI) diffusion through OPA was conducted using OPA pore water as background electrolyte. The U(VI) diffusion experiments were conducted in the absence and presence of citric acid.

The diffusion parameter values obtained for the HTO through-diffusion and the U(VI) in-diffusion in the absence of citric acid were in agreement with literature data. In the presence of citric acid the U(VI) diffusion was significantly retarded, which was attributed to a change in speciation. Probably, U(VI) was reduced to U(IV) within the three months the diffusion experiment was conducted.

Citric acid diffused slightly faster through OPA than small humic acid colloids. Based on modeling results it should be detectable in the receiving reservoir solution after about 250 days.

Speciation calculations using currently available uranium and citric acid thermodynamic data gave contrary results to the experimental observations. Instead of the calculated dominance of the $Ca_2UO_2(CO_3)_3(aq)$ complex in solution in the presence of citric acid, the respective diffusion profile ([U(VI)] : [citric acid] = 1 : 1000) and UV-vis spectra ([U(VI)] : [citric acid] = 1 : 10) revealed the significant influence of citric acid on U(VI). In both cases a citric acid mediated partly reduction of U(VI) to U(IV) was assumed. The study shows that the chemical system has to be investigated in more detail to clarify the occurring reactions. In particular, the U(VI)-citric acid species formed under these environmentally relevant conditions needs to be described spectroscopically, thermodynamically, and structurally.

9 Diffusion of U(VI) in montmorillonite at high ionic strengths

The migration behavior of radionuclides in clay rock is governed by molecular diffusion. Diffusion experiments can be used to determine the parameters of these migration processes. Most studies today focus on radionuclide diffusion in clay rock or compacted clay minerals at low ionic strengths (Glaus et al., 2007, 2010; González Sánchez et al., 2008; Jakob et al., 2009; Joseph et al., 2013b; Van Loon et al., 2003; Wu et al., 2014). In this study, diffusion experiments were conducted in both a mixed electrolyte (see section 7.1.1) as well as a NaCl solution of the same ionic strength. The mineral used in these studies was purified compacted montmorillonite. In a first step, HTO was diffused as a conservative tracer, which allows the determination of the rock capacity factor α, while in a second step, a U(VI) solution is contacted with the clay.

SWy-2 montmorillonite was purified according to Poinssot et al. (1999) and Bradbury and Baeyens (2009). In contrast to the procedure described in section 7.1, the step in which the <5 µm fraction is enriched was omitted. This was done to ensure a consistency of the dried clay that allows the clay to be ground easily. The ground clay was then pressed at Karlsruher Institut für Technologie, Institut für Nukleare Entsorgung (KIT-INE) into a clay tablet of 10.7 mm length and a diameter of 25.4 mm. This was then placed in a Teflon cell of compact design in which the reservoirs for the solutions that are contacted with the clay are in direct contact with the filters (Titanium, 25.4 x 0.75 mm, 0.5 µm nominal pore size, Mott Corporation, Farmington, CT, USA) placed on each side of the clay plug. Each reservoir has a volume of 100 mL. The diffusion cells were placed on two magnetic stirring plates (Color squid, IKA®-Werke GmbH & CO. KG, Staufen, Germany), one under each reservoir, so that the solutions in the reservoirs could be agitated by stirring discs (PTFE, 6x9 mm, Cowie Technologies, Middlesbrough, UK). For diffusion, a HTO solution ($c_{m,HTO}$ = 1 kBq mL^{-1}) and a ^{233}U(VI) solution ($c_{m,U(VI)}$ = 1×10^{-6} mol kg^{-1}) were used, the latter prepared as described in section 7.1.1. The mixed electrolyte (see section 7.1.1) and a NaCl solution of I = 3.02 mol kg^{-1}, i.e. identical ionic strength to the mixed electrolyte, were used as pore waters. The experimental procedure followed Van Loon et al. (2003), however, due to the design of the diffusion cells, the solutions were not exchanged, but remained in the reservoir for the duration of each part of the diffusion experiment.

The clay mineral was equilibrated in the inactive electrolyte solutions for 5.4 months. During this time, the pH_c was adjusted to 6.5. When pH stability over several days was reached, the electrolyte solutions in the reservoir were analyzed and exchanged against new solutions. Photon correlation spectroscopy showed that no colloidal particles could be found in the reservoirs. Crystallization of salts on the walls of the diffusion cells reduced the electrolyte concentration. In the diffusion experiment in NaCl, a calcium content of 3.7×10^{-3} mol kg^{-1} was present.

The HTO in-diffusion took place over 29 days. During this time, samples were collected daily in triplicate and analyzed by LSC (300 µL sample diluted with 2.7 mL Milli-Q water, dispersed in 20 mL Ultima Gold LLT). To keep the amount of solution constant, 900 µL of the appropri-

ate solution were added to the electrolyte solution reservoirs after sampling. Preliminary analysis of the data gave a rock capacity factor α of 0.39 (NaCl) and 0.76 (mixed electrolyte) respectively, and an effective diffusion coefficient D_e of 1.3×10^{-9} m² s^{-1} in NaCl and 9.8×10^{-10} m² s^{-1} in the mixed electrolyte. For the out-diffusion, the electrolyte solutions in the reservoirs were exchanged against inactive solutions and the sample frequency was reduced to twice a week. After the HTO out-diffusion, the U(VI) diffusion experiment was started. The solution was sampled once a week and analyzed by LSC (300 µL sample diluted with 2.7 mL Milli-Q water, dispersed in 20 ml Ultima Gold LLT). At the time of writing, U(VI) diffusion was still on-going.

10 Spatiotemporal observation of diffusion processes with PET for determination of heterogeneous effects on the core scale

10.1 Aim

The general aim of the work package was to establish PET (Positron Emission Tomography) as a reliable measuring method for quantitative determination of heterogeneous diffusion coefficients in clays. In the preceding project the suitability for imaging diffusive tracer transport was shown, however, open questions remained with respect to quantification and thus interpretation of the results. In particular, extremely high diffusion coefficients were estimated from the measurements. Therefore, the main focus was improvement of quantification, both by improving image quality and parameter determination method. Further experiments were conducted in order to understand experimental artefacts by sample alteration and damage.

10.2 Improvement of the PET-imaging procedure

The ClearPET-scanner, which is utilized in our institute, is a high-resolution scanner which is originally designed for biomedical research on small animals (Roldan et al., 2007). Over the period of the project, our concern was the higher impact of material density than that of biological tissue, which causes blurring and artefacts of the images. We had to improve the imaging algorithms in order to acquire high-quality quantitative images for parameter derivation and as reference for heterogeneous geochemical modeling.

Two issues of the image reconstruction procedure were identified and successfully addressed: normalization and scattering. This work on image improvement was largely based upon Monte-Carlo simulations of the physical processes, from radioactive decay of the tracer nuclide to detection in the detectors. Normalization is a calibration procedure which considers space-dependent inhomogeneities of sensitivity matrix, which is caused by the individual efficiencies of the detectors and their geometrical configuration. We found a strong impact of gaps between the detector cassettes, although the gantry is rotating in order to improve image homogeneity. The image deteriorating effect of these gaps is amplified by scattering and attenuation of radiation, because these cause events at locations that are not duly considered by the iterative image reconstruction procedure (Zakhnini et al., 2013).

10.2.1 Image reconstruction procedure and normalization

The original supplied image reconstruction software (STIR1.4-alpha) was updated to the recent version 3.0 which has more options for optimizing the normalization scheme (Thielemans et al., 2012). Normalization and attenuation correction where now applied directly on the original projection data. The normalization data are from the measurement on a homogeneously filled cylindrical phantom. It was found that gaps in the normalization projection (projection bins filled with zero), which are caused by the gaps between the detector cassettes,

have significant effect on image quality (Loukiala et al., 2010). Therefore, we fill the gaps with values from the projection of a synthetic unity image with the same geometry as the cylinder phantom used for the normalization measurement. Calibration of these inserted values with the minimum value of the non-empty bins of the measured normalization yielded the best suppression of ring artefacts. Star artefacts, which have been observed frequently with the first reconstruction procedure, could be eliminated completely by reducing the number of subsets from 10 to 2 in the OSEM – algorithm, at the cost of more cpu-time.

With these optimizations of the reconstruction algorithm image quality was largely improved. Reconstruction of measurements on phantoms with low density generally brought satisfactory results.

10.2.2 Scatter correction

In dense material we still experienced blurring of the images and again ring artefacts, which therefore were assigned to scattering effects. We therefore conducted Monte-Carlo simulations with OpenGATE (Jan et al., 2004) in order to identify scatter effects, quantify the scatter fraction and the impact of “false” coincidences (coincidences of nuclear gamma radiation, not from positron annihilation). These simulations yield projections of all detected coincidences, with the history of each event being known, in particular the number of Compton scattering events and the energy loss. It was found that the scatter fraction could be reduced to some extent by energy filtering (reducing the detection energy window from 250 – 750 keV to 400 – 650 keV), and that multiple scatter with a deviation of about 20° is dominating. We were able to correct measurements of simple source geometries with the help of these simulated scatter projections, which could be rated in comparison with images produced only from non-scattered events. However, the computation time of these simulations exceeds the measuring time by far.

The recent version of the reconstruction software (since STIR 2.1) supplies a simpler and faster approach, approximating the scatter deviation of the coincidences with a simplified Klein-Nishina equation (single scatter simulation SSS). Input data are the distribution of mass attenuation coefficients, as measure of the scatter cross section and an estimate of the source, which could be an uncorrected image. The result is unscaled and has to be calibrated in order to produce the due scatter fraction; we therefore still rely on an estimate of the scatter fraction which can be produced with one single Monte-Carlo simulation of a rough model. The scatter calibration was implemented as iterative procedure. In spite of the simplifications of the SSS it yields acceptable results for correction of the measured projections. The processing time of the SSS, which originally took 12 h for one projection, was optimized to about 40 min by simplification of the geometry.

The new reconstruction procedure was implemented as Python script which allows batch reconstruction and high flexibility for further improvements.

10.2.3 Error estimation, resolution, and detection threshold

There are fundamental differences between the well-known X-ray CT imaging modality and PET. CT responds to the material density. CT-data are commonly processed in order to produce structural images, segmenting the grey-level images into two or multiple domains with different density. Therefore, the most significant characteristics are spatial resolution and homogeneity of the mapping, in order to facilitate segmentation.

In contrast, PET responds to (tracer) concentration, which is the intensive thermodynamic parameter that is crucial in geochemical modeling. Concentration is a continuous value, referred to a finite test volume which is defined by the spatial resolution of the measuring method. Here, spatial resolution is the parameter of the response function which controls the smoothing of the image. More meaningful characteristics of PET images than spatial resolution are quantification errors and the detection threshold.

A rigorous error analysis of the PET imaging procedure is an intricate task (cf. e.g. Prekeges, 2013). The analysis starts on the detector level. Although the total number of recorded events is large (e.g. 10^7), the occupations of the detector positions (bins) are small numbers, responding to the Binomial distribution. The reconstruction procedure is a complicated surjective mapping method from the projection space of measurements to the image space, which requires additional parameters (normalization, attenuation correction, scatter correction) that are also subject to errors. Currently, the error propagation analysis of this complex procedure is not feasible, because we would have to analyze the system matrix with a size of several TBytes.

Instead, we estimate the error from the number of counts N that are projected to one voxel. This number is large; therefore we can consider the Poisson distribution with a relative error $\sigma = {}^{1}/_{\sqrt{N}}$. It is typically in the order of $\pm$10 % or less. However, we also have to consider systematic errors that are caused by deficiencies of the reconstruction algorithm and the parameter values. These are identifiable as imaging artefacts occurring in zones where the sensitivity – magnitude of the response function of the mapping from the projections to the image – is low. Eventually, these artefacts include zeros (e.g. from scatter-overcorrection) or errors in the order of a factor 2.

In summary, the error depends on the number of counts per voxel and is typically in the order of 10 %. In zones with lower sensitivity it eventually diverges and produces ring artefacts.

Apart from the relative error we have to consider a detection threshold of activity below which the source is not reliably detected. This threshold depends on the background level, detector properties and the reconstruction procedure. The background coincidence count rate, as deduced from blank measurements, is in the order of 500 cps. However, scattered events from strong sources can also be considered as background, in so far as they are not considered by the scatter correction procedure. A general threshold is caused by the number of events required to reconstruct one voxel. This threshold was determined with the help of Monte-

Carlo simulations of ^{22}Na-point sources in Opalinus Clay to be as low as 10 Bq, corresponding to a total of 50 counts in 18 min.

10.3 Measurements

In total we prepared and conducted PET-observations of diffusion processes on 12 Opalinus samples, most of them with ^{124}I as tracer. We tested the integrity of the samples during the experiment on blocks with a volume of 30 cm^3 which were cast in epoxy and which were prepared from fresh Opalinus cores. The upper surface was exposed to synthetic [^{124}I]-OPA-water according to Pearson (2003). Over an observation period of 4 weeks we observed significant swelling (up to 10 %), loss of integrity, and fast tracer transport into the sample. Thus, we have to consider alteration effects by unconfined swelling. This situation is not representative for conditions in the undisturbed host rock remote from the excavation damage zone (EDZ).

In order to observe diffusion on a larger scale and to reduce the alteration effect observed on small blocks we prepared horizontal drill cores (diameter 100 mm, length 80 mm) of Opalinus Clay from Mont Terri, which also were cast in epoxy. Perpendicular to the bedding, a blind hole (diameter 5 mm, length 50 mm) was drilled into the core to infill synthetic Opalinus pore water. After an equilibration period, which included observations with ^{124}I-labeled OPA-water, equilibration, the hole was filled with synthetic OPA-water, now labeled with ^{22}Na. Then it was closed with a screw, establishing a physically sealed source. The sample was stored at 20°C.

As example, we report the measurements on one sample (BLT 137/3): Beginning daily, with increasing time lag, we produced a sequence of 20 PET-images over a period of 150 days until the tracer was roughly equally distributed over the core (Fig. 83) (t = 0, 3, 6, 10, 13, 16, 20, 22, 27, 31, 35, 41, 48, 55, 69, 93, 112, 127, 143, 161 days). Because of the large amplitude range the images were scaled frame-wise. Fig. 84 shows the evolution of the maximum value, which is the reference, and the 90 % and 99.9 %-quantile. Fig. 85 shows slices in the direction of the major anisotropy axes. A gas bubble becomes visible, which at frame 1 had moved from its initial position at the bottom of the hole. The maximum projection in vertical direction is plotted as height-map at the bottom of each frame. It indicates that the diffusing tracer reaches the sample surface after 31 days at frame 10. Then, the tracer distribution homogenizes over the sample; therefore, the quantiles stabilize (Fig. 84) and the anisotropy of the distribution decreases until frame 18, which shows almost homogeneous tracer distribution.

Fig. 86 is an enlargement of the maximum projection. The shape of this distribution appears as roughly 10 mm thick rectangular block, rather than as an anisotropy ellipsoid, notwithstanding remaining indications for circular artefacts. This type of shape could be interpreted as an indication for diffusion along fine layering, rather than homogenous transversal anisotropic behavior. However, these findings should be assured by additional investigations (e.g. µCT, radiography and analysis of thin sections, as well as model simulations) and after further improvement of image quality.

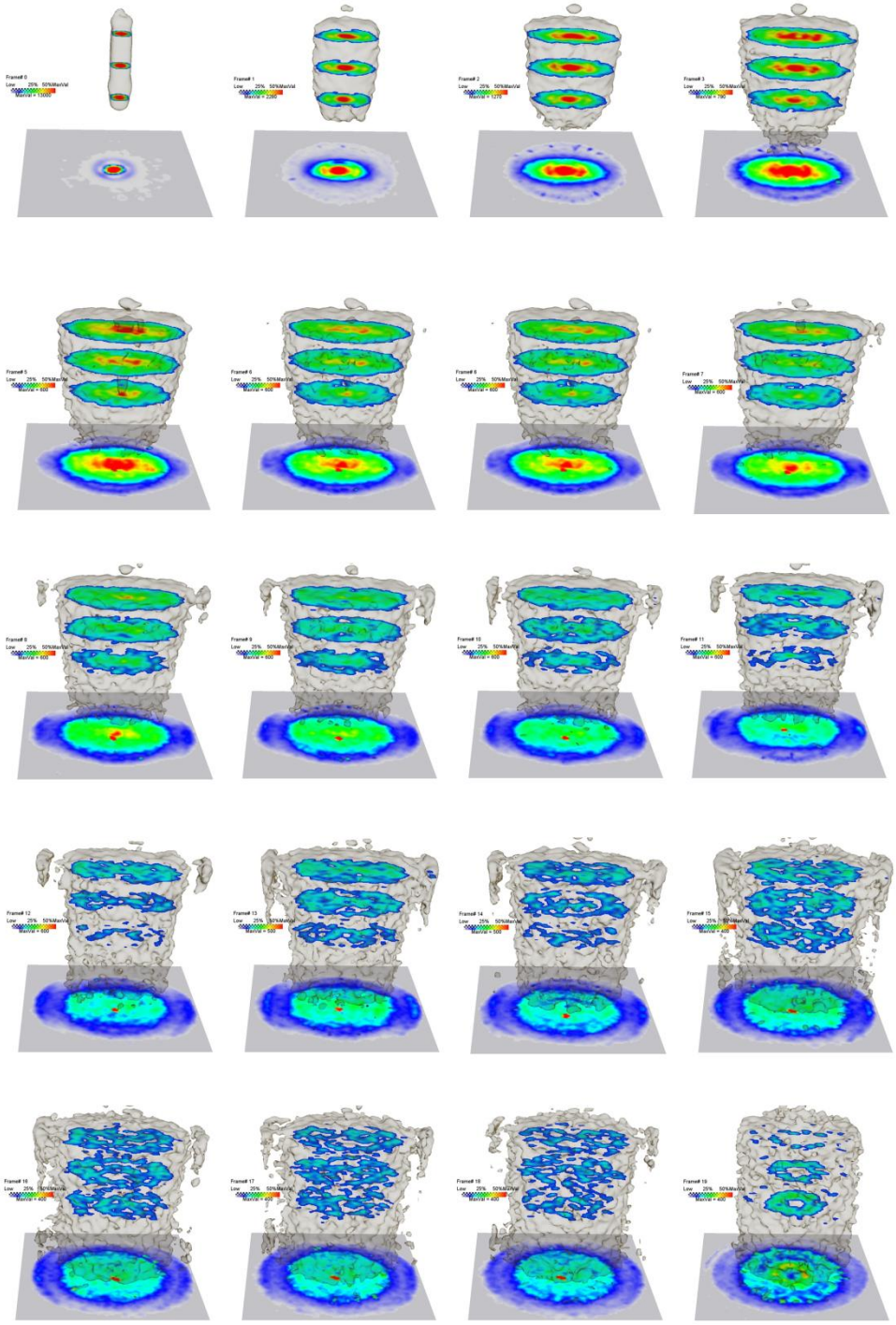

Fig. 83: 20 PET-frames of ^{22}Na-diffusion in a OPA-drill core (diameter: 100 mm, length 80 mm). At the bottom of each image: axial (vertical) maximum projection. Above: 3 horizontal slices through the source region; iso-surface of maximum/10, the scaling of the color scales is frame-wise, the maximum value of the color scale is half maximum total amplitude for each (amplitude distribution cf. Fig. 84).

Prior to the investigations with ^{22}Na we tested ^{124}I as PET-tracer (Fig. 87). In principle, its decay time (4.176 d) allows observations periods up to 1 month, sufficient for parameter derivations according to the procedure outlined below. However, the images are noisy, because of other “parasitic” γ-radiation (“false coincidences”), and the decreasing countrate causes an increasing error with time. Therefore, application of ^{124}I merely is a qualitative test method, rather than suited for quantitative estimations.

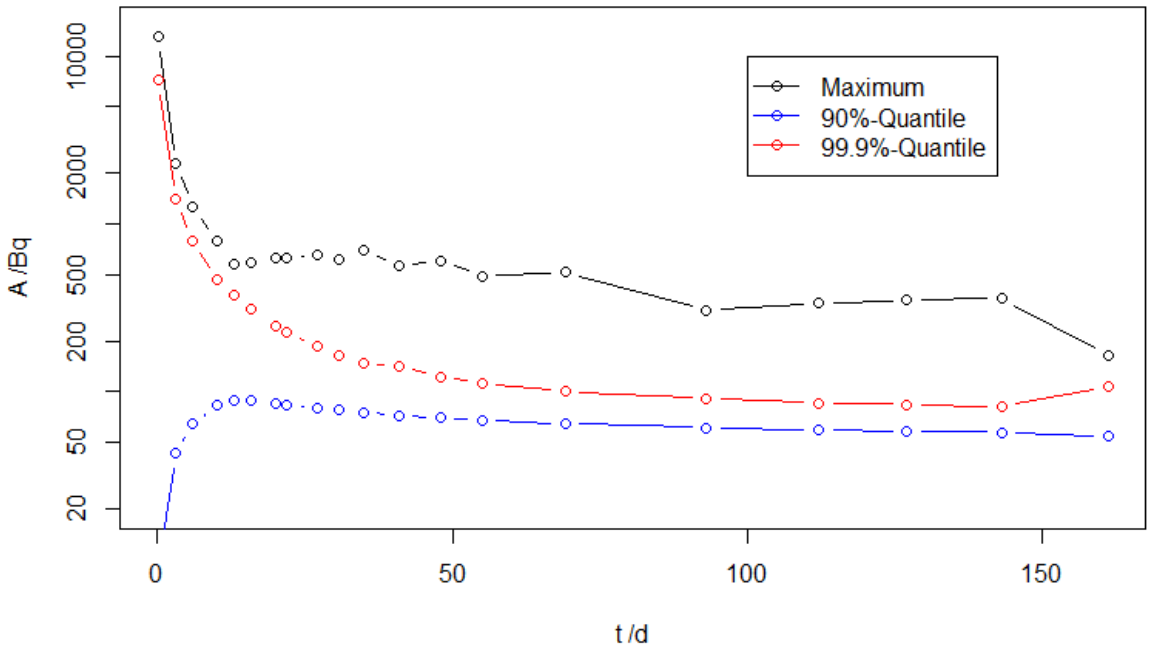

Fig. 84: Maximum, 99.9 %- and 90 %-quantiles of the amplitude vs. frame time. The color scale in Fig. 83 refers to the maximum.

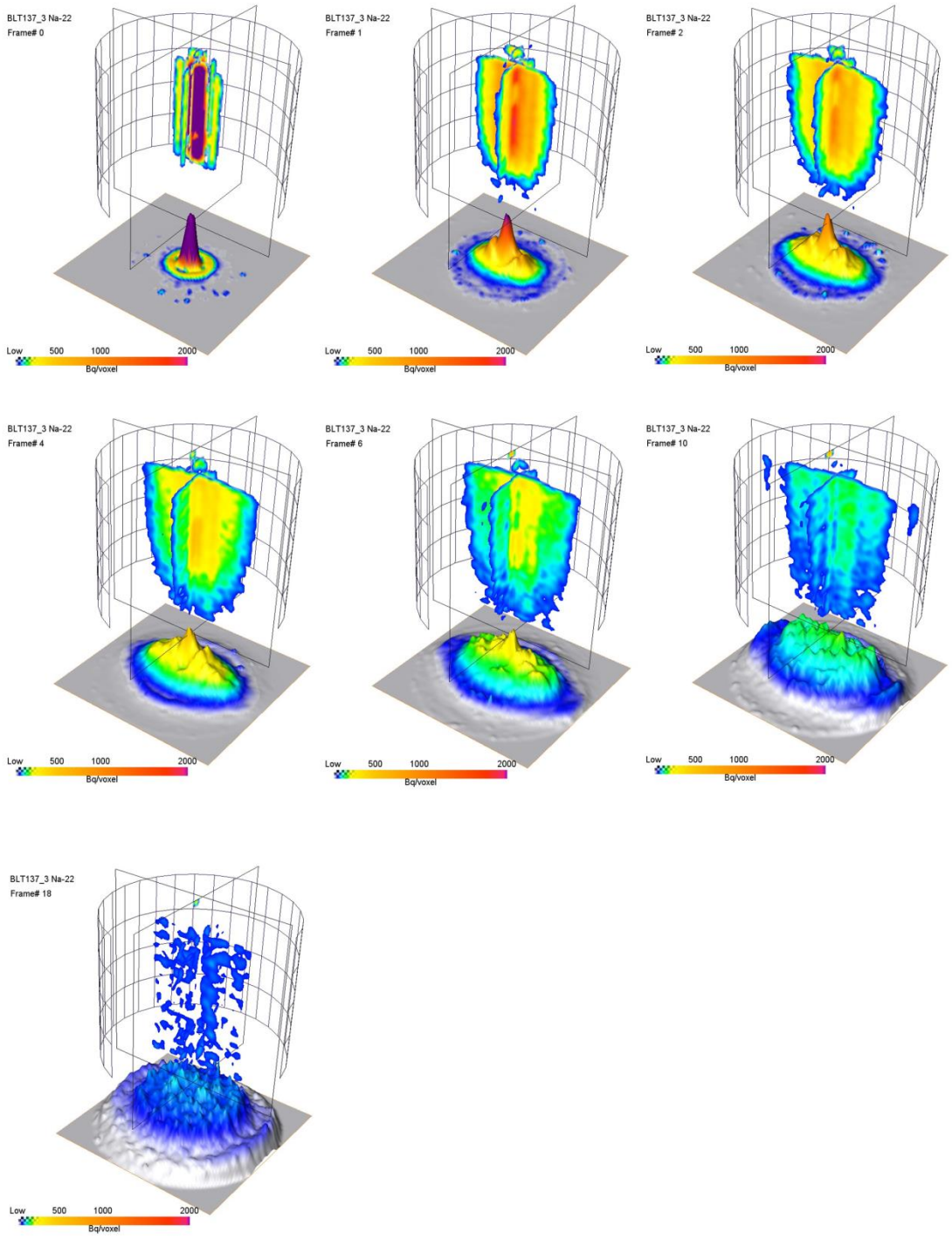

Fig. 85: Vertical slice representation of frames 0, 1, 2, 4, 6, 10, 18. At the bottom: axial projection of the maximum amplitude as height-map.

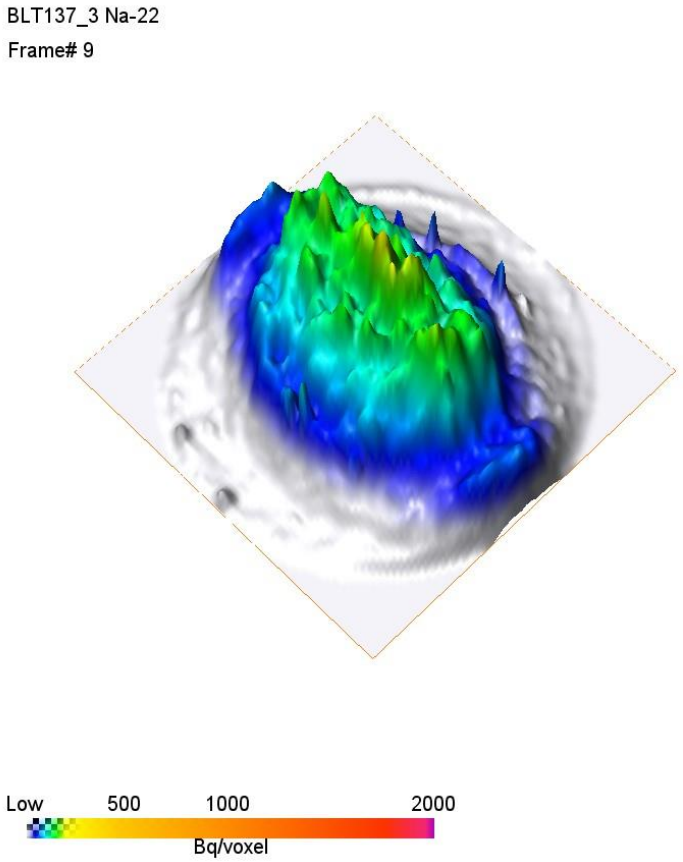

Fig. 86: Axial maximum projection of frame 9 (27 days).

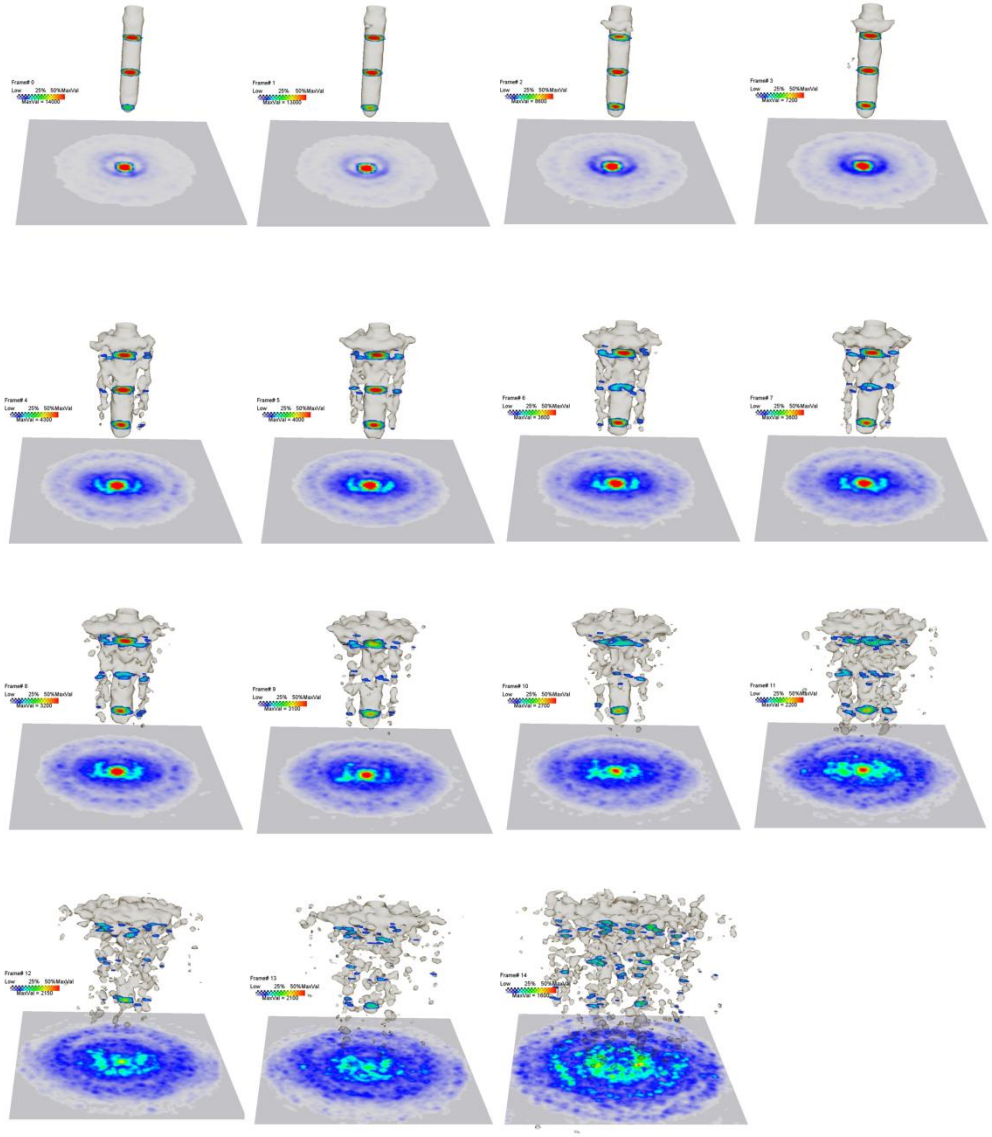

Fig. 87: 15 PET-frames of ^{124}I-diffusion in the same OPA-drill core. At the bottom of each image: axial (vertical) maximum projection. Above: 3 horizontal slices through the source region; iso-surface of maximum/10, the scaling of the color scales is frame-wise, the maximum value of the color scale is half maximum total amplitude for each (amplitude distribution cf. Fig. 88).

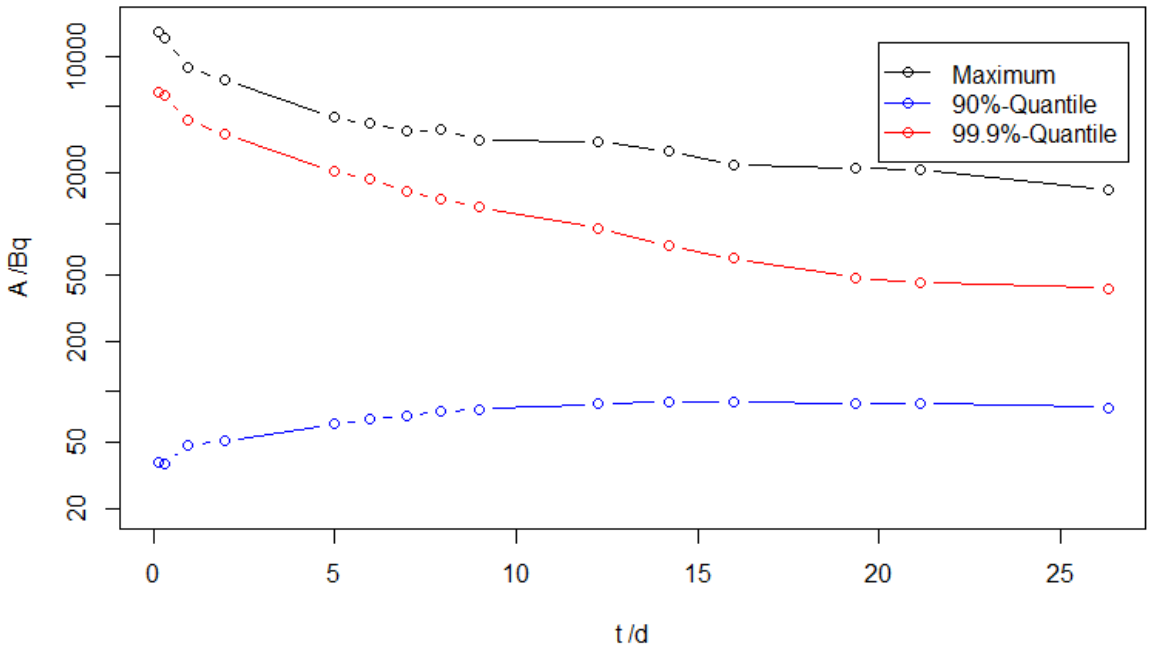

Fig. 88: Maximum, 99.9 %- and 90 %-quantiles of the amplitude of Fig. 87 vs. time.

10.4 Parameter derivation

Earlier, we developed a method for parameter derivation and attempted to derive these parameters from PET-data that were not scatter corrected (Schikora, 2012). We then derived rather high diffusion coefficients that were deviating from literature values (e.g. Van Loon et al., 2004). Therefore, we considered additional fast transport processes, which could be caused by suction and swelling effects. After a scatter correction technique became available, we conducted a similar procedure on corrected PET-data (Gerasch, 2015). First results are published in Kulenkampff et al. (2015).

Here we only consider the initial period, until the tracer propagation reached the surface of the sample. We aligned COMSOL multiphysics simulations of anisotropic diffusion in clay to our PET-observations and were able to clearly differentiate and evaluate likely explicit sample features and transport processes. From our non-invasive, spatio-temporal PET observations of the diffusion process in a real clay sample two 2D sets c_i(x,z) and c_i(y,z), are extracted and provided to the Optimization Module for the parameter estimation for Dxx=Dzz and Dyy. A sensitivity analysis quantifies the effects on uncertainties regarding porosity n, initial concentration c_0 and spatial resolution.

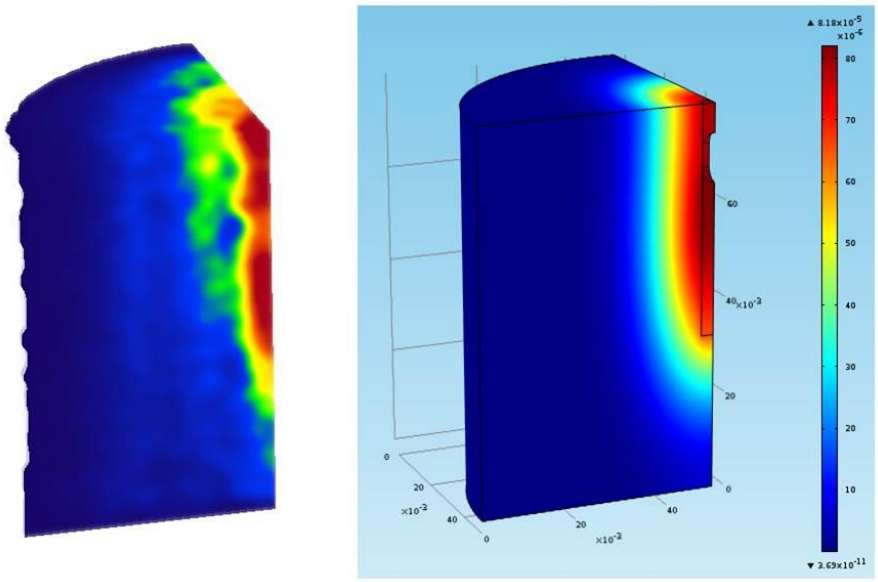

Fig. 89: Result of the optimum fit of the PET - tracer distribution (left) with a COMSOL Multiphysics FEM model (right) (scaled in molar concentrations).

The 4D simulation results nicely match quantitatively with our 4D experimental results obtained in GeoPET experiments. Fig. 89 shows a comparison of the experimental data with the simulated values. This method yielded the apparent diffusion coefficients in the principal directions, $D_{a,xx}$ = 1.1e-10 m^2/s and $D_{a,yy}$ = 3.4e 11 m^2/s, which are in accordance with results from through-diffusion experiments parallel and perpendicular to the bedding (Van Loon et al., 2004).

This method shall be improved in future to consider complete 3D+t-data sets instead of sequential optimization of data subsets from single frames. Also, it should consider more complex geochemical models, which is possible with PHREEQC-COMSOL-coupling, than simply including a constant K_d.

10.5 Conclusions

With the new image reconstruction algorithm and the improved parameter determination procedure it is now possible to yield reliable diffusion parameters from PET-measurements. The method is ready for application as rather rapid test procedure of diffusion properties on the scale of drill cores. Further improvements are possible and will reduce instrumental deficiencies that cause systematic – yet recognizable – errors.

A number of experimental requirements have been identified: Longer living PET-nuclides, like ^{22}Na should be preferred, rather than ^{124}I, because the observation period should be one month, and the detectability of the tracer decreases caused by radioactive decay, which is

negligible with ^{22}Na, and diffusional spreading. In order to reduce preparation damage and overburden release effects the sample should prepared immediately after retrieval and kept at simulated overburden conditions as far as possible. These requirements are compatible with PET-experiments. In the present studies, which were designed to develop and improve the method, such complications were not considered. Therefore, alteration effects are likely.

Smaller sample sizes could speed up the testing procedure. However, we experienced significant alterations of the samples on smaller samples. Also, then heterogeneous effects on the larger scale would be neglected which are detectable with PET imaging on larger scale samples. Heterogeneous effects on the larger scale, caused by e.g. more sandy layers and lenses, could significantly moderate the transport behavior, because they could cause preferential diffusional transport along localized zones and therefore affect both transport velocity and retention in an unfavorable way for the barrier function. We found indications for such effects, although they could not yet be quantified and they could also be due to experimental conditions, e.g. fracturing through swelling or stress release.

The derived diffusion parameters are not exclusively valid for available PET-nuclides. Following Appello et al. (2010), we can principally derive spatially resolved material parameters, like formation factors, which then can be considered for diffusion modeling of other types of ions. Then, only interaction parameters of the tracer, in particular Na^+-ions, and the other ions have to be determined in batch experiments.

11 Observation of reactive transport in fractured barrier rock

11.1 Aim

Mining operations and drilling inevitably produce an EDZ, which is caused by pressure release, build-up of differential stress, loss of formation water and air entry. One option to improve these degradations of the geological barrier is impregnation of waterglass (Bollingerfer et al., 2011). The success of effective injection into void structures depends on a number of factors: the reaction kinetics of the injected waterglass with salt and brines, the nature of the fractures, and the injection velocity. This rather complex process was not yet observed directly, but only the final results had been tested with destructive methods.

We developed a method to observe the waterglass injection process into salt rock and quantify the resulting modification of transport pathways with PET (Bittner, 2014). The results can be combined with numerical process simulation based on CT-imaging, allowing to improve fundamental process understanding and to verify the underlying assumptions and model codes.

11.2 Method

We are using a sylvinite core from Staßfurt of the type Z2KSTh. It is a cylindrical sample with a diameter of 100 mm and a length of 150 mm. Before our injection studies, the core had undergone a geomechanical triaxial test, which caused cone shaped internal fractures with a total porosity of 6 % and a slightly convex cylinder surface, which are clearly visible in the µCT-image (Fig. 90). The core itself was cast into a PMMA-cylinder with epoxy resin. PVC-end caps were adapted with a small dead volume of about 1.5 ml. The fluid was injected and ejected through central ports in the end caps.

Saturated sodium chloride solution with sediment was applied as injection test fluid and waterglass (sodium silicate, $Na_2SiO_3 + H_2O$) was used as impregnation agent. Sodium silicate in contact with salt solutions and evaporite minerals results in a fast formation of solids. The chemical and mineralogical composition of these solids depends on the concentration and type of salts. Waterglass also polymerizes at a reduction of the pH value, this can be done by simple dilution with water, or in contact with salt. Therefore, the sealing efficiency, i.e. depth of penetration and distribution, is a result of both injection rate and reaction kinetics.

We studied the impact of the fast reaction kinetics on small columns filled with granular salt, which were treated with waterglass and brine. The propagation of the fluids was observed with PET. Depending on flow rate, grain size, and pore fill we achieved a penetration depth of the waterglass of 1 to 10 mm before the injection pressure increased abruptly.

The injection study with PET-observation consists of five steps:

1) A saturated NaCl-solution labeled with [^{18}F]KF with an activity of 100 MBq was injected with a flowrate of 0.25 ml/min in order to visualize the effective flow paths of the brine and to quantifying the permeability of the core. The pressure was 0.3 bars, according to a permeability of 9e-15 m^2.

2) [^{18}F]KF-waterglass solution was injected into the wet core with a flowrate of 0.5 ml/min and shut-off pressure of 2.6 bars.

3) Again, [^{18}F]KF-saturated NaCl-solution was injected to allow for direct comparison with the initial brine flow experiment, flow rate: 0.25 ml/min, pressure: 0.6 bars, permeability 2e-15 m^2.

4) Second [^{18}F]KF-waterglass injection with higher flow rate (5 ml/min) and higher final injection pressure (5 bars), to improve the sealing result, after drying the sample with dry pressured air.

5) The final test with [^{18}F]KF-saturated NaCl-solution showed no significant change of the solution flow compared to step 3.

Exemplary images of these five phases are shown in Fig. 90.

11.3 Conclusions

The initial suite of PET-images showed two major transport zones, one central branch, and one branch along the contact of the fracture with the epoxy cast. The penetration of the waterglass followed these zones, but did not exceed a penetration depth of ca. 10 mm. The major part congealed as film on the sample surface and inhibited further penetration.

In this feasibility study we demonstrated the capabilities of process observations with PET for the study of injection methods for improving the barrier function of geological material. We did not intend to apply higher pressures or flow rates and therefore, in particular, no conclusions on the efficiency of waterglass injections for improvements of the geological barrier in salt rocks are drawn. Experiments with practically more relevant higher injection rates and endpoint pressures of around 50 bars would have implied significantly higher costs for pressure vessels and a high pressure injection system. However, the present study proves the capabilities of the method and its potential for observing and better understanding such coupled hydraulic-chemical processes.

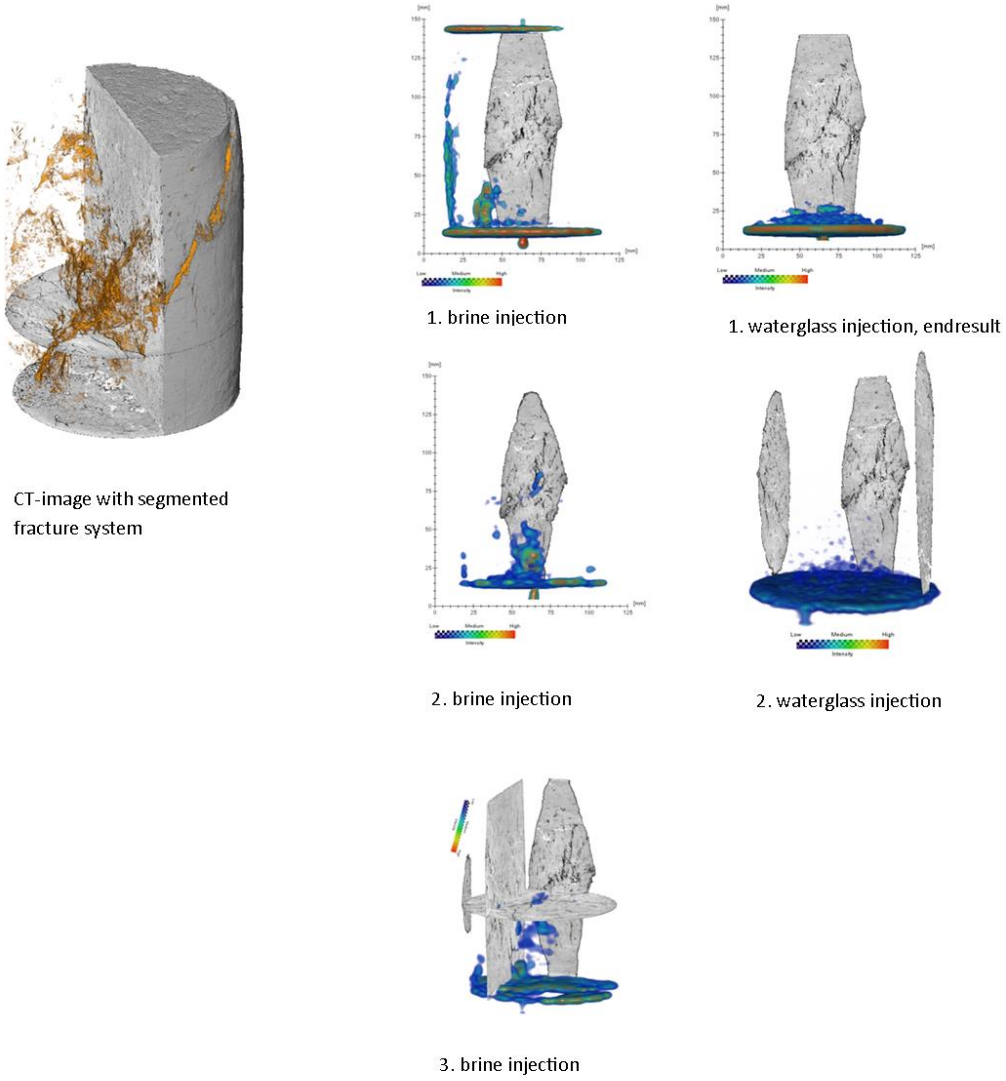

Fig. 90: µCT-image of the fracture system and exemplary images of the waterglass injection tests: Initial brine injection shows flow mainly along the outer edge of one fracture and through the sample, 1st waterglass injection penetrates up to ca. 15 mm and seals the surface, 2nd brine injection shows some sealing effect mainly of large voids, 2nd waterglass injection did not penetrate the volume and causes no improvement of the sealing effect, as can be seen in the 3rd brine injection.

12 References

Aiken, G.R.: Isolation and concentration techniques for aquatic humic substances, in: Humic substances in soil, sediment and water: Geochemistry and isolation (Aiken, G.R., MacKnight, D.M., Wershaw, R.L., MacCarthy, P., eds.). Wiley-Interscience, New York, pp. 363-385 (1985).

Akcay, H., Kurtulmuş, F.: Study of uranium sorption and desorption on some turkish clays. J. Radioanal. Nucl. Chem. 200 (6), 529-544 (1995).

Altmaier, M., Metz, V., Neck, V., Muller, R., Fanghänel, T.: Solid-liquid equilibria of $Mg(OH)_2$(cr) and $Mg_2(OH)_3Cl_x4H_2O$(cr) in the system Mg-Na-H-OH-Cl-H_2O at 25°C . Geochim. Cosmochim. Acta 67, 3595-3601 (2003).

Altmaier, M., Neck, V., Fanghänel, T.: Solubility of Zr(IV), Th(IV) and Pu(IV) hydrous oxides in $CaCl_2$ solutions and the formation of ternary Ca-M(IV)-OH complexes. Radiochim. Acta 96, 541-550 (2008).

Ams, D.A., Swanson, J.S., Szymanowski, J.E.S., Fein, J.B., Richmann, M., Reed, D.T.: The effect of high ionic strength on neptunium (V) adsorption to a halophilic bacterium. Geochim. Cosmochim. Acta 110, 45-57 (2013).

Appelo, C.A.J., Van Loon, L.R., Wersin, P.: Multicomponent diffusion of a suite of tracers (HTO, Cl, Br, I, Na, Sr, Cs) in a single sample of Opalinus Clay. Geochim. Cosmochim. Acta 74(4), 1201-1219 (2010).

Artinger, R., Kienzler, B., Schüßler, W., Kim, J.I.: Effects of humic substances on the ^{241}Am migration in a sandy aquifer: column experiments with Gorleben groundwater/sediment systems. J. Contam. Hydrol. 35, 261-275 (1998).

Atkins, P.W.: Physical Chemistry. Oxford University Press: Oxford (1998).

Bachmaf, S., Merkel, B.J.: Sorption of uranium(VI) at the clay mineral–water interface. Environ. Earth Sci. 63 (5), 925-934 (2011).

Bain, D.C., Smith, B.F.L.: Chemical analysis. In: Wilson, M.J. (Ed.), A Handbook of determinative methods in clay mineralogy. Blackie, New York, USA (1987).

Barkleit, A., Acker, M., Bernhard, G.: Europium(III) complexation with salicylic acid at elevated temperatures. Inorg. Chim. Acta 394, 535-541 (2013).

Bauer, A., Fiehn, B., Marquardt, C.M., Klein, M., Römer, J., Schäfer, T., Görtzen, A., Kienzler, B.: Results on the Pu Diffusion in the Opalinus Clay. 6th EC FP - FUNMIG IP. Stockholm. 2nd Annual Workshop Proceedings, pp. 231-237 (2006).

Benedetti, M.F., Milne, C.J., Kinniburgh, D.G., Van Riemsdijk, W.H., Koopal, L.K.: Metal ion binding to humic substances: Application of the non-ideal competitive adsorption model. Environ. Sci. Technol. 29, 446-457 (1995).

Bernhard, G., Geipel, G., Reich, T., Brendler, V., Amayri, S., Nitsche, H.: Uranyl(VI) carbonate complex formation: Validation of the $Ca_2UO_2(CO_3)_3$(aq.) species. Radiochim. Acta 89, 511-518 (2001).

Bertrand, P.A., Choppin, G.R.: Separation of actinides in different oxidation states by solvent extraction. Radiochim. Acta 31, 135-137 (1982).

Bittner, L.: Prozessbeobachtung von Vergütungsmaßnahmen im Salzgestein mittels Positronen Emissions Tomographie (GeoPET). Diploma thesis, Hochschule Zittau/Görlitz, Zittau (2014).

Bleise, A., Danesi, P.R., Burkart, W.: Properties, use and health effects of depleted uranium (DU): a general overview. J. Environ. Radioact. 64, 93-112 (2003).

Bollingerfehr, W., von Borstel, L.E., Engelhardt, H.-J., Müller, C., Schmidt, H.: Vergütung der Auflockerungszone im Salinar (VerA), Abschlussbericht FKZ 02E10649, DBE Technology GmbH (2011).

Bradbury, M.H., Baeyens, B.: A mechanistic description of Ni and Zn sorption on Na-montmorillonite. Part II: modelling. J. Contam. Hydrol. 27 (3), 223-248 (1997).

Bradbury, M.H., Baeyens, B.: Modelling the sorption of Zn and Ni on Ca-montmorillonite. Geochim. Cosmochim. Acta 63 (3), 325-336 (1999).

Bradbury, M.H., Baeyens, B.: Sorption of Eu on Na-and Ca-montmorillonites: experimental investigations and modelling with cation exchange and surface complexation. Geochim. Cosmochim. Acta 66 (13), 2325-2334 (2002).

Bradbury, M.H., Baeyens, B.: Modelling the sorption of Mn(II), Co(II), Ni(II), Zn(II), Cd(II), Eu(III), Am(III), Sn(IV), Th(IV), Np(V) and U(VI) on montmorillonite: Linear free energy relationships and estimates of surface binding constants for some selected heavy metals and actinides. Geochim. Cosmochim. Acta 69 (4), 875-892 (2005).

Bradbury, M.H., Baeyens, B.: Sorption modelling on illite. Part I: Titration measurements and the sorption of Ni, Co, Eu and Sn. Geochim. Cosmochim. Acta 73 (4), 990-1003 (2009).

Brewitz, W.: Eignungsprüfung der Schachtanlage Konrad für die Endlagerung radioaktiver Abfälle. GSF-T 136 (1982).

Bro, R.: PARAFAC: Tutorial and applications. Chemom. Intell. Lab. Syst. 38, 149-171 (1997).

Bünzli, J.-C., Piguet C.: Taking advantage of luminescent lanthanide ions. Chem. Soc. Rev. 34, 1048-1077 (2005).

Cacheris, W.P., Choppin, G.R.: Dissociation kinetics of thorium-humate complex. Radiochim. Acta 42, 185-190 (1987).

Catalano, J.G., Brown, G.E.: Uranyl adsorption onto montmorillonite: Evaluation of binding sites and carbonate complexation. Geochim. Cosmochim. Acta 69 (12), 2995-3005 (2005).

Chakraborty, S., Favre, F., Banerjee, D., Scheinost, A.C., Mullet, M., Ehrhardt, J.-J., Brendle, J., Vidal, L., Charlet, L.: U(VI) sorption and reduction by Fe(II) sorbed on montmorillonite. Environ. Sci. Technol. 44 (10), 3779-3785 (2010).

Chisholm-Brause, C.J., Berg, J.M., Matzner, R.A., Morris, D.E.: Uranium(VI) sorption complexes on montmorillonite as a function of solution chemistry. J. Colloid Interface Sci. 233 (1), 38-49 (2001).

Choppin, G.R., Clark, S.B.: The kinetic interactions of metal ions with humic acids. Mar. Chem. 36, 27-38 (1991).

Claret, F., Schäfer, T., Bauer, A., Buckau, G.: Generation of humic and fulvic acid from Callovo-Oxfordian clay under high alkaline conditions. Sci. Total Environ. 317, 189-200 (2003).

Collins, R.N., Saito, T., Aoyagi, N., Payne, T.E., Kimura, T., Waite, D.T.: Applications of time-resolved laser fluorescence spectroscopy to the environmental biogeochemistry of actinides. J. Environ. Qual. 40, 731-741 (2011).

COMSOL: COMSOL Multiphysics® 4.2a. Finite element analysis, solver and simulation software package for various physics and engineering applications. COMSOL, Inc., Burlington. http://www.comsol.com (2011).

Courdouan, A., Christl, I., Meylan, S., Wersin, P., Kretzschmar, R.: Isolation and characterization of dissolved organic matter from the Callovo-Oxfordian formation. Appl. Geochem. 22, 1537-1548 (2007a).

Courdouan, A., Christl, I., Meylan, S., Wersin, P., Kretzschmar, R.: Characterization of dissolved organic matter in anoxic rock extracts and in situ pore water of the opalinus clay. Appl. Geochem. 22, 2926-2939 (2007b).

Crank, J.: The mathematics of diffusion. Oxford University Press Inc., New York (1975).

Dagnelie, R.V.H., Descostes, M., Pointeau, I., Klein, J., Grenut, B., Radwan, J., Lebeau, D., Georgin, D., Giffaut, E.: Sorption and diffusion of organic acids through clayrock: Comparison with inorganic anions. J. Hydrol. 511, 619-627 (2014).

Deacon, G.B., Phillips, R.J.: Relationships between the carbon-oxygen stretching frequencies of carboxylato complexes and the type of carboxylate coordination. Coord. Chem. Rev. 33(3), 227-250 (1980).

Doherty, J.E., Hunt, R.J.: Approaches to highly parameterized inversion—a guide to using PEST for groundwater-model calibration. Scientific Investigations Report 2010–5169, US Geological Survey (2010).

Dong, W., Brooks, S.C.: Determination of the formation constants of ternary complexes of uranyl and carbonate with alkaline earth metals (Mg^{2+}, Ca^{2+}, Sr^{2+}, and Ba^{2+}) using anion exchange method. Environ. Sci. Technol. 40 (15), 4689-4695 (2006).

Dreissig, I., Weiss, S., Hennig, C., Bernhard, G., Zänker H.: Formation of uranium(IV)-silica colloids at near-neutral pH. Geochim. Cosmochim. Acta 75, 352-367 (2011).

Drobot, B., Steudtner, R., Raff, J., Geipel, G., Brendler, V., Tsushima, S.: Combining luminescence spectroscopy, parallel factor analysis and quantum chemistry to reveal metal speciation–a case study of uranyl(VI) hydrolysis. Chem. Sci. 6(2), 964-972 (2015).

Duffield, R.B., Calvin, M.: The stability of chelate compounds. III. Exchange reactions of copper chelate compounds. J. Am. Chem. Soc. 68, 557-561 (1946).

Edelstein, N.M., Klenze, R., Fanghänel, Th., Hubert, S.: Optical properties of Cm(III) in crystals and solutions and their application to Cm(III) speciation. Coord. Chem. Rev. 250, 948-973 (2006).

Fanghänel, T., Neck V., Kim J.I.: The ion product of H_2O, dissociation constants of H_2CO_3 and Pitzer parameters in the system $Na^+/H^+/OH^-/HCO_3^-/CO_3^{2-}/ClO_4^-/H_2O$ at 25°C. J. Sol. Chem. 25, 327-343 (1996).

Felipe-Sotelo, M., Edgar, M., Beattie, T., Warwick, P., Evans, N.D.M., Read, D.: Effect of anthropogenic organic complexants on the solubility of Ni, Th, U(IV) and U(VI). J. Hazard. Mater. 300, 553-560 (2015).

Felmy, A.R., Rai D., Mason M.J.: The solubility of hydrous thorium(IV) oxide in chloride media: Development of an aqueous ion-interaction model. Radiochim. Acta 55, 177-185 (1991).

Francis, A.J., Dodge, C.J., Gillow, J.B. and Papenguth, H.W.: Biotransformation of uranium compounds in high ionic strength brine by a halophilic bacterium under denitrifying conditions. Environ. Sci. Technol. 34, 2311-2317 (2000).

Francis, A.J., Gillow, J.B., Dodge, C.J., Harris, R., Beveridge, T.J., Papenguth, H.W.: Uranium association with halophilic and non-halophilic bacteria and archaea. Radiochim. Acta 92, 481-488 (2004).

Freundlich, H.: Ueber Kolloidfällung und Adsorption. Ztschr. F. Chem. u. Indus. Kolloide 1, 321-331 (1907).

Freyer, M., Walther, C., Stumpf, T., Buckau, G., Fanghänel, T.: Formation of Cm humate complexes in aqueous solution at pH_c 3 to 5.5: The role of fast interchange. Radiochim. Acta 97, 547-558 (2009).

Fröhlich, D.R., Amayri, S., Drebert, J., Reich, T.: Influence of humic acid on neptunium(V) sorption and diffusion in Opalinus Clay. Radiochim. Acta 101, 553-560 (2013).

Fröls, S., Dyall-Smith, M., Pfeifer, F.: Biofilm formation by haloarchaea. Environ. Microbiol. 14, 3159-3174 (2012).

Gaines Jr., G.L., Thomas, H.C.: Adsorption studies on clay minerals. ii. A formulation of the thermodynamics of exchange adsorption. J. Chem. Phys. 21 (4), 714-718 (1953).

Geckeis, H., Rabung, T., Ngo Manh, T., Kim, J.I., Beck, H.P.: Humic colloid-borne natural polyvalent metal ions: dissociation experiment. Environ. Sci. Technol. 36, 2946-2952 (2002).

Gerasch, R.: Simulation und Parameterschätzung von ^{22}Na Diffusion in einem Opalinus-Bohrkern mittels COMSOL Multiphysics und GeoPET-Datenabgleich. Diploma thesis, Brandenburgische Technische Universität Cottbus-Senftenberg, Senftenberg (2015).

Gillow, J.B., Francis, A.J., Papenguth, H.W.: The role of subterranean microbes in facilitating actinide migration at the Grimsel Test Site and Waste Isolation Pilot Plant. Radiochim. Acta 88, 769-774 (2001).

Glaus, M.A., Baeyens, B., Bradbury, M.H., Jakob, A., Van Loon, L.R., Yaroshchuk, A.E.: Diffusion of ^{22}Na and ^{85}Sr in montmorillonite: Evidence of interlayer diffusion being the dominant pathway at high compaction. Environ. Sci. Technol. 41, 478-485 (2007).

Glaus, M.A., Frick, S., Rossé, R., Van Loon, L.R.: Comparative study of tracer diffusion of HTO, $^{22}Na^{+}$ and $^{36}Cl^{-}$ in compacted kaolinite, illite and montmorillonite. Geochim. Cosmochim. Acta 74, 1999-2010 (2010).

Glaus, M.A., Rossé, R., Van Loon L.R., Yaroshchuk, A.E.: Tracer diffusion in sintered stainless steel filters: measurement of effective diffusion coefficients and implications for diffusion studies with compacted clays. Clays Clay Miner. 56, 677-685 (2008).

González Sánchez, F., Van Loon, L.R., Gimmi, T., Jakob, A., Glaus, M.A., Diamond, L.W.: Self-diffusion of water and its dependence on temperature and ionic strength in highly compacted montmorillonite, illite and kaolinite. Appl. Geochem. 23, 3840-3851 (2008).

Grenthe, I., Fuger, J., Konings, R.J.M., Lemire, R.J., Muller, A.B., Nguyen-Trung, C., Wanner, H.: Chemical Thermodynamics of Uranium. Nuclear Energy Agency (1992).

Gruber, C., Legat, A., Pfaffenhuemer, M., Radax, C., Weidler, G., Busse, H.-J., Stan-Lotter, H.: *Halobacterium noricense* sp. nov., an archaeal isolate from a bore core of an alpine Permian salt deposit, classification of *Halobacterium* sp. NRC-1 as a strain of *H. salinarum* and emended description of *H. salinarum*. Extremophiles 8, 431-439 (2004).

Guggenheim, E.A., Turgeon, J.C.: Specific interaction of ions. Trans. Faraday Soc. 51 (0), 747-761 (1955).

Guillaumont, R., Fanghänel, T., Neck, V., Fuger, J., Palmer, D.A., Grenthe, I., Rand, M.H.: Update on the Chemical Thermodynamics of Uranium, Neptunium, Plutonium, Americium and Technetium (OECD/NEA, ed.). Elsevier, Amsterdam (2003).

Heller, A., Barkleit, A., Foerstendorf, H., Tsushima, S., Heim, K., Bernhard, G.: Curium(III) citrate speciation in biological systems: An europium(III) assisted spectroscopic and quantum chemical study. Dalton Trans. 41, 13969-13983 (2012).

Horrocks, W.D., Sudnick, D.R.: Lanthanide ion probes of structure in biology - Laser-induced luminescence decay constants provide a direct measure of the number of metal-coordinated water-molecules. J. Am. Chem. Soc. 101(2), 334-340 (1979).

Hoth, P., Wirth, H., Reinhold, K., Bräuer, V., Krull, P., Feldrappe, H.: Endlagerung radioaktiver Abfälle in tiefen geologischen Formationen Deutschlands – Untersuchung und Bewertung von Tongesteinsformationen. Bundesanstalt für Geowissenschaften und Rohstoffe (BGR), Berlin/Hannover (2007).

Huang, W.H., Keller, W.D.: Dissolution of clay minerals in dilute organic acids at room temperature. Am. Mineral. 56, 1082-1095 (1971).

Hummel, W., Anderegg, G., Rao, L., Puigdomènech, I., Tochiyama, O.: Chemical Thermodynamics of Compounds and Complexes of U, Np, Pu, Am, Tc, Se, Ni and Zr with Selected Organic Ligands. Elsevier, Amsterdam (2005).

Hummel, W.: Radioactive contaminants in the subsurface: The influence of complexing ligands on trace metal speciation. Chem. Monthly 139, 459-480 (2008).

IAEA: Predisposal management of organic radioactive waste. Technical Reports Series No. 427, IAEA, Vienna (2004).

Jakob, A., Pfingsten, W., Van Loon, L.R.: Effects of sorption competition on caesium diffusion through compacted argillaceous rock. Geochim. Cosmochim. Acta 73, 2441-2456 (2009).

Jan, S., Santin, G., Strul, D., Staelens, S., Assie, K., Autret, D., Avner, S.: GATE: a simulation toolkit for PET and SPECT. Physics in Medicine and Biology 49(19), 4543-4561 (2004).

Joseph, C., Schmeide, K., Sachs, S., Brendler, V., Geipel, G., Bernhard, G.: Sorption of uranium(VI) onto Opalinus Clay in the absence and presence of humic acid in Opalinus Clay pore water. Chem. Geol. 284, 240-250 (2011).

Joseph, C., Schmeide, K.: Influence of citric acid on U(VI) diffusion in Opalinus Clay (in preparation).

Joseph, C., Stockmann, M., Schmeide, K., Sachs, S., Brendler, V., Bernhard, G.: Sorption of U(VI) onto Opalinus Clay: Effects of pH and humic acid. Appl. Geochem. 36, 104-117 (2013a).

Joseph, C., Van Loon, L.R., Jakob, A., Steudtner, R., Schmeide, K., Sachs, S., Bernhard, G.: Diffusion of U(VI) in Opalinus Clay: Influence of temperature and humic acid. Geochim. Cosmochim. Acta 109, 74-89 (2013b).

Jové Colón, C.F., Weck, P.F., Sassani, D.H., Zheng, L., Rutqvist, J., Steefel, C., Kim, K., Nakagawa, S., Houseworth, J., Birkholzer, J., Caporuscio, F.A., Cheshire, M., Rearick, M.S., McCarney, M.K., Zavarin, M., Benedicto, A., Kersting, A.B., Sutton, M., Jerden, J., Frey, K.E., Copple, J.M., Ebert, W.: Fuel Cycle Research and Development: Evaluation of Used Fuel Disposition in Clay-Bearing Rock (FCRD-UFD-2014-000056). SAND2014-18303 R, Sandia National Laboratories, Albuquerque, New Mexico (2014).

Kakihana, M., Nagumo, T., Okamoto, M., Kakihana, H.: Coordination structures for uranyl carboxylate complexes in aqueous solution studied by IR and ^{13}C NMR spectra. J. Phys. Chem. 91(24), 6128-6136 (1987).

Keizer, M.G., Van Riemsdijk, W.H.: ECOSAT – a computer program for the calculation of speciation and transport in soil-water systems (version 4.8). User manual, Wageningen University (2005).

Keller, C.: The Chemistry of the Transuranium Elements, Volume 3, Verlag Chemie GmbH, Weinheim, Germany (1971).

Kim, J.I., Klenze, R., Wimmer, H., Runde, W., Hauser, W.: A study of the carbonate complexation of Cm-III and Eu-III by time-resolved laser fluorescence spectroscopy. J. Alloys Compd. 213-214, 333-340 (1994).

Kimura, T., Choppin G.R.: Luminescence study on determination of the hydration number of Cm(III). J. Alloys Compd. 213-214, 313-317 (1994).

Kimura, T., Choppin, G.R., Kato, Y., Yoshida, Z.: Determination of the hydration number of Cm(III) in various aqueous solutions. Radiochim. Acta 72, 61-64 (1996).

Kimura, T., Kato, Y.: Luminescence study on hydration states of lanthanide(III)–polyaminopolycarboxylate complexes in aqueous solution. J. Alloys Compd. 277, 806-810 (1998).

King, S.J., Warwick, P., Hall, A., Bryan, N.D.: The dissociation kinetics of dissolved metal–humate complexes. Phys. Chem. Chem. Phys. 3, 2080-2085 (2001).

Kinniburgh, D.G., Milne, C.J., Benedetti, M.F., Pinheiro, J.P., Filius, J., Koopal, L.K., Van Riemsdijk, W.H.: Metal ion binding by humic acid: Application of the NICA-donnan model. Environ. Sci. Technol. 30, 1687-1698 (1996).

Kirishima, A., Onishi, Y., Sato, N., Tochiyama, O.: Determination of the thermodynamic quantities of uranium(VI)-carboxylate complexes by microcalorimetry. J. Chem. Thermodynamics 39, 1432-1438 (2007).

Klimmek, S.: Charakterisierung der Biosorption von Schwermetallen an Algen. PhD thesis, Technische Universität Berlin, Berlin (2003).

Kobayashi, T., Scheinost, A.C., Fellhauer, D., Gaona, X., Altmaier, M.: Redox behavior of Tc(VII)/Tc(IV) under various reducing conditions in 0.1 M NaCl solutions. Radiochim. Acta 101, 323-332 (2013).

Koopal, L.K., Van Riemsdijk, W.H., de Wit, J.C.M., Benedetti, M.F.: Analytical isotherm equations for multicomponent adsorption to heterogeneous surfaces. J. Colloid Interf. Sci. 166, 51-60 (1994).

Křepelová, A., Brendler, V., Sachs, S., Baumann, N., Bernhard, G.: U(VI)-kaolinite surface complexation in absence and presence of humic acid studied by TRLFS. Environ. Sci. Technol. 41 (17), 6142-6147 (2007).

Křepelová, A., Sachs, S., Bernhard, G.: Uranium(VI) sorption onto kaolinite in the presence and absence of humic acid. Radiochim. Acta 94 (12), 825-833 (2006).

Küchle, W., Dolg, M., Stoll, H., Preuss, H.: Energy-adjusted pseudopotentials for the actinides. Parameter sets and test calculations for thorium and thorium monoxide. J. Chem. Phys. 100, 7535-7542 (1994).

Kulenkampff, J., Gründig, M., Zakhnini, A., Gerasch, R., Lippmann-Pipke J.: Process tomography of diffusion with PET for evaluating anisotropy and heterogeneity. Clay Minerals, in press (2015).

Kümmel, R., Worch, E.: Adsorption aus wässrigen Lösungen. Dt. Verl. für Grundstoffindustrie: Leipzig (1990).

Laguerie, C., Aubry, M., Couderc, J.P.: Some physiochemical data on monohydrate citric acid solutions in water - Solubility, density, viscosity, diffusivity, pH of standard solution, and refractive index. J. Chem. Eng. Data 21, 85-87 (1976).

Lee, J.-Y., Gaona, X., Vespa, M., Dardenne, K., Rothe, J., Rabung, T., Altmaier, M., Yun, J.-I.: Formation and structural analysis of ternary Mg-UO_2-CO_3 complexes using TRLFS and EXAFS. 15th International Conference on the Chemistry and Migration Behaviour of Actinides and Fission Products in the Geosphere, Santa Fe, New Mexico, 303-304 (2015).

Lefèvre, G.: *In situ* Fourier-transform infrared spectroscopy studies of inorganic ions adsorption on metal oxides and hydroxides. Adv. Colloid Interface Sci. 107, 109-123 (2004).

Lemire, R.J., Berner, U., Musikas, C., Palmer, D.A., Taylor, P., Tochiyama, O.: Chemical Thermodynamics of Iron Vol. 13a, Part, OECD, NEA-TDB, North Holland, Amsterdam (2013).

Lippold, H., Müller, N., Kupsch, H.: Effect of humic acid on the pH-dependent adsorption of terbium(III) onto geological materials. Appl. Geochem. 20, 1209-1217 (2005).

Lippold, H., Lippmann-Pipke, J.: Effect of humic matter on metal adsorption onto clay materials: Testing the linear additive model. J. Contam. Hydrol. 109, 40-48 (2009).

Lippold, H., Eidner, S., Kumke, M.U., Lippmann-Pipke, J.: Diffusion, degradation or on-site stabilisation – identifying causes of kinetic processes involved in metal-humate complexation. Appl. Geochem. 27, 250-256 (2012).

Lippold, H., Lippmann-Pipke, J.: New insights into the dynamics of adsorption equilibria of humic matter as revealed by radiotracer studies. Geochim. Cosmochim. Acta 133, 362-371 (2014).

Liu, J.G., Luo, G.S., Pan, S., Wang, J.D.: Diffusion coefficients of carboxylic acids in mixed solvents of water and 1-butanol. Chem. Engineering Processing 43, 43-47 (2004).

Lloyd, J.R., Gadd, G.M.: The Geomicrobiology of Radionuclides. Geomicrobiol. J. 28, 383-386 (2011).

Loukiala, A., Tuna, U., Beer, S., Jahnke, S., Ruotsalainen, U.: Gap-filling methods for 3D PlanTIS data. Physics in Medicine and Biology 55(20), 6125-6139 (2010).

Lucks, C., Rossberg, A., Tsushima, S., Foerstendorf, H., Scheinost, A.C., Bernhard, G.: Aqueous uranium(VI) complexes with acetic and succinic acid: speciation and structure revisited. Inorg. Chem. 51, 12288-12300 (2012).

Lütke, L., Moll, H., Bachvarova, V., Selenska-Pobell, S., Bernhard, G.: The U(VI) speciation influenced by a novel *Paenibacillus* isolate from Mont Terri Opalinus clay. Dalton Trans. 42, 6979-6988 (2013).

Mansel, A., Kupsch, H.: Radiolabelling of humic substances with ^{14}C by azo coupling [^{14}C]phenyldiazonium ions. Appl. Rad. Isot. 65, 793-797 (2007).

Marquardt, C. (ed.): Beiträge zum geochemischen Langzeitsicherheitsnachweis eines Endlagers für radioaktive Abfälle. Wechselwirkung und Transport von Actiniden im natürlichen Tongestein unter Berücksichtigung von Huminstoffen und Tonorganika. Abschlussbericht, KIT (2011).

Marques Fernandes, M., Baeyens, B., Dähn, R., Scheinost, A.C., Bradbury, M.H.: U(VI) sorption on montmorillonite in the absence and presence of carbonate: A macroscopic and microscopic study. Geochim. Cosmochim. Acta 93, 262-277 (2012).

McGenity, T.J., Gemmell, R.T., Grant, W.D., Stan-Lotter, H.: Origins of halophilic microorganisms in ancient salt deposits. Environ. Microbiol. 2, 243-250 (2000).

Meleshyn, A., Azeroual, M., Reeck, T., Houben, G., Riebe, B., Bunnenberg, C.: Influence of (calcium-)uranyl-carbonate complexation on U(VI) sorption on Ca- and Na-bentonites. Environ. Sci. Technol. 43 (13), 4896-4901 (2009).

Milne, C.J., Kinniburgh, D.G., van Riemsdijk, W.H., Tipping, E.: Generic NICA-donnan model parameters for metal ion binding by humic substances. Environ. Sci. Technol. 37, 958-971 (2003).

Miyake, C., Nürnberg, H.W.: Co-ordination compounds of actinides. -I-The determination of the stability constants of uranyl complexes with anions of carboxylic acids. J. Inorg. Nucl. Chem. 29, 2411-2429 (1967).

Moll, H., Merroun, M.L., Hennig, Ch., Rossberg, A., Selenska-Pobell, S., Bernhard, G.: The interaction of *Desulfovibrio äspöensis* DSM 10631^T with plutonium. Radiochim. Acta 94, 815-824 (2006).

Moll, H., Johnsson, A., Schäfer, M., Pedersen, K., Budzikiewicz, H., Bernhard, G.: Curium(III) complexation with pyoverdins secreted by a groundwater strain of *Pseudomonas fluorescens*. Biometals 21, 219-228 (2008).

Moll, H., Lütke, L., Bachvarova, V., Steudner, R., Geißler, A., Krawczyk-Bärsch, E., Selenska-Pobell, S., Bernhard, G.: Microbial diversity in Opalinus Clay and interaction of dominant microbial strains with actinides. Wiss.-Techn. Berichte, HZDR-036, Helmholtz-Zentrum Dresden-Rossendorf, Dresden (2013) and Ref. therein.

Moll, H., Lütke, L., Bachvarova, V., Cherkouk, A., Selenska-Pobell, S., Bernhard, G.: Interactions of the Mont Terri Opalinus Clay isolate *Sporomusa* sp. MT-2.99 with curium(III) and europium(III). Geomicrobiol. J. 31, 682-696 (2014).

Moskvin, A.I.: Complex formation of the actinides with anions of acids in aqueous solutions. Radiokhimiya 11, 458-460 (1969).

Moulin, C., Wei, J., Van Iseghem, P., Laszak, I., Plancque, G., Moulin, V.: Europium complexes investigations in natural waters by time-resolved laser-induced fluorescence. Anal. Chim. Acta 296, 253-261 (1999).

Müller, K., Brendler, V., Foerstendorf, H.: Aqueous uranium(VI) hydrolysis species characterized by attenuated total reflection Fourier-transform infrared spectroscopy. Inorg. Chem. 47, 10127-10134 (2008).

Müller, K., Foerstendorf, H., Meusel, T., Brendler, V., Lefève, G., Comarmond, M.J., Payne, T.E.: Sorption of U(VI) at the TiO_2-water interface: an *in situ* vibrational spectroscopic study. Geochim. Cosmochim. Acta 76, 191-205 (2012).

Müller, K., Foerstendorf, H., Brendler, V., Rossberg, A., Stolze, K., Gröschel, A.: The surface reactions of U(VI) on γ-Al_2O_3 - *In situ* spectroscopic evaluation of the transition from sorption complexation to surface precipitation. Chem. Geol. 357, 75-84 (2013).

Nagra: Projekt Opalinuston. Synthese der geowissenschaftlichen Untersuchungsergebnisse. Entsorgungsnachweis für abgebrannte Brennelemente, verglaste hochaktive sowie langlebige mittelaktive Abfälle. Technischer Bericht 02-03, Nagra (2002).

Neu, M.P., Icopini, G.A., Boukhalfa, H.: Plutonium speciation affected by environmental bacteria. Radiochim. Acta 93, 705-714 (2005).

Ockenden, D.W., Welch, G.A.: The preparation and properties of some plutonium compounds. Part V. Colloidal quadrivalent plutonium. J. Chem. Soc., 3358-3363 (1956).

Ohnuki, T., Yoshida, T., Ozaki, T., Kozai, N., Sakamoto, F., Nankawa, T., Suzuki, J., Francis, A.J.: Modeling of the interaction of Pu(VI) with the mixture of microorganism and clay. J. Nucl. Sci. Technol. 46, 55-59 (2009).

Ozaki, T., Arisaka, M., Kimura, T., Francis, A.J., Yoshida, Z.: Empirical method for prediction of the coordination environment of Eu(III) by time-resolved laser-induced fluorescence spectroscopy. Anal. Bioanal. Chem. 374, 1101-1104 (2002).

Ozaki, T., Gillow, J.B., Kimura, T., Ohnuki, T., Yoshida, Z., Francis, A.J.: Sorption behavior of europium(III) and curium(III) on the cell surface of microorganisms. Radiochim. Acta 92, 741-748 (2004).

Pabalan, R.T., Turner, D.R.: Uranium(6+) sorption on montmorillonite: Experimental and surface complexation modeling study. Aquat. Geochem. 2 (3), 203-226 (1997).

Panak, P.J., Nitsche, H.: Interaction of aerobic soil bacteria with plutonium(VI). Radiochim. Acta 89, 499-504 (2001).

Parkhurst, D.L., Appelo, C.A.J.: Description of input and examples for PHREEQC version 3 - a computer program for speciation, batch-reaction, onedimensional transport, and inverse geochemical calculations. In: Book 6. U.S. Geological Survey Techniques and Methods, Ch. A43, p. 497 (2013).

Pearson, F.J.: Opalinus Clay experimental water: A1Type, Version 980318. PSI Internal report TM-44-98-07, Paul Scherrer Institut, Villigen PSI (1998).

Pearson, F., Bath, A., Boisson, J.-Y., Fernández, A.M., Gäbler, H.-E., Gaucher, E., Gautschi, A., Griffault, L., Hernán, P., Waber, H.N.: Mont Terri Project – Geochemistry of Water in the Opalinus Clay Formation at the Mont Terri Rock Laboratory. Reports of the Federal Office for Water and Geology (FOWG), Geology Series. F., 5: 321, (2003).

Peretyazhko, T., Zachara, J.M., Heald, S.M., Jeon, B.H., Kukkadapu, R.K., Liu, C., Moore, D., Resch, C.T.: Heterogeneous reduction of Tc(VII) by Fe(II) at the solid-water interphase. Geochim. Cosmochim. Acta 72, 1521-1539 (2008).

Peretyazhko, T.S., Zachara, J.M., Kukkadapu, R.K., Heald, S.M., Kutnyakov, I.V., et al.: Pertechnetate (TcO_4^-) reduction by reactive ferrous iron forms in naturally anoxic, redox transition zone sediments from the Hanford Site, USA. Geochim. Cosmochim. Acta 92, 48-66 (2012).

Petrov, V., Gaona, X, Fellhauer, D., Dardenne, K., Kalmykov, S., Altmaier, M.: Contribution to Migration Conference, Beijing (China) (2011).

Plancque, G., Moulin V., Toulhoat, P., Moulin C.: Europium speciation by time-resolved laser-induced fluorescence. Anal. Chim. Acta 478, 11-22 (2003).

Poinssot, C., Baeyens, B., Bradbury, M.H.: Experimental studies of Cs, Sr, Ni, and Eu sorption on Na-illite and the modelling of Cs sorption. NTB-99-04 (1999).

Prekeges, J.: Positron-Emission-Tomography. In: Nuclear Medicine Instrumentation, 195-252. Jones & Bartlett, Burlington (2013).

Quilès, F., Burneau, A.: Infrared and Raman spectra of uranyl(VI) oxo-hydroxo complexes in acid aqueous solutions: a chemometric study. Vib. Spectrosc. 23, 231-241 (2000).

Rao, L., Choppin, G.R., Clark, S.B.: A study of metal-humate interactions using cation exchange. Radiochim. Acta 66, 141-147 (1994).

Renshaw, J.C., Law, N., Geissler, A., Livens, F.R., Lloyd, J.R.: Impact of the Fe(III)-reducing bacteria *Geobacter sulfurreducens* and *Shewanella oneidensis* on the speciation of plutonium. Biogeochem. 94, 191-196 (2009).

Roldan, P.S., Chereul, E., Dietzel, O., Magnier, L., Pautrot, C., et al.: Raytest ClearPET(TM), a new generation small animal PET scanner. Nuclear Instruments and Methods in Physics Research Section A: Accelerators, Spectrometers, Detectors and Associated Equipment 571(1-2), 498-501 (2007).

Rossberg, A., Reich, T., Bernhard, G.: Complexation of uranium(VI) with protocatechuic acid – application of iterative transformation factor analysis to EXAFS spectroscopy. Anal. Bioanal. Chem. 376, 631-638 (2003).

Sachs, S., Křepelová, A., Schmeide, K., Koban, A., Günther, A., Mibus, J., Brendler, V., Geipel, G., Bernhard, G.: Joint Project: Migration of actinides in the system clay, humic substance, aquifer - Migration behavior of actinides (uranium, neptunium) in clays: Characterization and quantification of the influence of humic substances. Wissenschaftlich-Technische Berichte, FZD-460, Forschungszentrum Dresden-Rossendorf, Dresden (2007).

Schäfer, T., Claret, F., Bauer, A., Griffault, L., Ferrage, E., Lanson, B.: Natural organic matter (NOM)-clay association and impact on Callovo-Oxfordian clay stability in high alkaline solution: Spectromicroscopic evidence. J. Phys. IV 104, 413-416 (2003).

Schikora, J.: Simulation of diffusion-adsorption processes in natural geological media by means of COMSOL Multiphysics. Faculty of Mechanical Science and Engineering. Diploma thesis, Technische Universität Dresden, Dresden (2012).

Schmeide, K., Bernhard, G.: Sorption of Np(V) and Np(IV) onto kaolinite: Effects of pH, ionic strength, carbonate and humic acid. Appl. Geochem. 25 (8), 1238-1247 (2010).

Schmeide, K., Gürtler, S., Müller, K., Steudtner, R., Joseph, C., Bok, F., Brendler, V.: Interaction of U(VI) with Äspö diorite: A batch and *in situ* ATR FT-IR sorption study. Appl. Geochem. 49, 116-125 (2014).

Schmeide, K., Joseph, C.: Influence of organic ligands on U(VI) sorption onto Opalinus Clay between 10 and 50°C. Annual Report 2011, HZDR-013, Helmholtz-Zentrum Dresden-Rossendorf, Dresden, 41 (2012).

Schnurr, A., Marsac, R., Rabung, T., Lützenkirchen, J., Geckeis, H.: Sorption of Cm(III) and Eu(III) onto clay minerals under saline conditions: Batch adsorption, laser-fluorescence spectroscopy and modeling. Geochim. Cosmochim. Acta 151, 192-202 (2015).

Sémon, L., Boehme, C., Billard, I., Hennig, C., Lützenkirchen, K., Reich, T., Rossberg, A., Rossini, I., Wipff, G.: Do perchlorate and triflate anions bind to the uranyl cation in an acidic aqueous medium? A combined EXAFS and quantum mechanical investigation. Chem. Phys. Chem. 2, 591-598 (2001).

Skerencak, A., Höhne, S., Hofmann, S., Marquardt, C.M., Panak, P.J.: Spectroscopic studies on the thermodynamics of the complexation of trivalent curium with propionate in the temperature range from 20 to 90°C. J. Solution Chem. 42, 1-17 (2013).

Sladkov, V.: Uranyl complexation with acetate studied by means of affinity capillary electrophoresis. J. Chromatography A 1289, 133-138 (2013).

Sladkov, V.: Interaction of uranyl with acetate in aqueous solutions at variable temperatures. J. Chem. Thermodynamics 71, 148-154 (2014).

Spranger, F.: Immobilisierung von Tc(VII)/Tc(IV) an Eisenphasen. Bachelorarbeit, Technische Universität Dresden (2015).

Stan-Lotter, H., Fendrihan, H.: Halophilic Archaea: Life with desiccation, radiation and oligotrophy over geological times. Life 5, 1487-1496 (2015).

Staunton, S., Clay, P.G., Rees, L.V.C.: Diffusion of neptunium(V) in clays. Radiochim. Acta 49, 147-153 (1990).

Steudtner, R.: Zur Wechselwirkung von Uran mit den Bioliganden Citronensäure und Glucose. PhD thesis, Technische Universität Dresden, Dresden (2010).

Steudtner, R., Müller, K., Jäckel, E., Meyer, R., Schmeide, K., Günther A.: Uranium chemistry in citric acid solution. 4th EuCheMS Chemistry Congress, Prague (2012).

Suzuki, Y., Tanaka, K., Kozai, N., Ohnuki, T.: Effects of citrate, NTA, and EDTA on the reduction of U(VI) by Shewanella putrefaciens. Geomicrobiology J. 27, 245-250 (2010).

Swanson, J.S., Reed, D.T., Ams, D.A., Norden, D., Simmons, K.A.: Status report on the microbial characterization of halite and groundwater samples from the WIPP, Los Alamos National Laboratory, p. 1 (2012).

Thielemans, K., Tsoumpas, C., Mustafovic, S., Beisel, T., Aguiar, P., Dikaios, N., Jacobson, M.: STIR: software for tomographic image reconstruction release 2. Physics in Medicine and Biology 57(4), 867-883 (2012).

Thoenen, T.: Speciation calculations supporting the sorption data bases for argillaceous rocks and bentonite for the provisional safety analyses for SGT-E2. Arbeitsbericht NAB 12-52, Nagra, Wettingen (2014).

Thury, M., Bossart, P.: The Mont Terri Rock Laboratory, a new international research project in a Mesozoic shale formation, in Switzerland. Eng. Geol. 52, 347-359 (1999).

Tipping, E.: Cation binding by humic substances. Cambridge Environmental Chemistry Series, Vol. 12; Cambridge University Press: Cambridge, 2002.

Van Loon, L.R., Eikenberg, J.: A high-resolution abrasive method for determining diffusion profiles of sorbing radionuclides in dense argillaceous rocks. Appl. Radiat. Isot. 63, 11-21 (2005).

Van Loon, L.R., Soler, J.M., Bradbury, M.H.: Diffusion of HTO, $^{36}Cl^-$ and $^{125}I^-$ in Opalinus Clay samples from Mont Terri - Effect of confining pressure. J. Contam. Hydrol. 61, 73-83 (2003a).

Van Loon, L.R., Soler, J.M., Jakob, A., Bradbury, M.H.: Effect of confining pressure on the diffusion of HTO, $^{36}Cl^-$ and $^{125}I^-$ in a layered argillaceous rock (Opalinus Clay): diffusion perpendicular to the fabric. Appl. Geochem. 18, 1653-1662 (2003b).

Van Loon, L.R., Soler, J.M., Müller, W., Bradbury, M.H.: Anisotropic diffusion in layered argillaceous rocks: A case study with Opalinus Clay. Environ. Sci. Technol. 38(21), 5721-5728 (2004).

Van Loon, L.R., Soler, J.M.: Diffusion of HTO, $^{36}Cl^-$, $^{125}I^-$, and $^{22}Na^+$ in Opalinus Clay: Effect of Confining Pressure, Sample Orientation, Sample Depth and Temperature. PSI-Bericht 04-03, Paul Scherrer Institute, Villigen PSI (2004).

Wilson, R.E., Hu, Y.-J., Nitsche, H.: Detection and quantification of Pu(III, IV, V, and VI) using a 1.0-meter liquid core wave guide, Radiochim. Acta 93, 203-206 (2005).

Wolery, T.J.: EQ3/6, A software package for the geochemical modeling of aqueous systems, UCRL-MA-110662 Part I. Lawrence Livermore National Laboratory, Livermore (1992).

Wouters, K., Moors, H., Boven, P., Leys, N.: Evidence and characteristics of a diverse and metabolically active microbial community in deep subsurface clay borehole water. FEMS Microb. Ecol. 86, 458-473 (2013).

Wu, T., Amayri, S., Drebert, J., Van Loon, L.R., Reich, T.: Neptunium(V) sorption and diffusion in Opalinus Clay. Environ. Sci. Technol. 43, 6567-6571 (2009).

Wu, T., Wang, H., Zheng, Q., Li, J.Y.: Effect of organic matter on ^{125}I diffusion in bentonite. J. Radioanal. Nucl. Chem. 303, 255-260 (2015).

Wu, T., Wang, H., Zheng, Q., Zhao, Y. L., Van Loon, L. R.: Diffusion behavior of Se(IV) and Re(VII) in GMZ bentonite. Appl. Clay Sci. 101, 136-140 (2014).

Zakhnini, A., Kulenkampff, J., Sauerzapf, S., Pietrzyk, U., Lippmann-Pipke, J.: Monte Carlo simulations of GeoPET experiments: 3D images of tracer distributions (^{18}F, ^{124}I and ^{58}Co) in Opalinus Clay, anhydrite and quartz. Computers & Geosciences 57, 183-196 (2013).

13 Publications of the Helmholtz-Zentrum Dresden-Rossendorf (HZDR)

The following peer-reviewed publications, oral presentations and posters were published or presented at conferences in the 2011 to 2015 funding period to the actual project (02 E 10971) as well as to preceding projects financially supported from the BMWi (02 E 10156, 02 E 10176, 02 E 10618).

Publications (peer-reviewed):

Lippold, H., Lippmann-Pipke, J.: Dynamics of metal-humate complexation equilibria as revealed by isotope exchange studies – a matter of concentration and time. Geochim. Cosmochim. Acta (under review).

Poetsch, M., Lippold, H.: Effects of ionic strength and fulvic acid on the adsorption of Tb^{3+} and Eu^{3+} onto clay. J. Contam. Hydrol. (under review).

Kulenkampff, J., Gründig, M., Zakhnini, A., Lippmann-Pipke, J.: Process tomography of diffusion with PET for evaluating anisotropy and heterogeneity. Clay Minerals (in press).

Xiong, Q., Joseph, C., Schmeide, K., Jivkov, A.P.: Measurement and modelling of reactive transport in geological barriers for nuclear waste containment. Phys. Chem. Chem. Phys. 17, 30577-30589 (2015).

Moll, H., Lütke, L., Cherkouk, A.: Bacterial diversity in clay and actinide interactions with bacterial isolates in relation to nuclear waste disposal. In: Radionuclides in the Environment - Influence of chemical speciation and plant uptake on radionuclide migration. (Editoren: C. Walther, D.K. Gupta) Heidelberg, Springer Verlag (2015).

Krawczyk-Bärsch, E., Lütke, L., Moll, H., Bok, F., Steudtner, R., Rossberg, A.: A spectroscopic study on U(VI) biomineralization in cultivated Pseudomonas fluorescens biofilms isolated from granitic aquifers. Environ. Sci. Pollut. Res. 22, 4555-4565 (2015).

Moll, H., Lütke, L., Bachvarova, V., Cherkouk, A., Selenska-Pobell, S., Bernhard, G.: Interactions of the Mont Terri Opalinus Clay isolate Sporomusa sp. MT-2.99 with curium(III) and europium(III). Geomicrobiol. J. 31, 682-696 (2014).

Schmeide, K., Gürtler, S., Müller, K., Steudtner, R., Joseph, C., Bok, F., Brendler, V.: Interaction of U(VI) with Äspö diorite: A batch and *in situ* ATR FT-IR sorption study. Appl. Geochem. 49, 116-125 (2014).

Harzmann, S., Braun, F., Zakhnini, A., Weber, W.A., Pietrzyk, U., Mix, M.: Implementation of Cascade Gamma and Positron Range Corrections for I-124 Small Animal PET. IEEE Trans. Nucl. Sci. 61, 142-153 (2014).

Lippold, H., Lippmann-Pipke, J.: New insights into the dynamics of adsorption equilibria of humic matter as revealed by radiotracer studies. Geochim. Cosmochim. Acta 133, 362-371 (2014).

Zakhnini, A., Kulenkampff, J., Sauerzapf, S., Pietrzyk, U., Lippmann-Pipke, J.: Monte Carlo simulations of GeoPET experiments: 3D images of tracer distributions (^{18}F, ^{124}I and ^{58}Co) in Opalinus Clay, anhydrite and quartz. Computers & Geosciences 57, 183-196 (2013).

Joseph, C., Stockmann, M., Schmeide, K., Sachs, S., Brendler, V., Bernhard, G.: Sorption of U(VI) onto Opalinus Clay: Effects of pH and humic acid. Appl. Geochem. 36, 104-117 (2013).

Joseph, C., Van Loon, L.R., Jakob, A., Steudtner, R., Schmeide, K., Sachs, S., Bernhard, G.: Diffusion of U(VI) in Opalinus Clay: Influence of temperature and humic acid. Geochim. Cosmochim. Acta 109, 74-89 (2013).

Pietrzyk, U., Zakhnini, A., Axer, M., Sauerzapf, S., Benoit, D., Gaens, M.: EduGATE - basic examples for educative purpose using the GATE simulation platform. Zeitschrift für Medizinische Physik 23, 65-70 (2013).

Raditzky, B., Sachs, S., Schmeide, K., Barkleit, A., Geipel, G., Bernhard, G.: Spectroscopic study of americium(III) complexes with nitrogen containing organic model ligands. Polyhedron 65, 244-251 (2013).

Schmeide, K., Sachs, S., Bernhard, G.: Np(V) reduction by humic acid: Contribution of reduced sulfur functionalities to the redox behavior of humic acid. Sci. Total Environ. 419, 116-123 (2012).

Kremleva, A., Zhang, Y., Shor, A.M., Krüger, S., Joseph, C., Raditzky, B., Schmeide, K., Sachs, S., Bernhard, G., Rösch, N.: Uranyl(VI) complexation by sulfonate ligands: A relativistic density functional and time-resolved laser-induced fluorescence spectroscopy study. Eur. J. Inorg. Chem. 2012, 3636-3644 (2012).

Lippold, H., Eidner, S., Kumke, M.U., Lippmann-Pipke, J.: Diffusion, degradation or on-site stabilisation – identifying causes of kinetic processes involved in metal-humate complexation. Appl. Geochem. 27, 250-256 (2012).

Steudtner, R., Müller, K., Schmeide, K., Sachs, S., Bernhard, G.: Binary and ternary uranium(VI) humate complexes studied by attenuated total reflection Fourier-transform infrared spectroscopy. Dalton Trans. 40, 11920-11925 (2011).

PhD theses, diploma theses, bachelor theses:

Spranger, F.: Immobilisierung von Tc(VII)/Tc(IV) an Eisenphasen. Bachelor thesis, Technische Universität Dresden (2015).

Gerasch, R.: Simulation und Parameterschätzung von ^{22}Na-Diffusion in einem Opalinuston-Bohrkern mittels COMSOL Multiphysics und GeoPET-Datenabgleich. Master thesis, Brandenburgische Technische Universität Cottbus-Senftenberg (2015).

Bittner, L.: Prozessbeobachtung von Vergütungsmaßnahmen im Salzgestein mittels Positronen Emissions Tomographie (GeoPET). Diploma thesis, Hochschule Zittau/Görlitz (2014).

Joseph, C.: The ternary system U(VI) / humic acid / Opalinus Clay. PhD thesis, Technische Universität Dresden (2013).

Zehlike, L.: Durchführung von Sorptions- und Desorptionsversuchen von U(VI) an Montmorillonit. Bachelor thesis, Technische Universität Dresden (2013).

Schikora, J.: Simulation von Diffusions-Adsorptionsprozessen in natürlichem Gesteins-material mit COMSOL Multiphysics. Diploma thesis, Technische Universität Dresden (2012).

Oral presentations on conferences:

Fritsch, K., Schmeide, K.: U(VI) retention by montmorillonite at high salinities: Surface complexation modeling. International Workshop ABC-Salt (IV) - Actinide Brine Chemistry in a Salt-Based Repository. 14.-15.04.2015, Heidelberg, Germany.

Fritsch, K., Schmeide, K.: Montmorillonite as barrier material for uranium(VI) at high ionic strengths. 7th Mid-European Clay Conference, 16.-19.09.2014, Dresden, Germany.

Kulenkampff, J., Gründig, M., Zakhnini, A., Lippmann-Pipke, J.: Process tomography of diffusion with PET for evaluating anisotropy and heterogeneity. 7th Mid-European Clay Conference, 16.-19.09.2014, Dresden, Germany.

Gerasch, R., Kulenkampff, J., Lippmann-Pipke, J.: Parameter estimation of anisotropic diffusion in clay with COMSOL Multiphysics. COMSOL Conference 2014, 17.-19.09.2014, Cambridge, United Kingdom.

Moll, H., Lütke, L., Cherkouk, A., Bernhard, G.: Pu interaction with bacterial isolates from Mont Terri Opalinus Clay. Plutonium Futures - The Science 2014, 07.-12.09.2014, Las Vegas, USA.

Schmeide, K., Joseph, C., Brendler, V.: Uranium(VI) retention in clay and crystalline rock: How and why does it differ. 8th European Summer School on Separation Chemistry and Conditioning as well as Supramolecular, Intermolecular, Interaggregate Interactions, 07.-09.07.2014, Gustav-Stresemann-Institut, Bonn/Bad Godesberg, Germany.

Moll, H., Cherkouk, A.: Microorganisms and their impact on radionuclide speciation. 8th European Summer School on Separation Chemistry and Conditioning as well as Supramolecular, Intermolecular, Interaggregate Interactions, 07.-09.07.2014, Gustav-Stresemann-Institut, Bonn/Bad Godesberg, Germany.

Moll, H., Lütke, L., Cherkouk, A., Bernhard, G.: Actinide/Lanthanide interaction studies with a typical bacterial isolate from Mont Terri Opalinus Clay a potential host rock for nuclear waste disposal. IGD-TP Geodisposal 2014 Conference, 24.-26.06.2014, Manchester, United Kingdom.

Poetsch, M., Claus, M., Lippold, H.: Effect of ionic strength on the mobility of radionuclides in the presence of natural organic matter: Testing the Linear Additive Model. Goldschmidt Conference 2014, 08.-13.06.2014, Sacramento, USA.

Schmeide, K., Joseph, C., Fritsch, K.: Uranium(VI) and neptunium(V) retention by clay minerals and natural clay rock – Influence of clay organics, temperature and pore water salinity. 51st Annual Meeting of the Clay Minerals Society, 17.-21.05.2014, College Station, Texas, USA.

Schmeide, K., Joseph, C., Brendler, V.: U(VI) retention by potential host rocks: Comparison of clay and crystalline rock. RadChem 2014 - 17th Radiochemical Conference, 11.-16.05.2014, Mariánské Lázně, Czech Republic.

Moll, H., Lütke, L., Cherkouk, A., Bernhard, G.: Pu interaction studies with a typical bacterial isolate from Mont Terri Opalinus Clay. TD-246 Joint BN, GD, HT, MA Mont Terri Meeting, 10.-11.02.2014, St. Ursanne, Switzerland.

Bittner, L., Kulenkampff, J., Gründig, M., Lippmann-Pipke, J., Enzmann, F.: Direct observation of waterglass impregnation of fractured salt rock with positron emission tomography. International Conference on the Performance of Engineered Barriers: Backfill, Plugs & Seals, 06.-07.02.2014, Hannover, Germany.

Moll, H., Lütke, L., Cherkouk, A., Selenska-Pobell, S., Bernhard, G., Brendler, V.: Microbial influences on radionuclide behaviour – an example of less-understood problems and how to solve them. IGD-TP 4th Exchange Forum (EF4), 29.-30.10.2013, Prague, Czech Republic.

Wolf, M., Enzmann, F., Kulenkampff, J., Lippmann-Pipke, J.: 3D analysis of fluid flow in fissured salt rock. Migration'13 - 14th International Conference on the Chemistry and Migration Behaviour of Actinides and Fission Products in the Geosphere, 08.-13.09.2013, Brighton, United Kingdom.

Kulenkampff, J., Gründig, M., Korn, N., Zakhnini, A., Barth, T., Lippmann-Pipke, J.: Application of high-resolution positron-emission-tomography for quantitative spatiotemporal process monitoring in dense material. 7th World Congress on Industrial Process Tomography, 02.-05.09.2013, Krakow, Poland.

Fritsch, K., Schmeide, K.: Uranium(VI) sorption on montmorillonite in high ionic strength media. International Workshop ABC-Salt (III) - Actinide Brine Chemistry in a Salt-Based Repository. 15.-17.04.2013, Santa Fe, USA.

Kulenkampff, J., Gründig, M., Zakhnini, A., Lippmann-Pipke, J.: PET-Prozesstomographie von Transportvorgängen in Bohrkernen zur Verbesserung des Prozessverständnisses und zur Verifikation von Modellcodes. 73. Jahrestagung der Deutschen Geophysikalischen Gesellschaft, 04.-07.03.2013, Leipzig, Germany.

Joseph, C., van Loon, L. R., Jakob, A., Steudtner, R., Schmeide, K., Sachs, S., Bernhard, G.: Do elevated temperatures and organic matter influence the U(VI) diffusion through argillaceous rock? 5th International Meeting on "Clays in Natural and Engineered Barriers for Radioactive Waste Confinement", 22.-25.10.2012, Montpellier, France.

Kulenkampff, J., Gründig, M., Schikora, J., Zakhnini, A., Lippmann-Pipke, J.: Long-term spatiotemporal monitoring of diffusion processes in Opalinus drill cores with GeoPET and parameterization with COMSOL Multiphysics. 5th International Meeting on "Clays in Natural and Engineered Barriers for Radioactive Waste Confinement", 22.-25.10.2012, Montpellier, France.

Sauerzapf, S., Zakhnini, A., Weber, W., Pietrzyk, U., Mix, M.: Analyse und Optimierung einer Positronenreichweitenkorrektur innerhalb der iterativen Rekonstruktion für die Kleintierbildgebung. 43. Jahrestagung der Deutschen Gesellschaft für Medizinische Physik, 26.-29.09.2012, Jena, Germany.

Steudtner, R., Müller, K., Jäckel, E., Meyer, R., Schmeide, K., Günther, A.: Uranium chemistry in citric acid solution. 4th EuCheMS Chemistry Congress, 26.-30.08.2012, Prague, Czech Republic.

Lippold, H., Lippmann-Pipke, J.: Radiotracer studies on the kinetics and equilibrium characteristics of adsorption of humic matter. Goldschmidt 2012, 24.-29.06.2012, Montreal, Canada.

Zakhnini, A., Kulenkampff, J., Lippmann-Pipke, J., Pietrzyk, U.: GATE-based simulation in GeoSciences. OpenGATE collaboration meeting, 03.-04.05.2012, Athens, Greece.

Lippmann-Pipke, J., Kulenkampff, J., Gründig, M., Richter, M.: Matching 4D porous media fluid flow GeoPET data with COMSOL Multiphysics simulation results. COMSOL Multiphysics Konferenz, 26.-28.10.2011, Stuttgart/Ludwigburg, Germany.

Joseph, C., Van Loon, L.R., Jakob, A., Schmeide, K., Sachs, S., Bernhard, G.: Effect of temperature and humic acid on the U(VI) diffusion in compacted Opalinus Clay. 6th International Conference Uranium Mining and Hydrogeology (UMH VI), 18.-22.09.2011, Freiberg, Germany.

Posters presented at conferences:

Moll, H., Cherkouk, A., Bernhard, G.: Interaction of anaerobic Mont Terri Opalinus Clay bacteria with plutonium(VI). Migration'15 - 15th International Conference on the Chemistry and Migration Behaviour of Actinides and Fission Products in the Geosphere, 13.-18.09.2015, Santa Fe, USA.

Lippold, H., Lippmann-Pipke, J.: Complexation of f-elements with humic carriers – how dynamic is the equilibrium? Migration'15 - 15th International Conference on the Chemistry and Migration Behaviour of Actinides and Fission Products in the Geosphere, 13.-18.09.2015, Santa Fe, USA.

Kulenkampff, J., Gründig, M., Zakhnini, A., Schikora, J., Gerasch, R., Lippmann-Pipke, J.: Visualization of heterogeneous diffusion processes with PET aligned with 3D FE simulation results. 7th International Symposium on Process Tomography, 01.-03.09.2015, Dresden, Germany.

Kulenkampff, J., Gründig, M., Lippmann-Pipke, J.: High-resolution Positron-Emission-Tomography for ultrasensitive spatio-temporal monitoring of tracer transport in porous media. 7th International Conference on Porous Media, 18.-21.05.2015, Padova, Italy.

Lippmann-Pipke, J., Kulenkampff, J., Lippold, H., Stuhlfauth, C., Gerasch, R., Gründig, M.: Benchmarking of reactive transport visualisation (PET) by numerical modelling with COMSOL Multiphysics and PhreeqC. 7th International Conference on Porous Media, 18.-21.05.2015, Padova, Italy.

Bader, M., Drobot, B., Müller, K., Stumpf, T., Cherkouk, A.: Biosorption of uranium on the cells of the halophilic archaea Halobacterium noricense DSM 15987 under highly saline conditions. International Workshop ABC-Salt (IV) - Actinide Brine Chemistry in a Salt-Based Repository. 14.-15.04.2015, Heidelberg, Germany.

Fritsch, K., Schmeide, K.: Uranium retention by montmorillonite at high ionic strengths. Clays in natural and engineered barriers for radioactive waste confinement, 23.-26.03.2015, Brussels, Belgium.

Lippmann-Pipke, J., Stuhlfauth, C., Lippold, H., Kulenkampff, J., Enzmann, F.: Aligning 1D and 2D axial symmetric transport simulations with observations: consequences for the reactive transport. International Symposium of the German Priority Programme SPP 1315 Biogeochemical Interfaces in Soil - Towards a Comprehensive and Mechanistic Understanding of Soil Functions, 06.-08.10.2014, Leipzig, Germany.

Fritsch, K., Schmeide, K.: Influence of ionic strength on U(VI) sorption onto montmorillonite at high salinities. 8th European Summer School on Separation Chemistry and Conditioning as well as Supramolecular, Intermolecular, Interaggregate Interactions, 07.-09.07.2014, Gustav-Stresemann-Institut, Bonn/Bad Godesberg, Germany.

Cherkouk, A., Lütke, L., Moll, H., Bachvarova, V., Selenska-Pobell, S., Bernhard, G.: Microorganisms in potential host rocks for geological disposal of nuclear waste and their interactions with uranium. IGD-TP Geodisposal 2014 Conference, 24.-26.06.2014, Manchester, United Kingdom.

Fritsch, K., Schmeide, K.: Effect of high ionic strengths on U(VI) retention in montmorillonite. RadChem 2014 - 17th Radiochemical Conference, 11.-16.05.2014, Mariánské Lázně, Czech Republic.

Fritsch, K., Schmeide, K., Bernhard, G.: Investigation of the mobility of uranium(VI) in argillaceous rock at higher salinity. Migration'13 - 14th International Conference on the Chemistry and Migration Behaviour of Actinides and Fission Products in the Geosphere, 08.-13.09.2013, Brighton, United Kingdom.

Lippold, H., Lippmann-Pipke, J.: Radiotracer exchange studies on the reversibility of interaction processes related to humic-bound metal transport. Migration'13 – 14th International Conference on the Chemistry and Migration Behaviour of Actinides and Fission Products in the Geosphere, 08.-13.09.2013, Brighton, United Kingdom.

Moll, H., Lütke, L., Bachvarova, V., Geissler, A., Selenska-Pobell, S., Bernhard, G.: Bacterial diversity in Mont Terri Opalinus Clay and the influence of the bacterial Sporomusa sp. isolate on plutonium speciation. Migration'13 - 14th International Conference on the Chemistry and Migration Behaviour of Actinides and Fission Products in the Geosphere, 08.-13.09.2013, Brighton, United Kingdom.

Schikora, J., Kulenkampff, J., Gründig, M., Lippmann-Pipke, J.: Modelling and simulation of 4D GeoPET measurements with COMSOL Multiphysics 4.2a. EGU General Assembly 2012, 22.-27.04.2012, Vienna, Austria.

Schmeide, K., Steudtner, R., Bernhard, G.: Formation of U(VI) lactate and citrate complexes and their sorption onto Opalinus Clay between 10 and 60°C. Workshop "HiTAC – High Temperature Aqueous Chemistry", 09.11.2011, Karlsruhe, Germany.

Kulenkampff, J., Enzmann, F., Gründig, M., Wolf, M., Lippold, H., Lippmann-Pipke, J.: Direct observation of preferential transport pathways in salt rocks by means of GeoPET. International Workshop ABC-Salt (II) - Actinide Brine Chemistry in a Salt-Based Repository. 07.-08.11.2011, Karlsruhe, Germany.

Zakhnini, A., Kulenkampff, J., Sauerzapf, S., Lippmann-Pipke, J., Pietrzyk, U.: Monte Carlo simulations of a ClearPET: Scatter and attenuation of gamma rays in various rock formations. 2011 IEEE Nuclear Science Symposium and Medical Imaging Conference, 23.-29.10.2011, Valencia, Spain.

Schmeide, K., Joseph, C., Steudtner, R., Bernhard, G.: Influence of organic ligands and temperature on U(VI) sorption and diffusion in the system Opalinus Clay/Opalinus Clay pore water. Migration'11 - 13th International Conference on the Chemistry and Migration Behavior of Actinides and Fission Products in the Geosphere, 18.-23.09.2011, Beijing, China.

Schmeide, K., Joseph, C., Bernhard, G.: Sorption and diffusion of U(VI) in the system Opalinus Clay/pore water in the absence and presence of organic ligands. NEA ClayClub Workshop "Clays under Nano- to Microscopic Resolution", 06.-08.09.2011, Karlsruhe, Germany.

Steudtner, R., Schmeide, K., Bernhard, G.: U(VI) complexation with lactate and citrate in dependence on temperature (7-65°C). Goldschmidt 2011, 14.-19.08.2011, Prague, Czech Republic.

List of figures

Fig. 1: Proposed structures of the 1:1, 1:2, and 1:3 U(VI) propionate complexes (blue: uranium; red: oxygen; gray: carbon; light gray: hydrogen). 23

Fig. 2: Comparison of (a) DFT calculated band positions of the asymmetric stretching mode of the uranyl moiety and (b) experimentally observed values in the U(VI) propionate system ([U(VI)] = 5×10^{-3} mol kg^{-1}, 0.1 mol kg^{-1} propionate, pH from 0.98 to 5.03).....24

Fig. 3: Comparison of (a) DFT calculated band positions of the carboxylate region and (b) experimentally observed values in the U(VI) propionate system ([U(VI)] = 5×10^{-3} mol kg^{-1}, 0.1 mol kg^{-1} propionate, pH from 2.51 to 5.03). 25

Fig. 4: Static TRLFS spectra of the U(VI) propionate system ([U(VI)] = 5×10^{-4} mol kg^{-1}, 0 to 0.25 mol kg^{-1} propionate, 0.75 mol kg^{-1} $NaClO_4$). 26

Fig. 5: Extracted emission spectra for 5 components of the U(VI) propionate system ([U(VI)] = 5×10^{-4} mol kg^{-1}, 0 to 0.25 mol kg^{-1} propionate, 0.75 mol kg^{-1} $NaClO_4$).....27

Fig. 6: Species distribution based on luminescence spectroscopy and PARAFAC deconvolution ([U(VI)] = 5×10^{-4} mol kg^{-1}, 0 to 0.25 mol kg^{-1} propionate, 0.75 mol kg^{-1} $NaClO_4$).....27

Fig. 7: Slope analyses for the stepwise formation of $UO_2(Prop)_n^{[2-n]+}$ complexes a n = 1, 2, 3 at 20°C and *I* = 0.75 mol kg^{-1} $NaClO_4$.....28

Fig. 8: Linear SIT regression plots for the first, second and third complexation constant of the U(VI) propionate system at 20°C. 30

Fig. 9: Decrease of [^{242}Pu] in solution at $[^{242}Pu]_{initial}$: 46 mg/L in 0.1 M $NaClO_4$ at pH 4 and 6.1 after contact with 0.33 $g_{dry\ weight}$/L of (A, B) *Sporomusa* sp. MT-2.99 and (C, D) *Paenibacillus* sp. MT-2.2. The red line represents the best fit of the experimental data.....34

Fig. 10: Langmuir isotherms obtained in the *Sporomusa* sp. and the *Paenibacillus* sp. system at pH 4 and 6.1.....35

Fig. 11: Biosorption of Pu on *Sporomusa* sp. MT-2.99 at $[^{242}Pu]_{initial}$: 45 mg/L in 0.1 M $NaClO_4$ as a function of pH under steady state conditions.....36

Fig. 12: Redox potentials in the *Sporomusa* sp. MT-2.99 system at $[^{242}Pu]_{initial}$: 45 mg/L in 0.1 M $NaClO_4$ as a function of pH under steady state conditions. 36

Fig. 13: ^{242}Pu oxidation state distributions in the blank samples determined by solvent extraction as a function of the incubation time ($[^{242}Pu]_{initial}$: 104±11 mg/L, 0.1 M $NaClO_4$, pH 4).....37

Fig. 14: ^{242}Pu oxidation state distributions in the supernatants after separation of the cells determined by solvent extraction as a function of time A) *Sporomusa* sp. and B) *Paenibacillus* sp. ($[^{242}Pu]_{initial}$: 111±2 mg/L, [dry biomass] 0.34 g/L, 0.1 M $NaClO_4$, pH 4).....38

Fig. 15: ^{242}Pu oxidation state distributions in the biomass (*Sporomusa* sp. and P*aenibacillus* sp.) by solvent extraction over the time ($[^{242}Pu]_{initial}$: 15 to 110 mg/L, [dry biomass] 0.34 g/L, 0.1 M $NaClO_4$, pH 6.1 and 4).....39

Fig. 16: Decrease of the $[^{242}Pu]$ in solution at $[^{242}Pu]_{initial}$: 14 mg/L in 0.1 M $NaClO_4$ at pH 4 and 6.1 after contact with 0.34 g/L of (A, B) *Sporomusa* sp. MT-2.99 and (C) at pH 6.1 after contact with 0.22 g/L *Paenibacillus* sp. MT-2.2. The red and blue line represents the best fit of the experimental data.....40

Fig. 17: Percentage of the cell bound Pu extracted from the biomass with 1 M $HClO_4$. 41

Fig. 18: Time-dependent redox potentials measured in the *Sporomusa* sp. system in the presence of 10 mM Na-pyruvate at pH 4 and pH 6.1 ($[Pu]_{initial}$ = 14 mg/L, 0.1 M $NaClO_4$).....42

Fig. 19: ^{242}Pu oxidation state distributions in the blank samples determined by solvent extraction as a function of the incubation time ($[^{242}Pu]_{initial}$: 13.8±0.5 mg/L, 0.1 M $NaClO_4$, 10 mM Na-pyruvate, pH 6.1). 42

Fig. 20: ^{242}Pu oxidation state distributions in the supernatants after separation of the cells determined by solvent extraction as a function of time A) *Sporomusa* sp.: [dry biomass] 0.34 g/L at pH 4 and 6.1 and B) *Paenibacillus* sp.: [dry biomass] 0.22 g/L at pH 6.1 ($[^{242}Pu]_{initial}$: 14 mg/L, 0.1 M $NaClO_4$, 10 mM Na-pyruvate). 43

Fig. 21: ^{242}Pu oxidation state distributions in the biomass (*Sporomusa* sp. 0.34 g/L and P*aenibacillus* sp. 0.22 g/L) by solvent extraction over the time ($[^{242}Pu]_{initial}$: 14 mg/L, 0.1 M $NaClO_4$, 10 mM Na-pyruvate, pH 6.1 and 4 (only for *Sporomusa* sp.). 44

Fig. 22: Eu(III) association on *Halobacterium noricense* DSM-15987 after an incubation time of 1 h as a function of pC_{H+} ([Eu] 30 µM, [dry biomass] 0.5 g/L, 3 M NaCl). 49

Fig. 23: Luminescence emission spectra of 32±3 µM Eu(III) as a function of pH/pC_{H+} after 1 h of contact time in (A) 3 M NaCl with 0.5 g/L *Hbt. noricense* DSM-15987 and in (B) 0.1 M $NaClO_4$ with 0.02 g/L *Sporomusa* sp. MT-2.99. 50

Fig. 24: CE diagram of Eu(III) in *Halobacterium noricense* DSM-15987 suspensions in comparison to the Eu(III)-*Sporomusa* sp. system (Moll et al., 2013; Moll et al., 2014). 51

Fig. 25: ITFA results gained from the TRLFS spectra of the Eu(III)-*Hbt. noricense* system taken after 1 h of incubation time (Fig. 23 A). A: iterative target test (ITT) calculated species distribution of the components and B: ITFA extracted TRLFS component spectra (solid lines) and experimental data (dotted lines).....52

Fig. 26: Luminescence emission spectra of 0.3 µM Cm(III) as a function of pH/pC_{H+} taken after 1 h of incubation time in (A) 3 M NaCl with 0.5 g/L *Halobacterium noricense* DSM-15987 and in (B) 0.1 M $NaClO_4$ with 0.02 g/L *Sporomusa* sp. MT-2.99. 53

Fig. 27: ITFA results gained from the TRLFS spectra of the Cm(III)-*Hbt. noricense* DSM-15987 system (Fig. 26 A). A: iterative target test (ITT) calculated species distribution of the components and B: ITFA extracted TRLFS component spectra (solid lines) and experimental data (dotted lines).....54

Fig. 28: Kinetic of U(VI) sorption on cells of *Hbt. noricense* (pC_{H+} 6, [U(VI)] = 110 µM, 0.5 $g_{dry\ weight}$/L, triplicate). 56

Fig. 29: Agglomeration of *Hbt. noricense* cells with increasing time and uranium concentration.....56

Fig. 30: Biosorption of uranium on cells of *Hbt. noricense* in dependence on pC_{H+} and U(VI) concentration (48 h incubation time, triplicate).....57

Fig. 31: By tracking the sorption process with TRLFS, increasing uranium intensity is detectable in the samples from the cell pellets (black), whereas the intensity decreases in the samples from the supernatant. After 48 h almost no uranium is detectable in the supernatant, everything is bioassociated. 58

Fig. 32: Isotope exchange experiments for probing the equilibrium characteristics of metal-humate complexation (HA: humic acid, M: metal, M*: radioisotope), starting from the state of saturation. 59

Fig. 33: Isotope exchange experiments in a reverse procedure, starting from a very low metal load with the radioisotope M*.....60

Fig. 34: Isotherms of adsorption of Tb(III) onto flocculated humic acid, obtained with ^{160}Tb(III) as a radiotracer, which was added simultaneously or subsequently after different times of pre-equilibration with non-radioactive ^{159}Tb(III) (1 nM [^{160}Tb]Tb, 0.5 g L^{-1} HA Aldrich, 0.1 M $NaClO_4$, pH 4.0). 61

Fig. 35: Amount of [^{160}Tb]Tb(III) bound to humic acids after saturating with non-radioactive ^{159}Tb(III), shown as a function of exchange time for different times of pre-equilibration (1 nM [^{160}Tb]Tb, 2 mM ^{159}Tb, 0.5 g L^{-1} HA, 0.1 M $NaClO_4$, pH 4.0).....62

Fig. 36: Amount of [^{160}Tb]Tb(III) bound to humic acids after 1 h of exchange with ^{159}Tb(III), shown as a function of pre-equilibration time (conditions as in Fig. 35). 63

Fig. 37: Kinetic analysis of isotope exchange by fitting Eq. (4.3) (symbols: data set for HA Aldrich after 46 days of pre-equilibration, solid line: fitted curve calculated with the parameters k_1 = 1.20 d^{-1}, k_2 = 0.01 d^{-1}, x = 0.65). 64

Fig. 38: Adsorption of Tb(III) (pH 5) and Eu(III) (pH 7) onto Opalinus Clay in the presence of NaCl, $CaCl_2$ and $MgCl_2$. 68

Fig. 39: Adsorption of fulvic acid onto Opalinus Clay at pH 5 and 7 in the presence of NaCl, $CaCl_2$ and $MgCl_2$. 68

Fig. 40: Complexation of Tb(III) or Eu(III) with fulvic acid as a function of ionic strength at pH 5 and 7 in the presence of NaCl, $CaCl_2$ and $MgCl_2$. 69

Fig. 41: Adsorption of Tb(III) (pH 5) and Eu(III) (pH 7) on Opalinus Clay in the presence (empty symbols) and absence (full symbols) of fulvic acid as a function of ionic strength for NaCl, $CaCl_2$ and $MgCl_2$ as electrolytes. 70

Fig. 42: Adsorption of Tb(III) (pH 5) and Eu(III) (pH 7) on Opalinus Clay in the presence of fulvic acid as a function of ionic strength for $CaCl_2$ and $MgCl_2$ as electrolytes. The full symbols show the calculated values according to the linear additive model (Eq. (5.4)).....70

Fig. 43: Emission spectra of Eu-fulvate with different concentrations of $CaCl_2$. The spectrum in black represents the Eu^{3+} aquo ion, the spectrum in blue represents the Eu-fulvate complex without a background electrolyte. 72

Fig. 44: Percentage of Eu species in solution as a function of ionic strength for Na^+ and Ca^{2+}. Light colors: fulvate species, dark colors: aquo species.....72

Fig. 45: Emission spectra of Eu-fulvate with 500 µM (left) and 500 mM (right) of Na^+, Mg^{2+}, Ca^{2+}, Al^{3+} or Gd^{3+}. The spectrum in black represents the Eu^{3+} aquo ion, the spectrum in magenta represents the Eu-fulvate complex without a background electrolyte. 73

Fig. 46: Emission spectra of Eu-fulvate with 1 mM (left) and 200 mM (right) of ClO_4^-, NO_3^- or Cl^-. The spectrum in black represents the Eu^{3+} aquo ion, the spectrum in magenta represents the Eu-fulvate complex without a background electrolyte. 74

Fig. 47: Amount of Tb and Eu bound to fulvic acid at pH 5 and pH 7, respectively, plotted against ionic strength for NaCl, $CaCl_2$ and $MgCl_2$. Dark colors: experimental data, light colors: calculated data obtained with the NICA-Donnan model. 75

Fig. 48: Diffractograms of magnetite charges 1 and 2. 81

Fig. 49: Tc retention onto hematite and maghemite as function of a) S/L ratio ($[Tc(VII)]_{init}$ = 1×10^{-5} M, pH 4, 0.1 M NaCl, 2 d contact time) and b) contact time ($[Tc(VII)]_{init}$ = 1×10^{-5} M, pH 4, 0.1 M NaCl, S/L ratio: 1 g/L).....81

Fig. 50: Tc retention onto magnetite (pH 4) and siderite (pH 8.6) as function of contact time ($[Tc(VII)]_{init}$ = 1×10^{-5} M, S/L = 0.2 g/L, 0.1 M NaCl, N_2). 82

Fig. 51: Tc retention onto magnetite and siderite as function of pH value in a) 0.1 M NaCl and b) 1 M NaCl ($[Tc(VII]_{init}$ = 1×10^{-5} M, S/L = 0.2 g/L, N_2, 2 d contact time). 82

Fig. 52: Eh-pH diagram for Tc in 1 M NaCl (10 µM Tc, 25°C) calculated applying the extended Debye-Hückel equation. Redox potentials of selected Tc/magnetite samples monitored at the end of the sorption experiments are shown as blue squares.....83

Fig. 53: Redox potentials of selected Tc/magnetite and Tc/siderite samples (1 M NaCl, 25°C).....84

Fig. 54: Reference IR spectrum of pertechnetate ([Tc(VII] = 5×10^{-4} M, 0.1 M NaCl, 25°C)…84

Fig. 55: *in situ* ATR FT-IR spectra of Tc(VII) sorption on magnetite, hematite and maghemite after a contact time of 15 min. 85

Fig. 56: Tc *K*-edge XANES spectra of Tc(VII) reacted with magnetite in comparison to a TcO_4^- reference spectrum (sample characteristics are given in Table 10). 85

Fig. 57: Tc *K*-edge XANES spectra of Tc(VII) reacted with siderite in comparison to a TcO_4^- reference spectrum (sample characteristics are given in Table 10). 86

Fig. 58: Calculated U(VI) speciation in 3 mol kg^{-1} NaCl in absence (upper picture) and presence (lower picture) of CO_2 ($c_{U(VI)}$ = 1×10^{-6} mol kg^{-1}).....94

Fig. 59: Calculated U(VI) speciation in 1 mol kg^{-1} $CaCl_2$ in absence (upper picture) and presence (lower picture) of CO_2 ($c_{U(VI)}$ = 1×10^{-6} mol kg^{-1}).....94

Fig. 60: TRLFS spectra of U(VI) ($c_{m,U(VI)}$ = 1×10^{-6} mol kg^{-1}) in 3 mol kg^{-1} NaCl in depedence on pH. Left picture: absence of CO_2, right picture: presence of CO_2.....95

Fig. 61: U(VI) sorption kinetic in NaCl.....96

Fig. 62: Cation exchange of U(VI) in NaCl and $CaCl_2$ in dependence on ionic strength. 96

Fig. 63: U(VI) sorption in NaCl in dependence on pH and ionic strength in absence (closed symbols) and presence (open symbols) of CO_2.....97

Fig. 64: U(VI) sorption in $CaCl_2$ in dependence on pH and ionic strength in absence (closed symbols) and presence (open symbols) of CO_2. (Data points at pH_c 8 at I = 0.3 mol kg^{-1} were excluded from the fit due to carbonate content in the sample. Carbonate concentration could not be determined experimentally but was modeled to 2.1×10^{-5} mol kg^{-1}.).....98

Fig. 65: U(VI) sorption isotherm at I = 2 mol kg^{-1} and pH 5.3.....98

Fig. 66: U(VI) sorption on montmorillonite in $MgCl_2$ in presence of CO_2. Points connected for clarity.....99

Fig. 67: ATR FT-IR study of U(VI) sorption on montmorillonite at the sorption maximum in absence of CO_2 in D_2O ($c_{U(VI)}$ = 2×10^{-5} mol kg^{-1}, pH 6.8). Left picture: *in situ* spectra in 3 M NaCl. Right picture: comparison of U(VI) uptake in 0.3 and 3 M NaCl. 100

Fig. 68: U(VI) sorption in 3 mol kg^{-1} NaCl in absence (left) and presence (right) of CO_2 with contribution of U(VI) surface complexes to overall sorption. 102

Fig. 69: U(VI) sorption in 3 mol kg^{-1} $CaCl_2$ in absence (left) and presence (right) of CO_2 with contribution of U(VI) surface complexes to overall sorption. 102

Fig. 70: U(VI) sorption in $CaCl_2$ in presence of CO_2. Open symbols: Pre-equilibration time 1.5 weeks, closed symbols: 4.5 weeks. Points connected for clarity.....103

Fig. 71: Extrapolation of surface complexation constants in NaCl and $CaCl_2$ to I = 0. Closed symbols: log k in NaCl, open symbols: log k in $CaCl_2$. 104

Fig. 72: Calculated U(VI) speciation in mixed electrolyte in absence of CO_2 ($c_{U(VI)}$ = 1×10^{-6} mol kg^{-1}).....105

Fig. 73: TRLFS spectra of U(VI) ($c_{m,U(VI)}$ = 1×10^{-6} mol kg^{-1}) in mixed electrolyte in depedence on pH in absence of CO_2. 105

Fig. 74: U(VI) sorption isotherms in mixed electrolyte in absence of CO_2. 106

Fig. 75: Comparison of U(VI) sorption on different minerals in mixed electrolyte at 23°C and pH_c 6.5 in absence of CO_2. Experiment (a): 4 months equilibration time, experiment (b) and isotherm: 6 weeks pre-equilibration time. 107

Fig. 76: Surface complexation modeling of U(VI) sorption isotherms in mixed electrolyte (absence of CO_2). Left picture: Fit on isotherm data. Right picture: Use of surface complexation constants generated in pure electrolytes and calculated to composition and ionic strength of the mixed electrolyte.....109

Fig. 77: Comparison of results of different U(VI) sorption experiments on montmorillonite in mixed electrolyte at $c_{U(VI)}$ = 1×10^{-6} mol kg^{-1}. Experiment (a): 4 months equilibration time, experiment (b) and isotherm: 6 weeks pre-equilibration time. Solid line: Fit on isotherm data. Shaded line: Use of surface complexation constants generated in pure electrolyte and calculated to average ionic strength and composition of the mixed electrolyte after the end of the experiments. 110

Fig. 78: Experimental set-up used to investigate the U(VI) diffusion in the absence and presence of citric acid (based on (Van Loon et al., 2003a)). 113

Fig. 79**:** Redox potential as a function of time determined in the solutions of reservoir Cell 1, Cell 2, TTA, and UV-vis. Lines were drawn for visual reasons. 120

Fig. 80: UV-vis spectra of the UV-vis reservoir solution as a function of time. Spectra of $UO_2(CO_3)_3^{4-}$ and $(UO_2)_3(cit)_3(OH)_5^{8-}$ provided by Steudtner et al. (2012). 121

Fig. 81: Concentration profiles of ^{233}U(VI) in the absence (filled symbols) and presence (open symbols) of citric acid. 122

Fig. 82: Concentration profile of citric acid in the presence of ^{233}U(VI). 124

Fig. 83: 20 PET-frames of ^{22}Na-diffusion in a OPA-drill core (diameter: 100 mm, length 80 mm). At the bottom of each image: axial (vertical) maximum projection. Above: 3 horizontal slices through the source region; iso-surface of maximum/10, the scaling of the color scales is frame-wise, the maximum value of the color scale is half maximum total amplitude for each (amplitude distribution cf. Fig. 84). 133

Fig. 84: Maximum, 99.9 %- and 90 %-quantiles of the amplitude vs. frame time. The color scale in Fig. 83 refers to the maximum. 134

Fig. 85: Vertical slice representation of frames 0, 1, 2, 4, 6, 10, 18. At the bottom: axial projection of the maximum amplitude as height-map. 135

Fig. 86: Axial maximum projection of frame 9 (27 days). 136

Fig. 87: 15 PET-frames of ^{124}I-diffusion in the same OPA-drill core. At the bottom of each image: axial (vertical) maximum projection. Above: 3 horizontal slices through the source region; iso-surface of maximum/10, the scaling of the color scales is frame-wise, the maximum value of the color scale is half maximum total amplitude for each (amplitude distribution cf. Fig. 88). 137

Fig. 88: Maximum, 99.9 %- and 90 %-quantiles of the amplitude of Fig. 87 vs. time. 138

Fig. 89: Result of the optimum fit of the PET - tracer distribution (left) with a COMSOL Multiphysics FEM model (right) (scaled in molar concentrations). 139

Fig. 90: µCT-image of the fracture system and exemplary images of the waterglass injection tests: Initial brine injection shows flow mainly along the outer edge of one fracture and through the sample, 1st waterglass injection penetrates up to ca. 15 mm and seals the surface, 2nd brine injection shows some sealing effect mainly of large voids, 2nd waterglass injection did not penetrate the volume and causes no improvement of the sealing effect, as can be seen in the 3rd brine injection. 143

List of tables

Table 1: Summary of the complexation constants for the U(VI)/propionate system reported in the literature. 21

Table 2: Experimental pH_{exp} used. 22

Table 3: Overall thermodynamic stability constants log β of the three U(VI)-propionate complexes at variable ionic strengths. 29

Table 4: Overall thermodynamic stability constants log β at I = 0 and the determined ε(i,j)...31

Table 5: Langmuir absorption isotherm data. 35

Table 6: Pu loadings on *Sporomusa* sp. biomass at $[Pu]_{initial}$ = 14 mg/L. 41

Table 7: Spectroscopic properties of the identified Eu(III) species. 50

Table 8: NICA-Donnan parameters adjusted for Tb and Eu. All other parameters in Eqs. (5.6) - (5.9) were taken from Milne et al. (2003). 76

Table 9: Summary of batch sorption experiments. 79

Table 10: Summary of XAS samples. 80

Table 11: Specific surface areas (BET) of magnetite charges 1 and 2. 81

Table 12: Overview of conditions of batch sorption experiments conducted for this study. ...90

Table 13: Luminescence properties of the spectra measured in absence of CO_2. 95

Table 14: Luminescence properties of the spectra measured in presence of CO_2. 95

Table 15: Surface complexation constants in NaCl and $CaCl_2$ at I = 0. 104

Table 16: Luminescence properties of the spectra measured in mixed electrolyte. 106

Table 17: Freundlich coefficients of U(VI) sorption isotherms in mixed electrolytes. 106

Table 18: Surface complexation constants for modeling U(VI) sorption isotherms in the mixed electrolyte. 108

Table 19: Composition of OPA pore water according to Pearson (1998). 112

Table 20: Diffusion parameters determined by HTO diffusion experiments through OPA. ..117

Table 21: Conditions present in the solutions of reservoirs Cell 1, Cell 2, TTA, and UV-vis at the *beginning* of the diffusion experiment as well as the corresponding U(VI) speciation in the solution.....118

Table 22: Conditions present in the solutions of reservoirs Cell 1, Cell 2, TTA, and UV-vis at the *end* of the diffusion experiment as well as the corresponding U(VI) speciation in the solution.....119

Table 23: Parameter values for the ^{233}U(VI) diffusion in OPA in the absence and presence citric acid. 123

Table 24: Parameter values for the citric acid and humic acid diffusion in OPA in the presence ^{233}U(VI). 125

Acknowledgements

The authors thank the Federal Ministry for Economic Affairs and Energy (BMWi) and the Project Management Agency Karlsruhe (PTKA-WTE) for financial support (no. 02 E 10971).

We also thank Karsten Heim, Dr. Harald Foerstendorf and Dr. Katharina Müller for FT-IR measurements and for their help in spectra interpretation, Stephan Weiss, Christa Müller, Heidrun Neubert and Henry Lösch for technical support during UV-Vis and PCS measurements, Dr. Vinzenz Brendler for helpful discussions concerning SIT theory and surface complexation modelling as well as Prof. Dr. Satoru Tsushima for DFT calculations and Dr. Frank Bok for calculation of the E_h-pH diagram.

For support during TRLFS measurements and for discussion of laser spectroscopic results we thank Dr. Robin Steudtner, Björn Drobot, Dr. Nina Huittinen and Dr. Sascha Eidner (Universität Potsdam); Björn Drobot is especially thanked for PARAFAC deconvolution of the data. For scientific discussions on complexation studies we thank Dr. Andrej Skerencak-Frech (Universität Heidelberg) and Dr. Remi Marsac (Karlsruher Institut für Technologie). Dr. Xavier Gaona (Karlsruher Institut für Technologie) is acknowledged for his advice concerning pH measurements at high ionic strength.

For support during XAS measurements we thank Dr. Janeth Lozano-Rodriguez, Dr. Kristina Kvashnina, Dr. Natalia Shcherbina (Forschungszentrum Jülich) and Dr. Natallia Torapava (MAX IV Laboratory). For support in preparation of XAS samples we thank Felix Spranger, Carola Franzen and Stephan Weiss.

Furthermore, we thank Aline Ritter, Sabrina Gurlit, Stefanie Schubert, and Carola Eckardt for ICP-MS analyses, ion chromatography, TIC measurements, and BET determinations, Kathrin Nebe for the help during LSC measurements and Andrea Scholz for XRD measurements.

The authors thank the Bundesanstalt für Geowissenschaften und Rohstoffe (BGR) for providing clay samples, Velina Bachvarova and Dr. Sonja Selenska-Pobell for isolation of the strains and Monika Dudek for anaerobic cultivation of the bacterial isolates from Mont Terri Opalinus Clay. Moreover, the authors are thankful to Tomas Kupcik and Dr. Christian Marquardt (both from Karlsruher Institut für Technologie) for preparing clay tablets for diffusion experiments as well as to Christa Müller, Heidrun Neubert, Sylvia Gürtler, Nadine Lense, Stefanie Schubert, and Lisa Zehlike for technical support in the laboratory. Dr. Susanne Sachs is thanked for help in preparing the Pu-242 stock solution.

For support during PET measurements we thank Marion Gründig, Lars Bittner and Stefan Gruhne.

Technical support by Prof. Dr. Norbert Trautmann, Dr. Klaus Eberhardt and Beatrix Praast (Johannes Gutenberg-Universität Mainz) for the production of Tb-160 in the TRIGA Mark II reactor is gratefully acknowledged.

The authors are indebted for the use of the Cm-248 to the U.S. Department of Energy, Office of Basic Energy Sciences, through the transplutonium element production facilities at Oak Ridge National Laboratory which was made available as part of a collaboration between HZDR and the Lawrence Berkeley National Laboratory (LBNL).

Finally, we would like to thank all other colleagues who contributed to the success of the project.

HZDR
HELMHOLTZ ZENTRUM DRESDEN ROSSENDORF

Bautzner Landstr. 400
01328 Dresden, Germany
Telefon: +49 351 260-2436
Telefax: +49 351 260-3553
Email: k.schmeide@hzdr.de
http://www.hzdr.de